Chair of Physical Chemistry

Doctoral Thesis

Development of new materials for solid oxide fuel cell cathodes with superior performance and improved long-term stability

Dipl.-Ing. Christian Berger, BSc

March 2019

EIDESSTATTLICHE ERKLÄRUNG

Ich erkläre an Eides statt, dass ich diese Arbeit selbständig verfasst, andere als die angegebenen Quellen und Hilfsmittel nicht benutzt, und mich auch sonst keiner unerlaubten Hilfsmittel bedient habe.

Ich erkläre, dass ich die Richtlinien des Senats der Montanuniversität Leoben zu "Gute wissenschaftliche Praxis" gelesen, verstanden und befolgt habe.

Weiters erkläre ich, dass die elektronische und gedruckte Version der eingereichten wissenschaftlichen Abschlussarbeit formal und inhaltlich identisch sind.

AFFIDAVIT

I declare on oath that I wrote this thesis independently, did not use other than the specified sources and aids, and did not otherwise use any unauthorized aids.

I declare that I have read, understood, and complied with the guidelines of the senate of the Montanuniversität Leoben for "Good Scientific Practice".

Furthermore, I declare that the electronic and printed version of the submitted thesis are identical, both, formally and with regard to content.

Date 04.03.2019

_____

Signature Author
Christian, Berger
Matriculation Number: 00730620

Dedicated to my beloved wife Marlene Rosa-Maria

Acknowledgements

At first, I would like to thank Univ.-Prof. Dr. Werner Sitte (Head of the Chair of Physical Chemistry) for giving me the opportunity to work as a project- and university-assistant at the Chair of Physical Chemistry and to participate and present my research results on several national and international conferences.

A very special word of thanks goes to Assoc.Prof. Dr. Edith Bucher for the excellent supervision of my PhD-thesis and the great effort she made.

I would like to thank all colleagues from the Chair of Physical Chemistry for their warm welcome in the research group and the constructive and pleasant working time. Especially I want to thank DI Nina Schrödl for sharing the laboratory and fruitful discussions. I also would like to thank Dr. Andreas Egger, DI Peter Gsaxner and Ao. Univ.-Prof. DDr. Wolfgang Preis for their help regarding conductivity relaxation measurements, configuration of measurement setups and introduction to differential scanning calorimetry. I also would like to thank Karin Stanglauer for various support in the laboratory and performing EDX measurements. Additionally, I would like to thank Christina Nader and Mario Micu-Budisteanu for laboratory work assistance during their bachelor theses.

A special thank goes to Prof. Joachim Maier (Director of the Department Physical Chemistry of Solids at the Max Planck Institute for Solid State Research) and co-workers for giving me the opportunity to work 9 months during my PhD-thesis at the Max Planck Institute for Solid State Research in Stuttgart, Germany. I especially would like to acknowledge Dr. Rotraut Merkle for supervising me during the visiting research fellowship at the Max Planck Institute for Solid State Research and great discussions.

I would like to thank Dr. Christian Gspan and DI Judith Lammer from FELMI-ZFE Graz for performing TEM measurements and for giving me the opportunity to join the TEM sessions and Martina Dienstleder from FELMI-ZFE for the preparation of the TEM samples. For performing SEM-EDX measurements and always finding a time slot for me, I would like to thank Gerhard Hawranek (Department Physical Metallurgy and Materials Testing).

I want to thank the Österreichische Forschungsförderungsgesellschaft (FFG) and AVL List GmbH for funding my thesis in the projects SENTECH, ASYSII, and SOFC-SALT.

Finally, I want to thank my beloved wife Marlene Rosa-Maria Berger and my family for support.

Abstract

Solid oxide fuel cells (SOFCs) represent a highly efficient and sustainable future technology for stationary energy generation. Nevertheless, several obstacles need to be overcome in order to achieve a broad introduction in the commercial market. In this regard, one of the most critical factors is the limited long-term stability of the cells, especially of the cathode. Degradation of the cathode is frequently caused by contaminants, which are introduced through the air feed, or originate from stack components. These degradation effects can decrease the performance of the stack significantly during operation for several thousand hours. Thus, the development of long-term stable cathode materials with excellent mass and charge transport properties is one of the most important aspects of current research worldwide.

The first part of the present thesis focuses on synthesis and characterisation of novel SOFC cathode materials with perovskite structure. The aim is the development of compounds which show fast oxygen exchange kinetics, good ionic and electronic conductivities, as well as high tolerance against critical impurities. Single phase materials are synthesised and characterised regarding mass and charge transport properties and defect chemistry. The second part of the thesis focuses on the optimisation of the oxygen exchange kinetics of alkaline earth-free SOFC cathode materials with K_2NiF_4-type structure. These generally offer extraordinarily high oxygen diffusivities, but the oxygen exchange kinetics is limited by the surface exchange process. Thus, the aim is the synthesis and characterisation of new K_2NiF_4-type materials with significantly higher surface exchange coefficients for oxygen.

The results of the thesis show impressively that a series of promising SOFC cathode materials with fast oxygen exchange kinetics and high SO_2 tolerance could be developed by purposeful variation of the chemical composition. For various compositions of $La_{1-x}Ca_xFeO_3$ (with x=0.1 for LCF91, x=0.2 for LCF82, and x=0.25 for LCF7525) comprehensive data were acquired on important material parameters such as oxygen exchange kinetics, ionic- and electronic conductivity, thermal expansion coefficient, and oxygen nonstoichiometry as functions of temperature and oxygen partial pressure. Furthermore, the effect of changing the A-site cation from La to Pr at x=0.2 leading to $Pr_{0.8}Ca_{0.2}FeO_3$ (PCF82) is investigated. These studies lead to the conclusion that LCF82 shows the best material properties for application in SOFC-cathodes. However, with respect to increased long-term stability (SO_2 tolerance), PCF82 shows the most promise. Within this work, detailed insights into the mechanisms of cathode degradation were obtained down to the nanometre scale. This knowledge was used to develop and validate strategies for the improvement of long-term stability. With PCF82, island-like growth of

secondary phases, which are formed by reaction of the cathode material with sulphur dioxide, results in a relatively low degree of coverage of the surface with inactive phases. This characteristic feature of PCF82 leads to an increased long-term stability of the surface oxygen exchange kinetics under critical conditions. With the new K_2NiF_4-type materials, an increase in the chemical surface exchange coefficient of oxygen could be achieved by partial substitution of Ni with Co.

Table of contents

1) Introduction 8
2) Description of the study design 9
3) State of the art cathodes in solid oxide fuel cell technology 10
4) Contribution of this work to the scientific community 18
5) Characterisation techniques 23
5.1) X-ray powder diffraction (XRD) 23
5.1.1) Formation and characteristics of X-rays 23
5.1.2) Fundamentals of X-ray diffraction 25
5.1.3) Powder diffraction pattern 26
5.1.4) Rietveld refinement 28
5.2) Electronic conductivity and dc-conductivity relaxation measurements (EC/CR) 33
5.2.1) Sample geometry and electronic conductivity 33
5.2.2) Dc-conductivity relaxation measurements 34
5.2.3) Oxygen exchange kinetics 35
6) Summary of the results and conclusions 36
7) Literature 38
8) Publications 42
8.1) Publications submitted for this thesis 42
8.2) Additional Publications 42
9) Appendix 45
9.1) Contribution and apportionment of work for the publications 45
9.2) Full text of the publications submitted for this thesis 56

1) Introduction

Currently, the rising energy demand and the effort for minimal environmental impact are strong driving factors in the research for new energy systems. Energy is currently still generated mostly from fossil fuels, which have many drawbacks, especially in terms of environmental pollution and impeded availability. This led to increased efforts in research and development in both identification of alternative renewable energy resources, and improvement in energy conversion efficiency of alternative power generating devices [1-4].

Solid oxide fuel cells are very promising alternative power generation devices, which convert chemical energy into electrical energy and thermal energy. The chemical energy is provided by the reaction of fuel (H_2, CH_4, C_2H_5OH etc.) with an oxidant (usually O_2 from air). Major advantages of SOFCs are the low emissions and the high energy conversion efficiencies, because the energy generation is not limited by the Carnot cycle (overall efficiencies greater than 80 % could be achieved [1]). For instance, it was reported that a 100 kW SOFC system, operated on biogas as a fuel, reached an efficiency of 48.7 %, which is about 7 % higher than the commonly used gas turbine [5]. Typically, an SOFC consists of an anode and a cathode, which are separated with a thin electrolyte. As the name SOFC suggests, all cell components are based either on solid oxides, especially ceramics and ceramic-metal composites (electrolyte, cathode, and anode), or on metals (stainless steel interconnectors between single cells) [6-8]. The SOFC cathode is of major importance for the overall cell performance and therefore needs extensive study. During the oxygen reduction reaction, molecular oxygen adsorbs on the surface, dissociates and is incorporated into the electrolyte in the form of O^{2-} ions. For a high efficiency of these processes, the cathode material has to provide fast oxygen exchange kinetics, as well as sufficient ionic and electronic conductivities.

In addition, for successful commercialisation of SOFCs, strategies for reducing the costs for raw materials and processing, and increase long-term stability, have to be found. One promising way to reduce the degradation, is to lower the operation temperature from 1000°C to 600-800°C (intermediate temperature regime) [1]. Thus, novel cathode materials with reduced raw material costs, as well as superior performances in the intermediate temperature regime and high long-term stability, need to be developed to overcome the current obstacles for commercialisation.

2) Description of the study design

The aim of this thesis was to overcome some of the most important current issues in SOFC cathode development, such as degradation in cathode performance due to surface poisoning effects, limited cathode performance due to reduced oxygen exchange kinetics at intermediate temperatures, and insufficient thermal expansion compatibility between the cathode and the electrolyte.

At the beginning of this work, an extensive literature study was performed to obtain an overview of the performance of different cathode materials in the fresh state, as well as their degradation behaviour in sulphur dioxide containing atmospheres. Additionally, other important material parameters like the ionic and electronic conductivity, the thermal expansion coefficient and the oxygen exchange kinetics were also considered.

Based on the results from the literature study, two material classes were selected for their promising properties: Perovskite ferrites and cobaltites like $(La,Sr)(Fe,Co)O_{3-\delta}$ and K_2NiF_4-type oxides like $(La,Pr)_2NiO_{4+\delta}$.

Chapter 3 of this thesis describes the properties of the above-mentioned material classes in terms of crystal structure and oxygen exchange kinetics. The state of the art materials show good performance in their fresh state (in atmospheres without critical impurities), but this drastically changes in the SO_2 poisoned state.

Chapter 4 describes the actions that were implemented to improve the SO_2 tolerance in ferrite perovskites and to increase the oxygen exchange kinetics in the $Pr_2NiO_{4+\delta}$ based materials.

Chapter 5 describes the theoretical background of the measurement techniques used to obtain the published results.

3) State of the art cathodes in solid oxide fuel cell technology

Fuel cells convert chemical energy into electrical energy by oxidising fuel (for instance H_2 or CH_4) on the anode side and simultaneously reducing oxygen (to O^{2-}) on the cathode side. The migration of oxygen ions through the cathode and the electrolyte and the transfer of the electrons to the external consumer line close the circuit. In SOFC technology, all components are ceramic materials (or ceramic-metallic composites) and the operating temperatures range from 600 to 1000°C. With intermediate temperature solid oxide fuel cells (IT-SOFCs), operating temperatures are in the range of 600-850°C. A schematic of an SOFC with gas supply channels is shown in Figure 3-1a.

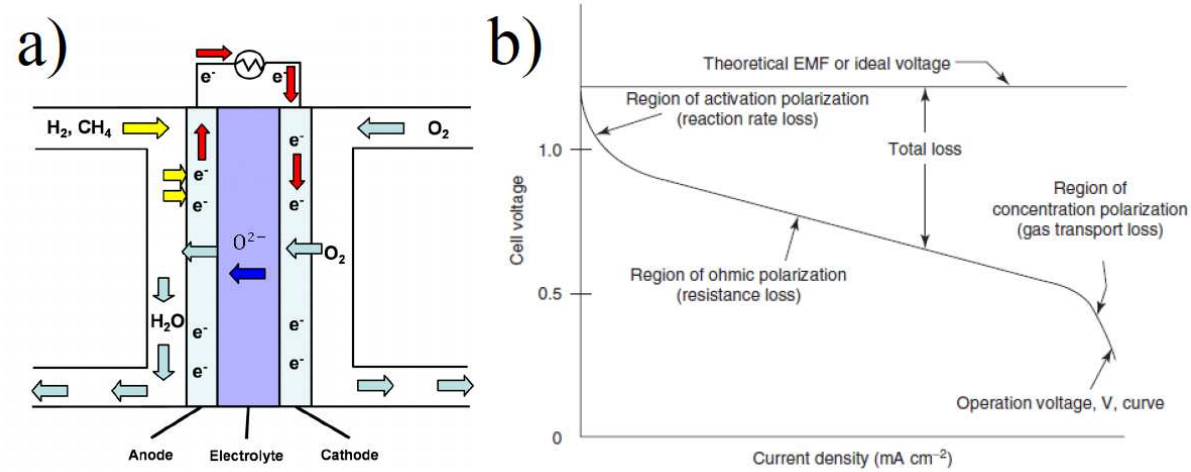

Figure 3.1: a) Working principle of an SOFC (single cell). Figure modified from [9]; b) Typical losses of an SOFC (single cell) compared to ideal voltage. Figure taken from [10].

Figure 3-1b shows the cell voltage as a function of the current density for an SOFC (single cell). The theoretical or ideal voltage, derived from the electromotoric force of the Nernst equation (Equation 3.1) is independent of the current density, whereas the actual operating voltage is a function of current density. The overall chemical reaction in a fuel cell can be written as shown in Reaction 3.1.

$$EMF = E^0 - \frac{R \cdot T}{4 \cdot F} \cdot \ln\left(\frac{p_{H_2O}^2}{p_{H_2}^2 \cdot p_{O_2}}\right) \qquad \text{(Equation 3.1)}$$

$$2H_2 + O_2 \rightleftharpoons 2H_2O \qquad \text{(Reaction 3.1)}$$

E^0… standard potential derived from Reaction 3.1

The overall loss of an SOFC is composed of several contributions. The effects which predominate at small current densities, called reaction rate losses or activation polarisation, are due to kinetic limitations in the reactions occurring at the anode and cathode. Hereby, the losses stemming from the oxygen incorporation reactions at the SOFC cathode, are usually predominating. The cell voltage loss in this region could be minimized by an optimisation of the cathode material itself (faster oxygen exchange kinetics, higher ionic and electronic conductivity and improved stability against pollutants from the environmental air or from the stack) and by improving the microstructure of the cathode and the cathode electrolyte interface. The losses at intermediate current densities are due to ohmic resistances in the cell, with the contribution of the electrolyte being most pronounced. At high current densities, losses due to gas transport limitations occur.

In the next chapter, commonly used SOFC cathode materials are discussed in terms of their crystal structure, oxygen exchange kinetics and stability against sulphur dioxide. Recent studies from literature showed that two types of material classes (perovskites and Ruddlesden-Popper phases) show desired properties for SOFC cathodes [3, 11-15]. Those are high ionic and electronic conductivity, fast oxygen exchange kinetics, as well as thermal stability and chemical compatibility with commonly used electrolyte ceramics. Kröger-Vink notation is used to describe the defect chemical reactions as seen in the following reactions [16].

Perovskites are a class of materials with the chemical formula ABX_3, where in our case the A-site is occupied by rare earth ions (La^{3+}, $Pr^{3+/4+}$, etc.), the B-site is occupied by transition metal ions ($Fe^{2+/3+/4+}$, $Co^{2+/3+/4+}$, etc.) and in the case of oxides, $X=O^{2-}$. Substitution on the A-site with alkaline earth ions, or reduction of the B-site ion, generates oxygen vacancies $V_O^{\cdot\cdot}$ according to Reaction 3.2 and Reaction 3.3 in the case of $La_{0.6}Sr_{0.4}CoO_{3-\delta}$ (LSC64). This formation of oxygen vacancies directly corresponds to an increase in the oxygen nonstoichiometry δ.

$$\tfrac{1}{2}O_2 + V_O^{\bullet\bullet} + 2\,Co_{Co}^{x} \rightleftharpoons O_O^{x} + 2\,Co_{Co}^{\bullet} \qquad \text{(Reaction 3.2)}$$

$$[O_O^{x}] + [V_O^{\bullet\bullet}] = 3, \text{ where } [V_O^{\bullet\bullet}] = \delta \qquad \text{(Reaction 3.3)}$$

The crystal structure of LSC64 is shown in Figure 3.2.

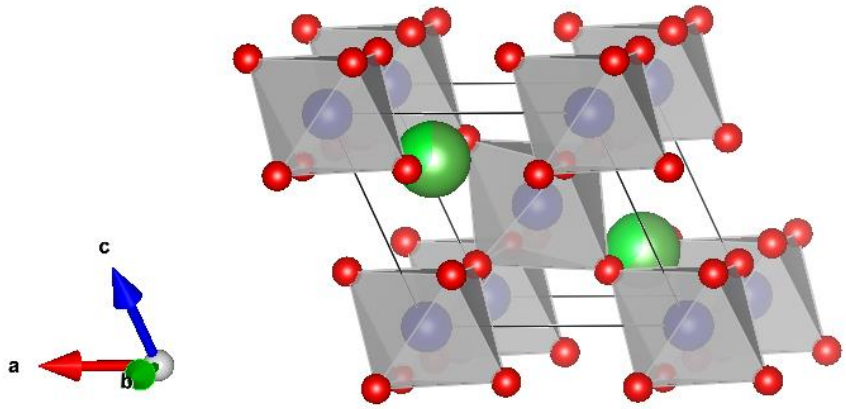

Figure 3.2: Crystal structure of the trigonal (*R-3c*) LSC64. Structural data taken from [17] and image generated with VESTA [18].

Figure 3.2 shows an extended unit cell of LSC64 with $Co^{2+/3+/4+}$ (in blue) located in the centre of the oxygen (in red) octahedra. On the A-site lattice La^{3+} and Sr^{2+} (in green) share atomic positions.

Another interesting material class are Ruddlesden-Popper (RP) phases. Their chemical formula $A_{n+1}B_nO_{3n+1}$ also consists of A- and B-site cations and the parameter n (whole number) represents the order of the Ruddlesden-Popper phase. $Pr_2NiO_{4+\delta}$ (PNO) is an example of a first order (n=1) RP-phase. In the case of n=1, the resulting crystal structure is also known as K_2NiF_4-type structure. The over-stoichiometric oxygen content of the alkaline earth-free material PNO is due to incorporation of interstitial oxygen O_i'' (charge-compensated by the formation of electron holes $h^{\cdot}$), which provides the basis for oxygen migration via interstitial transfer [19, 20]. The formation of oxygen interstitials is shown in Reaction 3.4.

$$\frac{1}{2}O_2 + V_i^x \rightleftharpoons O_i'' + 2\,h^{\cdot} \qquad \text{(Reaction 3.4)}$$

The crystal structure of PNO is shown in Figure 3.3.

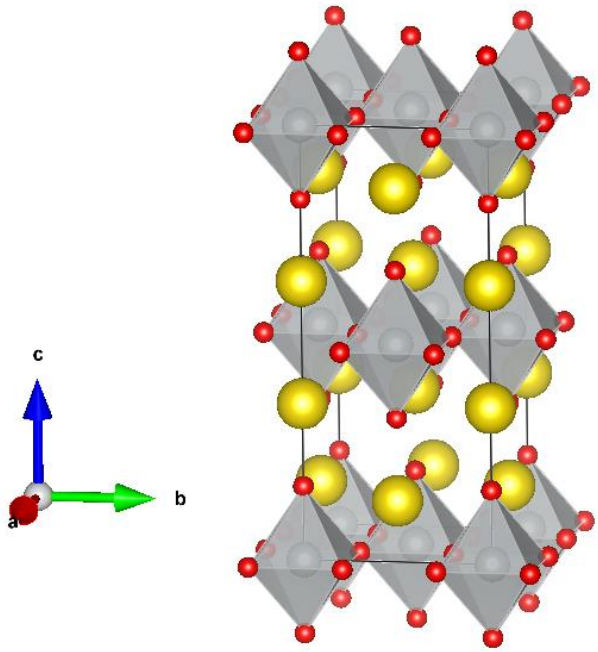

Figure 3.3: Crystal structure of the orthorhombic (*Fmmm*) PNO. Structural data taken from [21] and image generated with VESTA [18].

Figure 3.3 shows an extended unit cell of PNO with Ni^{2+} (in grey) located in the centre of the oxygen (in red) octahedra. Pr^{3+} (in yellow) is located on the A-site lattice.

As explained in detail in chapter 5.2, the possibility of a fast oxygen exchange reaction must be given for future SOFC cathodes. The following tables show literature data for surface exchange coefficients and bulk diffusion coefficients of oxygen of various materials (perovskites and first order Ruddlesden-Popper phases).

Table 3.1: Chemical oxygen surface exchange coefficients (k_{chem}) and chemical diffusion coefficients of oxygen (D_{chem}) of state of the art SOFC cathodes with perovskite structure. Data was taken from the literature. Table modified from the supplementary material of [22].

Compound	k_{chem} / cm s^{-1}	D_{chem} / cm^2 s^{-1}	T / K	Ref.
$La_{0.9}Sr_{0.1}FeO_{3-\delta}$	--	3×10^{-6} at 1×10^{-1} bar pO_2	998	[23]
$La_{0.6}Sr_{0.4}FeO_{3-\delta}$	3×10^{-5} at 1×10^{-2} bar pO_2	3×10^{-6} at 1×10^{-1} bar pO_2	998	[23]
$La_{0.6}Sr_{0.4}FeO_{3-\delta}$	9×10^{-5} at 6.7×10^{-4} bar pO_2	5×10^{-7} at 6.7×10^{-4} bar pO_2	973	[24]
$La_{0.8}Sr_{0.2}CoO_{3-\delta}$	--	3×10^{-7} at 1×10^{-1} bar pO_2	973	[25]
$La_{0.8}Sr_{0.2}CoO_{3-\delta}$	6×10^{-5} at 1×10^{-2} bar pO_2	5×10^{-7} at 1×10^{-1} bar pO_2	1023	[26]
$La_{0.6}Sr_{0.4}CoO_{3-\delta}$	3×10^{-5} at 1×10^{-2} bar pO_2	1×10^{-6} at 1×10^{-1} bar pO_2	973	[27]

Table 3.2: Tracer oxygen surface exchange coefficients (k^*) and tracer diffusion coefficients of oxygen (D^*) of state of the art SOFC cathodes with K_2NiF_4 structure. Data was taken from the literature.

Compound	k^* / cm s^{-1}	D^* / cm^2 s^{-1}	T / K	Ref.
$La_2NiO_{4+\delta}$	8×10^{-8} at 2×10^{-1} bar pO_2	2×10^{-8} at 2×10^{-1} bar pO_2	923	[28]
$La_2Ni_{0.9}Co_{0.1}O_{4+\delta}$	7×10^{-7} at 2×10^{-1} bar pO_2	2×10^{-8} at 2×10^{-1} bar pO_2	923	[28]
$Pr_2NiO_{4+\delta}$	7×10^{-7} at 2×10^{-1} bar pO_2	3×10^{-8} at 2×10^{-1} bar pO_2	887	[15]
$Pr_{1.9}Ni_{0.75}Cu_{0.25}O_{4+\delta}$	1×10^{-6} at 2×10^{-1} bar pO_2	3×10^{-7} at 2×10^{-1} bar pO_2	928	[29]
$Pr_{1.9}(Ni_{0.74}Cu_{0.25})_{0.95}Ga_{0.05}O_{4+\delta}$	3×10^{-7} at 2×10^{-1} bar pO_2	2×10^{-6} at 2×10^{-1} bar pO_2	928	[29]

Oxygen exchange parameters from the tables above (Table 3.1 and Table 3.2) were obtained under ideal laboratory conditions with pure test gases and with short time scales far from operation times in SOFC technology. However, under operation-relevant working conditions, there are several critical factors reducing the lifetime of cathode materials.

In the following, the origin of the most critical contaminants (Si, Cr, and SO_2), and their degradation mechanisms (according to literature), are explained in more detail.

Silicon originates from the glass seals which are used to separate the air and fuel gas streams and combine the single cells with an interconnector in the fuel cell stack. The interconnectors are fabricated from ferritic steels containing chromium to reduce corrosion effects, or from chromium based alloys [30, 31]. Studies showed that the presence of Si and Cr sources in dry atmosphere has no negative impacts on the ceramic cathode materials [32]. Nevertheless, under operation relevant conditions of fuel cells, the air contains significant amounts of humidity (which leads to the formation of volatile Cr and Si species), as well as traces of sulphur dioxide. Several studies showed the negative impact of Cr and Si on perovskites and K_2NiF_4-type materials in humid atmosphere [32-35]. The main degradation effect in both cases is the formation of secondary Cr and Si rich phases, which block the active sites for the oxygen

reduction reaction and therefore reduce the performance of the cell. The following reactions show the formation of volatile Cr and Si species in humid atmospheres [36, 37].

$$Cr_2O_3\ (s) + \frac{3}{2}O_2\ (g) \rightleftharpoons 2\ CrO_3\ (g) \qquad \text{(Reaction 3.6)}$$

$$Cr_2O_3\ (s) + 2\ H_2O\ (g) + \frac{3}{2}\ O_2 \rightleftharpoons 2\ CrO_2(OH)_2\ (g) \qquad \text{(Reaction 3.7)}$$

$$SiO_2\ (s) + 2\ H_2O\ (g) \rightleftharpoons Si(OH)_4\ (g) \qquad \text{(Reaction 3.8)}$$

The main degradation mechanisms in terms of SO_2-poisoning are the reactions of (acidic) sulphur dioxide with (basic) layers or particles of secondary phases which are usually present at the surface of SOFC cathode materials after longer operating times. These layers or particles may be composed of binary oxides AO, AO_2 or complex oxides like spinel AB_2O_4 or brownmillerite $A_2B_2O_5$, where A= Ca, Sr, Ba and B= Fe, Co. These reactions result in the formation of large sulphate crystals (e.g. $SrSO_4$) on the surface and those, similar to silicates or chromates which form due to Si- and Cr-poisoning, block the active sites on the surface for the oxygen reduction reaction. There are two ways to reduce the possibility of secondary phase formation on the surface of the cathode. The first is to reduce the lattice mismatch by choosing substituent ions with similar ionic radii to the host ions in the crystal lattice (see Table 3.3). The second is to reduce basicity of the compounds, to reduce the driving force for reaction with acidic impurities (Table 3.4).

Table 3.3: Ionic radii of selected ions depending on the coordination environment for perovskites and K_2NiF_4-type oxides according to Shannon et al. [38]. *no data for the coordination number XII available.

Ion	Coordination number	Ionic radius / Å
Ca^{2+}	XII	1.34
Sr^{2+}	XII	1.44
La^{3+}	XII	1.36
Pr^{3+}	IX*	1.18
Fe^{3+} (high spin)	VI	0.65
Co^{2+} (high spin)	VI	0.75
Ni^{2+}	VI	0.69

Table 3.4: Basicity values for binary oxides with standard deviations given in parentheses according to [39]. Oxides with a basicity less than -5 are purely basic, whereas purely acidic oxides only show positive values for basicity [39].

Oxide	Basicity	Oxide	Basicity
CaO	-7.5 (0.4)	SiO_2	0.9 (0.2)
SrO	-9.7 (0.4)	CrO_3	6.6 (0.8)
Fe_2O_3	-1.7	SO_2	7.1 (0.6)
CoO	-3.8	CO_2	5.5 (0.4)
La_2O_3	-6.1		
Pr_2O_3	-5.8		

The following chapter describes the strategies developed to improve SO_2 tolerance of the rare earth calcium ferrites investigated in this thesis, and the motivation to use Co as a dopant to enhance the surface oxygen exchange kinetics in K_2NiF_4-type oxides.

4) Contribution of this work to the scientific community

The primary aim of this thesis was to develop novel SOFC cathode materials with fast oxygen exchange kinetics, high ionic and electronic conductivities, as well as high tolerance against SO_2. As described in the previous chapter, Sr-containing perovskites show fast oxygen exchange kinetics, but poor performance in SO_2 containing atmospheres. As seen in chapter 3, acidic impurities often tend to react with basic secondary phases. By making adjustments in terms of ionic radii (all ionic radii taken from Shannon tables [38]), Sr^{2+} (XII) (1.44 Å) is replaced with Ca^{2+} (XII) (1.34 Å) to reduce the lattice mismatch compared to La^{3+} (XII) (1.36 Å), and the thermodynamic stability is improved by replacing Co with Fe (see Table 3.4). The following table shows selected kinetic parameters of Ca-substituted perovskites investigated in this thesis.

Table 4.1: Chemical oxygen surface exchange coefficients (k_{chem}) and chemical diffusion coefficients of oxygen (D_{chem}) of the promising Ca-containing SOFC cathodes with perovskite structure.

Compound	k_{chem} / cm s^{-1}	D_{chem} / cm^2 s^{-1}	T / K	Ref.
$La_{0.9}Ca_{0.1}FeO_{3-\delta}$	9×10^{-4} at 1×10^{-1} bar pO_2	7×10^{-6} at 1×10^{-1} bar pO_2	1073	[22]
$La_{0.8}Ca_{0.2}FeO_{3-\delta}$	6×10^{-3} at 1×10^{-1} bar pO_2	2×10^{-5} at 1×10^{-1} bar pO_2	1073	[40]
$La_{0.75}Ca_{0.25}FeO_{3-\delta}$	3×10^{-3} at 1×10^{-1} bar pO_2	9×10^{-6} at 1×10^{-1} bar pO_2	1073	[41]
$Pr_{0.8}Ca_{0.2}FeO_{3-\delta}$	2×10^{-3} at 1×10^{-1} bar pO_2	5×10^{-6} at 1×10^{-1} bar pO_2	1073	[40]

All of the compounds shown in Table 4.1 show faster oxygen exchange kinetics (taking temperature and oxygen partial pressure into account) than the state of the art materials mentioned in Table 3.1. Substituting Sr with Ca not only improves the oxygen exchange kinetics, but also the SO_2 tolerance as seen in Table 4.2 and Figure 4.1. Tests under conditions of accelerated aging were performed for LCF82 and PCF82 [42, 43].

Table 4.2: Impact of SO_2 on various SOFC cathode materials. The left column shows scanning electron microscopy images obtained with the secondary electron detector and the right column shows scanning transmission electron microscopy overview images of various lamellas. LSC64 and LCF82 images taken from [42, 44]. PCF82 images taken from [43].

Compound	SEM	STEM
LSC64	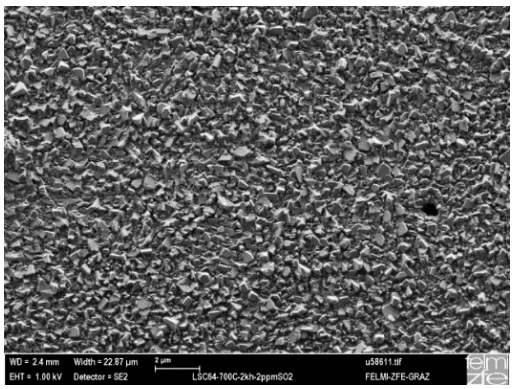	
LCF82	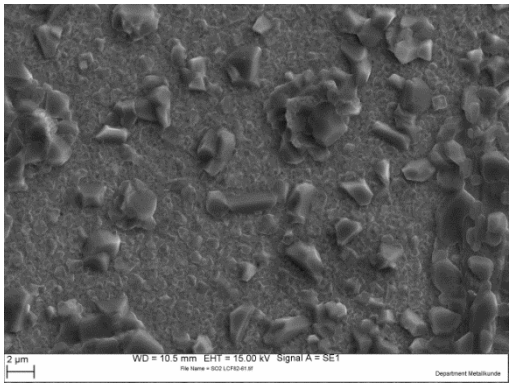	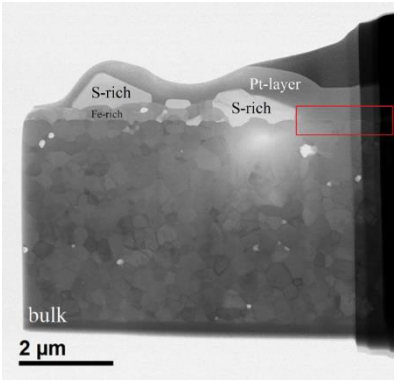
PCF82	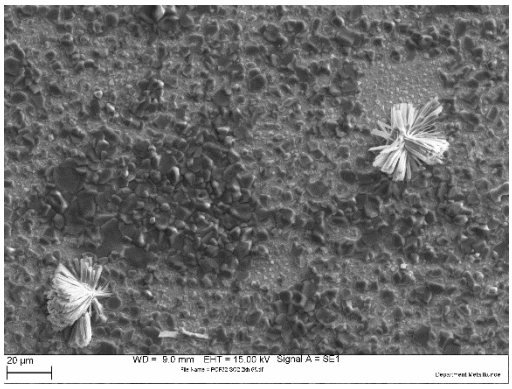	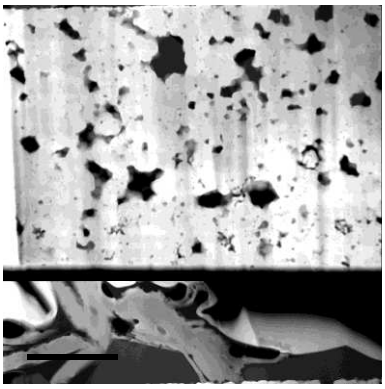

SEM and STEM images from Table 4.2 were recorded after 1000 h in SO_2-O_2-Ar (2 ppm SO_2) at 700°C. The surface coverage with secondary phases ($SrSO_4$ for $La_{0.6}Sr_{0.4}CoO_{3-\delta}$, $CaSO_4$ for $La_{0.8}Ca_{0.2}FeO_{3-\delta}$, $CaSO_4$ and $Pr_2(SO_4)_3$ for $Pr_{0.8}Ca_{0.2}FeO_{3-\delta}$) reduces from $La_{0.6}Sr_{0.4}CoO_{3-\delta}$ (80 %) over $La_{0.8}Ca_{0.2}FeO_{3-\delta}$ (40 %) to just (25 %) for $Pr_{0.8}Ca_{0.2}FeO_{3-\delta}$. The degree of surface coverage was estimated by using threshold analysis provided by the software ImageJ [45]. This trend could also be seen in k_{chem} shown in Figure 4.1.

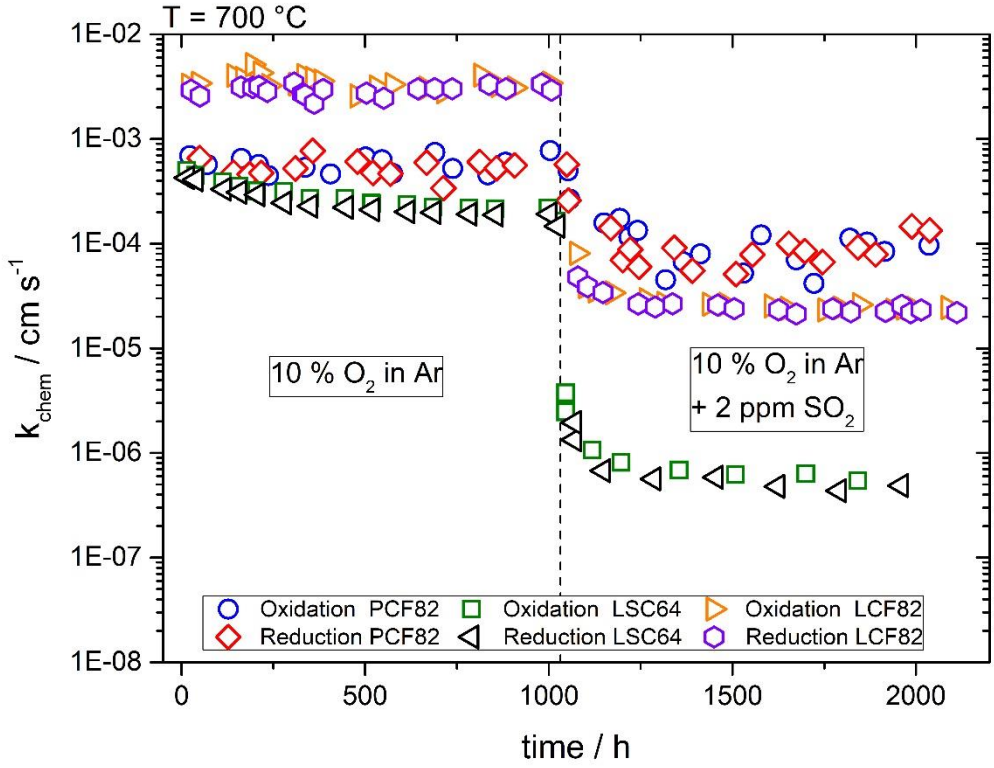

Figure 4.1: Dependence of the chemical surface exchange coefficients (k_{chem}) of various materials on time in atmospheres without and with SO_2.

During the first 1000 h in 10 % O_2 in Ar, LCF82 and PCF82 showed a stable behaviour with small deviations between oxidation and reduction reaction. LSC64 also showed a good match between oxidation and reduction reaction similar to LCF82 and PCF82, but k_{chem} for LSC64 decreased over time due to minor SO_2 impurities from the gas phase. Overall, LCF82 shows the highest values for k_{chem} during the first 1000 h without SO_2, followed by PCF82, which shows similar, but more stable values for k_{chem} compared to LSC64. After addition of 2 ppm SO_2, the surface exchange coefficient decreases for every material investigated in Figure 4.1, due to formation of blocking secondary phases on the surface. However, as seen in the SEM and STEM images of Table 4.2, the surface of LSC64 was almost completely covered and this explained the poor performance of LSC64 in sulphur containing atmospheres [44]. Approximately the same extent of degradation could be observed for LCF82. The major difference to LSC64 is the improved kinetics in the fresh state (without SO_2) and therefore higher values for k_{chem} in the degraded state (with additional 2 ppm SO_2). Further, the degree of coverage was less for LCF82 compared to LSC64 (see red square in STEM image for LCF82 in Table 4.2) [42]. The fastest surface oxygen exchange kinetics in SO_2 containing atmospheres could be achieved with PCF82 [43]. As seen in the SEM image in Table 4.2, large areas of the

sample surface were not affected by SO_2. Especially, areas next to the needle shaped $Pr_2(SO_4)_3$ crystals remain unaffected, although SO_2 reacts with the bulk area of PCF82 forming $CaSO_4$ on top of the surface and in the bulk region (see PCF82 STEM image in Table 4.2).

The second part of this thesis focuses on the improvement of oxygen exchange kinetics for alkaline earth-free SOFC cathode materials by introducing K_2NiF_4-type structures (first order Ruddlesden-Popper phases). K_2NiF_4-type oxides exhibit exceptionally high bulk diffusion coefficients for oxygen, but the kinetics is frequently limited by the surface oxygen exchange process, as seen in chapter 3. Table 3.2 shows two important trends. First, surface and bulk diffusion coefficients for Pr_2NiO_4 are higher than those of La_2NiO_4 and second, the substitution of 10 % Co on the Ni-site additionally improves the surface exchange kinetics of oxygen. The improved surface oxygen exchange behaviour of $Pr_2Ni_{0.9}Co_{0.1}O_4$ (PNCO) can be seen in Figure 4.2 [46].

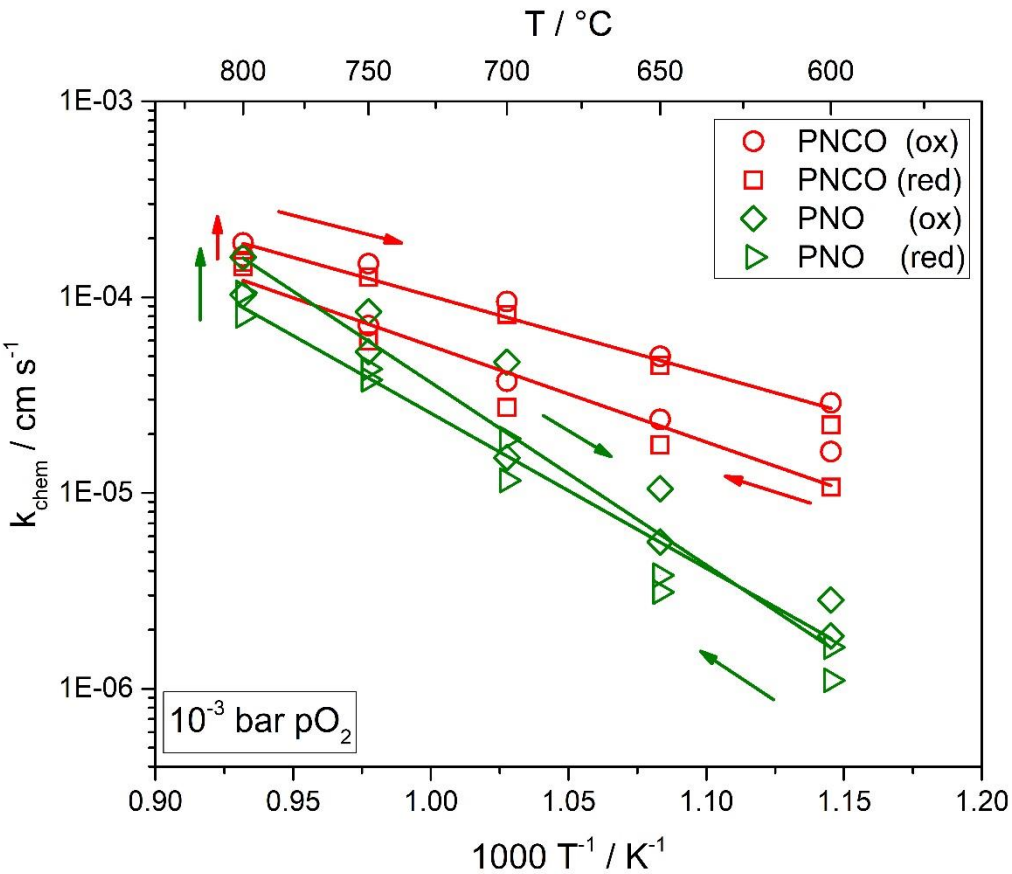

Figure 4.2: Chemical surface exchange coefficients of oxygen for PNO and PNCO [46]. The arrows indicate the sequence of measurements performed for every material.

Figure 4.2 indicates an increase in k_{chem} in the measurement cycle from 800 °C towards 600 °C for both investigated materials. Scanning transmission electron microscopy with energy dispersive X-ray spectroscopy was performed to investigate the surface near region of PNCO. Results of this experiment are shown in Figure 4.3 [46].

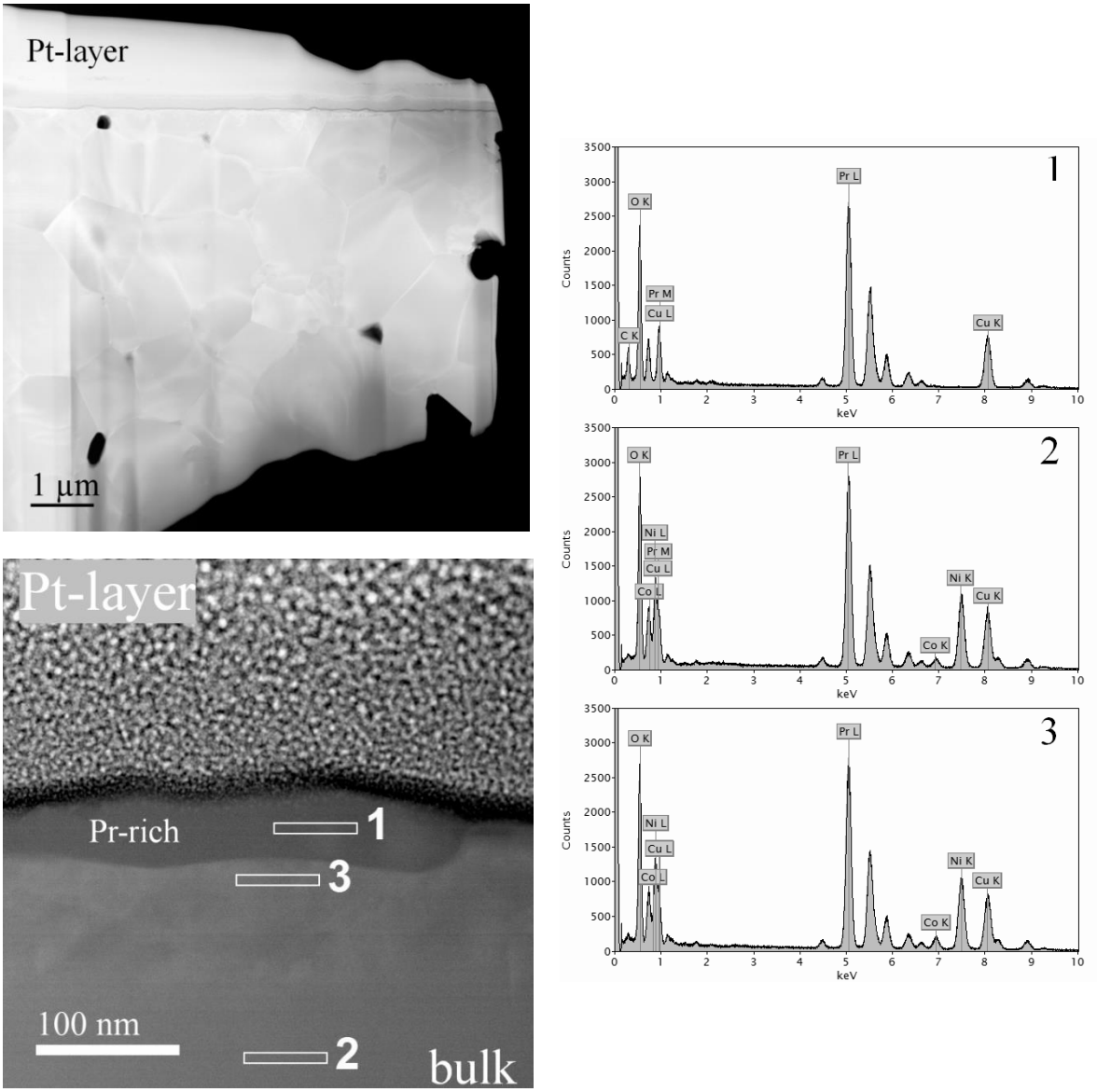

Figure 4.3: STEM-HAADF image of a PNCO lamella with EDX spectra. Spectrum 1 was recorded on the darker surface near spot pointing out the exsolution of Pr_6O_{11} (EDX gives Pr:O ratio of 35.7:64.3 at%). EDX measurements from the bulk area (spectrum 2) indicate the nominal composition of PNCO (Pr:Ni:Co:O ratio equals 27:14:2:57 at%) and spectrum 3 shows a small amount of additional Co signal next to the Pr enriched area. Figure was taken from [46].

Several studies confirmed that the exsolution of Pr_6O_{11} nanoparticles could have a positive impact on the surface oxygen exchange activity [47-50].

5) Characterisation techniques

The following chapters briefly the most important characterisation and measurement techniques used to achieve relevant data for the publications in this thesis.

5.1) X-ray powder diffraction (XRD)

This first section of the methodical part of the thesis focuses on the formation of X-rays, their interaction with crystalline samples and the resulting powder diffraction patterns, as well as information derived thereof by Rietveld refinement.

5.1.1) Formation and characteristics of X-rays

More than 120 years ago, Wilhelm Conrad Röntgen discovered a novel type of electromagnetic radiation called X-rays. Those X-rays fit between the area of ultra violet and γ-type radiation on the electromagnetic spectrum shown in Table 5.1-1 [51-53].

Table 5.1: Position of X-rays in the electromagnetic spectrum, modified from [52].

wavelength / nm	designation
770-400	visible light
400-200	near ultra violet
200-10	far ultra violet
10-0.002	X-rays
<0.002	γ-rays

X-rays form due to the impact of accelerated electrons on a metal substrate (anode in an X-ray tube). A fast-accelerated electron follows Einstein's equation (Equation 5.1-1) and concluding from this, the minimal wavelength (λ_{min}) of an X-ray quant is limited to the change in maximum energy (ΔE_{max}), which is a function of the accelerating voltage (V) [52].

$$\Delta E_{max} = e \cdot V = h \cdot \nu_{max} = \frac{h \cdot c}{\lambda_{min}} \qquad \text{(Equation 5.1-1)}$$

e… elementary charge of an electron ($1.60217662 \times 10^{-19}$ / A)

ν_{max}… maximum frequency

c… speed of light (299792458 / m s^{-1})

h… Planck's constant ($6.62607004 \times 10^{-34}$ / m^2 kg s^{-1})

According to Equation 5.1-1 for a given high voltage of 40 kV, the smallest possible wavelength is 0.309 Å. Also according to Equation 5.1-1 there is a probability, that the whole energy is transformed from the electron to the electromagnetic field of the core near region in the atom by just a single step. However, the most common case is that the energy is transferred in multiple parts, until the electron loses its motion. This is the main reason why there are many different wavelengths that all correspond to a certain energy called "Bremsstrahlung" [54]. To receive characteristic X-ray spectra of an X-ray tube, one has to improve the energy to excite a core near electron to obtain a line spectrum which overlaps with the continuous "Bremsstrahlung" [55]. All of the above-mentioned phenomena can clearly be seen in Figure 5.1-1.

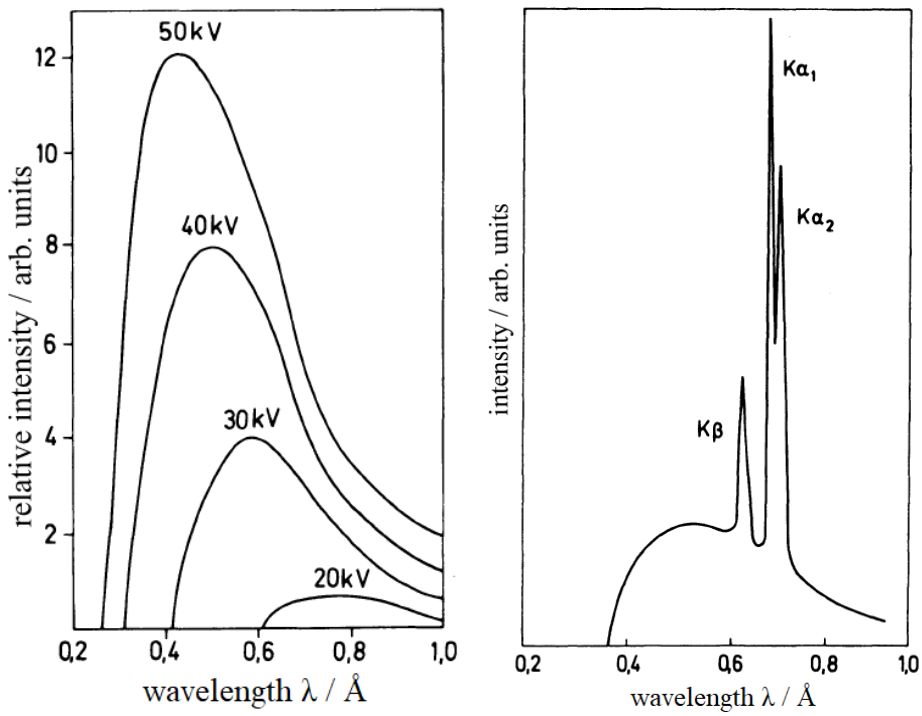

Figure 5.1-1: left) Smallest possible wavelength for a given accelerating voltage; right) Characteristic X-ray spectrum given by a Mo-Kα tube. Figures modified from [52].

5.1.2) Fundamentals of X-ray diffraction

The incident wave front build from the characteristic X-ray spectra interacts with the sample in various ways. The mathematical description of these interference phenomena was formulated by W.H. Bragg and W.L. Bragg [56]. This equation, called Bragg's law (Equation 5.1-2), combines the information on diffraction angle (Θ) and wavelength (λ) to the interplanar spacing distance (d_{hkl}). One important requirement for this is the presence of constructive interference in the lattice plane. The parameter n (has to be an integer) describes the order of reflection.

$$n \cdot \lambda = 2 \cdot d_{hkl} \cdot \sin(\Theta) \qquad \text{(Equation 5.1-2)}$$

The geometric relation of the above mentioned parameters und therefore the derivation of (Equation 5.1-2) is visualized in Figure 5.1-2.

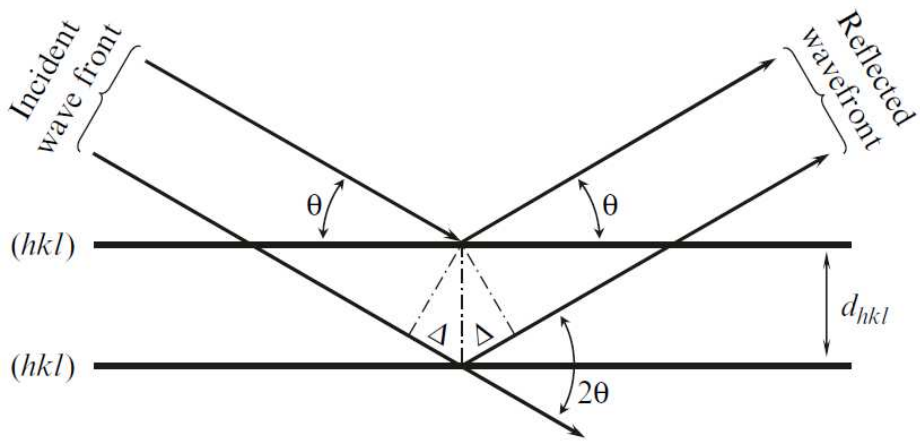

Figure 5.1-2: Geometrical derivation of Bragg's law. Modified from [57].

The triplets (*hkl*) are called Miller indices and each combination of these describes a specific plane, where each plane in a set of (*hkl*)-values may act as a separate scattering object. A very useful tool to explain the phenomena of diffraction was set up by P.P. Ewald [58]. The so-called Ewald sphere combines scattering vector (depends on the geometry of the experiment) and the reciprocal lattice (depends on orientation and the lattice parameters of a crystalline sample) to a simple geometrical concept [59]. For a geometrical construction of the Ewald sphere one has to draw the incident wave vector (s_0) in direction of the incident beam, which has a wavelength of λ^{-1}. Next, the sphere with the centre at the beginning point of s_0 and a radius of λ^{-1} is constructed. After that the scattered wave vector (s), which has also a radius of λ^{-1} is drawn. In the last construction part, the reciprocal lattice with the origin lying in s_0 has to be drawn. As shown in Figure 5.1-3 the reciprocal lattice points locate on the circle of the Ewald sphere [57].

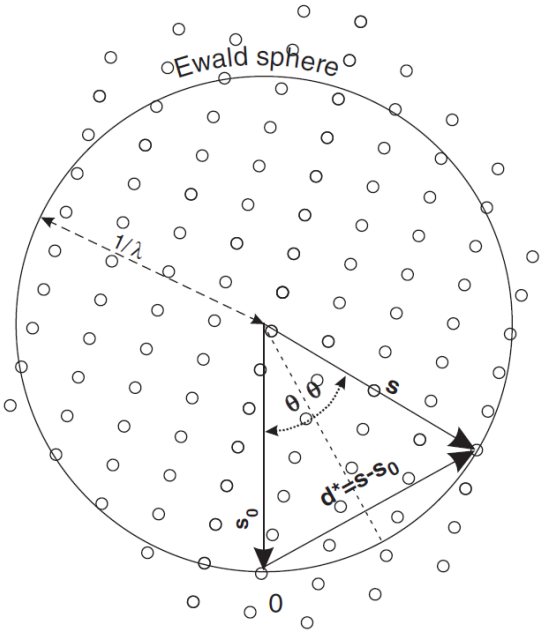

Figure 5.1-3: Geometrical construction of one circle of the Ewald sphere. The number "0" marks the origin of the reciprocal space. The figure was taken from [59].

5.1.3) Powder diffraction pattern

As described in the previous chapter, the monochromatic beam is scattered in a particular direction and this could be predicted by using Ewald sphere construction. However, when dealing with powder samples, there are a large number of randomly oriented grains and reciprocal lattices. For the case of randomly oriented grains, the lattice vectors d_{hkl} arrange on the surface of Ewald's sphere and the corresponding scattered vector is aligned with a cone angle of 4Θ, to the parallel cone axis of s_0. Assuming that there are infinite numbers of crystallites, the scattered vectors form constant cones with different intensities and diameters [60]. Those are called Debye rings [61] as seen in Figure 5.1-4 and Figure 5.1-5.

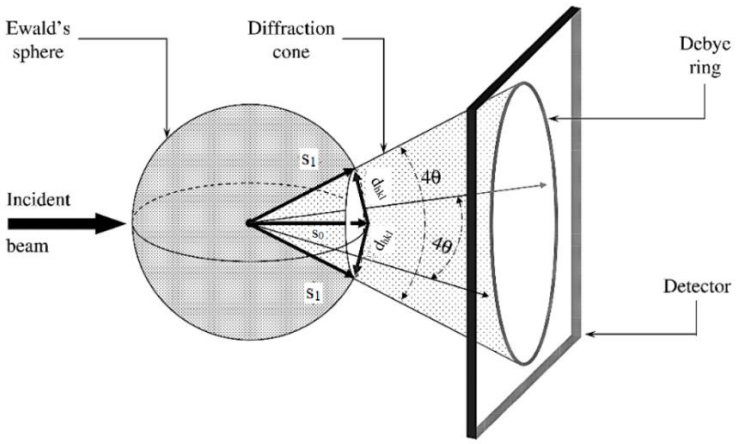

Figure 5.1-4: Schematic on the origin of the powder diffraction cone and formation of Debye rings. Modified from [57].

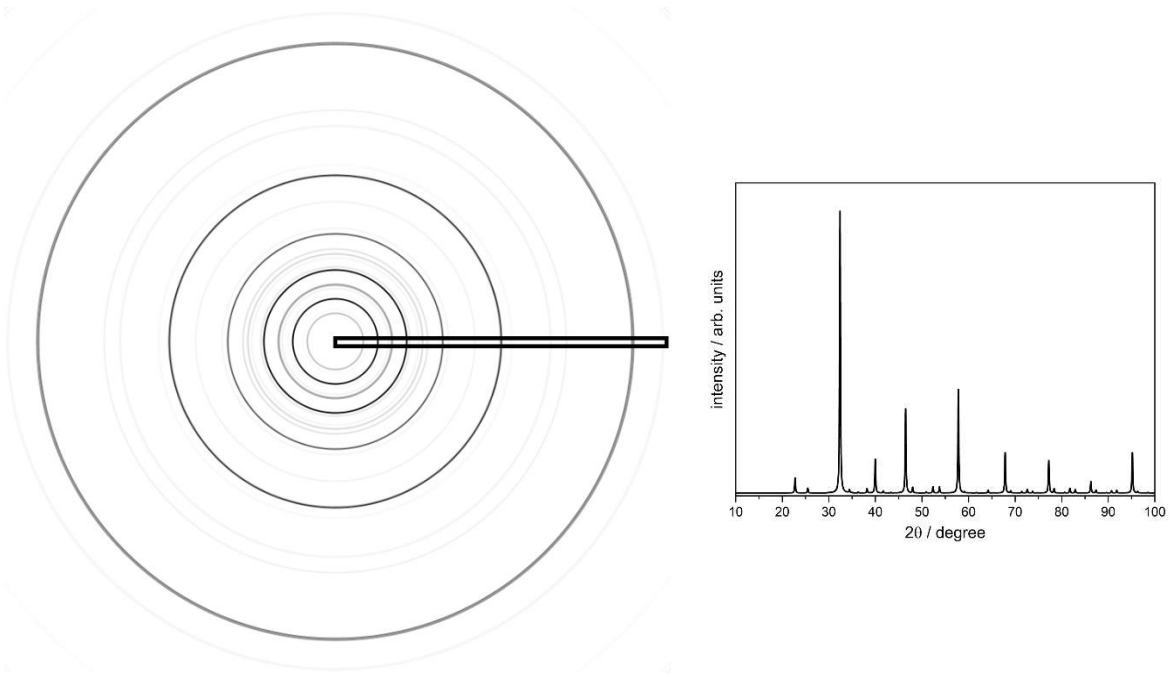

Figure 5.1-5: left) X-ray diffraction pattern of $La_{0.8}Ca_{0.2}FeO_{3-\delta}$ obtained by using Cu Kα radiation. The black box indicates the integrated area of the scattered intensity as a function of the resulting 2Θ angle shown on the right. Modified from data of Hudspeth et al. [62].

Wave aberrations cause the Ewald sphere to have finite thickness, and as a result the Bragg Peaks always have a nonzero width as a function of 2Θ [63]. As seen in the right part of Figure 5.1-5, a typical powder diffraction pattern consists of a relative intensity as a function of 2Θ. However, to get this angle dependence from the Debye rings, one has to integrate over the black box shown in Figure 5.1-5, because the detector works on radial coordinates (tan 2Θ) [59].

5.1.4) Rietveld refinement

In the previous chapters, the formation of X-rays and their interaction with polycrystalline samples, leading to powder patterns, was explained. This chapter mainly focusses on the data evaluation of powder diffractograms by using Rietveld refinement [52].

This is a mathematical tool to refine parameters necessary for structural investigations, but also additional parameters like sample and instruments effects, which have an impact on the diffraction pattern, can be taken into account. The algorithm used for this method is a least squares process, with the aim of finding the closest possible match between the measured data and the structural model including instrument and sample effects. A crucial requirement for this technique is the presence of a suitable structural model, wherein the data of similar (already described structures) could be used as a starting point for the refinement. Nowadays, computational ab initio methods could also generate useful starting conditions for the refinement of unknown structures from powder diffraction data [52, 64-68].

The following equation (Equation 5.1-3) shows the calculated intensity (y_{ci}) at a certain point i.

$$y_{ci} = S \cdot \sum_{hkl} L_{hkl} \cdot |F_{hkl}|^2 \cdot \Phi(2\Theta_i - 2\Theta_{hkl}) \cdot P_{hkl} \cdot A \cdot S_r \cdot E + y_{bi} \qquad \text{(Equation 5.1-3)}$$

hkl… Miller's indices

S… scaling factor (important for quantitative phase analysis)

L_{hkl}… Lorentz-, polarisation- and multiplicity-factor

F_{hkl}… structure factor for a specific (*hkl*) Bragg reflex

Φ… function for the reflex profile

P_{hkl}… factor for preferential orientation

A… absorption factor

S_r… factor for the surface roughness

E… extinction coefficient

y_{bi}… intensity of the background at a certain positon i

The algorithm behind this method is to align the calculated values y_{ci} to the measured data-points y_{oi} by obtaining a best fit (minimization of the parameter S_y) for the least squares refinement (Equation 5.1-4) [69, 70].

$$S_y = \sum_i w_i (y_{oi} - y_{ci})^2 \qquad \text{(Equation 5.1-4)}$$

w… weighting factor defined as $w = y_{oi}^{-1}$

Besides the position of a Bragg reflex (given by the lattice constants and the space group), the intensity of each reflex is very important. Those intensities (I_{hkl}) are proportional to the square of the structure factor ($|F_{hkl}|^2$) which is defined in Equation 5.1-5 [71].

$$F_{hkl} = \sum_{j=1}^{N} N_j \cdot f_j \cdot e^{-M_j} \cdot e^{[2\pi i(hx_j + ky_j + lz_j)]} \qquad \text{(Equation 5.1-5)}$$

N_j…. position multiplier for the atomic position j, defined as occupation number divided by multiplicity of the position j

M_j… temperature factor (caused by thermal motion parallel to the scattering vector)

f_i… atomic scattering factor

The next important parameter for a structural refinement of powder diffraction data is the background y_{bi}. To avoid high background signals in crystalline samples, it is important to prevent radiation of the sample holder and to exclude fluorescence effects of the sample by using a secondary monochromatic. After taking all these issues into account, the following equation with an 8th-order polynomial should describe the background by refining the parameter B_p (origin of the background function) quite well [52, 57].

$$y_{bi} = \sum_{m=0}^{8} B_m \left[\left(\frac{2\theta_i}{B_p}\right) - 1\right]^m \qquad \text{(Equation 5.1-6)}$$

B_m… the m refined polynomials

Another major contribution to the refinement of a powder diffraction pattern is given by the mathematical description of the peak shape. The variation of the peak shape (e.g. broadening) could be caused by either the instrumental profile (depended on the hardware and the measurement method), or the so-called intrinsic diffraction profile, which is mainly controlled by the sample specifications (e.g. crystallite size, degree of crystallinity and microstrain). To cover every measurement point of a Bragg reflex, it is important to model the function Φ (described in Equation 5.1-3) with a set of analytical functions depending on the geometrical form of the peak. There are a few different functions available so far and three of these are

described in the following section. The first one, a Gauß-function G (Equation 5.1-7), could be used to describe peak shapes with nearly ideal normal distribution, as it's common in neutron diffraction data or low angle X-ray scattering [52, 72].

$$P(2\theta_i - 2\theta_{hkl}) = \frac{\sqrt{4\cdot\ln(2)}}{H_{hkl}} \cdot e^{\frac{-4\cdot\ln(2)\cdot(2\theta_i - 2\theta_{hkl})^2}{H_{hkl}^2}} = G \qquad \text{(Equation 5.1-7)}$$

H_{hkl}… full width at half maximum of the reflex *hkl*

The second one, a Lorentz-function L (Equation 5.1-8), could be used to describe very broad peak shapes, which tend to occur at high diffraction angles [52, 72].

$$P(2\theta_i - 2\theta_{hkl}) = \frac{2}{H_{hkl}\pi} \cdot \frac{1}{\left[1+\frac{4\cdot(2\theta_i - 2\theta_{hkl})^2}{H_{hkl}^2}\right]} = L \qquad \text{(Equation 5.1-8)}$$

The third one, a modified Thompson-Cox-Hastings-pseudo-Voigt-function TCHZ (Equation 5.1-9a-d), could be used to combine the advantages of the Equations 5.1-7 and Equation 5.1-8 to fit peaks with Gaussian and Lorentzian contribution [52, 73].

$$P(2\theta_i - 2\theta_{hkl}) = \eta \cdot L + (1-\eta)\cdot G \text{ where } \eta = \sum_{i=1}^{3} C_i \cdot \left(\frac{\Gamma_L}{\Gamma}\right)^i \qquad \text{(Equation 5.1-9a)}$$

C_i… numerical constant

Γ… total full width at half maximum, the indices L (Lorentz) and G (Gauss) indicate the contribution of the corresponding function to the full width at half maximum.

$$\Gamma = \sqrt[5]{\sum_{i=0}^{5} \Gamma_L^i \cdot \Gamma_G^{5-i}} \qquad \text{(Equation 5.1-9b)}$$

$$\Gamma_G = \sqrt{u \cdot tan^2(\Theta) + v \cdot \tan(\Theta) + w + \frac{z}{cos^2(\Theta)}} \qquad \text{(Equation 5.1-9c)}$$

$$\Gamma_L = x \cdot \tan(\Theta) + \frac{y}{\cos(\Theta)} \qquad \text{(Equation 5.1-9d)}$$

The parameters u, v, w, x, y and z are adjusted during refinement.

A graphical comparison of the previously mentioned profile functions is given in Figure 5.1-6.

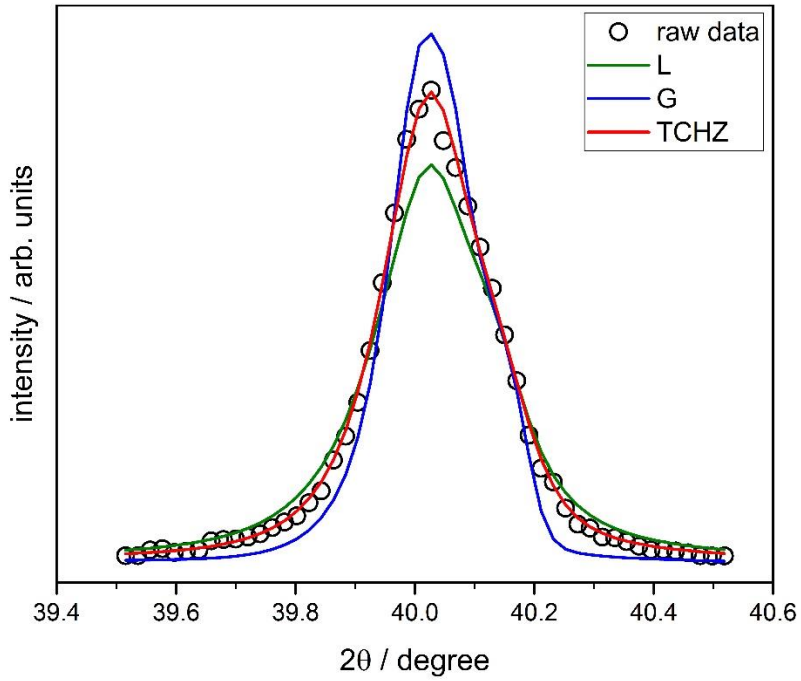

Figure 5.1-6: Single peak from a XRD powder diffraction pattern (dots) with the corresponding profile functions (lines). The TCHZ approach results in the best matching peak shape. Modified data from [40].

As previously described in this chapter, the main goal of the Rietveld refinement is to minimize the function S_y (Equation 5.1-4) in order to achieve a small discrepancy between calculated and measured profile. To obtain comparable results, several quality factors are introduced in Table 5.1-2 [52, 69].

Table 5.1-2: Quality parameters for Rietveld refinement

$R_B = \frac{\sum_{hkl} \lvert I_{hkl}(\text{obs}) - I_{hkl}(\text{calc}) \rvert}{\sum_{hkl} I_{hkl}(\text{obs})}$	$R_{wp} = \left[\frac{\sum_i w_i \cdot (y_{oi} - y_{ci})^2}{\sum_i w_i \cdot (y_{oi})^2}\right]^{\frac{1}{2}}$
$R_{exp} = \left[\frac{(N - P + C)}{\sum_i w_i \cdot (y_{oi})^2}\right]^{\frac{1}{2}}$	$S = GOF = \frac{R_{wp}}{R_{exp}} = \left[\frac{\sum_i w_i \cdot (y_{oi})^2}{(N - P + C)}\right]^{\frac{1}{2}}$

N… number of measurement points

P… refined parameters

C… applied constraints

w_i… weighting factor for the measurement point j, defined as $w_i = y_{oi}^{-1}$ similar to (Equation 5.1-4)

The Bragg value R_B does not rely on actual Bragg-intensities. Although they are very similar to intensities obtained from single crystal diffraction, they only refer to calculated data from the structural model. For simple mathematical reasons, the weighted quality factor R_{wp} is the most significant one, because it takes all kinds of sample characteristics into account. These could, for example, be the presence of contaminations on the sample (additional reflexes), or changes in signal to background intensities (fluorescence effects). The R_{exp} value in combination with the R_{wp} value represents an important quality factor, the so-called GOF (goodness of fit) parameter. As the theoretical value equals unity, a good quality value is a GOF close to 1.3 [52].

5.2) Electronic conductivity and dc-conductivity relaxation measurements (EC/CR)

This chapter primarily focusses on the determination of the electronic conductivity and the oxygen exchange kinetics of dense sintered ceramic compounds.

5.2.1) Sample geometry and electronic conductivity

A common way to determine the electronic conductivity is to measure the resistivity on a rectangular shaped sample with four contact points as seen in Figure 5.2-1a [74]. To perform such measurements, one has to apply a current between point A and B, simultaneously measuring the voltage between the points C and D. It is very important that the points C and D are in sufficient distance to A and B, to avoid irregularities in the current flow. The voltage drop between the contacts C and D, and the applied current, lead to the measured value for resistivity. A big disadvantage of this technique is the dependence of the specific resistivity on the sample geometry. To overcome the problem of an unknown current distribution, a different geometry, called van der Pauw geometry, is used as shown in Figure 5.2-1b [75, 76]. This technique is applicable for arbitrarily shaped samples, with the limitation of a uniform thickness and small contact areas. The first resistive value $R_{AB,CD}$ is obtained by applying a current between A and B and measuring the voltage drop between C and D, while the second resistive value $R_{BC,DA}$ is obtained by applying a current between B and C and measuring the voltage drop between D and A. The resulting specific electronic conductivity can be calculated by using Equation 5.2-1 [76].

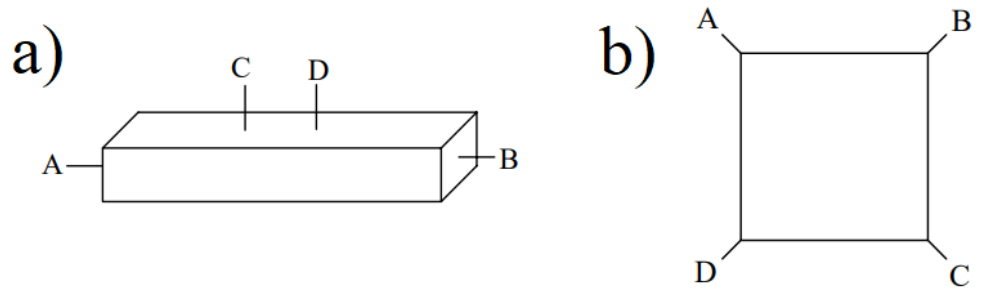

Figure 5.2-1: a) conventional resistivity measurement. b) van der Pauw geometry taken from [76].

$$e^{-\pi \cdot R_{AB,CD} \cdot \frac{L}{\rho}} + e^{-\pi \cdot R_{BC,DA} \cdot \frac{L}{\rho}} = 1 \qquad \text{(Equation 5.2-1)}$$

L… thickness of the sample

ρ… specific resistivity (the specific electronic conductivity is defined as $\sigma = \frac{1}{\rho}$)

5.2.2) Dc-conductivity relaxation measurements

Besides high ionic and electronic conductivities, fast oxygen exchange kinetics (fast oxygen reduction on the surface and fast diffusion of O^{2-} ions in the bulk of the material) are the key factors for potential SOFC cathodes. This part of the chapter focuses on the determination of the kinetic parameters by using the dc-conductivity relaxation technique (Figure 5.2-2).

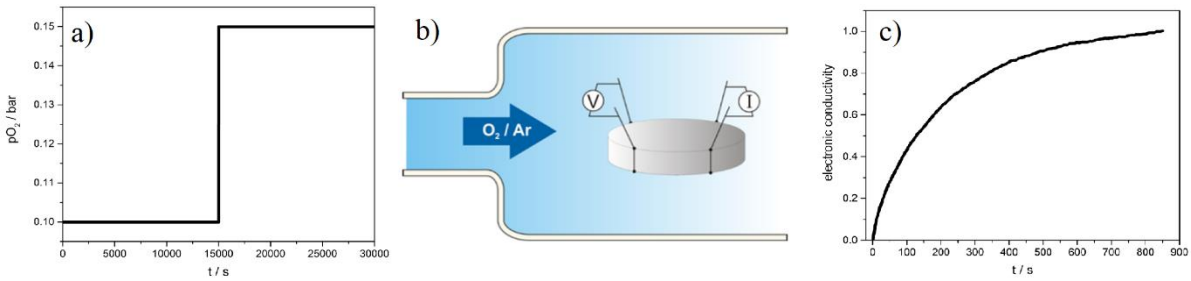

Figure 5.2-2: a) ideal pO_2 change in the conductivity relaxation setup. b) glass reactor with sample in van der Pauw geometry. c) normalised conductivity relaxation curve of LCF82 at 700°C and pO_2 = 0.15 bar. Figure b) taken from [77].

For the experimental setup, a dense (above 95 % relative density) and finely polished sample (with four contacts applied in van der Pauw geometry similar to Figure 5.2-1b) is needed [22, 40, 42, 46]. The contacted sample is placed inside a glass reactor and equilibrated under well-defined oxygen partial pressure conditions, while simultaneously recording the ohmic resistance. To determine the kinetic parameters, a small change in the oxygen partial pressure, causing a change of the measured resistance (and therefore the conductivity) is applied. The resulting conductivity relaxation behaviour is described by the time dependent changes in the normalized specific conductivity calculated according to Equation 5.2-2.

$$\bar{\sigma}_t = \frac{\sigma_t - \sigma_0}{\sigma_\infty - \sigma_0} \qquad \text{(Equation 5.2-2)}$$

In this formula, σ_0 is the electronic conductivity at an equilibrated state before the pO_2 change, whereas σ_∞ is the electronic conductivity at an equilibrated state at an infinite time scale after the pO_2 change. σ_t is the electronic conductivity at a certain time during the relaxation process.

The obtained response ($\bar{\sigma}_t$) of the sample as a function of time is called relaxation curve (see Figure 5.2-2c). The following chapter describes the information on surface exchange and chemical diffusion, which can be obtained from such curves.

5.2.3) Oxygen exchange kinetics

In order to obtain the chemical surface exchange coefficient k_{chem} and/or the chemical bulk diffusion coefficient D_{chem} of oxygen, a nonlinear fitting procedure of the relaxation curve has to be done. This is achieved in three steps. The first fitting procedure would assume that the oxygen exchange is strictly dominated by the incorporation of oxygen on the surface of the material as seen in Equation 5.2-3 [78, 79].

$$\ln(1-\sigma_{norm}) = -\frac{2\cdot k_{chem}}{L}\cdot t \qquad \text{(Equation 5.2-3)}$$

A bulk diffusion dominated procedure occurs if the ordinate intercept of the ln(1-σ) vs. t plot is around -0.21 (Equation 5.2-4).

$$\ln(1-\sigma_{norm}) = \ln\left(\frac{8}{\pi^2}\right) - \frac{D_{chem}\cdot\pi^2}{L^2}\cdot t \qquad \text{(Equation 5.2-4)}$$

The last nonlinear fitting procedure (only used if no satisfactory solution for just k_{chem} or D_{chem} is achieved), involves both parameters k_{chem} and D_{chem} and is shown in Equation 5.2-5 and Figure 5.2-3. These expressions and the application of this technique were already described in literature [23, 26, 79-85].

$$\ln(1-\sigma_{norm}) = \ln\left\{\frac{2\cdot k_{chem}^2}{\frac{D_{chem}^2\cdot\gamma^2\cdot\left[\frac{k_{chem}\cdot L}{D_{chem}}\right]^2}{4}+\frac{\gamma^2\cdot L^2}{4}+\frac{k_{chem}\cdot L}{2\cdot D_{chem}}}\right\} - D_{chem}\cdot\gamma^2\cdot t \qquad \text{(Equation 5.2-5)}$$

L… thickness of the sample

γ… eigenvalue defined as $\gamma = \tan\left(\frac{\gamma\cdot L}{2}\right) = \frac{k_{chem}}{D_{chem}}$

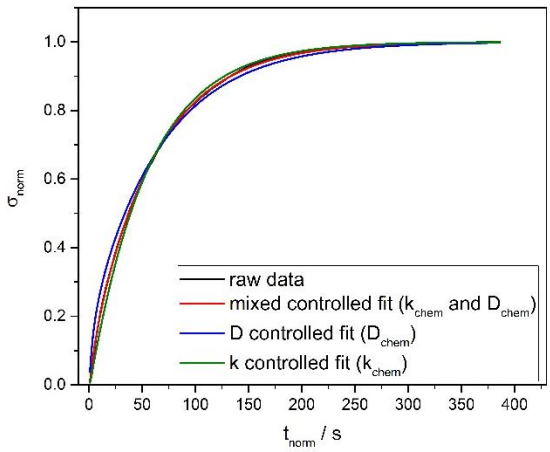

Figure 5.2-3: Conductivity relaxation curve for LCF82 at 700°C and pO_2 = 0.1 bar. The best fit was achieved with the model assuming mixed controlled kinetics (Equation 5.2-5).

6) Summary of the results and conclusions

In the current thesis four materials with perovskite structure ($La_{0.9}Ca_{0.1}FeO_{3-\delta}$, $La_{0.8}Ca_{0.2}FeO_{3-\delta}$, $La_{0.75}Ca_{0.25}FeO_{3-\delta}$, and $Pr_{0.8}Ca_{0.2}FeO_{3-\delta}$) and two alkaline earth-free materials with K_2NiF_4 structure ($Pr_2NiO_{4+\delta}$, $Pr_2Ni_{0.9}Co_{0.1}O_{4+\delta}$) were successfully synthesised and characterised with respect to crystal structure, defect chemistry, thermal expansion behaviour, and mass and charge transport properties. X-ray powder diffraction with subsequent Rietveld analysis delivered important information on the phase purity and the crystal structure of the investigated materials. Additional information concerning the chemical composition and microstructure was obtained via scanning electron microscopy on the fresh (as prepared) as well as the degraded samples.

Dc-conductivity relaxation measurements were performed in O_2/Ar atmospheres (ideal conditions; very low impurity contents), and for selected materials ($La_{0.8}Ca_{0.2}FeO_{3-\delta}$ and $Pr_{0.8}Ca_{0.2}FeO_{3-\delta}$) in SO_2 containing atmospheres (accelerated aging conditions; 2 ppm SO_2 at 700°C). Very fast oxygen exchange kinetics was found for all investigated materials in SO_2 free atmospheres (e.g. $k_{chem} = 6\times10^{-3}$ cm s^{-1} at $pO_2 = 0.1$ bar and T = 800°C for $La_{0.8}Ca_{0.2}FeO_{3-\delta}$). Even after SO_2 poisoning, both $La_{0.8}Ca_{0.2}FeO_{3-\delta}$ and $Pr_{0.8}Ca_{0.2}FeO_{3-\delta}$ showed superior performance and an increased SO_2 tolerance compared to the state of the art material $La_{0.6}Sr_{0.4}CoO_{3-\delta}$. Post mortem analysis was performed with scanning electron microscopy, X-ray photoelectron spectroscopy, and analytical transmission electron microscopy to investigate degradation mechanism involved.

CR measurements on $Pr_2NiO_{4+\delta}$ and $Pr_2Ni_{0.9}Co_{0.1}O_{4+\delta}$ showed fast oxygen exchange kinetics in the fresh state at low pO_2 and moderate temperatures (e.g. $k_{chem} = 2\times10^{-6}$ cm s^{-1} at $pO_2 = 1\times10^{-3}$ bar and T = 600°C for $Pr_2NiO_{4+\delta}$). The partial substitution of Ni^{2+} with Co^{2+} further increased the surface exchange rate by one order of magnitude to $k_{chem} = 2\times10^{-5}$ cm s^{-1} at $pO_2 = 1\times10^{-3}$ bar and T = 600°C for $Pr_2Ni_{0.9}Co_{0.1}O_{4+\delta}$. An in-situ increase in k_{chem} for both materials was observed during CR measurements (approximately half an order of magnitude). This could be explained due to an exsolution of catalytically active Pr_6O_{11} nanoparticles on the surface.

It can be concluded that perovskites from the series $(La,Pr,Ca)FeO_3$ exhibit very high oxygen exchange activities and improved tolerance against SO_2. In terms of mass and charge transport properties, $La_{0.8}Ca_{0.2}FeO_{3-\delta}$ shows superior performance compared to the other investigated perovskites and the state of the art SOFC cathode material $La_{0.6}Sr_{0.4}CoO_3$. Another very promising SOFC cathode material, $Pr_{0.8}Ca_{0.2}FeO_{3-\delta}$, exhibits fast oxygen exchange kinetics and

the lowest affinity to react with SO_2. Additionally, it could be shown that Co-substitution in K_2NiF_4-type materials significantly increases the oxygen exchange kinetics.

7) Literature

[1] Z. Shao, M.O. Tade, *Intermediate-Temperature Solid Oxide Fuel Cells: Materials and Applications*, Springer-Verlag, Berlin Heidelberg (2016).

[2] J. Larminie, A. Dicks, *Fuel cell systems explained*, John Wiley & Sons Ltd., Chichester, UK (2003).

[3] T. Ishihara, Editor, *Perovskite oxide for solid oxide fuel cells*, Springer, New York (2009).

[4] A. Bocarsly, D.M.P. Mingos, Editors, *Fuel Cells and Hydrogen Storage*, Springer, Berlin Heidelberg (2011).

[5] R.L. Fagbenle, A.B.C. Oguaka, O.T. Olakoyejo, *Applied Thermal Engineering* **27** (2007) (13) 2220.

[6] J.T.S. Irvine, P. Connor, *Solid Oxide Fuels Cells: Facts and Figures - Past Present and Future Perspectives for SOFC Technologies*, Springer-Verlag, London (2013).

[7] R. O'Hayre, S.-W. Cha, W. Colella, F.B. Prinz, *Fuel Cell Fundamentals*, John Wiley & Sons, Inc., Hoboken, New Jersey (2016).

[8] G. Kaur, *Solid Oxide Fuel Cell Components - Interfacial Compatibility of SOFC Glass Seals*, Springer International Publishing (2016).

[9] J. Milewski, J. Lewandowski, *Analysis of Design and Construction of Solid Oxide Fuel Cell in Terms of their Dynamic Operation* (2010).

[10] X.-D. Zhou, S.C. Singhal, In: J. Garche, Editor, *Encyclopedia of Electrochemical Power Sources*, Elsevier, Amsterdam (2009), p.1-16.

[11] K.-D. Kreuer, *Fuel cells - Selected entries from the encyclopedia of sustainability science and technology*, Springer-Verlag, New York (2013).

[12] S.B. Adler, *Chemical Reviews* **104** (2004) (10) 4791.

[13] V.V. Kharton, A.A. Yaremchenko, A.L. Shaula, M.V. Patrakeev, E.N. Naumovich, D.I. Logvinovich, J.R. Frade, F.M.B. Marques, *Journal of Solid State Chemistry* **177** (2004) (1) 26.

[14] M.S.D. Read, M.S. Islam, G.W. Watson, F.E. Hancock, *Journal of Materials Chemistry* **11** (2001) 2597.

[15] E. Boehm, J.M. Bassat, P. Dordor, F. Mauvy, J.C. Grenier, P. Stevens, *Solid State Ionics* **176** (2005) (37-38) 2717.

[16] F.A. Kröger, H.J. Vink, In: F. Seitz, D. Turnbull, Editors, *Solid State Physics*, Academic Press (1956), p.307-435.

[17] V.G. Sathe, A.V. Pimpale, V. Siruguri, S.K. Paranjpe, *Journal of Physics: Condensed Matter* **8** (1996) (21) 3889.

[18] K. Momma and F. Izumi, *J. Appl. Crystallogr.* **44** (2011) 1272.

[19] A.C. Tomkiewicz, M. Tamimi, A. Huq, S. McIntosh, *Journal of Materials Chemistry A* **3** (2015) (43) 21864.

[20] A. Chroneos, D. Parfitt, J.A. Kilner, R.W. Grimes, *Journal of Materials Chemistry* **20** (2010) 266.

[21] Y.-U.K. Young Kee Chung, Song Ho Byeon, *Bulletin of the Korean Chemical Society* **16** (1995) (2) 120.

[22] C. Berger, E. Bucher, W. Sitte, *Solid State Ionics* **299** (2017) 46.

[23] J.E. ten Elshof, M.H.R. Lankhorst, H.J.M. Bouwmeester, *Journal of the Electrochemical Society* **144** (1997) (3) 1060.

[24] W. Sitte, E. Bucher, P. Ried, A. Mai, F. Tietz, Oxygen exchange properties of perovskite-type cathode materials obtained by different techniques, In: U. Bossel, Editor, *7th European Solid Oxide Fuel Cell Forum*, Lucerne, Switzerland (2006), p.File No. B065, p. 1-8.

[25] M.H.R. Lankhorst, H.J.M. Bouwmeester, *Journal of the Electrochemical Society* **144** (1997) (4) 1261.

[26] L.M. van der Haar, M.W. den Otter, M. Morskate, H.J.M. Bouwmeester, H. Verweij, *Journal of the Electrochemical Society* **149** (2002) (3) J41.

[27] A. Egger, E. Bucher, M. Yang, W. Sitte, *Solid State Ionics* **225** (2012) 55.

[28] J.A. Kilner, C.K.M. Shaw, *Solid State Ionics* **154** (2002) 523.

[29] J. Hyodo, K. Tominaga, Y.-W. Ju, S. Ida, T. Ishihara, *Solid State Ionics* **256** (2014) 5.

[30] N. Shaigan, W. Qu, D.G. Ivey, W. Chen, *Journal of Power Sources* **195** (2010) (6) 1529.

[31] S. Frangini, A. Masci, S.J. McPhail, T. Soccio, F. Zaza, *Materials Chemistry and Physics* **144** (2014) (3) 491.

[32] N. Schrödl, A. Egger, C. Gspan, T. Höschen, F. Hofer, W. Sitte, *Solid State Ionics* **322** (2018) 44.

[33] N. Schrödl, E. Bucher, A. Egger, P. Kreiml, C. Teichert, T. Höschen, W. Sitte, *Solid State Ionics* **276** (2015) 62.

[34] N. Schrödl, E. Bucher, C. Gspan, A. Egger, C. Ganser, C. Teichert, F. Hofer, W. Sitte, *Solid State Ionics* **288** (2016) 14.

[35] M. Perz, E. Bucher, C. Gspan, J. Waldhäusl, F. Hofer, W. Sitte, *Solid State Ionics* **288** (2016) 22.

[36] E.J. Opila, N.S. Jacobson, D.L. Myers, E.H. Copland, *JOM* **58** (2006) (1) 22.

[37] E.J. Opila, D.L. Myers, N.S. Jacobson, I.M.B. Nielsen, D.F. Johnson, J.K. Olminsky, M.D. Allendorf, *The Journal of Physical Chemistry A* **111** (2007) (10) 1971.

[38] R.D. Shannon, *Acta Crystallographica A* **32** (1976) 751.

[39] D.W. Smith, *Journal of Chemical Education* **64** (1987) (6) 480.

[40] C. Berger, E. Bucher, A. Windischbacher, A.D. Boese, W. Sitte, *Journal of Solid State Chemistry* **259** (2018) 57.

[41] C. Berger, E. Bucher, C. Gspan, W. Sitte, *Journal of Solid State Chemistry* **273** (2019) 92.

[42] C. Berger, E. Bucher, C. Gspan, A. Menzel, W. Sitte, *Journal of the Electrochemical Society* **164** (2017) (10) F3008.

[43] C. Berger, E. Bucher, C. Gspan, A. Menzel, W. Sitte, *Solid State Ionics* **326** (2018) 82.

[44] E. Bucher, C. Gspan, W. Sitte, *Solid State Ionics* **272** (2015) 112.

[45] C.A. Schneider, W.S. Rasband, K.W. Eliceiri, *Nature Methods* **9** (2012) 671.

[46] C. Berger, E. Bucher, A. Egger, A.T. Strasser, N. Schrödl, C. Gspan, J. Hofer, W. Sitte, *Solid State Ionics* **316** (2018) 93.

[47] A.L. Shaula, E.N. Naumovich, A.P. Viskup, V.V. Pankov, A.V. Kovalevsky, V.V. Kharton, *Solid State Ionics* **180** (2009) (11) 812.

[48] S.Y. Jeon, M.B. Choi, H.N. Im, J.H. Hwang, S.J. Song, *Journal of Physics and Chemistry of Solids* **73** (2012) (5) 656.

[49] C. Nicollet, A. Flura, V. Vibhu, A. Rougier, J.-M. Bassat, J.-C. Grenier, *International Journal of Hydrogen Energy* **41** (2016) (34) 15538.

[50] R. Chiba, H. Aono, K. Kato, *ECS Transactions* **57** (2013) (1) 1831.

[51] W.C. Röntgen, *Aus den Sitzungsberichten der Würzburger Physik.-medic. Gesellschaft* (1895).

[52] H. Krischner, B. Koppelhuber-Bitschnau, *Röntgenstrukturanalyse und Rietveldmethode*, Springer Fachmedien Wiesbaden GmbH (1994).

[53] K. Sridharan, In: K. Sridharan, Editor, *Spectral Methods in Transition Metal Complexes*, Elsevier (2016), p.1-12.

[54] A. Omar, P. Andreo, G. Poludniowski, *Radiation Physics and Chemistry* **148** (2018) 73.

[55] J.A. Bearden, *Reviews of Modern Physics* **39** (1967) (1) 78.

[56] W.H. Bragg, W.L. Bragg, *Proceedings of the Royal Society of London. Series A* **88** (1913) (605) 428.

[57] P.Z. Vitalij Pecharsky, *Fundamentals of Powder Diffraction and Structural Characterization of Materials, Second Edition*, Springer US (2009).

[58] P.P. Ewald, *Physik. Z.* **14** (1913) 465.

[59] R. E. Dinnebier, S.J.L. Billinge, *Principles of Powder Diffraction*, RSC Publishing (2008).

[60] D. Louër, In: J.C. Lindon, G.E. Tranter, D.W. Koppenaal, Editors, *Encyclopedia of Spectroscopy and Spectrometry (Third Edition)*, Academic Press, Oxford (2017), p.723-731.

[61] P.S. P. Debye, *Nachrichten von der Gesellschaft der Wissenschaften zu Göttingen, Mathematisch-Physikalische Klasse* (1916).

[62] J.M. Hudspeth, G.A. Stewart, A.J. Studer, D.J. Goossens, *Journal of Physics and Chemistry of Solids* **72** (2011) (12) 1543.

[63] J.C.H. Spence, N.A. Zatsepin, C. Li, *Philosophical Transactions of the Royal Society B: Biological Sciences* **369** (2014) (1647).

[64] M.W. Lufaso, P.M. Woodward, *Acta Crystallographica Section B* **57** (2001) (6) 725.

[65] H. Rietveld, *Acta Crystallographica* **22** (1967) (1) 151.

[66] H. Rietveld, *Journal of Applied Crystallography* **2** (1969) (2) 65.

[67] R.A. Young, *The Rietveld Method*, International Union of Crystallography (1995).

[68] L.B. McCusker, R.B. Von Dreele, D.E. Cox, D. Louer, P. Scardi, *Journal of Applied Crystallography* **32** (1999) (1) 36.

[69] W.I. David, *J Res Natl Inst Stand Technol* **109** (2004) (1) 107.

[70] B. Vandeginste, *Journal of Chemometrics* **3** (1989) (3) 544.

[71] W. Massa, *Kristallstrukturbestimmung*, Vieweg+Teubner, Wiesbaden (2007).

[72] R.A. Young, D.B. Wiles, *Journal of Applied Crystallography* **15** (1982) (4) 430.

[73] P. Thompson, D.E. Cox, J.B. Hastings, *Journal of Applied Crystallography* **20** (1987) (2) 79.

[74] Y. Singh, *International Journal of Modern Physics: Conference Series* **22** (2013) 745.

[75] L.J. van der Pauw, *Philips Research Reports* **13** (1958) (1) 1.

[76] *Quantum Design, Application Note 1076-304, Rev. A0* (2007).

[77] A. Egger, Rare earth nickelates as cathodes for solid oxide fuel cells, *Department of General, Analytical and Physical Chemistry*, University of Leoben, Austria (2013), p.231.

[78] W. Preis, E. Bucher, W. Sitte, *Journal of Power Sources* **106** (2002) 116.

[79] W. Preis, E. Bucher, W. Sitte, *Solid State Ionics* **175** (2004) 393.

[80] J. Maier, *Solid State Ionics* **112** (1998) (3-4) 197.

[81] J.A. Lane, J.A. Kilner, *Solid State Ionics* **136-137** (2000) 997.

[82] M.W. den Otter, H.J.M. Bouwmeester, B.A. Boukamp, H. Verweij, *Journal of the Electrochemical Society* **148** (2001) (2) J1.

[83] W. Preis, M. Holzinger, W. Sitte, *Monatshefte für Chemie* **132** (2001) 499.

[84] H.J.M. Bouwmeester, M.W. den Otter, B.A. Boukamp, *Journal of Solid State Electrochemistry* **8** (2004) 599.

[85] R.A. De Souza, *Physical Chemistry Chemical Physics* **8** (2006) (7) 890.

[86] FactSage^{Ó} 7.0, 1976-2015 Thermfact and GTT Technologies.

[87] P. Stadelmann, Electron Microscopy Software (Java Version) 3.2830U2008, CIME-EPFL Switzerland (2008).

[88] *VASP TST Tools*, http://theory.cm.utexas.edu/vtsttools/ (12.01.2017).

[89] P.M. Price, E. Rabenberg, D. Thomsen, S.T. Misture, D.P. Butt, *Journal of the American Ceramic Society* **97** (2014) (7) 2241.

8) Publications

8.1) Publications submitted for this thesis

1) Berger, C.; Bucher, E.; Gspan, C.; Menzel, A.; Sitte, W., Impact of SO_2 on the oxygen exchange kinetics of the promising SOFC/SOEC air electrode material $La_{0.8}Ca_{0.2}FeO_{3-\delta}$. Journal of The Electrochemical Society 2017, **164** (10), F3008-F3018.

2) Berger, C.; Bucher, E.; Windischbacher, A.; Boese, A. D.; Sitte, W., Strontium-free rare earth perovskite ferrites with fast oxygen exchange kinetics: Experiment and theory. Journal of Solid State Chemistry 2018, **259**, 57-66.

3) Berger, C.; Bucher, E.; Egger, A.; Strasser, A. T.; Schrödl, N.; Gspan, C.; Hofer, J.; Sitte, W., Synthesis and characterization of the novel K_2NiF_4-type oxide $Pr_2Ni_{0.9}Co_{0.1}O_{4+\delta}$. Solid State Ionics 2018, **316**, 93-101.

4) C. Berger, E. Bucher, C. Gspan, W. Sitte, Crystal structure, oxygen nonstoichiometry, and mass and charge transport properties of the Sr-free SOFC/SOEC air electrode material $La_{0.75}Ca_{0.25}FeO_{3-\delta}$. Journal of Solid State Chemistry 2019, **273**, 92-100.

8.2) Additional Publications

1) Berger, C.; Bucher, E.; Sitte, W., Mass and charge transport properties of $La_{0.9}Ca_{0.1}FeO_{3-\delta}$. Solid State Ionics 2017, **299**, 46-54.

2) Berger, C.; Bucher, E.; Gspan, C.; Menzel, A.; Sitte, W., Long-term stability of oxygen surface exchange kinetics of $Pr_{0.8}Ca_{0.2}FeO_{3-\delta}$ against SO_2-poisoning. Solid State Ionics 2018, **326**, 82-89.

International Presentations

1) Oral presentation at E-MRS Spring Meeting 02.05.2016 in Lille, France; Symposium on Solid State Ionics; Title: ”Mass and charge transport properties of $La_{0.9}Ca_{0.1}FeO_{3-\delta}$”
2) Oral presentation at International Conference on Solid State Ionics 21 19.06.2017 in Padua, Italy; Symposium on Solid oxide fuel cells and electrolyzers; Title: ”Synthesis and characterization of the novel K_2NiF_4-type oxide $Pr_2Ni_{0.9}Co_{0.1}O_{4+\delta}$”
3) Oral presentation at E-MRS Spring Meeting 22.06.2018 in Strasbourg, France; Symposium on Solid State Ionics; Title: ”Oxygen surface exchange kinetics of $Pr_2(Ni,Co)O_{4+\delta}$ thin film model electrodes”

National Presentations

1) Poster presentation at “16. Österreichische Chemietage 2015” in Innsbruck; Title: ”Synthesis and Characterization of Calcium Substituted $LaFeO_3$ as a Potential SOFC Cathode”, 21.09.2015
2) Poster presentation at “5. GÖCH Symposium 2016 Physikalische Chemie in Österreich” in Salzburg; Title “Mass and charge transport properties of $La_{0.9}Ca_{0.1}FeO_{3-\delta}$“, 14.04.2016
3) Poster presentation at “International FOXSI Conference 2016” in Vienna; Title: ”Oxygen exchange kinetics of $La_{0.9}Ca_{0.1}FeO_{3-\delta}$”, 23.05.2016
4) Oral presentation at Workshop „Keramik in Österreich 2018“ organised by the Austrian Ceramic Society; Title: ”Strontium freie Seltenerd-Perowskit Ferrite mit rascher Sauerstoffaustauschkinetik: Synthesemethoden und Charakterisierung“, 15.02.2018

Entire List of Publications (h=9)

[1] C. Berger, E. Bucher, C. Gspan, W. Sitte, Journal of Solid State Chemistry **273** (2019) 92.

[2] C. Berger, E. Bucher, C. Gspan, A. Menzel, W. Sitte, *Solid State Ionics* **326** (2018) 82.

[3] C. Berger, E. Bucher, A. Egger, A.T. Strasser, N. Schrödl, C. Gspan, J. Hofer, W. Sitte, *Solid State Ionics* **316** (2018) 93

[4] C. Berger, E. Bucher, A. Windischbacher, A.D. Boese, W. Sitte, *Journal of Solid State Chemistry* **259** (2018) 57.

[5] C. Berger, E. Bucher, C. Gspan, A. Menzel, W. Sitte, *J. Electrochem. Soc.* **164** (2017) (10) F3008.

[6] C. Berger, E. Bucher, W. Sitte, *Solid State Ionics* **299** (2017) 46.

[7] F.A. Mautner, C. Berger, R.C. Fischer, S.S. Massoud, R. Vicente, *Polyhedron* **134** (2017) 126.

[8] F.A. Mautner, C. Berger, C. Gspan, B. Sudy, R.C. Fischer, S.S. Massoud, *Polyhedron* **130** (2017) 136.

[9] F.A. Mautner, C. Berger, R.C. Fischer, S.S. Massoud, *Inorganica Chimica Acta* **439** (2016) 69.

[10] F.A. Mautner, C. Berger, S.S. Massoud, *Journal of Molecular Structure* **1110** (2016) 114.

[11] F.A. Mautner, C. Berger, R.C. Fischer, S.S. Massoud, *Polyhedron* **111** (2016) 86.

[12] F.A. Mautner, C. Berger, R.C. Fischer, S.S. Massoud, *Inorganica Chimica Acta* **448** (2016) 34.

[13] F.A. Mautner, C. Berger, E. Domian, R.C. Fischer, S.S. Massoud, *Journal of Molecular Structure* **1122** (2016) 234.

[14] F.A. Mautner, M. Scherzer, C. Berger, R.C. Fischer, R. Vicente, S.S. Massoud, *Polyhedron* **85** (2015) 20.

[15] F.A. Mautner, M. Scherzer, C. Berger, R.C. Fischer, R. Vicente, S.S. Massoud, *Polyhedron* **85** (2015) 329.

[16] F.A. Mautner, M. Scherzer, C. Berger, R.C. Fischer, S.S. Massoud, *Inorganica Chimica Acta* **425** (2015) 46.

[17] F.A. Mautner, C. Berger, M. Scherzer, R.C. Fischer, L. Maxwell, E. Ruiz, R. Vicente, *Dalton Transactions* **44** (2015) (42) 18632.

[18] F.A. Mautner, C. Berger, M.J. Dartez, Q.L. Nguyen, J. Favreau, S.S. Massoud, *Polyhedron* **69** (2014) 48.

[19] J. Cano, F.A. Mautner, C. Berger, R.C. Fischer, R. Vicente, *Polyhedron* **50** (2013) (1) 240.

[20] F.A. Mautner, C. Berger, B. Sudy, R.C. Fischer, A. Escuer, R. Vicente, J. Cano, L. Ohrstrom, M.A.M. Abu-Youssef, M.A.S. Goher, *Acta Crystallographica Section A* **69** (2013) (a1) s624.

[21] F.A. Mautner, B. Sudy, C. Berger, R.C. Fischer, R. Vicente, *Polyhedron* **42** (2012) (1) 95.

9) Appendix

9.1) Contribution and apportionment of work for the publications

C. Berger, E. Bucher, C. Gspan, A. Menzel, W. Sitte, Journal of The Electrochemical Society 164 (2017) (10) F3008.

Christian Berger (first-author) synthesized the new compound $La_{0.8}Ca_{0.2}FeO_{3-\delta}$ (LCF82) and performed all experimental works, leading to the publication of this work, by himself. Christian Berger independently performed all synthesis and manufacturing tasks to proof the higher sulphur dioxide tolerance of LCF82. Christian Berger broadly performed the preparation of the manuscript.

The contribution of Edith Bucher in this work was the supervision of Christian Berger in the usual extent of his PhD-thesis.

The contribution of Christian Gspan in this work was the acquisition of the scanning transmission electron microscopy (STEM) images and discussing the measurement data with Christian Berger.

The contribution of Alexander Menzel in this work was the collection of X-ray photoelectron spectroscopy (XPS) data. Alexander Menzel verified the data interpretation done by Christian Berger.

The contribution of Werner Sitte (co-author) corresponded in proofreading of the manuscript.

The following points describe the contribution and apportionment of work "C. Berger, E. Bucher, C. Gspan, A. Menzel, W. Sitte, Journal of The Electrochemical Society 164 (2017) (10) F3008." in more detail.

Contribution of Christian Berger (first-author)

- Synthesis
  - Idea for increasing the calcium concentration on the A-site lattice of the ABO_3 perovskite to 20 % (coordinated with Edith Bucher)
  - Titration and preparation of the stock solutions
  - Calculation of the sample mass
  - Performance of a "Sol-Gel" method (glycine nitrate process)
  - Adaptation of the calcination temperature from previous publication on LCF91
- Powder processing and sintering
  - Optimisation of the grinding procedure
  - Measurement on particle size distribution
  - Pressing and determination of the optimal sinter temperature in the dilatometer
  - Manipulation of the sinter body (cutting, grinding and polishing)

- Basic characterisation
    - X-ray powder diffraction measurement (performed by V. Terziyska, Montanuniversitaet Leoben)
        - Sample phase composition was proved by Christian Berger
    - Scanning electron microscopy (performed by G. Hawranek, Montanuniversitaet Leoben); interpretation and preparation of various figures for publication by Christian Berger
- Oxygen exchange and electronic conductivity measurements
    - Samples in van der Pauw geometry with various thicknesses were prepared
    - Mounting of the sample in the measurement cell
    - Measurements at various temperatures ($600 \leq T/°C \leq 800$) and fixed oxygen partial pressure ($pO_2 = 1\times10^{-1}$ to 1.5×10^{-1} bar) to determine the oxygen surface exchange coefficients (k_{chem}), oxygen bulk diffusion coefficients (D_{chem}) and the electronic conductivity
    - Long-term experiment (1000 h) on the determination of k_{chem}, D_{chem} and the electronic conductivity at 700°C in 10 % O_2 in Ar and 15 % O_2 in Ar, respectively
    - Additional long-term experiment (1000 h) in sulphur dioxide containing atmosphere (2 ppm SO_2 admixed to the test gas mentioned above)
- Surface and interface analysis
    - Interpretation of the STEM results performed together with Christian Gspan
    - Interpretation and discussion of the XPS results together with Alexander Menzel
- Suggestion of a sulphur dioxide induced degradation mechanism of LCF82
    - Description of the degradation behaviour, by taking all measurement results into account
    - Formulation of chemical reactions that may occur during degradation
    - Comparing those results to values obtained from thermodynamic calculations (calculations performed by Edith Bucher with the software FactSage [86])
- Preparation of text and figures for the publication

Contribution of Edith Bucher (co-author)

- Supervision of Christian Berger in the usual extent of his PhD-thesis
- Calculation of predominance diagrams for further investigation of the degradation behaviour of LCF82 under sulphur dioxide containing atmospheres
- Preparation of Figure 12 in the manuscript
- Assistance in literature research
- Proofreading of the manuscript
- Submitting of the manuscript to the Journal "Journal of the Electrochemical Society" (corresponding author) as a Creative Commons Attribution Non-Commercial No Derivatives 4.0 License

Contribution of Christian Gspan (co-author)

- Recording of STEM images and analytical measurements (energy dispersive X-ray spectroscopy) in presence of Christian Berger
- Supported Christian Berger with JEMS [87] calculation of Fe_2O_3 phase and assistance during figure preparation process

Contribution of Alexander Menzel (co-author)

- Recording of XPS data
- Precise discussion of resulted data with the co-authors

Contribution of Werner Sitte (co-author, head of the Chair of Physical Chemistry)

- Proofreading of the manuscript

C. Berger, E. Bucher, A. Windischbacher, A.D. Boese, W. Sitte, Journal of Solid State Chemistry 259 (2018) 57.

Christian Berger (first-author) has synthesized the new compound $Pr_{0.8}Ca_{0.2}FeO_{3-\delta}$ (PCF82), compared it with the promising SOFC air electrode material LCF82 and additionally managed to perform all experimental works, leading to the publication of this work, by himself. Christian Berger independently performed the defect chemical modelling, as well as the interpretation of transport properties under the supervision of Edith Bucher (co-author). Christian Berger used the knowledge gained in the publication "C. Berger, E. Bucher, W. Sitte, Solid State Ion. 299 (2017) 46." to further improve the defect chemical model of Ca-containing rare earth perovskites. Christian Berger largely performed the preparation of the manuscript.

The contribution of Edith Bucher in this work was the supervision of Christian Berger in the usual extent of his PhD-thesis.

The contribution of Andreas Windischbacher in this work was to perform complex theoretical calculations concerning oxygen vacancy formation energies and oxygen position and transport pathways in the FeO_6 octahedron.

The contribution of Daniel A. Boese in this work was to monitor and supervise the calculations performed by Andreas Windischbacher. He also contributed in proofreading of the manuscript.

The contribution of Werner Sitte (co-author) corresponded in proofreading of the manuscript.

The following points describe the contribution and apportionment of work "C. Berger, E. Bucher, A. Windischbacher, A.D. Boese, W. Sitte, Journal of Solid State Chemistry 259 (2018) 57." in detail.

Contribution of Christian Berger (first-author)

- Synthesis
    - Investigation of different rare earth elemental compositions according to literature (coordinated with Edith Bucher)
    - Titration and preparation of the stock solutions
    - Calculation of the sample mass
    - Performance of a "Sol-Gel" method (glycine nitrate process)
    - Systematic study of calcination temperature for PCF82
- Powder processing and sintering for PCF82 (values for LCF82 have already been optimised in the publication "C. Berger, E. Bucher, C. Gspan, A. Menzel, W. Sitte, Journal of The Electrochemical Society 164 (2017) (10) F3008.")
    - Optimisation of the grinding procedure
    - Measurement on particle size distribution
    - Pressing and determination of the optimal sinter temperature in the dilatometer
    - Manipulation of the sinter body (cutting, grinding and polishing)

- Basic characterisation
    - X-ray powder diffraction measurement (performed by V. Terziyska, Montanuniversitaet Leoben); interpretation and Rietveld refinement performed by Christian Berger
        - Quantification of main and secondary phases
        - Determination of space group and lattice constants
        - Determination of atomic positions
    - Differential scanning calorimetry (performed by Christian Berger); interpretation and comparison of the received values to literature values also by Christian Berger
    - Determination of the thermal expansion coefficient for various oxygen partial pressures
- Oxygen exchange and electronic conductivity measurements
    - Samples in van der Pauw geometry with various thicknesses were prepared
    - Mounting of the sample in the measurement cell
    - Measurements at various temperatures and oxygen partial pressures to determine the oxygen surface exchange coefficients (k_{chem}), oxygen bulk diffusion coefficients (D_{chem}) and the electronic conductivity
- Defect chemical modelling
    - Adaptation and implementation of a defect model that was applied in "C. Berger, E. Bucher, W. Sitte, Solid State Ion. 299 (2017) 46."
    - The obtained information from defect modelling was used to interpret trends in electronic conductivity (and mobility of the charge carriers), oxygen self-diffusion coefficients, oxygen vacancy diffusion and trends in ionic conductivity
- Preparation of text and figures for the publication

Contribution of Edith Bucher (co-author)

- Supervision of Christian Berger in the usual extent of his PhD-thesis
- Suggestions for defect chemical modelling (programming in Mathematica)
- Assistance in literature research
- Proofreading of the manuscript
- Submitting of the manuscript to the Journal "Journal of Solid State Chemistry" (corresponding author)

Contribution of Andreas Windischbacher (co-author)

- Performance of complex theoretical calculations using VASP [88] code.
    - projector-augmented wave (PAW) method
    - compare computational predictions with experimental data by using Monkhorst-Pack k-point meshes

Contribution of Daniel A. Boese (co-author)

- Supervision of the calculations performed by Andreas Windischbacher
- Provide scientific input for theoretical calculation methods
- Proofreading of the manuscript

Contribution of Werner Sitte (co-author, head of the Chair of Physical Chemistry)

- Proofreading of the manuscript

C. Berger, E. Bucher, A. Egger, A.T. Strasser, N. Schrödl, C. Gspan, J. Hofer, W. Sitte, Solid State Ion. 316 (2018) 93.

Christian Berger (first-author) synthesized the new compound $Pr_2Ni_{0.9}Co_{0.1}O_{4+\delta}$ (PNCO) for the first time with a "Sol-Gel" method. Christian Berger independently performed the interpretation of all measurement results and mainly performed the preparation of the manuscript.

The contribution of Edith Bucher in this work was the supervision of Christian Berger in the usual extent of his PhD-thesis.

The contribution of Andreas Egger, Nina Schrödl and Johannes Hofer in this work was the supervision of experiments performed by Anna T. Strasser for her Master Thesis. Andreas Egger additionally improved the manuscript quality due to fruitful scientific discussions and proofreading of the manuscript. Nina Schrödl additionally contributed in proofreading of the manuscript.

The contribution of Christian Gspan in this work was the acquisition of the scanning transmission electron microscopy (STEM) images and analytic information obtained from EDX and EELS (electron energy loss spectroscopy) and discussing the measurement data with Christian Berger.

The contribution of Werner Sitte (co-author) corresponded in proofreading of the manuscript.

The following points describe the contribution and apportionment of work "C. Berger, E. Bucher, A. Egger, A.T. Strasser, N. Schrödl, C. Gspan, J. Hofer, W. Sitte, Solid State Ion. 316 (2018) 93." in detail.

Contribution of Christian Berger (first-author)

- Synthesis
  - Selection of the chemical composition based on an extensive literature study (coordinated with Andreas Egger and Edith Bucher)
  - Titration and preparation of the stock solutions
  - Calculation of the sample mass
  - Performance of a "Sol-Gel" method (glycine nitrate process) to prove the feasibility of preparation of the single phase compound
  - Systematic study of calcination temperature
- Powder processing and sintering
  - Optimisation of the grinding procedure
  - Measurement on particle size distribution
  - Pressing and determination of the optimal sinter temperature in the dilatometer
  - Manipulation of the sinter body (cutting, grinding and polishing), performed at Max Planck Institute for Solid State Research Stuttgart, Germany by Christian Berger

- Basic characterisation
    - X-ray powder diffraction measurement (performed by Nina Schrödl); interpretation and Rietveld refinement performed by Christian Berger
        - Quantification of main and secondary phases
        - Determination of space group and lattice constants
        - Determination of atomic positions
    - Scanning electron microscopy (performed by G. Hawranek, Montanuniversitaet Leoben); interpretation and preparation of various figures for publication by Christian Berger. EDX analysis was performed by Karin Stanglauer (Montanuniversitaet Leoben); interpretation and tabulation by Christian Berger
    - Differential scanning calorimetry (measured by Anna T. Strasser, supervised by Edith Bucher and Nina Schrödl); interpretation and comparison of the effect of Co-substitution on the phase transition temperature by Christian Berger
    - Determination of the thermal expansion coefficient for various oxygen partial pressures performed by Christian Berger and Anna T. Strasser
    - Thermogravimetric analysis of PNO and PNCO with Edith Bucher and Rotraut Merkle (Max Planck Institute for Solid State Research Stuttgart, Germany)
- Preparation of text and figures for the publication

Contribution of Edith Bucher (co-author)

- Supervision of Christian Berger in the usual extent of his PhD-thesis
- Performance of thermogravimetric measurements
- Proofreading of the manuscript
- Submitting of the manuscript to the Journal "Solid State Ionics" (corresponding author)

Contribution of Andreas Egger (co-author)

- Improvement of the manuscript quality due to an extension of the section on thermogravimetry and differential scanning calorimetry (discussions with Edith Bucher and Christian Berger)
- Supervision of experiments performed by Anna T. Strasser within her Master Thesis
- Proofreading of the manuscript

Contribution of Anna T. Strasser (co-author)

- Synthesis of PNCO via a freeze drying process (under supervision of Nina Schrödl and Johannes Hofer)
    - The phase stability was checked by Christian Berger in a previous experiment
- Powder processing and sintering of PNO and PNCO
- Oxygen exchange and electronic conductivity measurements
    - Samples in van der Pauw geometry with various thicknesses were prepared
    - Mounting of the sample in the measurement cell
    - Measurements at various temperatures and oxygen partial pressures to determine the oxygen surface exchange coefficients (k_{chem}) and the electronic conductivity

Contribution of Nina Schrödl (co-author)

- Synthesis of PNCO via a freeze drying process with Anna T. Strasser
- Supervision of experiments performed by Anna T. Strasser within her Master Thesis
- Proofreading of the manuscript

Contribution of Christian Gspan (co-author)

- Recording of STEM images and analytical measurements (energy dispersive X-ray spectroscopy) in presence of Nina Schrödl
- Proofreading of the manuscript

Contribution of Johannes Hofer (co-author)

- Synthesis of PNCO via a freeze drying process with Anna T. Strasser
- Proofreading of the manuscript

Contribution of Werner Sitte (co-author, head of the Chair of Physical Chemistry)

- Proofreading of the manuscript

C. Berger, E. Bucher, C. Gspan, W. Sitte, Journal of Solid State Chemistry 273 (2019) 92.

Christian Berger (first-author) synthesized the Ca-substituted compound $La_{0.75}Ca_{0.25}FeO_{3-\delta}$ (LCF7525) and additionally accomplished to perform all experimental works, leading to the publication of this work, by himself. Christian Berger independently performed the description of structural and transport properties, as well as a defect chemical modelling approach. Christian Berger widely performed the preparation of the manuscript.

The contribution of Edith Bucher in this work was the supervision of Christian Berger in the usual extent of his PhD-thesis.

The contribution of Christian Gspan in this work was highly focused on transmission electron microscopy imaging.

The contribution of Werner Sitte (co-author) corresponded in proofreading of the manuscript.

The following points describe the contribution and apportionment of work "C. Berger, E. Bucher, C. Gspan, W. Sitte, Journal of Solid State Chemistry **273** (2019) 92." in detail.

Contribution of Christian Berger (first-author)

- Synthesis, powder processing and sintering
    - Increase of Ca-concentration on the A-site of the ABO_3 perovskite to 25 % (to stay below the stability limit of ~35 % Ca-concentration on A-site previously reported in literature [89])
    - Calculation of the sample mass
    - Performance of a "Sol-Gel" method (citric acid, ethylenediaminetetraacetate route), to avoid the titration step and increase the product yield
    - Adaptation of the calcination temperature from the previous LCF-PCF works from Berger et al. [22, 40]
    - Optimisation of the grinding procedure
    - Measurement on particle size distribution
    - Pressing and determination of the optimal sinter temperature in the dilatometer
    - Manipulation of the sinter body (cutting, grinding and polishing)
- Basic characterisation
    - X-ray powder diffraction measurement, interpretation and Rietveld refinement performed by Christian Berger
        - Quantification of main and secondary phases
        - Determination of space group and lattice constants
        - Determination of atomic positions
        - Comparing structural parameters as a function of Ca-concentration
    - Scanning electron microscopy (performed by G. Hawranek, Montanuniversitaet Leoben); interpretation and preparation of various figures for publication by Christian Berger

    - Differential scanning calorimetry (measured by Edith Bucher); interpretation and comparison of the received values to literature values by Christian Berger
    - Determination of the thermal expansion coefficient for various oxygen partial pressures using a dilatometer
- Oxygen exchange and electronic conductivity measurements
    - Samples in van der Pauw geometry with various thicknesses were prepared
    - Mounting of the sample in the measurement cell
    - Measurements at various temperatures and oxygen partial pressures to determine the oxygen surface exchange coefficients (k_{chem}), oxygen bulk diffusion coefficients (D_{chem}) and the electronic conductivity
- Defect chemical modelling
    - Adaptation and implementation of a defect model
    - Self-diffusion coefficients of oxygen as well as oxygen vacancies, and their corresponding activation energies were calculated
    - The ionic conductivity was calculated by using Nernst-Einstein equation
- Preparation of text and figures for the publication

Contribution of Edith Bucher (co-author)

- Supervision of Christian Berger in the usual extent of his PhD-thesis
- Support in defect chemical modelling (programming in Mathematica)
- Assistance in literature research
- Proofreading of the manuscript
- Submitting of the manuscript to the Journal "Journal of Solid State Chemistry" (corresponding author)

Contribution of Christian Gspan (co-author)

- Recording of STEM images and analytical measurements (energy dispersive X-ray spectroscopy) in presence of Christian Berger.
- Proofreading of the manuscript

Contribution of Werner Sitte (co-author, head of the Chair of Physical Chemistry)

- Proofreading of the manuscript

9.2) Full text of the publications submitted for this thesis

JES Focus Issue on Oxygen Reduction and Evolution Reactions for High Temperature Energy Conversion and Storage

Impact of SO_2 on the Oxygen Exchange Kinetics of the Promising SOFC/SOEC Air Electrode Material $La_{0.8}Ca_{0.2}FeO_{3-\delta}$

Christian Berger,[a] Edith Bucher,[a,z] Christian Gspan,[b] Alexander Menzel,[c] and Werner Sitte[a,*]

[a]*Chair of Physical Chemistry, Montanuniversitaet Leoben, A-8700 Leoben, Austria*
[b]*Institute of Electron Microscopy and Nanoanalysis (FELMI), Graz University of Technology & Graz Centre for Electron Microscopy (ZFE), Austrian Cooperative Research (ACR), A-8010 Graz, Austria*
[c]*Institute of Physical Chemistry, University of Innsbruck, A-6020 Innsbruck, Austria*

The mass and charge transport properties of $La_{0.8}Ca_{0.2}FeO_{3-\delta}$ (LCF82) were determined at 600–800°C and $pO_2 = 0.1$ bar. The electronic conductivity is in the range of 112 S cm^{-1} at 700°C. The chemical surface exchange coefficient (k_{chem}) and the chemical diffusion coefficient of oxygen (D_{chem}) were measured. LCF82 shows exceptionally fast oxygen exchange kinetics in pure O_2-Ar at 700°C. Long-term measurements at 700°C in pure O_2-Ar showed an excellent stability of the kinetic parameters during 1000 h. However, when 2 ppm of sulfur dioxide were added, k_{chem} decreased by a factor of 40 within the first 24 h. After further 1000 h, the total decrease in k_{chem} amounted to two orders of magnitude. Post-test analyses of LCF82 were performed by SEM-EDXS, XPS, and STEM. Ca-enrichment and La-/Fe-depletion of the LCF82 surface occurred during the first 1000 h without SO_2. At the surface of the sample exposed to 2 ppm SO_2 for additional 1000 h, $CaSO_4$ crystals with diameters of 1–2 μm and an underlying layer of Fe_2O_3 (thickness approx. 300–450 nm) were found. Remarkably, LCF82 shows faster oxygen exchange kinetics than $La_{0.6}Sr_{0.4}CoO_{3-\delta}$ even in the degraded state. Therefore, LCF82 is suggested as a promising material for SOFC and SOEC air electrodes.
© The Author(s) 2017. Published by ECS. This is an open access article distributed under the terms of the Creative Commons Attribution Non-Commercial No Derivatives 4.0 License (CC BY-NC-ND, http://creativecommons.org/licenses/by-nc-nd/4.0/), which permits non-commercial reuse, distribution, and reproduction in any medium, provided the original work is not changed in any way and is properly cited. For permission for commercial reuse, please email: oa@electrochem.org. [DOI: 10.1149/2.0041710jes] All rights reserved.

Manuscript submitted March 2, 2017; revised manuscript received May 8, 2017. Published June 1, 2017. *This paper is part of the JES Focus Issue on Oxygen Reduction and Evolution Reactions for High Temperature Energy Conversion and Storage.*

Mixed-conducting perovskites like $La_{1-x}Sr_xCoO_{3-\delta}$ (LSC) and $La_{1-x}Sr_xCo_{1-y}Fe_yO_{3-\delta}$ (LSCF) are frequently applied as air electrodes in solid oxide fuel cells (SOFCs) and solid oxide electrolyser cells (SOECs) due to their fast oxygen exchange kinetics, high electronic conductivities, and significant ionic conductivities.[1–5] In these materials, substitution of La^{3+} with Sr^{2+} is used to increase the oxygen nonstoichiometry and oxygen ionic conductivity (ionic charge compensation by formation of oxygen vacancies), as well as the electronic conductivity (electronic charge compensation by oxidation of Co^{3+}/Fe^{3+} to Co^{4+}/Fe^{4+}).[6–8] However, various studies have shown that Sr tends to segregate to the surface via the grain boundaries to relieve mechanical stress in the material which occurs due to the mismatch in the ionic radii of La^{3+}(XII) (1.36 Å) and Sr^{2+}(XII) (1.44 Å).[9–14] Lee et al.[15] performed an experimental study on the segregation of Ba^{2+}, Ca^{2+}, and Sr^{2+} in $LnMnO_3$ (Ln = La, Sm) which was complemented by density functional theory (DFT) calculations and analytical modelling. The results showed that the segregation of the alkaline earth metal ions is driven not only by elastic energy minimization (due to the size mismatch of La^{3+} and $Ba^{2+}/Sr^{2+}/Ca^{2+}$) but also by electrostatic forces. The latter were reported to occur due to interactions between the substituent (effective negative charge) and charged defects (for instance oxygen vacancies with effective positive charge) at the surface and in the space charge zone near the surface, leading to electrostatic attraction of the alkaline earth metal ion from the surface and electrostatic repulsion from the bulk.[15] Further, these authors showed that the tendency for surface segregation decreases with decreasing size mismatch of the substituent with the La^{3+} ion in the series $Ba^{2+} > Sr^{2+} > Ca^{2+}$.

Long-term investigations of LSC and LSCF have shown that the Sr-enriched surfaces and grain boundaries react with impurities such as Cr and Si, which are transported via the gas phase, and SO_2, which is present with approximately 1–100 ppb in ambient air, and that these effects causes a severe degradation of the oxygen exchange properties.[10,16–23]

One possible approach to decrease the mismatch in the ionic radii of La^{3+}(XII) (1.36 Å) and the divalent substituent, is to replace Sr^{2+}(XII) (1.44 Å) with Ca^{2+}(XII) (1.34 Å).[9] Recent short-term investigations under laboratory conditions in pure O_2-Ar atmospheres showed that perovskites from the series $(La,Ca)FeO_{3-\delta}$ show a high activity toward oxygen reduction, as well as good electronic and ionic conductivities.[24–31] However, the long-term stability of $(La,Ca)FeO_{3-\delta}$, which is a key issue for the application of these materials as air electrodes in SOFCs and SOECs, has yet to be demonstrated, especially under application-relevant conditions in atmospheres containing contaminants.

In the present work, the composition $La_{0.8}Ca_{0.2}FeO_{3-\delta}$ (LCF82) is investigated with respect to the oxygen exchange kinetics and the electronic conductivity in the short-time domain in pure O_2-Ar atmosphere as a function of temperature. In addition, the long-term stability of LCF82 is tested for 2000 h in O_2-Ar without and with 2 ppm SO_2 at 700°C, since previous studies on perovskites such as LSC and LSCF showed that sulfur dioxide poisoning is an especially critical issue for IT-SOFC cathodes.[21,32–35] In contrast to ambient air, which contains 1–100 ppb of SO_2, the present amount of sulfur dioxide is relatively high. Thus, the results from this study are to be understood in terms of accelerated testing.

After long-term in-situ dc-conductivity relaxation measurements, degraded LCF82 samples are analyzed with scanning electron microscopy (SEM) with energy dispersive X-ray spectroscopy (EDXS), X-ray photoelectron spectroscopy (XPS), and analytical scanning transmission electron microscopy (STEM). Based on these results, a tentative degradation mechanism for the SO_2-poisoning of LCF82 is proposed.

Experimental

$La_{0.8}Ca_{0.2}FeO_{3-\delta}$ (LCF82) powder was synthesized by a glycine nitrate process starting from 1 M aqueous nitrate solutions prepared from $La(NO_3)_3 \cdot 6H_2O$, $Ca(NO_3)_2 \cdot 4H_2O$, and $Fe(NO_3)_3 \cdot 9H_2O$ (all reagents purchased from Sigma Aldrich, analytical grade quality). Stoichiometric amounts of each stock solution were mixed and blended with glycine in the ratio of one mole glycine per mole cation. Due to

*Electrochemical Society Member.
zE-mail: edith.bucher@unileoben.ac.at

Downloaded on 2018-07-09 to IP 193.170.16.194 address. Redistribution subject to ECS terms of use (see ecsdl.org/site/terms_use) unless CC License in place (see abstract).

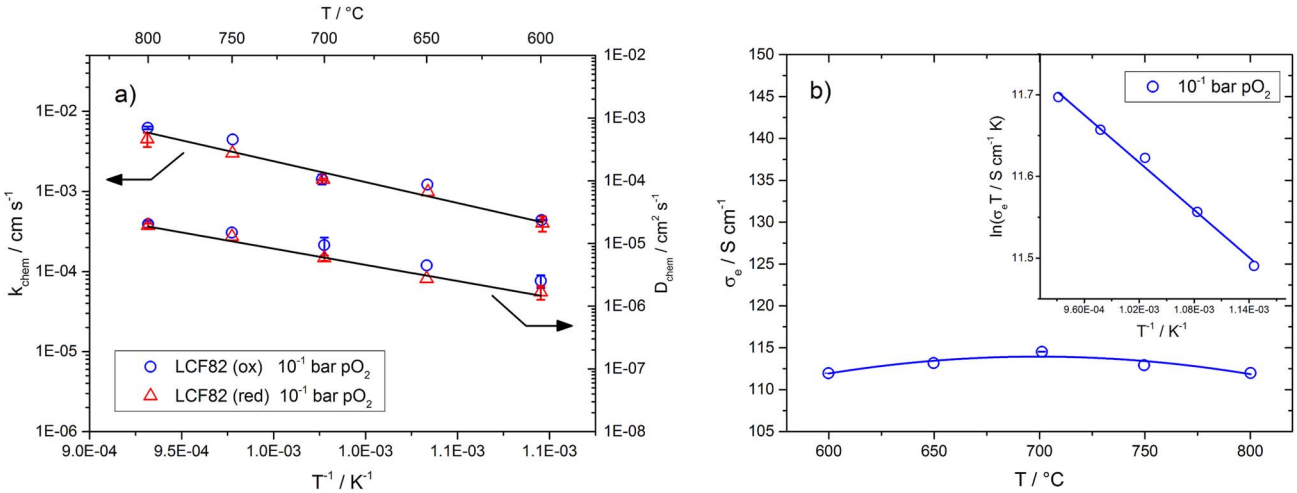

Figure 1. a) Chemical surface exchange coefficient of oxygen (k_{chem}) and chemical diffusion coefficient of oxygen (k_{chem}) of LCF82; b) electronic conductivity including the Arrhenius plot; all data were measured at 10^{-1} bar pO_2 in the temperature range of $600 \leq T/°C \leq 800$.

heat-treatment, the resulting water free gel ignited at approximately 250°C. The resulting raw ash was calcined at 1000°C, ball milled, isostatically pressed, and sintered for 2 h in air at 1100°C with heating and cooling rates of 1 K min^{-1}, similar to the procedure described elsewhere.[24] For scanning electron microscopy, samples were polished and thermally etched (1050°C, heating and cooling rates 5 K min^{-1}). Thin, dense samples were obtained by cutting pieces from a sintered rod with 97 % of the theoretical density using a diamond wire saw, and polishing with diamond discs down to a fineness of 1 µm. A 503 µm thick sample with a cross section of approximately 5 × 5 mm^2 was contacted in four-point van der Pauw geometry[36] using sulfur-free gold paste (MaTecK) and gold wires (Ögussa).

Based on the results of the pre- and post-test analyses it is estimated that the concentrations of impurities other than sulfur (which was added in the degradation test with 2 ppm SO_2) were very low. SEM-EDX analyses of the fresh and degraded samples showed no elements other than La, Ca, Fe, O (and S after 1000 h in SO_2-O_2-Ar atmosphere), see Scanning electron microscopy section. In the XPS elemental depth profiles of the fresh specimen carbon was detected within the first 100 nm, see X-ray photoelectron spectroscopy section. This is assumed to deposit on the sample during storage in ambient air at room temperature in the form of very thin carbonate layers. During the conductivity relaxation experiments at 600–800°C and $pO_2 = 0.10$–0.15 bar (O_2-Ar atmosphere) these carbon layers should be decomposed within relatively short time and should therefore not influence the measured chemical surface exchange coefficients. XPS analyses of the degraded samples showed S in the SO_2-poisoned sample but no significant amounts of other impurities, see X-ray photoelectron spectroscopy section. Analogously, no impurities other than sulfur were found in the STEM analyses, see Analytical transmission electron microscopy section.

Impurities in the test gases without SO_2 (10 or 15 % O_2, rest Ar) and with SO_2 (10 or 15 % O_2, 2 ppm SO_2, rest Ar) were not specified by the supplier (Linde Gas GmbH, Austria). However, a rough estimation of the impurity content in the gas mixtures could be made based on the specifications for the pure gases (Ar 5.0: $H_2O \leq 3$ ppm, hydrocarbons ≤ 0.2 ppm; O_2 5.0: $H_2O \leq 3$ ppm, hydrocarbons ≤ 0.2 ppm, $CO_2 \leq 0.2$ ppm; all data provided by Linde Gas GmbH, Austria).

During the conductivity relaxation experiments the samples were placed in a quartz glass reactor in a dry test gas flow. Impurities from the furnace, which was outside of the reactor, can therefore be excluded. The transport of Si-species via the gas phase and Si-poisoning of the samples can be assumed to be negligible since only dry test gases (estimated humidity ≤ 3 ppm; see above) were used. According to previous studies[10,16,18,19,37] and thermodynamic data[38–40] Si-transport in the form of $Si(OH)_4(g)$ occurs in oxidizing atmospheres only in the presence of significant amounts of $H_2O(g)$.

The gold paste, which was used to attach the electrical contacts for conductivity relaxation experiments, was free of S, Pb, and Cd according to the specifications of the supplier (MaTecK GmbH, Germany). SEM-EDX analyses of the dried gold paste (before burn-out of organic components) showed no elements other than Au, C, and O.

The chemical surface exchange coefficient (k_{chem}), as well as the chemical diffusion coefficient of oxygen (D_{chem}), were obtained from in-situ dc-conductivity relaxation experiments, which were conducted in van der Pauw electrode configuration.[41] The electrical conductivity change of the sample, which occurred due to a step-wise change of the oxygen partial pressure, was recorded using small pO_2-steps in the range $1.0 \times 10^{-1} \leq pO_2/\text{bar} \leq 1.5 \times 10^{-1}$ (conditions close to equilibrium). A four-way valve was used for (manually) switching between the gas mixtures with different oxygen content. A constant total gas flow of 2 dm^3 h^{-1} was applied, and the measurements were performed in oxidizing and reducing directions. During all experiments a constant current of 40 mA (current density ~1.6 mA mm^{-2}) was applied to the sample with a precision current source (Keithley 2400) and the voltage was measured as a function of time using a sensitive digital voltmeter (Keithley 182). The applied current resulted in a burden voltage of 50–55 mV (600–800°C) depending on temperature. Instrument control and data read-out were realized with a computer-based data acquisition system with the software *LabVIEW* (National Instruments).

The kinetic parameters (k_{chem} and D_{chem}) were obtained from non-linear least squares fits of the solution of the diffusion equation to the conductivity relaxation data.[42–44] The model assumes that the oxygen surface exchange reaction obeys first-order kinetics, and that both kinetic parameters are constant during the pO_2-step. Multiple measurements of k_{chem} and D_{chem} were performed at various temperatures in order to estimate the experimental errors (see error bars in Fig. 1a). During the long-term measurements at constant temperature the errors in the kinetic parameters were ≤ 25 % in the test segment without SO_2 and ≤ 8 % in the test segment with SO_2. As described in[42] significant errors in the determination of k_{chem} and D_{chem} may occur during measurements of kinetically fast materials when flush time effects are neglected. Therefore, the flush time of the empty reactor (τ) used for the present experiments was previously determined with a miniaturized potentiometric oxygen sensor with an internal Ir/IrO_2 reference and an integrated S-type thermocouple (MicroPoas, Setnag) which was mounted in the reactor close to the usual positon of the sample. The response of the sensor voltage to a step-wise change in

Downloaded on 2018-07-09 to IP 193.170.16.194 address. Redistribution subject to ECS terms of use (see ecsdl.org/site/terms_use) unless CC License in place (see abstract).

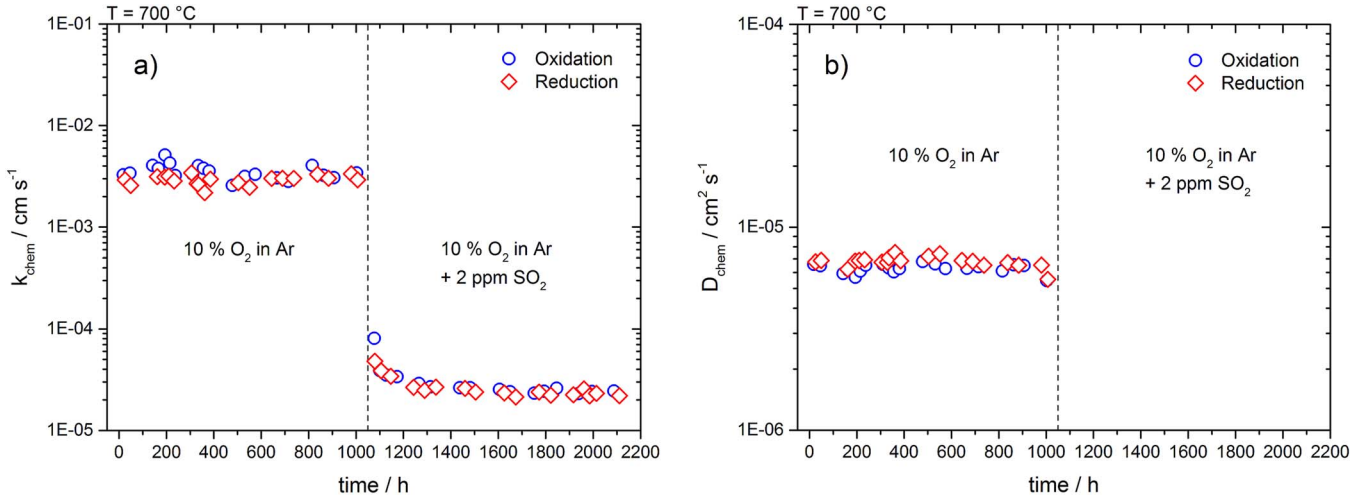

Figure 2. a) Long-term measurements of the chemical surface exchange coefficient of oxygen and b) the chemical diffusion coefficient of oxygen of LCF82 at 10^{-1} bar pO_2 and 700°C; after the first 1000 h 2 ppm SO_2 were added to the test gas.

the pO_2 was recorded as a function of time. From these data the flush time of the empty reactor was determined by nonlinear least squares regression using the equation for a continuously ideally stirred tank reactor.[42] The flush time amounted to $\tau = 1$ s and was taken into account in the determination of k_{chem} and D_{chem} of LCF82. It is estimated that the highest values of the kinetic parameters which could be reliably measured with the present setup are approximately $k_{chem} = 1 \times 10^{-2}$ cm s^{-1} and $D_{chem} = 5 \times 10^{-5}$ cm^2 s^{-1}.

Scanning electron microscopy with energy dispersive X-ray spectroscopy (SEM-EDXS) was carried out on a Zeiss EVO50 microscope with an EDX Oxford Instruments Inca detector. High-resolution SEM images were recorded in secondary electron (SE) and backscattered electron (BSE) mode at an acceleration voltage of 15 kV.

X-ray photoelectron spectroscopy (XPS) was performed with a Thermo MultiLab 2000 spectrometer with an alpha 110 hemispherical analyzer (Thermo Electron) in the constant analyzer energy mode (pass energy 100 eV, overall energy resolution 2.2 eV). A twin crystal monochromator provided Al Kα radiation (1486.6 eV) with a focus of 650 μm in diameter. Elemental depth profiles were obtained by Ar ion etching using an EX05 Ion Gun from Thermo Electron, providing a 3 keV beam with a diameter of approximately 50 μm, which automatically scanned over an area of at least 2 × 2 mm^2, irradiating the surface at an ion current of 1.0 μA. In this way, a uniform sputter rate was ensured in the central area of the crater. The sputter rate, crater form, and crater position were determined previously by sputtering a ZnS/MgF_2 multilayer-system (optical filter) with known thickness. It should be noted that the elemental depth profiles may be influenced by preferential sputtering, but a detailed quantitative analysis of these effects is beyond the scope of this study. Therefore, all details referring to the depth of specific features in the following text, as well as the scales in the elemental depth profiles, should be understood in terms of "approximate depth". Nevertheless, the present method allows a direct comparison of the various samples and yields valuable information on the changes in the surface elemental distribution due to different pre-treatments. In order to perform the background subtraction, an S-shaped Shirley background function was used. After background subtraction, the areas of the detected XPS core-level peaks were used to calculate the atomic concentration (at. %) of each constituent, taking into account the analyzer's transmission function and the sensitivity factors of the elements. Systematic errors may originate in data processing and interpretation (variation of background functions, evaluation of different peaks etc.) and are estimated to a factor of 1.05–1.20 (5–20 %). Additional effects like preferential sputtering (see above), sample composition, surface morphology etc. may also play a role. The errors thus introduced may be substantial, but are difficult to estimate.

The sample preparation for the TEM investigation was carried out on a focused ion beam (FIB) microscope FEI NOVA 200 Nanolab. For comparison with the experiment, diffraction patterns for particular zone axes were calculated with the software JEMS.[45] TEM investigations were performed with a TITAN^3 G2 60–300 from FEI at 300 keV accelerating voltage. The microscope is equipped with a C_S–probe corrector for the scanning transmission electron microscopy mode (STEM) and with the Super-X detector system from the company Bruker. STEM images were recorded both with a high angle annular dark field (HAADF) and a bright field (BF) detector at the same time. In some cases the annular dark field (ADF) detector was used instead of the BF detector to get a better contrast between the different crystals, and to reach a better imaging of the crystal formation.

Results and Discussion

Oxygen exchange kinetics and electronic conductivity.—In-situ dc-conductivity relaxation measurements were performed in the temperature range of $600 \leq T/°C \leq 800$ at $pO_2 = 1 \times 10^{-1}$ bar to determine the kinetic parameters (k_{chem}, D_{chem}) of LCF82 in the short-time domain and under laboratory conditions (O_2-Ar atmosphere) (Figure 1a). Both kinetic parameters could be obtained simultaneously from each conductivity relaxation curve, which indicates a mixed-controlled kinetics. The results show that LCF82 exhibits excellent oxygen exchange and oxygen transport properties. For example $k_{chem} = 6 \times 10^{-3}$ cm s^{-1} and $D_{chem} = 2 \times 10^{-5}$ cm^2 s^{-1} were obtained for LCF82 at 800°C, and $k_{chem} = 1.5 \times 10^{-3}$ cm s^{-1} and $D_{chem} = 6 \times 10^{-6}$ cm^2 s^{-1} at 700°C. The activation energies for k_{chem} and D_{chem} are 42±4 kJ mol^{-1} and 43±7 kJ mol^{-1}, respectively. The electronic conductivity is in the range of $112 \leq \sigma_e/S\ cm^{-1} \leq 117$ (600–800°C) with an activation energy of 8±1 kJ mol^{-1} (Figure 1b). Therefore, the oxygen exchange kinetics of LCF82 is comparable, and in part even superior, to that of well-known IT-SOFC cathode materials like $La_{0.5}Sr_{0.5}CoO_{3-\delta}$ ($k_{chem} = 1 \times 10^{-3}$ cm s^{-1}, $D_{chem} = 2.5 \times 10^{-6}$ cm^2 s^{-1} at 700°C and $pO_2 = 1 \times 10^{-1}$ bar),[46] $La_{0.6}Sr_{0.4}CoO_{3-\delta}$ ($k_{chem} = 2 \times 10^{-4}$ cm s^{-1}, $D_{chem} = 1 \times 10^{-6}$ cm^2 s^{-1} at 700°C and $pO_2 = 1 \times 10^{-1}$ bar),[46] and $Ba_{0.5}Sr_{0.5}Co_{0.8}Fe_{0.2}O_{3-\delta}$ ($k_{chem} = 1 \times 10^{-3}$ cm s^{-1}, $D_{chem} = 8 \times 10^{-6}$ cm^2 s^{-1} at 700°C and $pO_2 = 1 \times 10^{-2}$ bar).[47]

Results on the long-term stability of the oxygen exchange kinetics of LCF82 are shown in Figure 2. During the first 1000 h, the kinetic parameters (k_{chem}, D_{chem}) were monitored as a function of time at 700°C and $pO_2 = 0.1$ bar without SO_2. Under these conditions, the chemical surface exchange coefficient (Figure 2a) and the chemical diffusion coefficient of oxygen (Figure 2b) exhibited an excellent stability without noticeable degradation over the whole time span of 1000 h. In earlier, similar experiments at 700°C, $La_{0.6}Sr_{0.4}CoO_{3-\delta}$

Downloaded on 2018-07-09 to IP 193.170.16.194 address. Redistribution subject to ECS terms of use (see ecsdl.org/site/terms_use) unless CC License in place (see abstract).

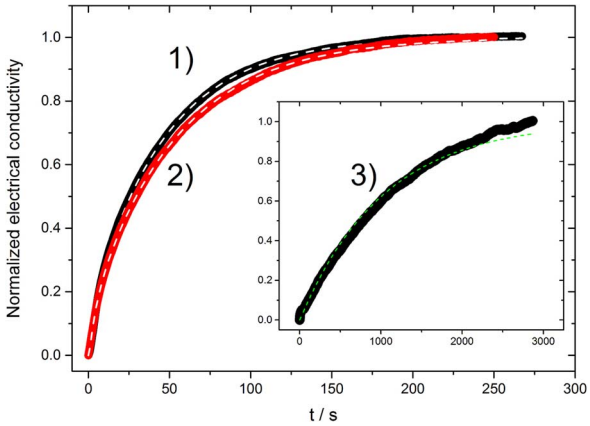

Figure 3. Examples of normalized conductivity relaxation curves of LCF82 at 700°C and $pO_2 = 0.1$ bar; (1) at the beginning of the experiment, (2) after 1000 h in pure O_2-Ar, and (3) after another 1000 h in the presence of 2 ppm SO_2; non-linear least square fits of the solution of the diffusion equation (dashed lines) to the experimental data (solid lines) are shown.

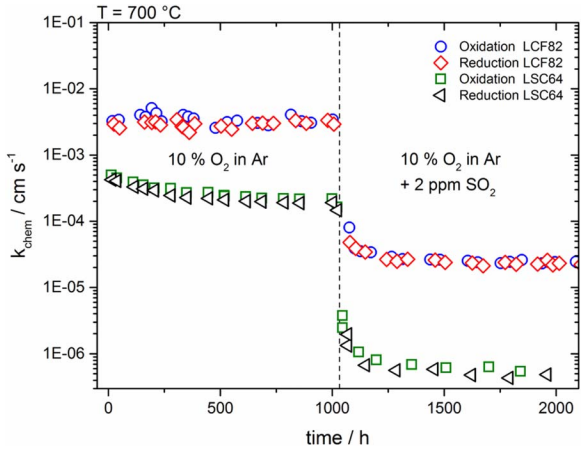

Figure 4. Comparison of long-term measurements of the chemical surface exchange coefficient of oxygen for LCF82 and $La_{0.6}Sr_{0.4}CoO_{3-\delta}$ (LSC64) at 10^{-1} bar pO_2 (dry O_2-Ar) and 700°C; after the first 1000 h 2 ppm SO_2 were added to the test gas. Data for LSC64 were taken from Reference 34.

showed a moderate degradation (decrease in k_{chem} by a factor of 2.5–10) already during 1000 h in O_2-Ar atmosphere which was ascribed to the formation of minor amounts of $SrSO_4$ due to trace impurities in the test gases (estimated to few ppb SO_2).[21,34]

After adding 2 ppm of sulfur dioxide to the O_2-Ar atmosphere ($pO_2 = 0.1$ bar) at 700°C a significant degradation of LCF82 was observed (Figure 2). Within the first 24 h, k_{chem} decreased from 3×10^{-3} cm s^{-1} to 8×10^{-5} cm s^{-1}. Approximately 200 h after the addition of SO_2, the surface exchange coefficient stabilized at $k_{chem} = 2.5 \times 10^{-5}$ cm s^{-1} and remained constant until the end of testing at t = 2100 h. Examples of conductivity relaxation curves in O_2-Ar atmosphere without and with SO_2 are plotted in Figure 3. Nonlinear least square fits of the solution of the diffusion equation to the conductivity relaxation curves showed that the kinetics was mixed-controlled in pure O_2-Ar atmosphere, and rate-controlled by the surface exchange process under conditions of SO_2-poisoning. This indicates that sulfur dioxide poisoning affects mainly the near-surface region of LCF82, and that the chemical diffusion coefficient either remains constant, or shows only a minor decrease in the presence of SO_2. For this reason, D_{chem} could not be obtained at t >1050 h (Figure 2b). The results of the post-test analyses given in Scanning electron microscopy–Analytical transmission electron microscopy sections confirm this assumption.

However, even in the SO_2-poisoned state, LCF82 still shows relatively fast oxygen exchange kinetics. By comparing the long-term stability of the chemical surface exchange coefficients of LCF82 and $La_{0.6}Sr_{0.4}CoO_{3-\delta}$[21] at 700°C in O_2-Ar atmosphere with 2 ppm SO_2, it

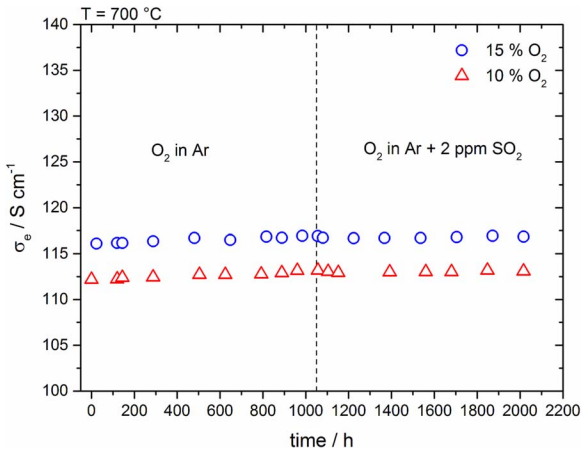

Figure 5. Electronic conductivity of LCF82 as a function of time; an O_2-Ar test gas with $pO_2 = 0.10$ bar was used during the first 1000 h. Then 2 ppm SO_2 were added during additional 1000 h.

becomes evident that LCF82 exhibits higher k_{chem} values in the fresh and degraded state (Figure 4). In addition, the total decrease in k_{chem} during 1000 h in the presence of 2 ppm sulfur dioxide is smaller for LCF82 (2 orders of magnitude) than for $La_{0.6}Sr_{0.4}CoO_{3-\delta}$ (3 orders of magnitude[21]).

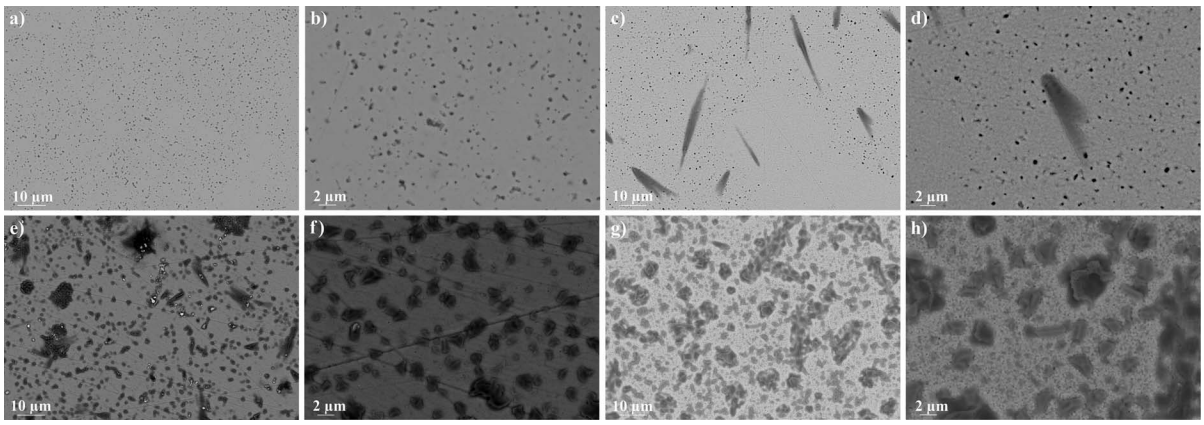

Figure 6. SEM analyses of LCF82 samples after different pre-treatments (for details see Table I); (a,b) LCF82-fresh, (c,d) LCF82-fresh (after thermal etching), (e,f) LCF82-woSO_2, and (g,h) LCF82-wSO_2. All images were recorded in the BSE mode.

Downloaded on 2018-07-09 to IP 193.170.16.194 address. Redistribution subject to ECS terms of use (see ecsdl.org/site/terms_use) unless CC License in place (see abstract).

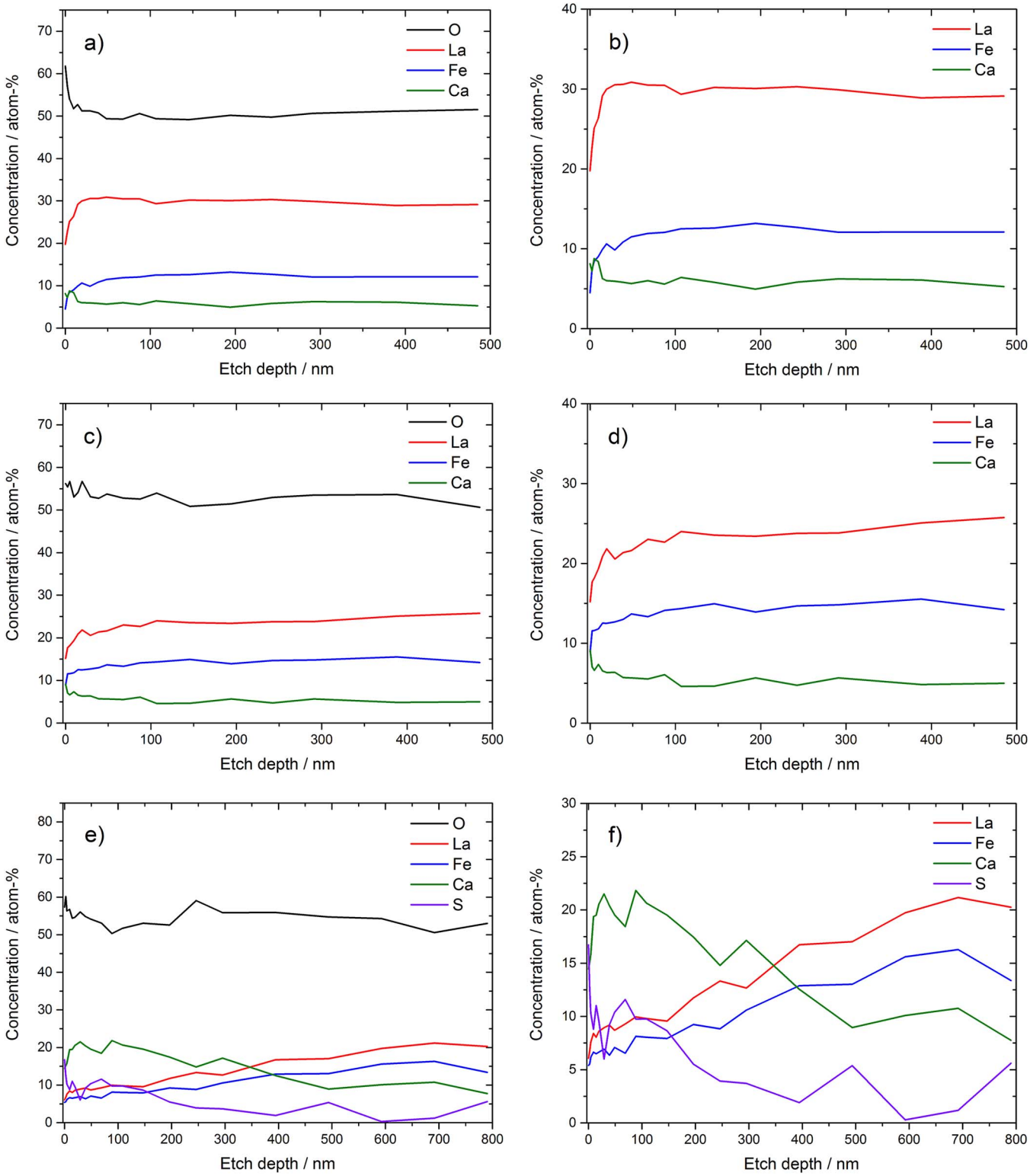

Figure 7. XPS elemental depth profiles of LCF82; (a) freshly polished sample, (c) after 1000 h in dry O_2-Ar with $pO_2 = 0.10$ bar, (e) after additional 1000 h with 2 ppm SO_2. The cation depth profiles (b), (d) and (f) are detailed views of the corresponding specimens (a), (b), and (c) (neglecting oxygen). Absolute values may be subject to systematic errors (refer to text for details).

Figure 5 shows the electronic conductivity of LCF82 as a function of time at 700°C and $pO_2 = 0.1$ bar. The electronic conductivity remains stable at $\sigma_e = 117 \pm 1$ S cm^{-1} for 2000 h and is not affected by sulfur dioxide poisoning. This is in agreement with the long-term data of the oxygen exchange kinetics (Figure 2) and the results of the post-test analyses (Figures 6–10), which show that the degradation in SO_2-containing atmosphere mainly affects the near-surface region.

Scanning electron microscopy.—In order to obtain further insight into the origin of the observed decrease in k_{chem}, SEM-EDX analyses

Downloaded on 2018-07-09 to IP 193.170.16.194 address. Redistribution subject to ECS terms of use (see ecsdl.org/site/terms_use) unless CC License in place (see abstract).

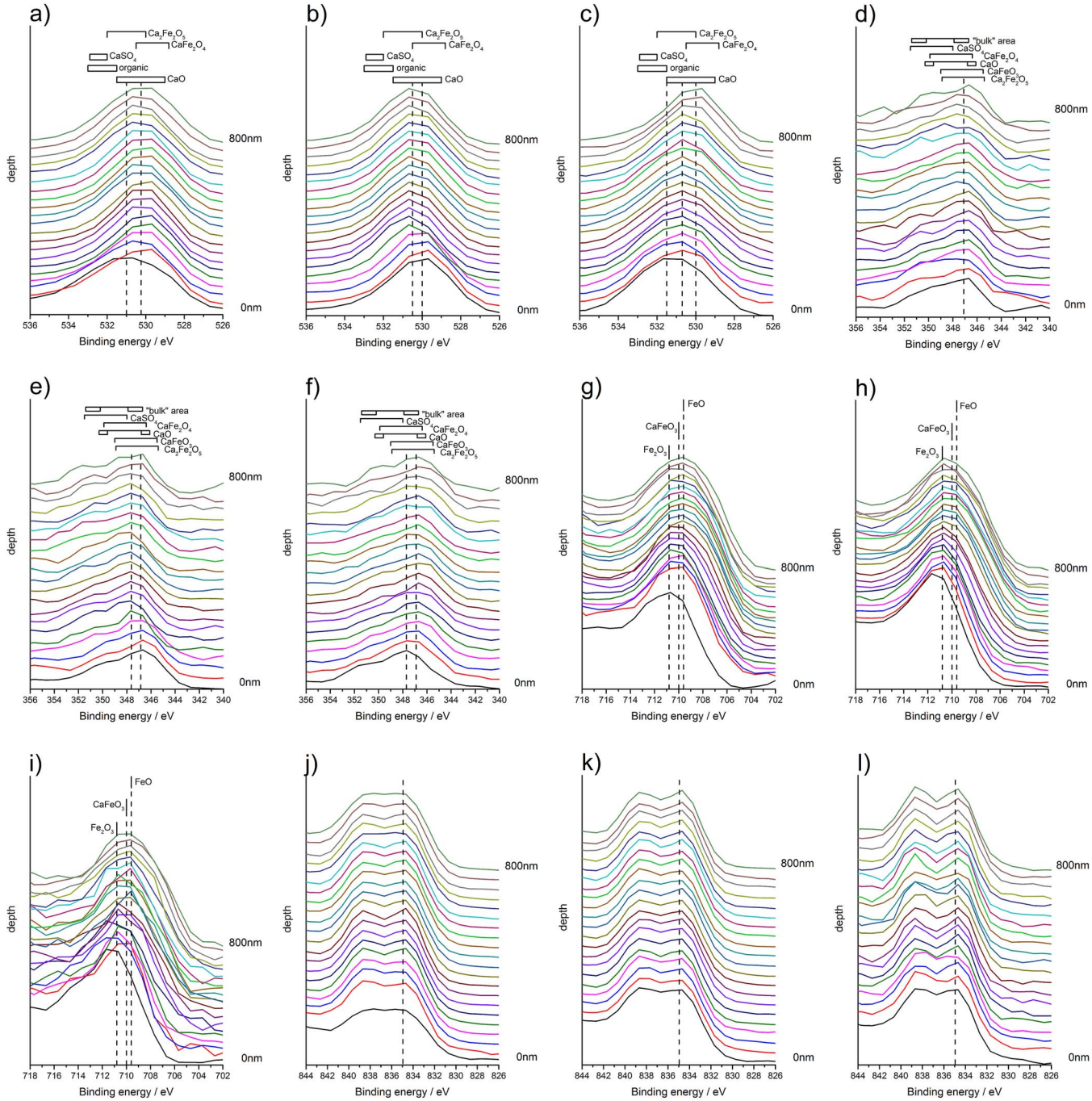

Figure 8. Comparison of the O 1s (a, b, c), Ca 2p (d, e, f), Fe 2p (g, h, i), and La 3d 5 (j, k, l) XPS core level spectra of LCF82 measured at different sample depths. The core level spectra are given for samples LCF82-fresh (a, d, g, j), LCF82-woSO_2 (b, e, h, k), and LCF82-wSO_2 (c, f, i, l). The La 3d 5 line at 835 eV was used to correct the calibration on the energy scale. Reference data for the compounds $Ca_2Fe_2O_5$, $CaFe_2O_4$, $CaFeO_3$,[58] CaO,[55–57,62,63] $CaSO_4$,[59,60] Fe_2O_3,[64–66] and FeO[66,67] were taken from the literature.

were performed with respect to changes in the surface morphology and elemental composition. Experimental conditions for fresh and degraded samples are summarized in Table I. Figures 6a and 6b show the surface of the fresh sample, while Figures 6c and 6d display the thermally etched sample. A smooth surface with small grooves (presumably due to grain pull-out from the polishing procedure) is found in the fresh as well as in the thermally etched sample. In addition, some needle shaped crystals with dimensions of approximately $4 \times 10\ \mu m^2$ are observed on the thermally etched surface. These crystals (Figures 6c and 6d), as well as the homogeneous, smooth regions, were investigated with energy dispersive X-ray spectroscopy (see supplementary material Figures S-1 and S-2). In the homogeneous regions of the surface, the nominal composition of LCF82 was found. EDX analyses of the needle-like crystals revealed that these are rich in calcium, iron and oxygen.

After 1000 h at 700°C in pure O_2-Ar atmosphere ($pO_2 = 0.10$ bar), irregularly shaped dark crystals with a size of 2 μm length and 1 μm broadness are found on the surface (Figures 6e and 6f). The dark crystals exhibit the same EDX spectra as the needle-like crystals, which were found on the surface of the thermally etched sample (see supplementary material Figures S-2 and S-3, respectively), and are rich in Ca, Fe, and O.

Downloaded on 2018-07-09 to IP 193.170.16.194 address. Redistribution subject to ECS terms of use (see ecsdl.org/site/terms_use) unless CC License in place (see abstract).

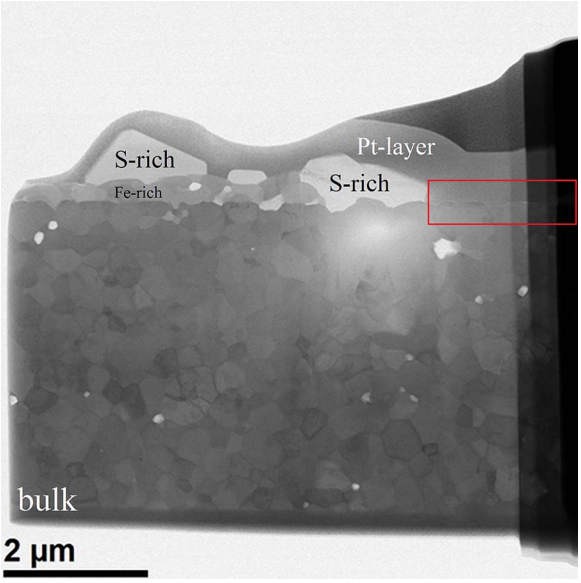

Figure 9. Cross-sectional STEM bright field image of LCF82-wSO_2. The Pt protection layer on top was deposited during the sample preparation for the TEM. Note the free (un-degraded) area on the surface indicated by the red rectangle.

Figures 6g and 6h show the surface of the sample after additional 1000 h in O_2-Ar atmosphere with 2 ppm SO_2. A significant part of the surface is covered with small (1×1 μm^2) crystals and isolated bigger (up to 3×3 μm^2) irregularly shaped ones. EDX spectra (see example given in the supplementary material Figure S-4) of both the small and bigger crystals show S, Ca, and O as the main constituents, with the Ca:S ratio being close to unity. This indicates the formation of $CaSO_4$, as confirmed by STEM in Analytical transmission electron microscopy section. The percentage of the free (oxygen exchange-active) and degraded surface areas was determined from the SEM-BSE image in Fig. 6g using the software *ImageJ* (freeware, https://imagej.nih.gov/ij/), see supplementary material Figure S-5. The inactive regions amount to approximately 40% of the surface, while approximately 60% of the surface remain free.

X-ray photoelectron spectroscopy.—In order to study the average chemical composition of the near-surface region, depth profiles were recorded using XPS depth profiling with Ar-sputtering. In the fresh state (sample LCF82-fresh, details see Table I) the elemental depth profiles are homogeneous, with only a slight enrichment of Ca and O and a decrease in the La and Fe concentration within the first 10 nm (Figures 7a and 7b). This is in accordance with the SEM-EDX analyses of the fresh sample (Figure 6b) which showed a smooth and homogeneous surface. Similarly to the observed Ca-enrichment, the surface segregation of Sr has been frequently reported in the literature for mixed conducting perovskites such as (La,Sr)(Co,Fe,Mn)$O_{3-\delta}$.[48–52] Comparing the elemental depth profiles of the fresh sample to those of the specimen treated for 1000 h in O_2-Ar atmosphere without SO_2 (LCF82-woSO_2; details see Table I), the enrichment of Ca as well as the depletion of La and Fe on the surface becomes more pronounced (occurring within the first 100 nm), (Figures 7c and 7d). Figures 7e and 7f show the XPS depth profiles of the SO_2-poisoned sample LCF82-wSO_2 (details see Table I). The significant changes in the surface morphology, which are observed in the SEM images (Figures 6g and 6h) after additional 1000 h in O_2-Ar atmosphere with 2 ppm SO_2, are accompanied by pronounced changes in the chemical composition of the near-surface region. A significant amount of sulfur is found in LCF82-wSO_2, even after sputtering to approximately 800 nm depth. Since the Ca and S concentration profiles show the same trend with depth, it could be assumed that these signals stem from the $CaSO_4$ crystals on the surface of LCF82-wSO_2 (compare SEM images in Figures 6g and 6h and STEM results in Analytical transmission electron microscopy section). This assumption is also supported by the characteristic energy of the S 2p peak of 169–170 eV[53] (see supplementary material Figure S-6).

The cation elemental depth profiles in Figure 7f show a decrease in S and Ca with increasing depth and an increase in La and Fe. In a depth of 800 nm, the cation concentrations of LCF82-wSO_2 are similar to those in LCF82-fresh and LCF82-woSO_2 after sputtering to 200–400 nm depth. It should be mentioned, that even though a constant composition over depth is measured in the elemental depth profiles after a certain time of Ar-sputtering (in a certain sample depth), this composition will usually not be identical to the bulk (nominal) composition, due to the effect of preferential sputtering.[16,54]

XPS core level spectra obtained at different sputter depths were analyzed in order to identify the phases formed in the near-surface region (Figure 8). The O 1s core level spectra are given in Figures 8a, 8b, and 8c, for specimens LCF82-fresh, LCF82-woSO_2, and LCF82-wSO_2, respectively. The O 1s spectra of LCF82-fresh and LCF82-woSO_2 (Figures 8a and 8b) could be interpreted by the formation of CaO,[55–57] $Ca_2Fe_2O_5$[58] (within the first 30 nm), and/or $CaFe_2O_4$[58] (from 30 to 800 nm in depth). In LCF82-wSO_2 (Figure 8c) the additional formation of $CaSO_4$[59,60] could be assumed. However, based only on the information from the O 1s and Ca 2p spectra it is not possible to clearly distinguish between the different oxide species on the surface. The Fe 2p XPS core shell spectra are given in Figures 8g, 8h, and 8i for LCF82-fresh, LCF82-woSO_2, and LCF82-wSO_2, respectively. No shift in the binding energies was observed for the Fe 2p XPS core shell spectra, just the formation of Fe_2O_3 at 710 eV binding energy. This is in agreement with the results of STEM analyses (Analytical transmission electron microscopy section) and the predominance diagrams (see supplementary material Figure S-6). To correct the binding energy on the x-axis of the plots in Figures 8a-8h, the La 3d 5 signals (Figures 8j, 8k, and 8l for LCF82-fresh, LCF82-woSO_2, and LCF82-wSO_2, respectively) were used, because the La 3d 5 signal at 835 eV remained constant over all measured depths and samples). However, it should be considered that due to relatively large step size the alignment of the La 3d 5 peak could only be done with a precision of ± 0.1 eV.

Analytical transmission electron microscopy.—TEM analyses were performed in order to study the distribution, crystal structure, and chemical composition of the secondary phases in the SO_2-poisoned sample LCF82-wSO_2 (details on sample pre-treatment see Table I). The overview cross sectional STEM bright field (BF) image of LCF82-wSO_2 is given in Figure 9, and examples of regions with different chemical composition are indicated. Figure 10 shows a detail from this image with higher magnification and in the high-angle annular dark field (HAADF) mode, which provides a Z-contrast. The EDX spectrum obtained from area 1 in Figure 10 gives the chemical composition of one of the large (0.75 μm height and 1.67 μm maximum broadness) S-rich crystals, which appear in dark gray. The elements found are mainly Ca, S, and O, with a ratio of Ca:S close to unity, which indicates the formation of $CaSO_4$. Beneath these large crystals, a medium gray region, which is rich in Fe and O, is found (area 2 in Figure 10). STEM-BF and STEM-HAADF images from this region and the corresponding Fast Fourier Transformations (FFT) are shown in Figure 11. The distances and angles of the reflections in reciprocal space in the FFT give evidence that the iron rich phase consists of Fe_2O_3 (Figure 11). This information could also be confirmed by the predominance diagram of the Ca-Fe-O-S system at 700°C (see supplementary material Figure S-7), which indicates that Fe_2O_3 is indeed the predominating phase under the experimental conditions of the experiment ($pO_2 = 0.1$ bar, $pSO_2 = 2 \times 10^{-6}$ bar).[61] The average thickness of the degraded surface zone ($CaSO_4$ and Fe_2O_3) is approximately 500–1000 nm, which is in good agreement with the results of the XPS depth profiles (Figures 7e and 7f). Underneath the $CaSO_4$ and Fe_2O_3 crystals, the dense LCF82 bulk phase (area 3 in Figure 10) is found, with an average grain size of approximately 300 nm.

Downloaded on 2018-07-09 to IP 193.170.16.194 address. Redistribution subject to ECS terms of use (see ecsdl.org/site/terms_use) unless CC License in place (see abstract).

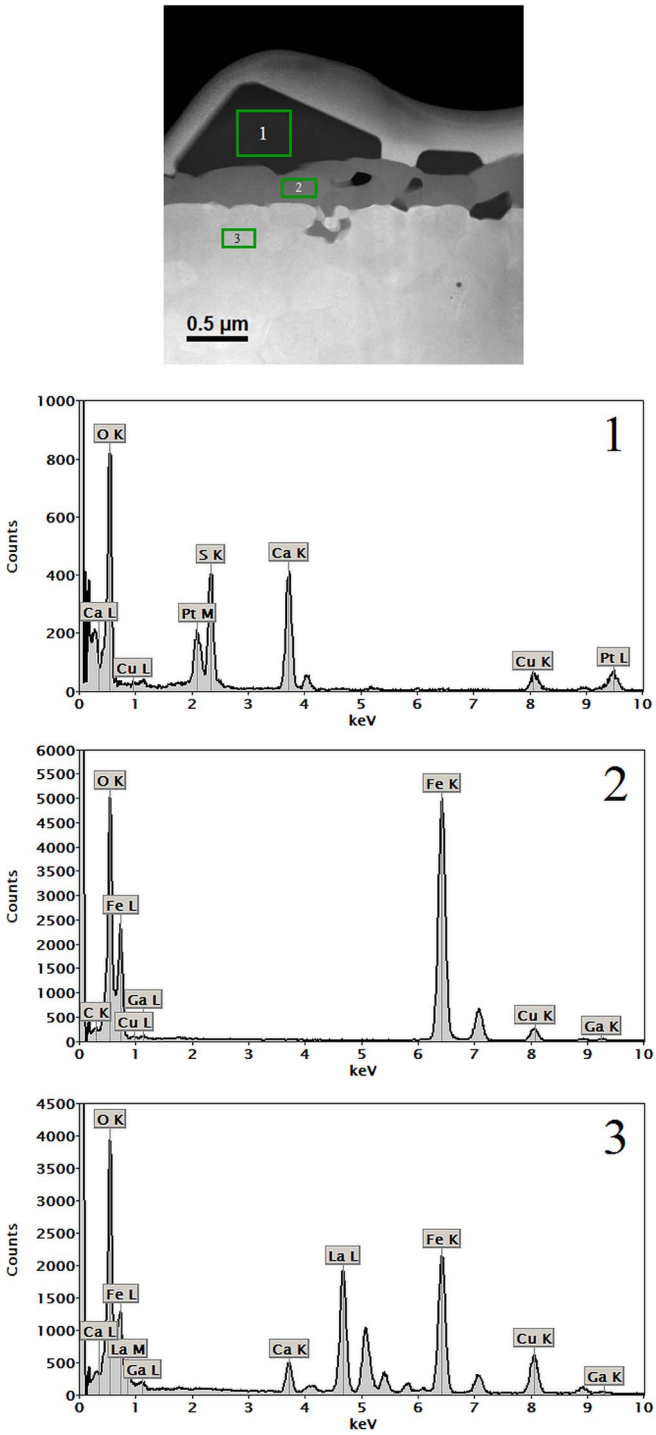

Figure 10. Cross-sectional STEM HAADF image of LCF82-wSO_2 with EDX spectra from different sample regions. Spectrum 1 was recorded on the large $CaSO_4$ crystal, spectrum 2 on the Fe_2O_3 phase, and spectrum 3 in the bulk of the specimen. The Cu, Ga, and Pt signals in the EDXS are artefacts from the sample holder, or introduced during the TEM preparation respectively.

It should be particularly emphasized that the degraded sample also exhibits regions which are not covered by inactive secondary phases, see for example the upper right area of the surface in Figure 9 marked by the red rectangle. In these regions, which can also be observed in the SEM images in Figures 6g and 6h, the original oxygen exchange-active LCF82 surface remains. Presumably, these "free" areas account for the relatively fast oxygen exchange kinetics of LCF82 even in the SO_2-poisoned state.

Table I. Experimental conditions and pre-treatments for LCF82 samples.

Sample name	Experimental condition
LCF82-fresh	Fresh sample; smoothly polished
LCF82-wSO_2	1000 h at 700°C in pure O_2-Ar atmosphere ($pO_2 = 0.10$ bar)
LCF82-wSO_2	1000 h at 700°C in pure O_2-Ar atmosphere ($pO_2 = 0.10$ bar) and additional 1000 h at 700°C in O_2-Ar atmosphere ($pO_2 = 0.10$ bar) with 2 ppm SO_2

The bright spots in the bulk area of the LCF82 lamella (Figure 9) were analyzed by an EDXS line scan (see for example Figure S-8 in the supplementary material). The resulting EDX signal profile showed that these are small pores or cavities.

Degradation mechanism for SO_2-poisoning of LCF82.—Based on the long-term in-situ measurements of the oxygen exchange kinetics (Oxygen exchange kinetics and electronic conductivity section) and the post-test analyses by the complementary techniques of SEM-EDX, XPS, and analytical TEM (sections Scanning electron microscopy–Analytical transmission electron microscopy) the following degradation mechanism is suggested, involving two steps, in SO_2-free (1) and SO_2-rich (2) atmospheres. For further illustration, a scheme of the proposed degradation mechanism is displayed in Figure 12.

(1) Enrichment of the surface with Ca and Fe in SO_2-free atmospheres (Figures 12a and 12b): Thermal etching (1050°C), or prolonged treatment of LCF82 at moderate temperatures (1000 h at 700°C) lead to an enrichment of Ca and Fe in the near-surface region. The formation of isolated, needle-like crystals is observed. It is assumed that these crystals are composed of $CaFe_2O_4$ and/or $Ca_2Fe_2O_5$. The size of these crystals increases with increasing time. However, this effect seems to have a negligible impact on the oxygen (surface) exchange kinetics.

(2) Surface-poisoning by chemical reaction with SO_2(g) atmospheres (Figures 12c and 12d): The $CaFe_2O_4$ and/or $Ca_2Fe_2O_5$ crystals formed in stage 1 react with sulfur dioxide from the gas phase. The phases $CaSO_4$ and Fe_2O_3 could be identified in the degraded sample. Thus, the following tentative reactions can be formulated:

$$CaFe_2O_4 + SO_2 + \tfrac{1}{2}\,O_2 \rightleftharpoons CaSO_4 + Fe_2O_3 \qquad [1]$$

$$Ca_2Fe_2O_5 + 2SO_2 + O_2 \rightleftharpoons 2CaSO_4 + Fe_2O_3 \qquad [2]$$

$CaSO_4$ occurs in the form of relatively large, angular crystals, which are found on top of or next to the Fe_2O_3 grains. After 1000 h at 700°C in the presence of 2 ppm SO_2, approximately 40 % of the sample surface is covered by these oxygen exchange-inactive secondary phases (see Scanning electron microscopy section). However, a significant amount of the surface remains unaffected. This may explain the relatively fast oxygen exchange kinetics of LCF82 even in the SO_2-poisoned state.

Comparison of the degradation behavior of LCF82 and $La_{0.6}Sr_{0.4}CoO_{3-\delta}$ (LSC64).—According to the results from the present long-term study, the surface exchange coefficient k_{chem} of LCF82 decreases by a factor of 120 during 1000 h at 700°C in an atmosphere with 2 ppm SO_2 (Figure 4), and the surface is covered by approximately 40 % inactive phases (supplementary material Figure S-5). In the case of $La_{0.6}Sr_{0.4}CoO_{3-\delta}$ (LSC64), which was equally pre-treated, virtually the whole surface was covered, and k_{chem} decreased by a factor of 400 (Figure 4, data from Ref. 21). However, it is difficult to say in which way the decrease in k_{chem} scales with the percentage of surface

Downloaded on 2018-07-09 to IP 193.170.16.194 address. Redistribution subject to ECS terms of use (see ecsdl.org/site/terms_use) unless CC License in place (see abstract).

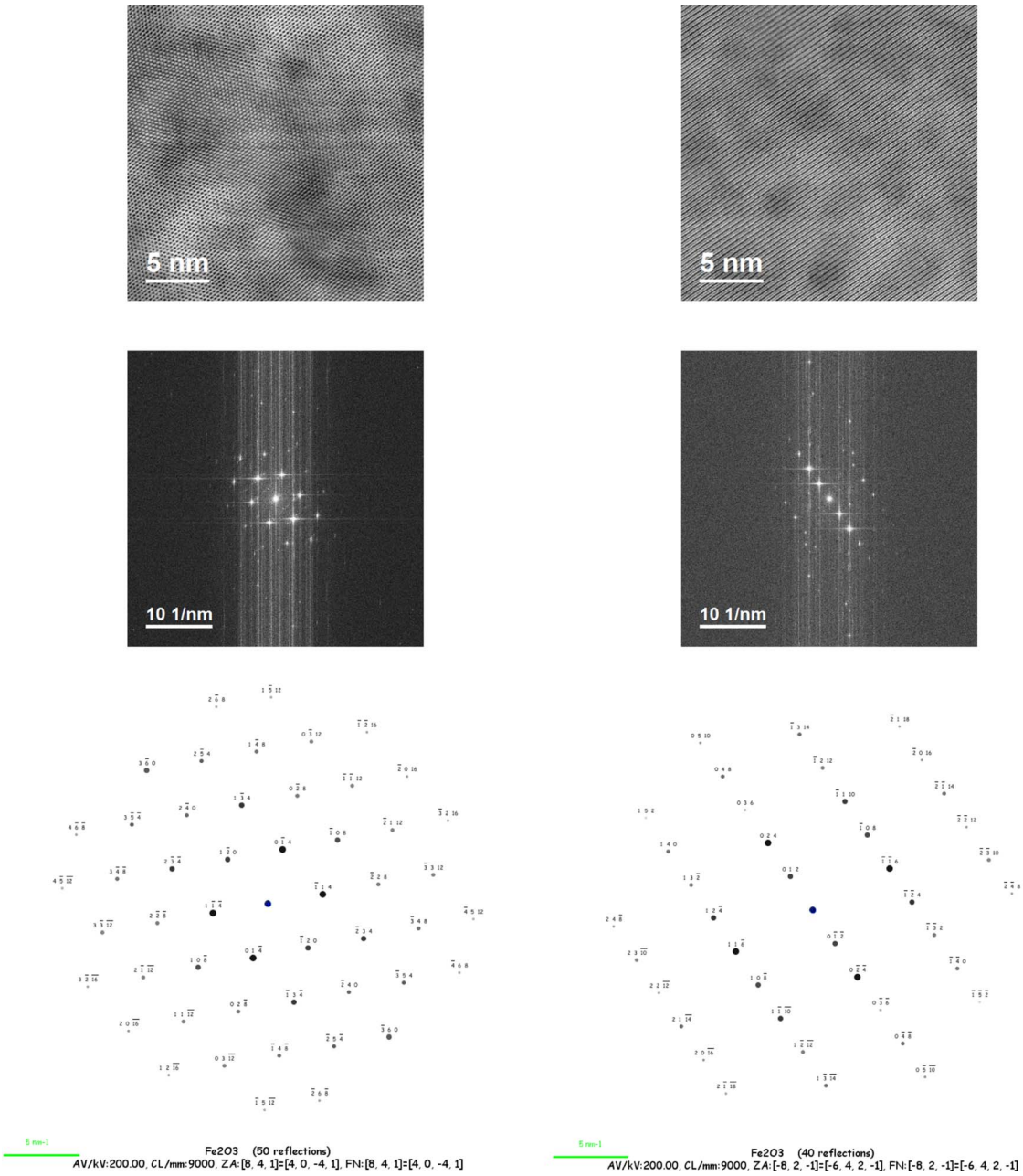

Figure 11. STEM BF image (left column) and STEM HAADF image (right column) from the Fe_2O_3 phase on the LCF82-wSO_2 sample; calculated FFT pattern and reference pattern associated with lattice vectors of Fe_2O_3.

covered by the secondary phases. In addition, it is to be expected that the surface covered by these phases is probably not completely inactive for oxygen exchange, but has rather a strongly reduced activity (even LSC64 with almost entirely covered surface showed a significantly reduced but still measureable oxygen exchange activity[21]). Nevertheless, it cannot be excluded that the seemingly "free" LCF82 surfaces additionally contribute to the degradation. Potential effects could be very thin Ca- or Ca-S-rich layers on top of these regions, which decrease the oxygen exchange activity. However, even when present, these few atom layers thin zones could probably not be resolved even with STEM.

Lee et al.[15] found in their study on the segregation of Ba^{2+}, Ca^{2+}, and Sr^{2+} in $LnMnO_3$ (Ln = La, Sm) that even though the trend for surface segregation decreases with decreasing size mismatch with the La^{3+} ion in the series $Ba^{2+} > Sr^{2+} > Ca^{2}+$, the kinetics for segregation were faster for the smaller Ca^{2+} ion than for the larger Ba^{2+} and Sr^{2+} ions. Thus, Ca^{2+} would, from the thermodynamic point of view, show less tendency to segregate to the surface than Ba^{2+} and Sr^{2+}, but the segregation of the larger ions could be kinetically limited, at least at lower temperatures.[15] This is in agreement with the experimental results from the present investigation on LCF82 and previous work on $La_{0.6}Sr_{0.4}CoO_{3-\delta}$ (LSC64).[21] LCF82 exhibits larger but much more isolated particles of secondary phases with a high amount of "free" (un-degraded) surfaces, while LSC64 (treated under analogous conditions) shows a thinner degraded surface zone but with a virtually complete surface coverage (see supplementary material Figure S-9). A comparison of k_{chem} of LCF82 and LSC64 shows clearly that the material substituted with Ca (LCF82) has a higher surface exchange activity and a better long-term stability than the Sr-substituted compound LSC64 (Figure 4).

Downloaded on 2018-07-09 to IP 193.170.16.194 address. Redistribution subject to ECS terms of use (see ecsdl.org/site/terms_use) unless CC License in place (see abstract).

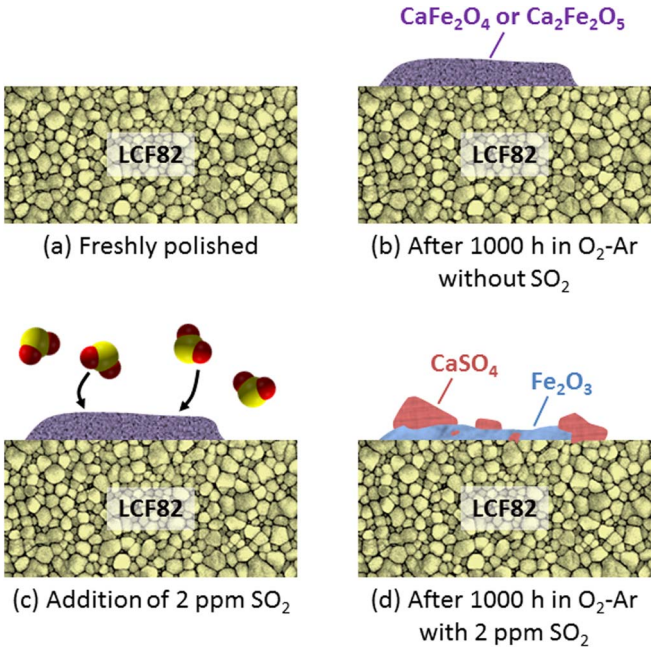

Figure 12. Scheme of the suggested degradation mechanism; a) freshly polished LCF82 sample, b) after 1000 h in O_2-Ar without SO_2 (formation of needle shaped crystals), c) reaction of gaseous SO_2 with the Ca- and Fe-rich crystals on the surface, and d) formation of $CaSO_4$ and Fe_2O_3.

Conclusions

The chemical oxygen surface exchange coefficient (k_{chem}) and the chemical diffusion coefficient of oxygen (D_{chem}) of $La_{0.8}Ca_{0.2}FeO_{3-\delta}$ (LCF82), as well as the electronic conductivity, were determined at 600–800°C and $pO_2 = 0.1$ bar in the short-time domain. It was found that LCF82 exhibits very fast oxygen exchange kinetics and the chemical surface exchange coefficient is even higher than that of $La_{0.6}Sr_{0.4}CoO_{3-\delta}$ under comparable conditions. The electronic conductivity was $\geq$100 S cm^{-1}.

Long-term in-situ measurements of k_{chem} and D_{chem} of LCF82 at 700°C in a pure O_2-Ar atmosphere with $pO_2 = 0.1$ bar showed an excellent stability of the oxygen exchange kinetics over a time span of 1000 h. After the addition of 2 ppm SO_2 a significant decrease of k_{chem} by two orders of magnitude was observed. Post-test analyses of degraded samples with different pre-treatments by SEM-EDX, XPS, and TEM indicate that the degradation mechanism involves the enrichment of the surface with Ca, Fe, and O, and a chemical reaction with SO_2, which leads to the formation of $CaSO_4$ and Fe_2O_3 in an approximately 500–1000 nm thick region on the surface. However, a significant area of the surface remains free of these oxygen exchange-inactive secondary phases, which may be the cause for the relatively fast oxygen exchange kinetics of LCF82 even after exposure to 2 ppm SO_2 (conditions of accelerated testing, compared to 1–100 ppb in ambient air) for 1000 h.

Due to the results from short-term and long-term testing, LCF82 seems to be a promising material for SOFC and SOEC air electrodes, which are operated at intermediate temperatures (600–800°C) in ambient air. Further investigations on the long-term stability of LCF82 are planned under consideration of additional application-relevant conditions (influence of humid atmospheres, presence of other impurities such as Cr and Si, etc.).

Acknowledgments

Financial support by the Austrian Ministry for Transport, Innovation and Technology (bmvit) and AVL List GmbH (Austria) within the program 'Mobilität der Zukunft' (project no. 845334) is gratefully acknowledged. Furthermore, the authors thank G. Hawranek (Montanuniversitaet Leoben) for SEM analysis, and Martina Dienstleder (Graz Centre for Electron Microscopy) for the FIB preparation.

References

1. M. Gasik, *Materials for fuel cells*, CRC Press, Boca Raton (2008).
2. T. Ishihara, Editor, *Perovskite oxide for solid oxide fuel cells*, Springer, New York (2009).
3. D. Marinha, L. Dessemond, and E. Djurado, *Current Inorganic Chemistry*, **3**(1), 2 (2013).
4. D. Stolten and B. Emonts, Editors, *Fuel cell science and engineering: Materials, processes, systems and technology*, Wiley-VCH, Weinheim, Germany (2012).
5. K.-D. Kreuer, Editor, *Fuel Cells - Selected Entries from the Encyclopedia of Sustainability Science and Technology*, Springer-Verlag, New York (2013).
6. J. Mizusaki, M. Yoshihiro, S. Yamauchi, and K. Fueki, *J. Solid State Chem.*, **58**, 257 (1985).
7. E. Bucher and W. Sitte, *J. Electroceram.*, **13**, 779 (2004).
8. L.-W. Tai, M. M. Nasrallah, H. U. Anderson, D. M. Sparlin, and S. R. Sehlin, *Solid State Ionics*, **76**, 259 (1995).
9. R. D. Shannon, *Acta Crystallographica A*, **32**, 751 (1976).
10. N. Schrödl, E. Bucher, C. Gspan, A. Egger, C. Ganser, C. Teichert, F. Hofer, and W. Sitte, *Solid State Ionics*, **288**, 14 (2016).
11. H. Ding, A. V. Virkar, M. Liu, and F. Liu, *Physical Chemistry Chemical Physics*, **15**, 489 (2013).
12. W. Jung and H. L. Tuller, *Energy & Environmental Science*, **5**(1), 5370 (2012).
13. G. M. Rupp, H. Téllez, J. Druce, A. Limbeck, T. Ishihara, J. Kilner, and J. Fleig, *Journal of Materials Chemistry A*, **3**(45), 22759 (2015).
14. W. Araki, M. Miyashita, and Y. Arai, *Solid State Ionics*, **290**, 18 (2016).
15. W. Lee, J. W. Han, Y. Chen, Z. Cai, and B. Yildiz, *Journal of the American Chemical Society*, **135**(21), 7909 (2013).
16. E. Bucher, C. Gspan, T. Höschen, F. Hofer, and W. Sitte, *Solid State Ionics*, **299**, 26 (2017).
17. M. Perz, E. Bucher, C. Gspan, J. Waldhäusl, F. Hofer, and W. Sitte, *Solid State Ionics*, **288**, 22 (2016).
18. N. Schrödl, E. Bucher, A. Egger, P. Kreiml, C. Teichert, T. Höschen, and W. Sitte, *Solid State Ionics*, **276**, 62 (2015).
19. E. Bucher, C. Gspan, F. Hofer, and W. Sitte, *Solid State Ionics*, **230**, 7 (2013).
20. C. C. Wang, K. O'Donnell, L. Jian, and S. P. Jiang, *J. Electrochem. Soc.*, **162**(6), F507 (2015).
21. E. Bucher, C. Gspan, and W. Sitte, *Solid State Ionics*, **272**, 112 (2015).
22. F. Wang, K. Yamaji, D.-H. Cho, T. Shimonosono, H. Kishimoto, M. E. Brito, T. Horita, and H. Yokokawa, *J. Electrochem. Soc.*, **158**(11), B1391 (2011).
23. A. J. Schuler, Z. Wuillemin, A. Hessler-Wyser, and J. Van Herle, Sulfur as pollutant species on the cathode side of a SOFC system, In: S. C. Singhal, Editor, *11th Intern. Symp. Solid Oxide Fuel Cells (SOFC-XI)*, The Electrochemical Society, Vienna, Austria (2009), p.2845.
24. C. Berger, E. Bucher, and W. Sitte, *Solid State Ionics*, **299**, 46 (2017).
25. M.-H. Hung, M. V. M. Rao, and D.-S. Tsai, *Mater. Chem. Phys.*, **101**(2), 297 (2007).
26. R. Andoulsi, K. Horchani-Naifer, and M. Férid, *Ceramics International*, **39**(6), 6527 (2013).
27. R. Pushpa, D. Daniel, and D. P. Butt, *Solid State Ionics*, **249–250**, 184 (2013).
28. M. S. Hassan, K.-B. Shim, and O. B. Yang, *J. Nanosci. Nanotechnol.*, **11**(2), 1429 (2011).
29. Y.-H. Chen, Y.-J. Wei, X.-Q. Liu, and G.-Y. Meng, *Wuji Huaxue Xuebao*, **21**(5), 673 (2005).
30. U. Russo, L. Nodari, M. Faticanti, V. Kuncser, and G. Filoti, *Solid State Ionics*, **176**(1–2), 97 (2005).
31. P. A. Zink, K. J. Yoon, U. B. Pal, and S. Gopalan, *Electrochemical and Solid-State Letters*, **12**(10), B141 (2009).
32. F. Wang, H. Kishimoto, K. Develos-Bagarinao, K. Yamaji, T. Horita, and H. Yokokawa, *J. Electrochem. Soc.*, **163**(8), F899 (2016).
33. F. Wang, K. Yamaji, D. H. Cho, T. Shimonosono, M. Nishi, H. Kishimoto, M. E. Brito, T. Horita, and H. Yokokawa, *Fuel Cells*, **13**(4), 520 (2013).
34. E. Bucher, C. Gspan, F. Hofer, and W. Sitte, *Solid State Ionics*, **238**, 15 (2013).
35. F. Wang, K. Yamaji, D.-H. Cho, T. Shimonosono, H. Kishimoto, M. E. Brito, T. Horita, and H. Yokokawa, *Solid State Ionics*, **225**, 157 (2012).
36. L. J. van der Pauw, *Philips Res. Rep.*, **13**(1) 1 (1958).
37. E. Bucher, W. Sitte, F. Klauser, and E. Bertel, *Solid State Ionics*, **208**, 43 (2012).
38. E. J. Opila, D. S. Fox, and N. S. Jacobson, *J. Am. Ceram. Soc.*, **80**(4), 1009 (1997).
39. N. S. Jacobson, E. J. Opila, D. L. Myers, and E. H. Copland, *Journal of Chemical Thermodynamics.*, **37**(10), 1130 (2005).
40. E. J. Opila, N. S. Jacobson, D. L. Myers, and E. H. Copland, *JOM*, **58**(1), 22 (2006).
41. W. Preis, M. Holzinger, and W. Sitte, *Monatsh. Chem.*, **132**, 499 (2001).
42. M. W. den Otter, H. J. M. Bouwmeester, B. A. Boukamp, and H. Verweij, *J. Electrochem. Soc.*, **148**(2) , J1 (2001).
43. W. Preis, E. Bucher, and W. Sitte, *J. Power Sources*, **106**, 116 (2002).
44. W. Preis, E. Bucher, and W. Sitte, *Solid State Ionics*, **175**, 393 (2004).
45. P. Stadelmann, Electron Microscopy Software (Java Version) 3.2830U2008, CIME-EPFL Switzerland (2008).
46. A. Egger, E. Bucher, M. Yang, and W. Sitte, *Solid State Ionics*, **225**, 55 (2012).
47. E. Bucher, A. Egger, P. Ried, W. Sitte, and P. Holtappels, *Solid State Ionics*, **179**, 1032 (2008).

Downloaded on 2018-07-09 to IP 193.170.16.194 address. Redistribution subject to ECS terms of use (see ecsdl.org/site/terms_use) unless CC License in place (see abstract).

48. Z. Cai, M. Kubicek, J. Fleig, and B. Yildiz, *Chemistry of Materials*, **24**(6), 1116 (2012).
49. H. Yokokawa, N. Sakai, T. Horita, K. Yamaji, M. E. Brito, and H. Kishimoto, *J. Alloys Compd.*, **452**(1), 41 (2008).
50. T. T. Fister, D. D. Fong, J. A. Eastman, P. M. Baldo, M. J. Highland, P. H. Fuoss, K. R. Balasubramaniam, J. C. Meador, and P. A. Salvador, *Applied Physics Letters*, **93**, 151904/1 (2008).
51. P. A. W. van der Heide, *Surface and Interface Analysis*, **33**(5), 414 (2002).
52. R. A. De Souza and J. A. Kilner, *Solid State Ionics*, **126**, 153 (1999).
53. H. Peisert, T. Chassé, P. Streubel, A. Meisel, and R. Szargan, *Journal of Electron Spectroscopy and Related Phenomena*, **68**, 321 (1994).
54. R. Behrisch and W. Eckstein, Sputtering by Particle Bombardment, *Topics in Applied Physics*, Vol. **110**, Springer, Berlin Heidelberg (2007).
55. T. Hanawa and M. Ota, *Biomaterials*, **12**(8), 767 (1991).
56. H. Van Doveren and J. A. T. H. Verhoeven, *Journal of Electron Spectroscopy and Related Phenomena*, **21**(3), 265 (1980).
57. H. F. Franzen, J. Merrick, M. Umaña, A. S. Khan, D. T. Peterson, J. R. McCreary, and R. J. Thorn, *Journal of Electron Spectroscopy and Related Phenomena*, **11**(4), 439 (1977).
58. A. T. Kozakov, A. G. Kochur, V. I. Torgashev, K. A. Googlev, S. P. Kubrin, V. G. Trotsenko, A. A. Bush, and A. V. Nikolskii, *Journal of Alloys and Compounds*, **664**, 392 (2016).
59. A. B. Christie, J. Lee, I. Sutherland, and J. M. Walls, *Applications of Surface Science*, **15**(1), 224 (1983).
60. J. Baltrusaitis, C. R. Usher, and V. H. Grassian, *Physical Chemistry Chemical Physics*, **9**(23), 3011 (2007).
61. J. Van Herle, A. J. McEvoy, and K. R. Thampi, *Electrochim. Acta*, **41**(9) , 1447 (1996).
62. H. Seyama and M. Soma, *Journal of the Chemical Society, Faraday Transactions 1: Physical Chemistry in Condensed Phases*, **80**(1), 237 (1984).
63. B. Demri and D. Muster, *Journal of Materials Processing Technology*, **55**(3), 311 (1995).
64. J. C. Langevoort, I. Sutherland, L. J. Hanekamp, and P. J. Gellings, *Applied Surface Science*, **28**(2), 167 (1987).
65. S. L. T. Andersson and R. F. Howe, *The Journal of Physical Chemistry*, **93**(12), 4913 (1989).
66. N. S. McIntyre and D. G. Zetaruk, *Analytical Chemistry*, **49**(11), 1521 (1977).
67. D. D. Hawn and B. M. DeKoven, *Surface and Interface Analysis*, **10**(2–3), 63 (1987).

Downloaded on 2018-07-09 to IP **193.170.16.194** address. Redistribution subject to ECS terms of use (see **ecsdl.org/site/terms_use**) unless CC License in place (see abstract).

Supplementary Material

Impact of SO_2 on the oxygen exchange kinetics of the promising SOFC/SOEC air electrode material $La_{0.8}Ca_{0.2}FeO_{3-\delta}$

Christian Berger [a], Edith Bucher [a,*], Christian Gspan [b], Alexander Menzel [c], Werner Sitte [a]

[a] *Chair of Physical Chemistry, Montanuniversitaet Leoben, Franz-Josef-Straße 18, A-8700 Leoben, Austria*

[b] *Institute of Electron Microscopy and Nanoanalysis (FELMI), Graz University of Technology & Graz Centre for Electron Microscopy (ZFE)*
Austrian Cooperative Research (ACR) Steyrergasse 17, A-8010 Graz, Austria

[c] *Institute of Physical Chemistry, University of Innsbruck, Innrain 80-82, A-6020 Innsbruck. Austria*

Contents

1. Scanning electron microscopy 3

2. X-ray photoelectron spectroscopy 7

3. Predominance diagrams 8

4. Analytical transmission electron microscopy 9

5. Comparison of the degradation behaviour of $La_{0.8}Ca_{0.2}FeO_{3-\delta}$ (LCF82) and $La_{0.6}Sr_{0.4}CoO_{3-\delta}$ (LSC64) 10

6. References 11

1. Scanning electron microscopy

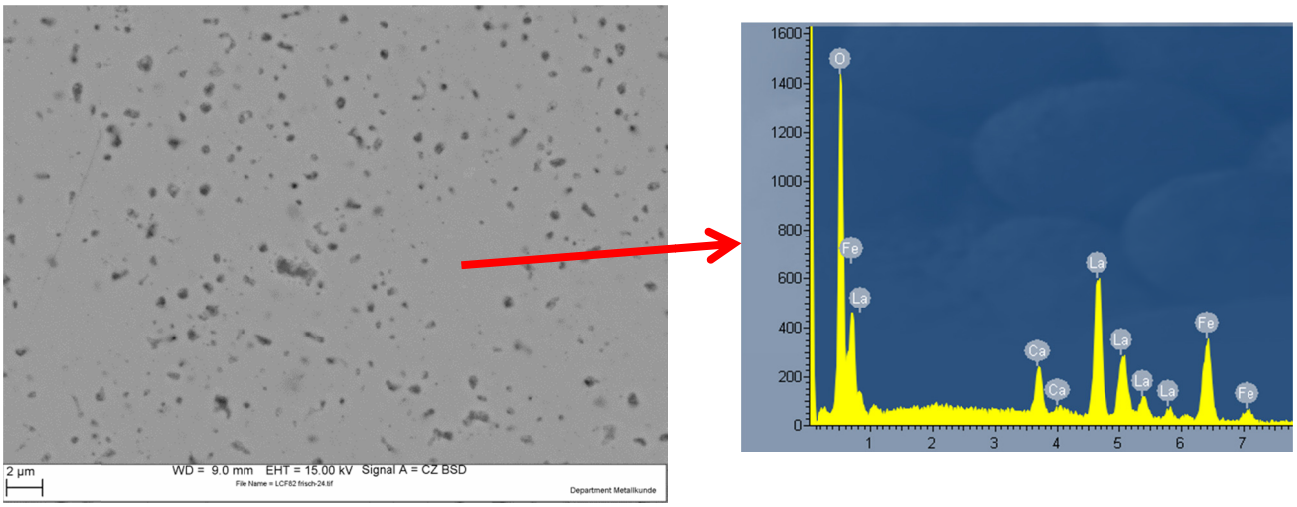

Figure S-1. SEM-EDX analyses from the surface of sample LCF82-fresh; the nominal composition of LCF82 is found in the homogeneous region (compare EDX spectrum). Small holes on the surface result from the polishing process (grain pull-out). Energies in the EDX spectrum are given in keV.

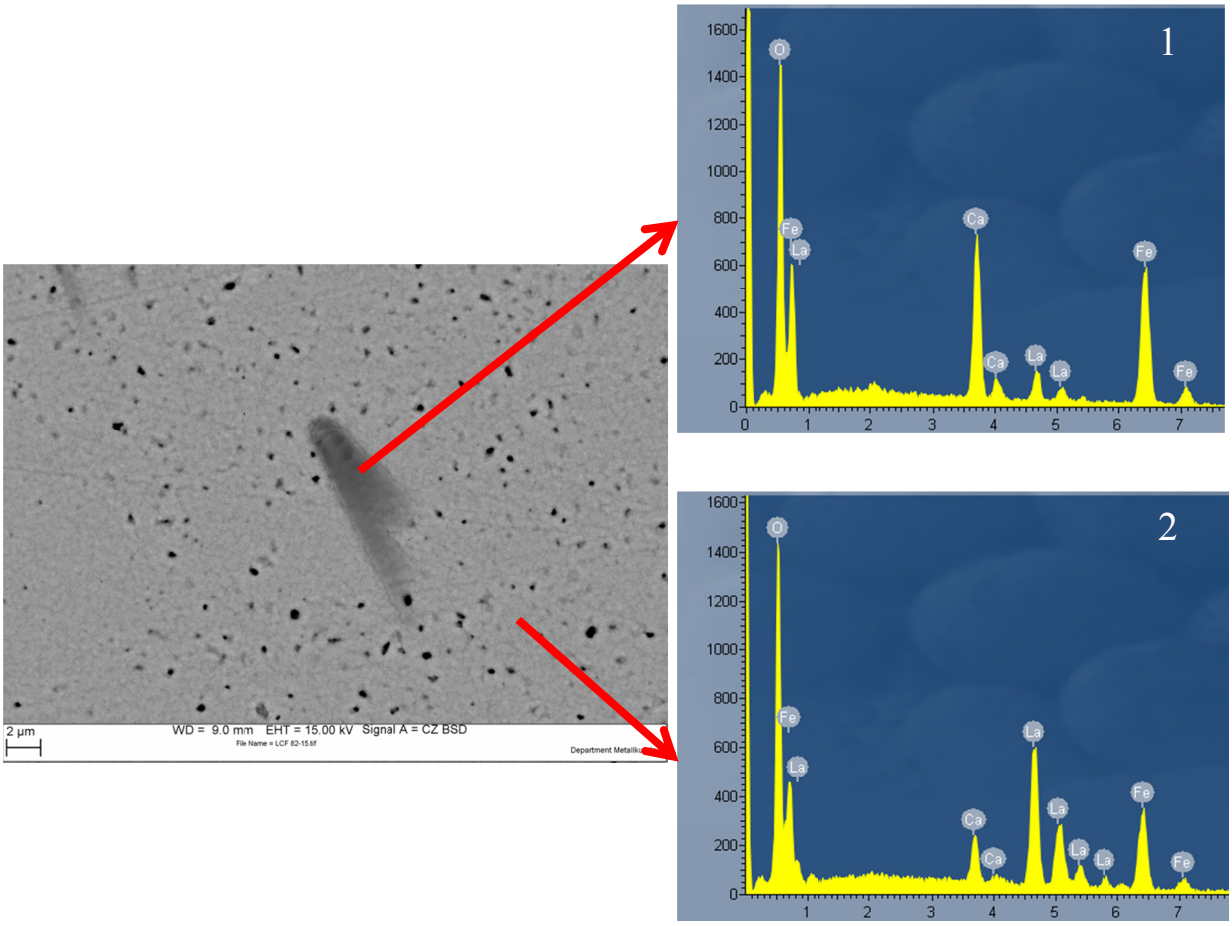

Figure S-2. SEM-EDX analyses from the surface of sample LCF82-thermally-etched; Ca and Fe is enriched in the dark needle-like crystals (EDX 1); the nominal composition of LCF82 is found in the homogeneous regions of the surface (EDX 2). Energies in the EDX spectra are given in keV.

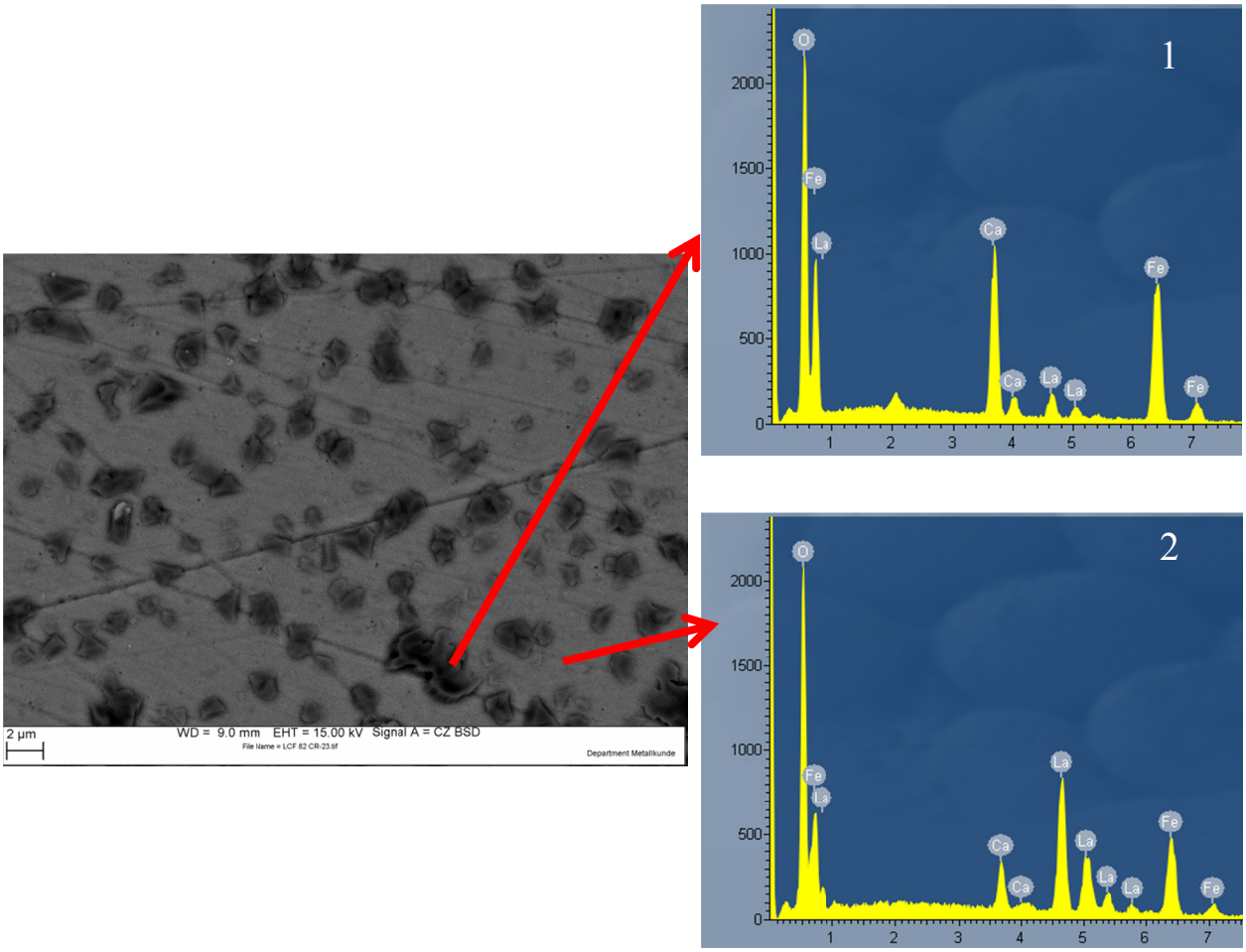

Figure S-3. SEM-EDX analyses from the surface of sample LCF82-woSO_2; the irregularly shaped crystals are rich in Ca, Fe, and O (EDX 1). The matrix shows the nominal composition of LCF82 (EDX 2). Energies in the EDX spectra are given in keV.

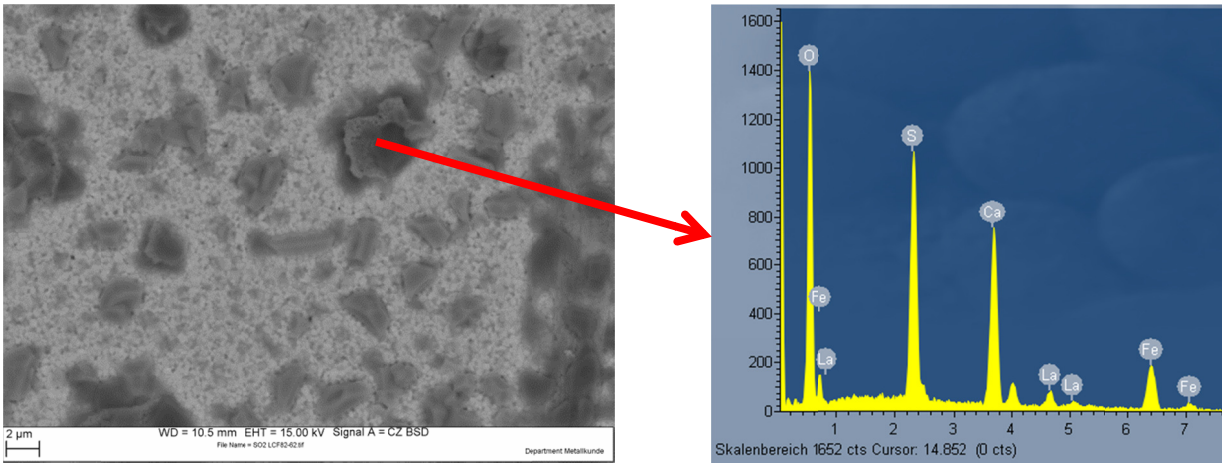

Figure S-4. SEM-EDX analyses from the surface of sample LCF82-wSO_2; the irregularly shaped crystals are rich in Ca, S, and O. The EDX spectrum shows that the ratio of Ca to S is close to unity. Energies in the EDX spectrum are given in keV.

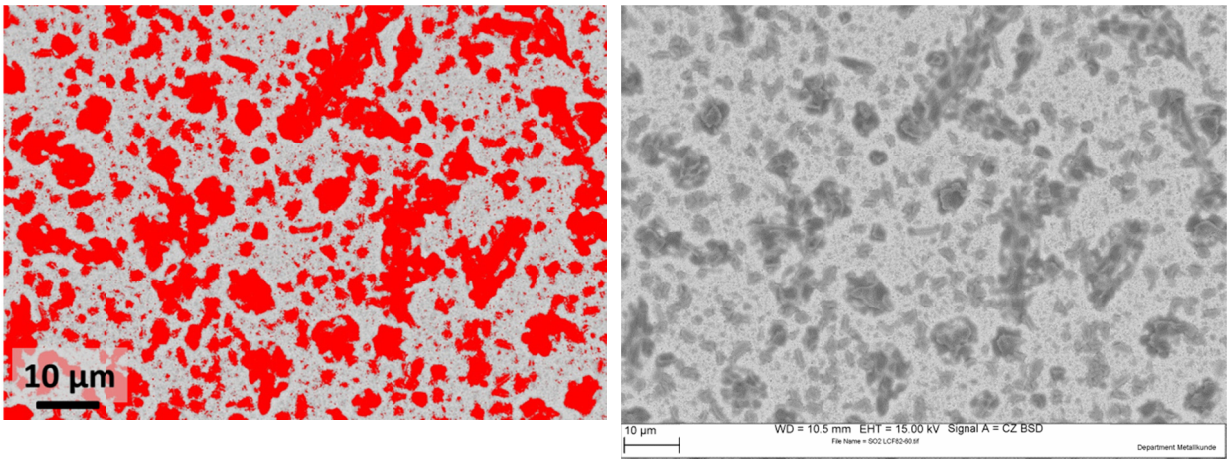

Figure S-5. Analysis of the free (oxygen exchange-active) and degraded surface areas of sample LCF82-wSO_2 (left); free areas (approximately 60 %) are shown in grey, degraded areas (approximately 40 %) are shown in red; The analysis was performed with the software *ImageJ* (freeware, https://imagej.nih.gov/ij/) using the SEM-BSE image from Fig. 6g (right).

2. X-ray photoelectron spectroscopy

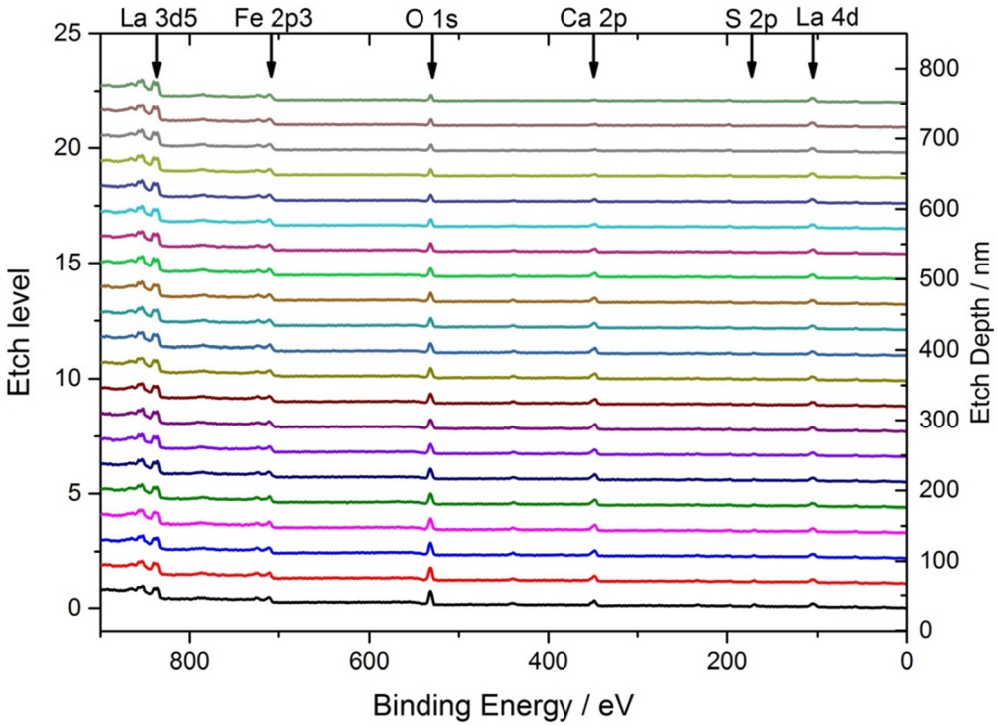

Figure S-6. XPS binding energies at different etch levels of LCF82-wSO_2. Values for selected peaks are listed in Table S-1.

Table S-1. Binding energies for the signals in Figure S-5. All energies are given in eV.

Name	Start BE	Peak BE	End BE	FWHM
Ca2p	358.66	346.86	338.05	5.72
O1s	538.44	530.86	519.91	4.36
S2p	179.45	169.15	151.82	3.51
La3d5	842.83	834.82	820.09	4.05
Fe2p3	717.07	710.27	700.28	5.11
La4d	117.73	104.28	96.12	6.49

3. Predominance diagrams

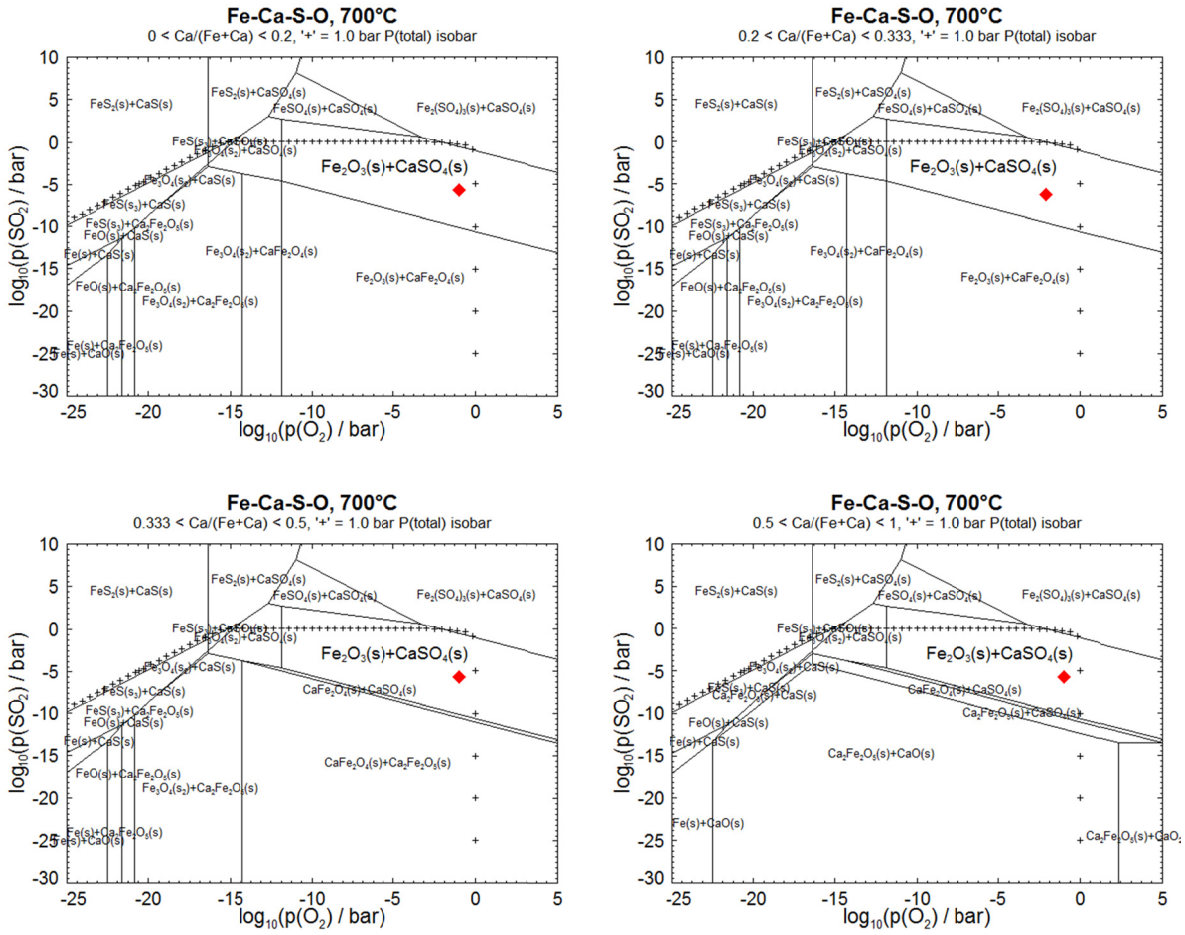

Figure S-7. Predominance diagrams for the Ca-Fe-O-S system at 700°C calculated for different Ca/(Ca+Fe) ratios with the software FactSage© [1]. The calculations are intended as an approximation for the formation of secondary phases during poisoning of $La_{0.8}Ca_{0.2}FeO_{3-\delta}$ (LCF82) with SO_2. Calculations including the $La_{0.8}Ca_{0.2}FeO_{3-\delta}$ phase were not possible due to the lack of thermodynamic data for LCF82. However, under the experimental conditions of the experiment (pO_2=0.10 bar, pSO_2=2×10^{-6} bar; indicated by the red diamonds), all diagrams predict the formation of $CaSO_4$ and Fe_2O_3, in agreement with the secondary phases found in the post-test analyses of the sample (Figures 10 and 11).

4. Analytical transmission electron microscopy

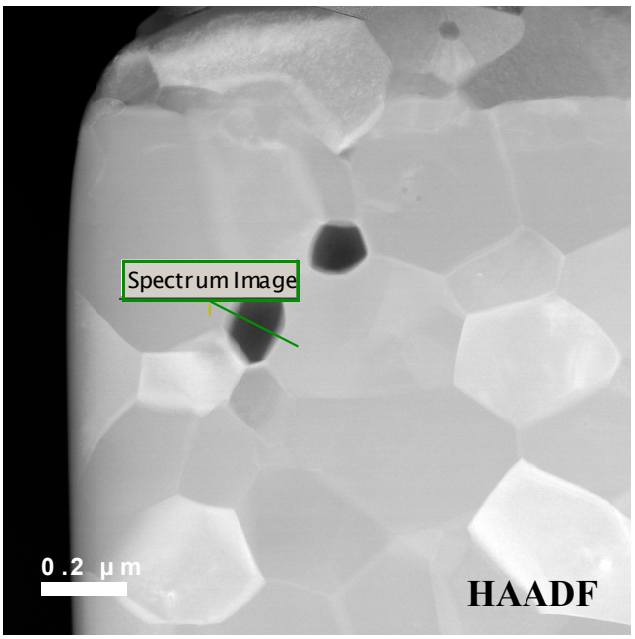

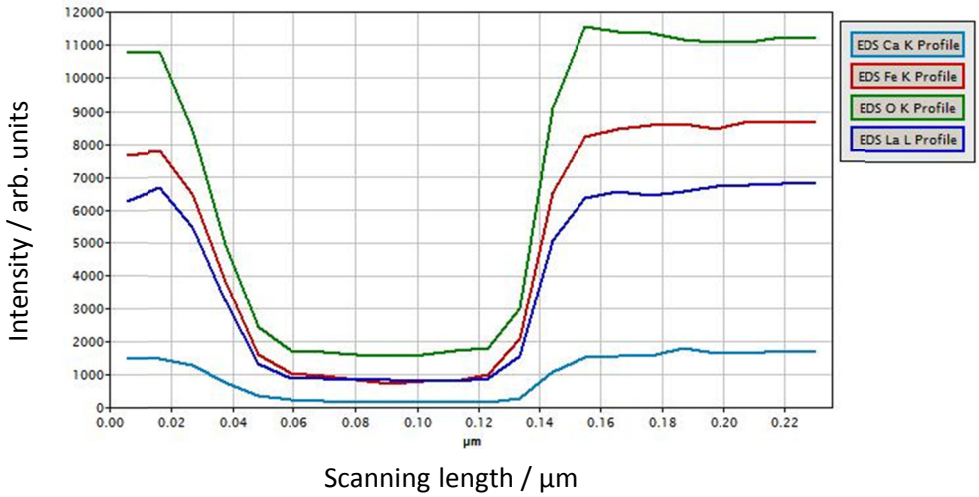

Figure S-8. HAADF image of one of the dark spots in the LCF82-wSO_2 bulk region. It is confirmed that these regions are small pores or cavities since a simultaneous depletion of all element signals occurs over the diameter of the investigated pore.

5. Comparison of the degradation behaviour of $La_{0.8}Ca_{0.2}FeO_{3-\delta}$ (LCF82) and $La_{0.6}Sr_{0.4}CoO_{3-\delta}$ (LSC64)

$La_{0.8}Ca_{0.2}FeO_{3-\delta}$ (LCF82)

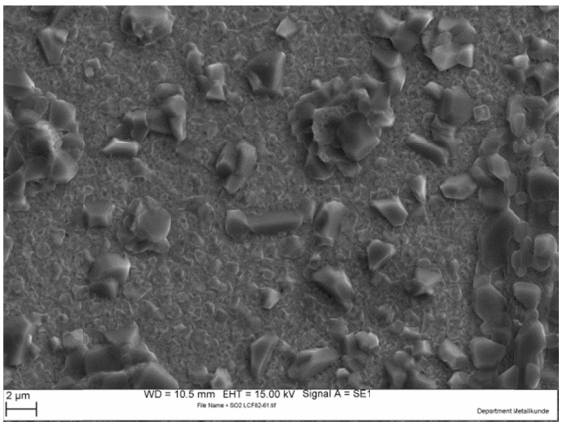

SEM-SE image of $La_{0.8}Ca_{0.2}FeO_{3-\delta}$ after 1 kh in SO_2-O_2-Ar (2 ppm SO_2) at 700°C; Larger but more isolated particles are found; a significant amount of free surfaces remains (approximately 60 % of total surface area).

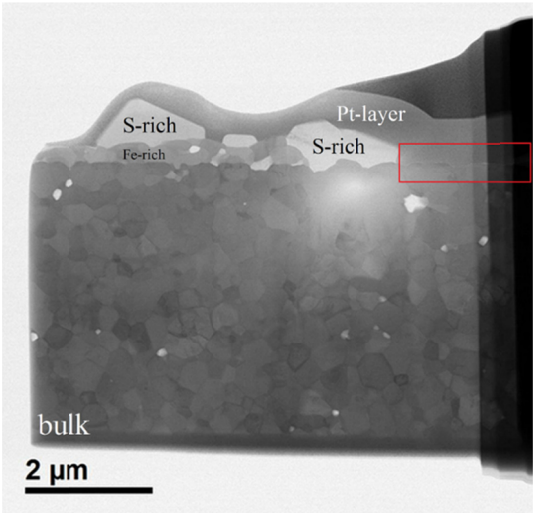

Fig. 9 (present manuscript) Cross-sectional STEM bright field image of $La_{0.8}Ca_{0.2}FeO_{3-\delta}$ after 1000 h in SO_2-O_2-Ar (2 ppm SO_2) at 700°C. Larger but more isolated particles are found. Note the free (not degraded) area on the surface indicated by the red rectangle.

$La_{0.6}Sr_{0.4}CoO_{3-\delta}$ (LSC64; results from [2])

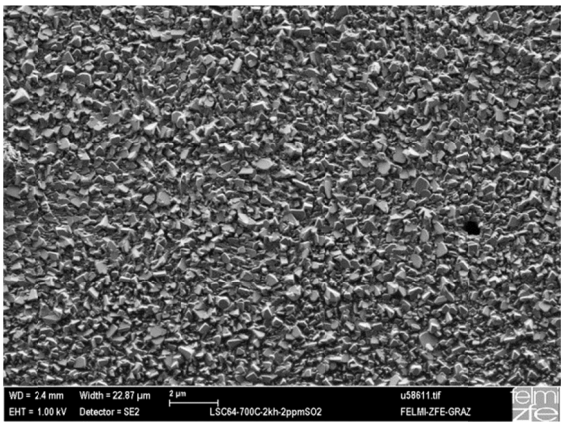

Fig. 2 (b) from [2]; SEM-SE image of the surface of $La_{0.6}Sr_{0.4}CoO_{3-\delta}$ after 1000 h in SO_2-O_2-Ar (2 ppm SO_2) at 700°C; Smaller particles are found, but these cover the whole surface.

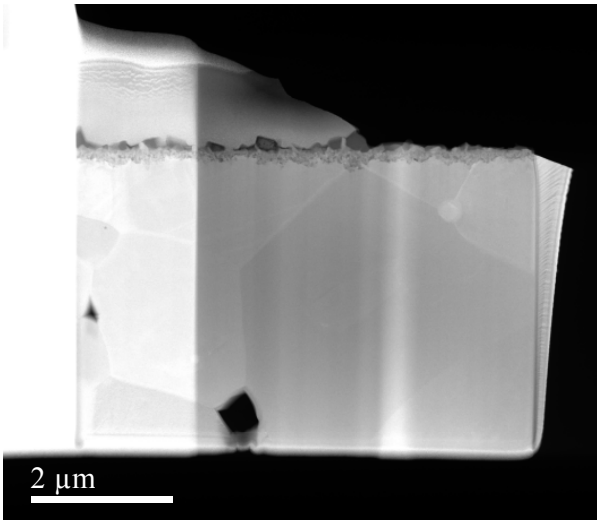

STEM image of $La_{0.6}Sr_{0.4}CoO_{3-\delta}$ after 1000 h in SO_2-O_2-Ar (2 ppm SO_2) at 700°C from study [2] (not shown in the original publication); The sample shows a thinner layer of secondary phases but no free (not degraded) surface areas in contrast to the degraded LCF82 sample (left column).

Figure S-9. Comparison of degraded LCF82 and LSC64 samples.

6. References

[1] FactSage© 7.0, 1976-2015 Thermfact and GTT Technologies.

[2] E. Bucher, C. Gspan, W. Sitte, *Solid State Ionics* **272** (2015) 112.

Journal of Solid State Chemistry 259 (2018) 57–66

Contents lists available at ScienceDirect

Journal of Solid State Chemistry

journal homepage: www.elsevier.com/locate/jssc

Strontium-free rare earth perovskite ferrites with fast oxygen exchange kinetics: Experiment and theory

Christian Berger[a], Edith Bucher[a,*], Andreas Windischbacher[b], A. Daniel Boese[b], Werner Sitte[a]

[a] Montanuniversitaet Leoben, Franz-Josef-Straße 18, 8700 Leoben, Austria
[b] Institute of Chemistry, Karl-Franzens-Universität Graz, Heinrichstraße 28, 8010 Graz, Austria

ARTICLE INFO

Keywords:
Lanthanum calcium ferrite
Praseodymium calcium ferrite
Solid oxide fuel cell cathode
Crystal structure
Defect chemistry
Oxygen exchange kinetics
Electronic conductivity
Ionic conductivity

ABSTRACT

The Sr-free mixed ionic electronic conducting perovskites $La_{0.8}Ca_{0.2}FeO_{3-\delta}$ (LCF82) and $Pr_{0.8}Ca_{0.2}FeO_{3-\delta}$ (PCF82) were synthesized via a glycine-nitrate process. Crystal structure, phase purity, and lattice constants were determined by XRD and Rietveld analysis. The oxygen exchange kinetics and the electronic conductivity were obtained from in-situ dc-conductivity relaxation experiments at 600–800 °C and $1\times10^{-3}\leq pO_2/bar\leq0.1$. Both LCF82 and PCF82 show exceptionally fast chemical surface exchange coefficients and chemical diffusion coefficients of oxygen. The oxygen nonstochiometry of LCF82 and PCF82 was determined by precision thermogravimetry. A point defect model was used to calculate the thermodynamic factors of oxygen and to estimate self-diffusion coefficients and ionic conductivities. Density Functional Theory (DFT) calculations on the crystal structure, oxygen vacancy formation as well as oxygen migration energies are in excellent agreement with the experimental values. Due to their favourable properties both LCF82 and PCF82 are of interest for applications in solid oxide fuel cell cathodes, solid oxide electrolyser cell anodes, oxygen separation membranes, catalysts, or electrochemical sensors.

1. Introduction

Perovskite-type oxides $ABO_{3-\delta}$ (with A=rare earth element or acceptor substituent, B=transition metal) represent a well-known class of mixed ionic electronic conductors which are of interest for basic research and various applications [1–3]. For instance, the air electrodes of intermediate temperature (600–800 °C) solid oxide fuel cells (SOFCs) and solid oxide electrolyser cells (SOECs) utilize (La,Sr)(Co,Fe)$O_{3-\delta}$ perovskites for the efficient conversion of the chemical energy of various fuels into electrical energy [4–6]. Recently, A-site substituted perovskite-type ferrites caused much attention due to their high ionic and electronic conductivities, their chemical stability in reducing atmospheres, relatively low thermal expansion coefficients, and their good long-term chemical stability in sulphur containing atmospheres [7–10]. The series $La_{1-x}Sr_xFeO_{3-\delta}$ (LSF) has been thoroughly studied in terms of defect chemistry [11–13], charge transport properties [14–16], and long term degradation due to different contaminants (Cr, Si, and SO_2) to test SOFC cathodes at operational conditions [17–19]. However, in order to further improve the material properties, as well as the lifespans and reliability of these compounds in technical applications, it is necessary to develop new materials with fast oxygen exchange kinetics and high thermodynamic stability. In this respect, one possible approach is to minimize the mismatch of the ionic radii of the A-site ions to prevent degradation due to mechanical stress and cation segregation [20]. The ionic radius of Sr^{2+} (XII) (1.44 Å) [21] is much larger compared to La^{3+} (XII) (1.36 Å) [21]. This can lead to the segregation of Sr towards grain boundaries and surfaces in order to relieve mechanical stress [20]. These Sr-enriched areas react with impurities from the gas phase (Cr, Si, SO_2 etc.) forming secondary phases, which inhibit the oxygen reduction process [22–24]. As a promising alternative to reduce the mismatch in the ionic radius, the smaller ion Ca^{2+} (XII) (1.34 Å) [21] can be used instead of Sr in these ferrites to obtain $La_{1-x}Ca_xFeO_{3-\delta}$. Compared to the well-characterized LSF series, only a few investigations on material properties of $La_{1-x}Ca_xFeO_{3-\delta}$ are available so far [25–33]. A study on defect chemistry, mass and charge transport properties, and oxygen exchange kinetics of $La_{0.9}Ca_{0.1}FeO_{3-\delta}$ was recently published [34], as well as an investigation on the long-term stability of $La_{0.8}Ca_{0.2}FeO_{3-\delta}$ in SO_2 containing atmospheres [35]. Especially, only few studies on ferrite-based perovskites with varying A-site composition (other than La and Sr) are available. This is somewhat surprising, since the effects of the nature of the A-site cations on material properties have already been shown for similar solid solutions such as $Ln_{1-x}Sr_xCoO_{3-\delta}$ and $Ln_{1-x}Sr_xCo_{1-y}Fe_yO_{3-\delta}$ [36–38].

* Corresponding author.
E-mail address: edith.bucher@unileoben.ac.at (E. Bucher).

https://doi.org/10.1016/j.jssc.2017.12.019
Received 13 September 2017; Received in revised form 13 December 2017; Accepted 15 December 2017
Available online 16 December 2017
0022-4596/ © 2017 Elsevier Inc. All rights reserved.

The present study reports on the synthesis, crystal structure, defect chemistry, and various material properties (thermal expansion coefficient, electronic and ionic conductivities, oxygen surface exchange and diffusion coefficients) of the Ca-substituted ferrites $La_{0.8}Ca_{0.2}FeO_{3-\delta}$ (LCF82) and $Pr_{0.8}Ca_{0.2}FeO_{3-\delta}$ (PCF82). The influence of the A-site host cation (La^{3+} or Pr^{3+}) is investigated, while keeping the concentration of the A-site substituent (Ca^{2+}) constant. To the best of the authors' knowledge, the current paper contains the first results on the oxygen exchange kinetics of PCF82 at 600–800 °C under conditions close to equilibrium (small pO_2 gradients).

While perovskites containing La and Sr, such as $(La,Sr)(Fe,Co)O_{3-\delta}$, have been studied before by computational methods [39–41], there have been no similar investigations on the Ca or Pr containing structures. Thus, calculations on $A_{1-x}Ca_xFeO_{3-\delta}$ (A=La, Pr) were performed simulating similar Ca-content and oxygen nonstoichiometries as the experimental material to support the experiments. We compare the computed perovskite structures and their oxygen migration energies to the experimental data and include thermal effects via the harmonic oscillator approximation.

2. Experimental and computational details

2.1. Sample preparation

$La_{0.8}Ca_{0.2}FeO_{3-\delta}$ (LCF82) and $Pr_{0.8}Ca_{0.2}FeO_{3-\delta}$ (PCF82) powders were synthesized via a sol-gel method (glycine-nitrate-process), starting with 1 M aqueous nitrate solutions prepared from $La(NO_3)_3{\cdot}6H_2O$, $Pr(NO_3)_3{\cdot}6H_2O$, $Ca(NO_3)_2{\cdot}4H_2O$, and $Fe(NO_3)_3{\cdot}9H_2O$ (all chemicals provided by Sigma Aldrich, analytical grade quality). Stoichiometric amounts of each nitrate-solution were mixed and blended with glycine in the ratio of one mole glycine per mole cation. Similar to the process described in [34], water evaporation lead to the formation of a gel which ignited at approximately 250 °C. The resulting ash was calcined at 1000 °C and ball milled for 24 h to obtain a monomodal particle size distribution with an average particle size of 0.90 µm for LCF82, and 0.77 µm for PCF82, respectively (Fig. S-1, Supplementary material). Cylindrical pellets (length×diameter ≈ 9×5 mm) of LCF82 and PCF82 were uniaxially pressed at 5.00 kbar (maximum load 1 t), and sintered at 1100 °C for 2 h. For thermal expansion measurements, the front faces of the sintered cylinders were polished to obtain parallel ends. For conductivity relaxation experiments, as well as electrical conductivity measurements, the powders were isostatically pressed at 3.00 kbar and sintered at 1100 °C for 2 h. Sample densities were determined from the mass and geometry of the sintered pellets. Theoretical densities were obtained from Rietveld refinement (see Table S-1 Supplementary material). The density of the sintered LCF82 sample was 97% of the theoretical density (ρ_{theor}=6.3195 g cm^{-3}). The PCF82 sample exhibited 95% of the theoretical density (ρ_{theor}=6.3181 g cm^{-3}). From these dense samples, thin plates with 5×5 mm^2 cross-section and thicknesses of 200–1300 µm were prepared for measurements of the oxygen exchange kinetics and the electrical conductivity (see Section 2.3). The chemical composition of sintered LCF82 and PCF82 pellets was checked by energy dispersive X-ray spectroscopy (EDX) using an EDX Oxford Instruments detector (model 6272) in an energy range up to 20 keV (see Table S-2 Supplementary material). Three iterations on each sample were measured (neglecting oxygen), to get a good overall estimation on the cation stoichiometries. The measured values of the cation stoichiometry agree well with the theoretical values (nominal composition). Minor deviations between measured and theoretical values could be explained by the measurement uncertainty which is estimated to ± (2–3) at%.

2.2. Crystallographic and thermal analysis

X-ray diffraction (XRD) of the calcined LCF82 and PCF82 powders was performed with a diffractometer (BRUKER-AXS D8 Advance) using a Cu K α radiation source operated at 40 kV and 40 mA. The diffractograms were recorded at room temperature with a scanning rate of 0.01° s^{-1}. Lattice parameters were obtained from fitting the peak positions to an orthorhombic unit cell using the computer software MAUD [42].

The thermal expansion of LCF82 and PCF82 was measured in the temperature range of 30≤T/°C≤1000 at heating rates of 1 K min^{-1} in the oxygen partial pressure range of $1\times10^{-3}\leq pO_2/bar\leq1$, using a dilatometer (DIL 402/PC4, Netzsch). The cylindrically shaped, sintered sample was 5.1 mm in diameter and 6.9 mm in length for LCF82 and 4.9 mm in diameter and 6.8 mm in length for PCF82.

Differential scanning calorimetry (High Temperature DSC 404C Pegasus® with TASC 414/3 A controller and PU1 power unit) of the sintered LCF82 and PCF82 powder was performed in the range of 20≤T/°C≤1000 at a heating rate of 20 K min^{-1} with an isotherm at 1000 °C for 10 min and a gas flow of 50 ml min^{-1} Ar 5.0.

The oxygen nonstochiometry of LCF82 and PCF82 was determined by precision thermogravimetry (TG) using a symmetric thermobalance (Setaram model TAG 2416). Small amounts (approx. 50 mg) of the sintered powders were placed in a platinum crucible. Different oxygen partial pressures were adjusted with mass flow controllers (red-y, Vögtlin Instruments AG) using mixtures of O_2 4.5, Ar 5.0, and a test gas of 1% O_2 in Ar. An in-situ oxygen sensor with Ir/IrO_2-reference (Setnag, France) was used to determine the oxygen partial pressure close to the sample during each experiment. Experiments were performed in the isothermal and isobaric mode. The agreement between data from both experimental modes was checked, in order to confirm that all data were acquired under equilibrium conditions. Based on literature data for the similar compounds $La_{0.8}Ca_{0.2}FeO_{3-\delta}$ [25], $La_{0.8}Sr_{0.1}FeO_{3-\delta}$ and $La_{0.75}Sr_{0.25}FeO_{3-\delta}$ [15], and $La_{0.8}Sr_{0.2}FeO_{3-\delta}$ [43] it was assumed that $\delta \rightarrow 0$ at room temperature and pO_2=0.2 bar for LCF82 and PCF82.

2.3. Electronic conductivity and conductivity relaxation measurements

The electronic conductivity was measured as a function of temperature and pO_2 by the four-point dc van der Pauw method using a Keithley model 2400 as combined current source and voltmeter. The chemical surface exchange coefficient k_{chem} as well as the chemical diffusion coefficient of oxygen D_{chem} were obtained from in-situ four-point dc-conductivity relaxation experiments which were conducted in van der Pauw electrode configuration [44]. The dense samples had a cross section of approximately 5×5 mm^2 and were contacted with gold wires and gold paste. Platelets with two different thicknesses were used for each material, on the one hand to check the reproducibility of the data, and on the other hand to obtain both k_{chem} and D_{chem} in wider T- and pO_2-ranges. The thicknesses of the specimens were 503 and 1268 µm (LCF82) and 209 and 502 µm (PCF82). The electrical conductivity responses of the samples to step-wise changes of the oxygen partial pressure were recorded. The kinetic parameters (k_{chem} and D_{chem}) were obtained from nonlinear least squares fits of the solution of the diffusion equation to the conductivity relaxation data [11,45,46]. In order to study the oxygen exchange kinetics close to equilibrium, small pO_2-steps were performed in the oxygen partial pressure ranges 1.0×10^{-1} – 1.5×10^{-1}, 1.0×10^{-2} – 1.5×10^{-2}, and 1.0×10^{-3} – 1.5×10^{-3} bar, in oxidizing and reducing directions using O_2-Ar mixtures at a constant total gas flow of 2 dm^3 h^{-1}.

2.4. Computational details

Experimental [47] as well as computational [48] data of (La,Sr) $FeO_{3-\delta}$ indicated that a slightly different Sr-content had no effect on formation and migration energies of the oxygen vacancies. Assuming the same behaviour for Ca-containing compounds, the calculations were performed on $A_{0.75}Ca_{0.25}FeO_{3-\delta}$ (A=La, Pr) structures (indicated

in the following as LCF and PCF) in order to avoid the calculation of much bigger supercells, which would have been required for $A_{0.8}Ca_{0.2}FeO_{3-\delta}$ (A=La, Pr). The energy calculations were performed using the Vienna Ab Initio Simulation Package (VASP) [49,50] version 5.4.1. Potentials constructed with the projector-augmented wave (PAW) method as provided by the VASP library [51] were used. Due to convergence problems with the structures containing praseodymium, 'softer' VASP potentials of all components were employed for the calculation of PCF. For LCF, both pseudopotentials virtually yielded the same results. All calculations were performed with the exchange correlation functional of Perdew, Burke, and Ernzerhof (PBE) [52], using the D3 dispersion correction [53] with Becke-Johnson damping [54].

An energy cut-off of 600 eV for LCF and of 400 eV for the softer PCF calculation was set. The LCF calculations were carried out using a 4×3×4 Monkhorst-Pack k-point mesh and the PCF calculations a 4×4×3 Monkhorst-Pack k-point mesh for the unit cell optimization. To compare computational predictions with experimental data, supercells consisting of 80 and 160 atoms were constructed, requiring 2×3×2 and 2×2×2 (LCF) and 2×2×3 and 2×2×2 (PCF) Monkhorst-Pack k-point meshes. The energy convergence was set to 10^{-5} eV. We also corrected for zero-point energies and temperature effects by calculating numerical frequencies at the gamma point and using the harmonic oscillator (HO) approximation.

Oxygen migration was examined using the nudged elastic band (NEB) [55] approach for finding the saddle point. Here, we utilized the climbing-image NEB (Cl-NEB) method [56,57] as implemented in the VASP 5.2 transition state theory tools from the University of Texas [58].

3. Results and discussions

3.1. Crystal structure

The X-ray diffraction patterns of LCF82 and PCF82 are illustrated in Fig. 1. The lattice constants of the orthorhombic unit cells are given in Fig. S-2 (Supplementary material), in comparison with literature data. Data of the lattice constants, cell volumes, and tolerance factors are summarized in Table 1. Fe-O bond lengths and Fe-O-Fe binding angles are listed in Table 2. All reflections of LCF82 are indexed in orthorhombic perovskite with space group *Pnma*, in analogy to the previously reported structure of $La_{0.9}Ca_{0.1}FeO_{3-\delta}$ (LCF91) [34,62]. The orthorhombic perovskite PCF82 has the space group *Pbnm* (Fig. 1). Both diffraction patterns and the refined lattice constants (Fig. S-2; Supplementary material) match well with the previously reported data

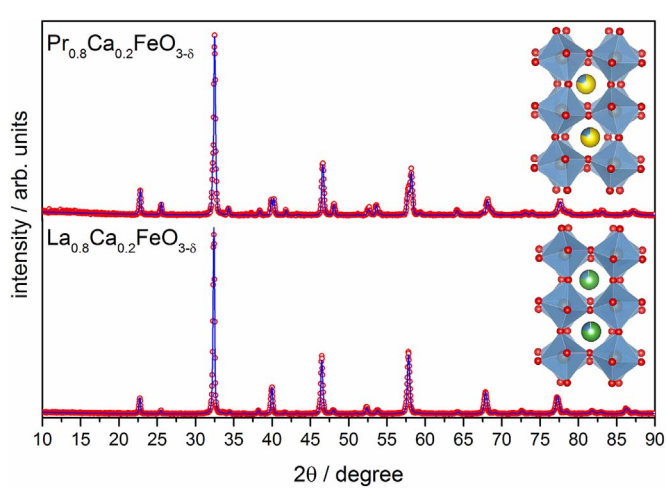

Fig. 1. Powder diffraction patterns (circles) and Rietveld refinement (lines) of LCF82 and PCF82 with the respective crystal structures.

Table 1
Lattice parameters of LCF82 and PCF82 obtained from Rietveld structural refinement in the orthorhombic space group *Pnma* for LCF82 and *Pbnm* for PCF82 in comparison with computational results (PBE-D3) and tolerance factors.

	a / Å	b / Å	c / Å	V / Å^3	*t*
LCF82	5.5105(3)	7.7985(4)	5.5341(3)	237.8204	0.953
PBE-D3	5.384	7.675	5.410	223.6	
PCF82	5.4787(2)	5.5433(2)	7.7726(3)	236.0544	0.903
PBE-D3	5.397	5.400	7.677	223.7	

Table 2
Selected Fe-O bond lengths and Fe-O-Fe bond angles of LCF82 obtained from Rietveld structural refinement in the orthorhombic space group *Pnma* for LCF82 and *Pbnm* for PCF82 in comparison with computational results (PBE-D3).

	Fe1-O1 / Å	Fe1-O2 / Å	Fe1-O2 / Å	Fe1-O1-Fe1 / °	Fe1-O2-Fe1 / °
LCF82	1.98248(10)	1.99882(8)	1.98660(8)	159.1093(16)	156.9222(10)
PBE-D3	1.91	1.93	1.92	159.6	160.2
PCF82	2.00753(8)	2.00087(6)	1.98597(6)	150.9013(15)	155.6187(7)
PBE-D3	1.92	1.94	1.93	157.2	161.6

for LCF82 [59] and PCF82 [33]. In the powder diffractogram of PCF82, peak-splittings are evident at 2 θ-values of 39.92° (022), 40.24° (202), 57.70° (132), 57.91° (024), and 58.19° (312) lattice planes. These match reflexions (overlapping due to lower intensity) of LCF82 at 2 θ-values of 39.93° (022), 40.02° (220), 57.74° (123) and 57.88° (321) lattice planes. PCF82 is a single phase material, while LCF82 shows approximately 1.5 wt% of a $Ca_2Fe_2O_5$ (brownmillerite) impurity phase evident at 33.56° 2 θ. However, it is assumed that the small amount of the latter secondary phase has a negligible effect on the material properties of LCF82. The tolerance factor *t* (Table 1) was calculated according to Eq. (1) to describe the deviation from the ideal cubic perovskite structure [37,60].

$$t = \frac{0.8\, r_A + 0.2\, r_{A'} + r_O}{\sqrt{2}\,(r_B + r_O)} \quad (1)$$

For estimation of *t*, the following ionic radii from [21] under consideration of coordination number and charge were used: r_A represents $r(La^{3+})$=1.36 Å, or $r(Pr^{3+})$=1.179 Å, respectively; $r_{A'}$ denotes $r(Ca^{2+})$=1.34 Å; for r_B the value $r(Fe^{3+}$(high spin))=0.645 Å was used; r_O is given by $r(O^{2-})$=1.40 Å. The numerical pre-factors (0.8 and 0.2) describe the site occupancy for A-site substitution in the ABO_3 perovskite system. For the ideal cubic perovskite structure the tolerance factor is unity, whereas LCF82 (*t*=0.953) and PCF82 (*t*=0.903) show slight deviations from the cubic structure towards the orthorhombic structure by tilting of the FeO_6 octahedra (compare also Fig. 1). The *t* value for PCF82 is lower compared to LCF82. This may be due to the partial oxidation of Fe^{3+} to Fe^{4+} due to electronic charge compensation of the partial substitution of Pr^{3+} with Ca^{2+}, similar to the analogous effect reported for Sr^{2+} substituted perovskites [61]. It has to be mentioned that the calculated tolerance factors assume an ideal cation stoichiometry (A:A':B=8:2:10) with the A-site being occupied exclusively by La^{3+}(Pr^{3+}) and Ca^{2+} and the B-site by Fe^{3+} (high spin). Even though EDX analyses of LCF82 and PCF82 suggest that the actual compositions of the materials are close to the theoretically expected cation stoichiometry (see Table S-2 Supplementary material), the measurement uncertainty of the method is too large to exclude that small deviations in the range of one (or several) tenth atomic percent occur. Further, valence changes, for example from Pr^{3+} to Pr^{4+}, may occur if PCF82 is slightly sub-stoichiometric in CaO, or due to changes in the oxygen nonstoichiometry. In this case, it cannot be excluded that a small amount of Pr^{4+} is incorporated on the B-site. Further, the

valence state of Fe will be affected by changes in the oxygen nonstoichiometry. Due to all these considerations, the tolerance factors of LCF82 and PCF82 given above are to be understood as approximations.

For the computational study, the orthorhombic unit cells obtained from the diffraction experiments were taken and the geometries relaxed. The small deviations of the lattice constants of about −2% as displayed in Table 1 are on the one hand due to thermal expansion and the optimization performed at 0 K (while XRD measurements were done at room temperature), on the other hand they are within the error limit of the functional used. The calculated Fe-O bond lengths and Fe-O-Fe binding angles are shown in Table 2. The good accordance of the lattice constants and the associated binding properties justifies the decision of simplifying the ratio of A (A=La, Pr): O=5:1 to 4:1 and supports the finding in references [47] and [48]. Thus, we decided to use these simplified structures in our further studies.

3.2. Thermal expansion, phase transitions, and oxygen nonstoichiometry

The relative thermal expansion ($\Delta L/L_0$) of LCF82 and PCF82 was measured over a temperature range of $30 \leq T/°C \leq 1000$ at different oxygen partial pressures $1\times10^{-3} \leq pO_2/bar \leq 1$, Fig. 2. For each measurement, the samples were heated up to 1000 °C and cooled down (all rates were 1 K min^{-1}) at a given pO_2, followed by an isotherm for 2 h at 30 °C, and a second heating and cooling cycle under identical conditions. Before each experiment, the samples were usually equilibrated in a different pO_2 (due to heating and cooling in ambient air during sintering, or due to thermal expansion measurements in a different gas atmosphere). Therefore, non-equilibrium effects may affect the data obtained in the first temperature sweep, especially at low temperatures when oxygen exchange kinetics is slow. In order to minimize errors thus introduced, a second temperature sweep with the same pO_2 was performed with all measurements, and the slope of the second heating step was used for calculation of the thermal expansion coefficients (TECs).

Price et al. reported phase transition temperatures for the (La,Ca) $FeO_{3-\delta}$ system [63], which are also appearing in the case of LCF82 as a change of the slope in the thermal expansion curve (region I and II in Fig. 2). PCF82 shows no such slope changes, when measured under the same conditions. All obtained TECs are listed in Table S-3 (Supplementary material). In region I (which includes the typical operating temperatures of IT-SOFCs and IT-SOECs), thermal expansion coefficients of LCF82 and PCF82 match those of common solid electrolytes like $Ce_{0.9}Gd_{0.1}O_2$ (GDC; 12.5×10^{-6} K^{-1} [64]) and 8 mol-% yttria-stabilized zirconia (YSZ; 10.8×10^{-6} K^{-1} [65]). This may be an advantage in the technical application, since similar TECs of the electrolyte and the electrode prevent delamination during heating and cooling of SOFCs and SOECs [66]. LCF82 and PCF82 show significantly lower TECs than the state-of-the-art material $La_{0.6}Sr_{0.4}CoO_{3-\delta}$ (18.9×10^{-6} K^{-1} [67]). Therefore, LCF82 and PCF82, as well as the lanthanum calcium ferrites in [68], or $La_{0.9}Ca_{0.1}FeO_{3-\delta}$ (12.4×10^{-6} K^{-1} [34]), would result in a much better mechanical stability on YSZ/GDC electrolytes than the Co-containing state-of-the-art IT-SOFC or -SOEC air electrode materials. It has to be mentioned that the expansion shown in Fig. 2 includes contributions of both thermal and chemical expansion. The latter effect is due to the progressive decrease in oxygen stoichiometry with increasing temperature and decreasing oxygen partial pressures. In agreement with the oxygen nonstoichiometry of LCF82 and PCF82 shown in Fig. 3, the slopes of the expansion curves (resp. the TEC values shown in Table S–3; Supplementary material) increase at T≥750 °C and with decreasing pO_2. Also, in agreement with the higher oxygen nonstoichiometry of LCF82 compared to PCF82 (Figs. 3a and 3f), the TEC of LCF82 at T≥750 °C is higher than that of PCF82. However, a detailed deconvolution of thermal and chemical contributions to the total expansion is beyond the scope of this study.

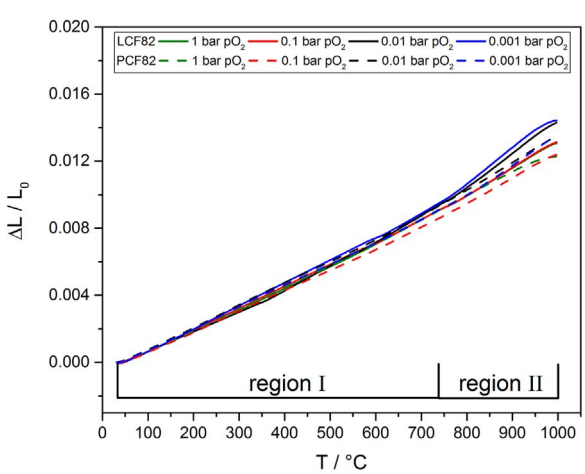

Fig. 2. Expansion curves of LCF82 (note two different temperature regions) and PCF82 (constant slope over the investigated temperature range) at different oxygen partial pressures. The expansion behaviour includes contributions from thermal and chemical expansion.

The previously mentioned phase transition of LCF82 at the borderline between regions I and II (~740 °C) can be assigned to the reversible change from the orthorhombic to the rhombohedral structural modification previously described by Price et al. [63]. Indeed, differential scanning calorimetry (DSC) (Fig. S-3, Supplementary material) shows a phase transition with an onset temperature of approximately 720 °C in Ar. The maximum of the temperature peak occurs at approximately 740 °C, which agrees well with the observed change in the thermal expansion behaviour (Fig. 2; Table S-3 in Supplementary material).

Precision thermogravimetry of LCF82 at $600 \leq T/°C \leq 900$ and $1\times10^{-3} \leq pO_2/bar \leq 0.1$ shows that the oxygen nonstoichiometry δ increases with increasing temperature and decreasing oxygen partial pressure (Fig. 3). In the case of PCF82, the oxygen nonstoichiometry could only be determined as a function of pO_2 at 900 °C (Fig. 3). At lower temperatures the mass changes of PCF82 upon changes of the oxygen partial pressure were too small to determine reliable values of δ. The oxygen nonstoichiometries of both LCF82 and PCF82 are smaller than those of other SOFC cathode materials with high Co- and/or Sr-content, such as $La_{0.4}Sr_{0.6}CoO_{3-\delta}$ [69,70] and $La_{0.4}Sr_{0.6}FeO_{3-\delta}$ [12,15]. This is due to the higher concentration of A-site substituents in $La_{0.4}Sr_{0.6}CoO_{3-\delta}$ and $La_{0.4}Sr_{0.6}FeO_{3-\delta}$, as well as to the more facile reduction of Co, compared to Fe [15,16,71], leading to ionic charge compensation by the formation of oxygen vacancies ($V_O^{\bullet\bullet}$).

To simulate the oxygen nonstoichiometry at working temperature range (Fig. 3), two supercells containing 80 and 160 atoms were created for both structures by expanding the unit cell. Based on recent computational work of references [39], the atoms were arranged in linear chains of calcium surrounded by layers of the correlated rare earth ion, as this conformation is lowest in energy. Removing an oxygen atom of both supercells resulted in oxygen nonstoichiometry of 0.0625 and 0.03125, respectively. These values are slightly larger than the measured ones. To go to smaller nonstoichiometries, the supercells would become even larger and computationally prohibitive. Optimizing the structures, the lattice constants were fixed while allowing for internal ionic relaxation. Both structures were used to calculate the vacancy formation enthalpy as well as the oxygen migration energy. As a small change of δ showed no effect on the energy, the results refer to the 80 atoms structure. Further information on the energies of the two different supercells can be found in the Supplementary section (Table S-4).

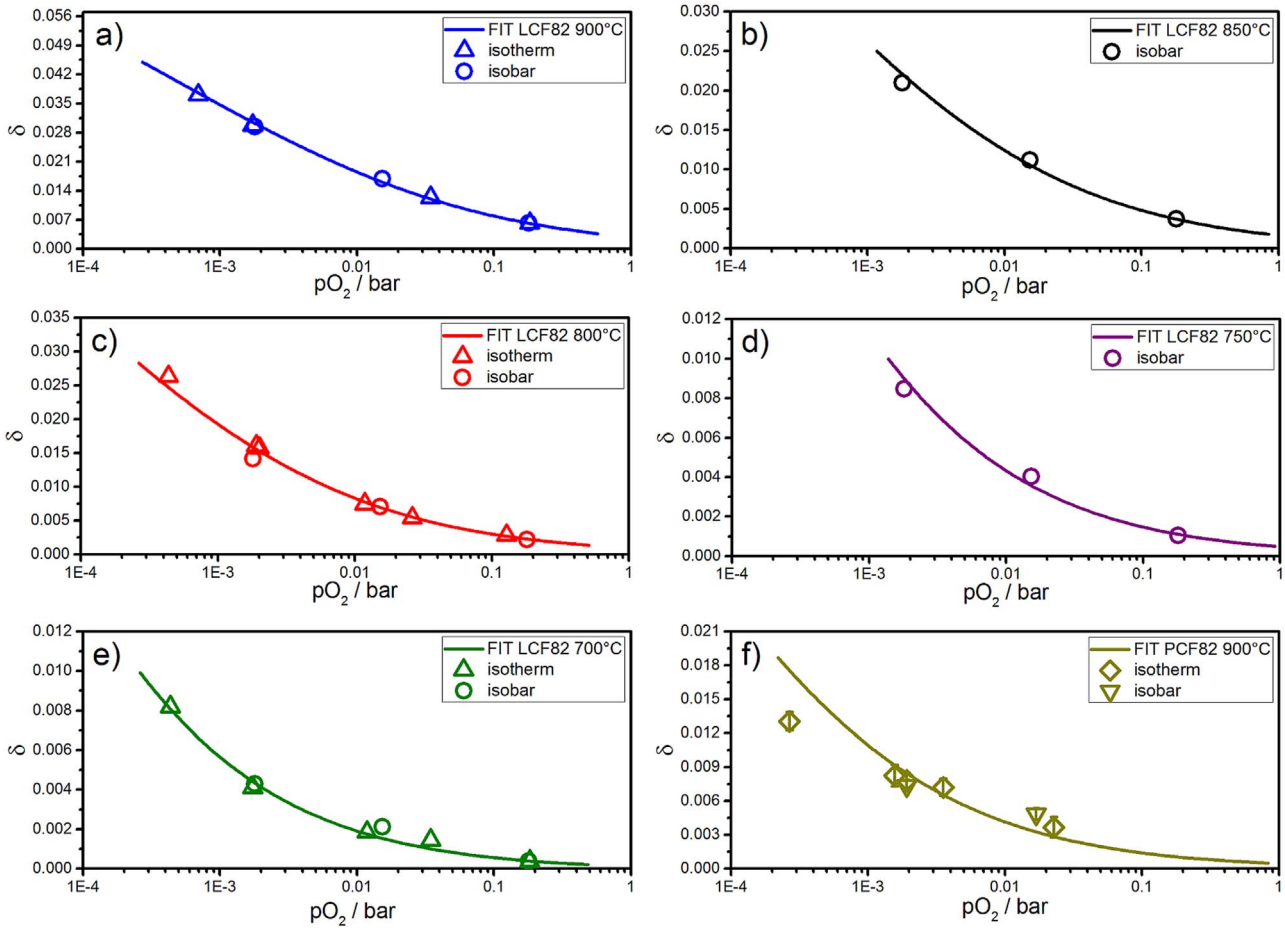

Fig. 3. Oxygen nonstoichiometry as a function of the oxygen partial pressure at different temperatures; a)-e) 900–700 °C for LCF82; f) 900 °C for PCF82; Data points for LCF82 were obtained from isothermal (up triangle) and isobaric measurements (circles). Data points for PCF82 were obtained from isothermal (diamond) and isobaric measurements (down triangle). Lines are nonlinear least squares fits to the defect model (equation 9, Supplementary material).

3.3. Defect chemical model

The oxygen nonstoichiometry of LCF82 (700–900 °C) and PCF82 (900 °C) can be described by an ideal point defect model, which was developed by Mizusaki et al. [72]. Details on the defect model are given in the Supplementary material. Nonlinear least squares fits of the defect model to the experimental data of δ as a function of pO_2 at various temperatures are shown in Fig. 3. The oxygen nonstoichiometry of LCF82 is described well by the model at T=700–900 °C (Figs. 3a-3e). In the case of PCF82, deviations occur between data and fit at 900 °C (Fig. 3f). On the one hand, these deviations may be due to the relatively small weight changes (small δ values in the range of 0.003–0.015) which are thus affected by larger experimental errors, and the limited number of data points available in a relatively narrow pO_2 range. On the other hand, it cannot be excluded that additional effects play a role, such as formation of Pr^{4+} on the A-site and/or incorporation of Pr^{4+} on the B-site. In the latter case, the defect model would have to be adapted in order to consider additional defect species ($Pr_{Pr}^{\bullet}$, $Pr_{Fe}^{\bullet}$), the corresponding defect equilibria, and thermodynamic equilibrium constants. However, since there is only a limited number of experimental data points available (Fig. 3f), and the occurrence of Pr^{4+} on the A- and/or B-site cannot be verified, it would not be justified to apply a more complicated defect model with additional fit parameters.

The equilibrium constants K_{red}, which are obtained as fit parameters from nonlinear regression at various temperatures, are summarized in Fig. S-4 in the Supplementary material for LCF82 and PCF82. Using K_{red}, the concentrations of the defect species $[Fe_{Fe}^{x}]$, $[Fe_{Fe}^{\bullet}]$, $[O_{O}^{x}]$, and $[V_{O}^{\bullet\bullet}]$ can be calculated. The pO_2 dependences of the defect concentrations are plotted in Brouwer diagrams in the Supplementary material (Fig. S-5 and Fig. S-6). Due to deviations between data and fit in the case of PCF82 at 900 °C (Fig. 3f), the value for K_{red} and the Brouwer diagram of PCF82 may be associated with higher uncertainty.

3.4. Electronic conductivity

The electronic conductivities σ_e of LCF82 and PCF82 are given as a function of temperature at different oxygen partial pressures in Fig. 4a. For LCF82 a maximum of the electronic conductivity of σ_e=110 S cm^{-1} is reached at 700 °C and pO_2=0.1 bar. In comparison, PCF82 shows σ_e=59 S cm^{-1} under the same conditions. The activation energies for electronic conduction were obtained from the slopes of $\ln(\sigma_e \bullet T)$ vs. T^{-1} plots, and are summarized in Table 3.

As shown in Fig. 3, PCF82 has a lower oxygen nonstoichiometry than LCF82 under comparable experimental conditions. According to the electroneutrality condition (Eqs. (2) and (3), respectively, Supplementary material), this would mean that PCF82 should have a higher concentration of electron holes (Fe^{4+}) and thus a higher electronic conductivity than LCF82. However, as evident from Fig. 4a this is not the case, presumably because both LCF82 and PCF82 show relatively small oxygen nonstoichiometries with $2\,[V_{O}^{\bullet\bullet}] \ll [Fe_{Fe}^{\bullet}]$. This indicates that other factors (chemical nature and valence of A-site host cation, structural parameters etc.) are responsible for the difference in the electronic transport properties of LCF82 and PCF82. Ren et al. [61] showed, by studying various Sr-containing ferrites, that the ionic radius of the A-site host cations has a pronounced effect on the electronic

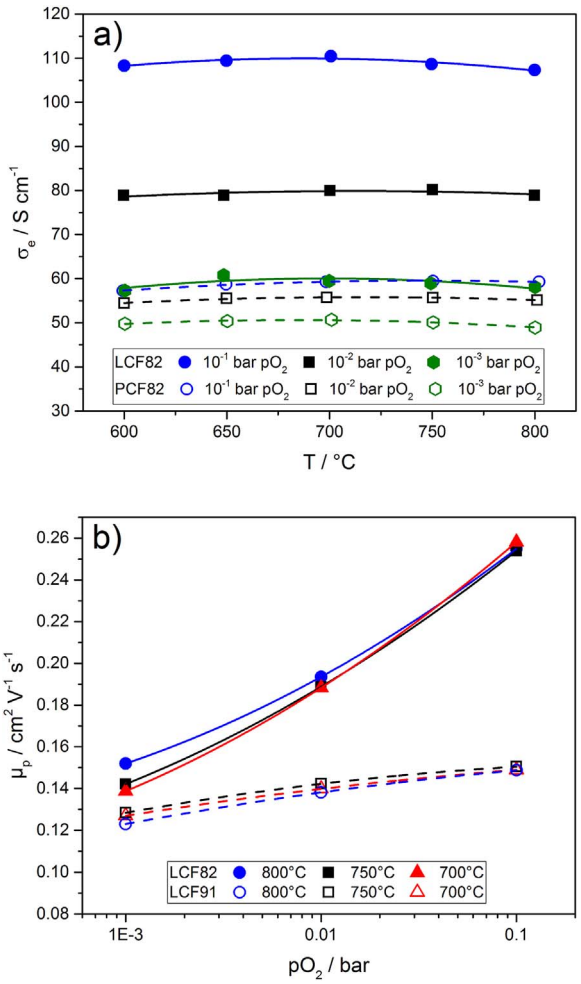

Fig. 4. a) Electronic conductivities of LCF82 and PCF82 as a function of temperature and oxygen partial pressure; b) electronic charge carrier mobilities of LCF82 as a function of the oxygen partial pressure at different temperatures (data of LCF91 [34] are given for comparison); Lines are guides for the eye.

transport properties. $La_{0.8}Sr_{0.2}FeO_{3-\delta}$ and $Pr_{0.8}Sr_{0.2}FeO_{3-\delta}$ [61] show electronic conductivities which are comparable to those of the Ca-containing perovskites LCF82 and PCF82, respectively. This dependence on A-site host cation radius was also previously described for materials with higher alkaline earth metal ion concentration (x= 0.5) in the series $Ln_{0.5}Sr_{0.5}FeO_{3-\delta}$ (Ln=La, Pr, Sm, ...) [73]. Electronic conduction in perovskite ferrites is commonly assumed to occur by a small polaron hopping mechanism, which takes place along the Fe-O-Fe pathway [34,74–76]. High electron conduction is possible when the O 2p and Fe 3d orbitals overlap [77,78], which is mainly achieved by certain Fe-O binding distances and Fe-O-Fe angles. These parameters are listed for LCF82 and PCF82 in Table 2. It is important to consider, that structural distortion (expressed by the deviation of the tolerance factor from unity, Table 1), is decreasing the Fe-O bond length due to an increased overlap between the electron conducting O 2p and Fe 3d orbitals with increasing A-site ionic radius. This has been shown for Sr-doped perovskites and could also be applied to the Ca-doped compounds [61,79–82]. In the case of PCF82, electronic charge compensation my also occur by the oxidation of Pr^{3+} to Pr^{4+}, which is not possible with La^{3+} in LCF82 [61]. This effect may lead to a lower concentration of electron holes (Fe^{4+}) in PCF82 and contribute to the lower electrical conductivity compared to LCF82 [83–85]. In addition to the number of electronic charge carriers, the mobility of the electron holes has an impact on the magnitude of the electronic conductivity. Using the formula unit concentration of the electron holes p=[Fe^{4+}] obtained from the defect model, and the molar volume V_m determined by XRD and Rietveld refinement, the following equation may be used to estimate the mobility of the p-type electronic charge carriers μ_p

$$\mu_p = \frac{\sigma_e V_m}{N_A e p (1 - p)} \quad (2)$$

where N_A is Avogadro's constant and e the elementary charge [14,86]. However, this analysis could only be performed for LCF82, due to the limited data available for δ=f(pO_2,T) of PCF82 (compare Sections 3.2 and 3.3). The mobilities of electron holes in LCF82 are given as a function of oxygen partial pressure at different temperatures in Fig. 4b. The temperature dependence of μ_p is relatively weak, analogously to the previously studied material $La_{0.9}Ca_{0.1}Fe_{3-\delta}$ (LCF91) [34]. An increase in the electronic charge carrier mobility of LCF82 is found with increasing pO_2, which may be ascribed to a decrease in the oxygen vacancy concentration (compare Fig. 3). As also described in the detailed investigation on the electronic charge transport properties of LCF91 [34], the presence of oxygen vacancies leads to a decrease in the electronic conductivity which occurs along the Fe-O-Fe pathways in the structure. In comparison with LCF91, LCF82 shows higher electron hole mobilities than LCF91 (Fig. 4b).

3.5. Oxygen exchange kinetics and ionic conductivity

The chemical surface exchange coefficients k_{chem} and the chemical diffusion coefficients D_{chem} of oxygen of LCF82 and PCF82 are given in Fig. 5 and Fig. 6 as a function of temperature at different oxygen partial pressures. A good agreement between oxidation and reduction experiments was observed. It was possible to determine k_{chem} for both materials at $1\times10^{-3} \leq pO_2/bar \leq 0.1$ and $600 \leq T/°C \leq 800$ (Fig. 5). LCF82 shows its highest value for $k_{chem}=6\times10^{-3}$ cm s^{-1} at pO_2=0.1 bar and T=800 °C. With reducing oxygen partial pressure (from 0.1 to 1×10^{-3} bar pO_2) the values for k_{chem} decrease. A minimum of $k_{chem}=1\times10^{-4}$ cm s^{-1} is found at $pO_2=1\times10^{-3}$ bar. In the lower pO_2 region (from 1×10^{-2} to 1×10^{-3} bar pO_2) PCF82 exhibits faster oxygen surface exchange kinetics than LCF82. Tamimi et al. [87] found similar results for the $Ln_{0.5}Sr_{0.5}Co_{0.8}Fe_{0.2}O_{3-\delta}$ (Ln=La, Pr, Nd) series. They

Table 3
Activation energies E_a of various material parameters of LCF82 and PCF82 at different oxygen partial pressures.

E_a / kJ mol^{-1}						
	LCF82			PCF82		
Parameter	@ pO_2=0.1 bar	@ pO_2=0.01 bar	@ pO_2=0.001 bar	@ pO_2=0.1 bar	@ pO_2=0.01 bar	@ pO_2=0.001 bar
σ_e	8 ± 0.8	9 ± 0.2	7 ± 0.5	9 ± 0.4	9 ± 0.7	7 ± 0.4
k_{chem}	99 ± 16	94 ± 19	134 ± 18	138 ± 10	97 ± 4	69 ± 19
k_O	110 ± 28	74 ± 20	83 ± 2	–	–	–
D_{chem}	97 ± 10	85 ± 12	–	141 ± 4	129 ± 8	140 ± 10
D_O	92 ± 3	82 ± 3	–	–	–	–
D_V	65 ± 10	44 ± 8	–	–	–	–
σ_{ion}	103 ± 1	66 ± 1	–	–	–	–

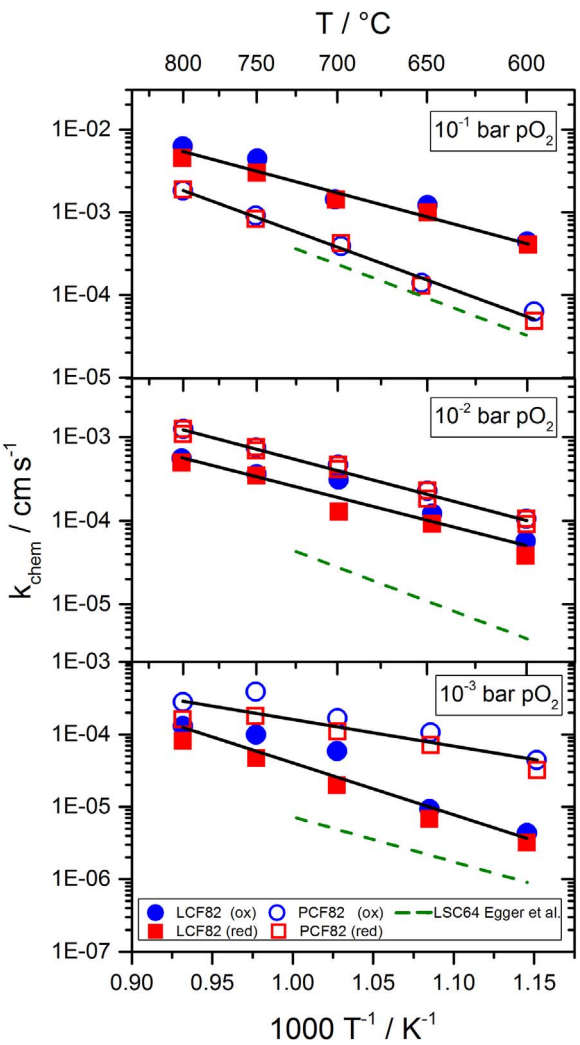

Fig. 5. Arrhenius plots of the chemical surface exchange coefficients (k_{chem}) of LCF82 (solid symbols) and PCF82 (open symbols) at different oxygen partial pressures; the twofold standard deviation of multiple measurements is close to the size of the symbols. For comparison, data of LSC64 from Egger et al. [88] are given (dashed line). Activation energies for k_{chem} of LCF82 and PCF82 are summarized in Table 3. The activation energies for LSC64 are in the range of $114 \leq E_a/kJ\ mol^{-1} \leq 155$ [88].

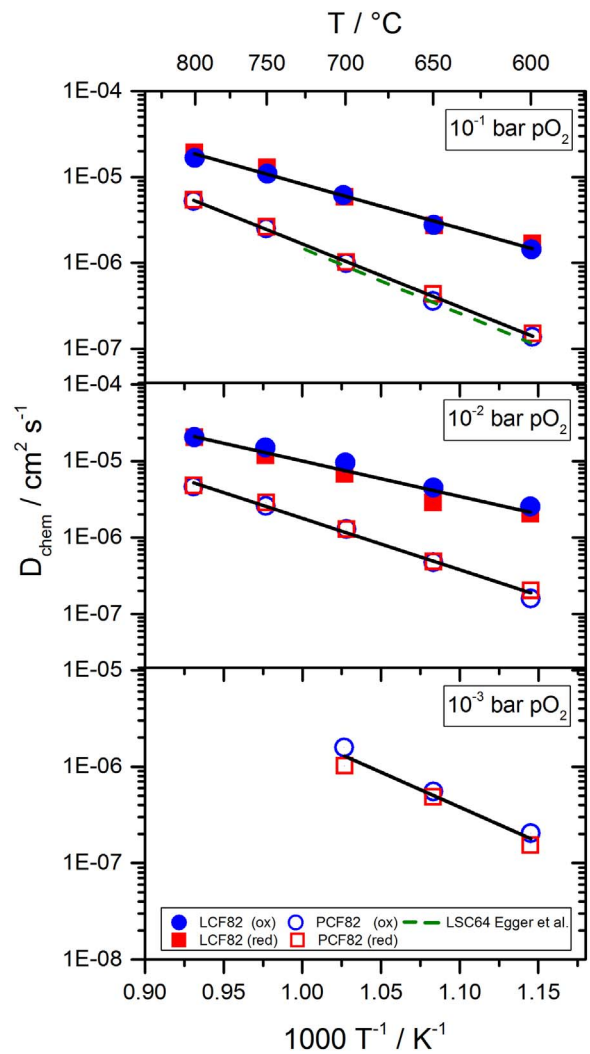

Fig. 6. Arrhenius plots of the chemical diffusion coefficients of oxygen (D_{chem}) of LCF82 (solid symbols) and PCF82 (open symbols) at different oxygen partial pressures; the twofold sigma standard deviation of multiple measurements is close to the size of the symbols. For comparison, data of LSC64 from Egger et al. [88] are given (dashed line). Activation energies for D_{chem} of LCF82 and PCF82 are summarized in Table 3. The activation energy for LSC64 at 10^{-1} bar pO_2 is 129 kJ mol^{-1} [88].

reported higher oxygen exchange rates for $Pr_{0.5}Sr_{0.5}Co_{0.8}Fe_{0.2}O_{3-\delta}$ compared to $La_{0.5}Sr_{0.5}Co_{0.8}Fe_{0.2}O_{3-\delta}$, which they ascribed to the higher oxygen mobility in the Pr compound.

In comparison with literature data of the well-known SOFC cathode material $La_{0.6}Sr_{0.4}CoO_{3-\delta}$ (LSC64) both LCF82 and PCF82 show significantly higher chemical surface exchange coefficients (Fig. 5). It should be noted that considerable scattering in the values of the oxygen surface exchange coefficients of mixed conducting transition metal oxides is frequently observed with literature data, and even in values determined in the same laboratory. These differences may be due to the preparation and pre-treatment of the samples (purity of the raw materials, thermal history, electrical contacting, measurements setup, etc.). However, since the measurements on LCF82, PCF82, and LSC64, which are compared in this work, were performed in our lab with the same sample preparation methods, same contacting, and in the same experimental setup, the trends observed here should - to the best of the authors' knowledge - be reliable.

Values for D_{chem} were obtained for LCF82 and PCF82 in the temperature range of 600–800 °C and pO_2 range from 0.1 to 0.01 bar (Fig. 6). At 1×10^{-3} bar pO_2 it was only possible to measure D_{chem} for PCF82 from 600 to 700 °C, because at higher temperatures the surface exchange process limits the kinetics. For the same reason, the determination of D_{chem} was not possible for LCF82 at $pO_2=1\times10^{-3}$ bar. LCF82 exhibits the highest value for $D_{chem}=2\times10^{-5}$ $cm^2\ s^{-1}$ at 800 °C and $pO_2=0.1$ bar, whereas the value of PCF82 is approximately one order of magnitude lower than that of LCF82.

Cherry et al. [89] performed theoretical calculations on the dependence of ionic radius and migration energies in orthorhombic perovskites with various A-site elements. They concluded that perovskites substituted with smaller A-site cations, for instance Ca^{2+}, exhibit lower migration energies, and therefore faster oxygen diffusion. This trend agrees with the measured chemical diffusion coefficients of oxygen of LCF82 and PCF82 (Fig. 6), which show lower activation energies (Table 3) and faster oxygen diffusion, compared to state-of-the-art SOFC cathodes like $La_{0.6}Sr_{0.4}CoO_{3-\delta}$ (LSC64).

The activation energies E_a for k_{chem} and D_{chem} of LCF82 and PCF82 are given in Table 3. At high oxygen partial pressure (1×10^{-1} and 1×10^{-2} bar) E_a of both kinetic parameters is lower for LCF82 than for PCF82. At lower oxygen partial pressure, a higher activation energy is found for k_{chem} of LCF82 compared to PCF82.

Self-diffusion coefficients for oxygen, D_O, and self-diffusion coefficients for the oxygen vacancies, D_V, were estimated from the measured chemical diffusion coefficients by the relation $D_{chem} = \gamma_O D_O$, where γ_O is

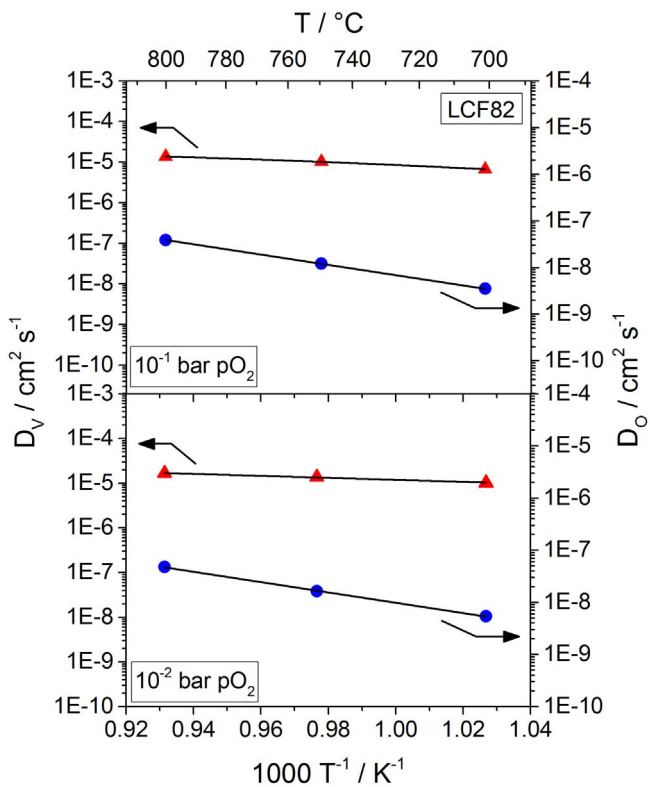

Fig. 7. Arrhenius plots of self-diffusion coefficients of oxygen (D_O) and oxygen vacancies (D_V) of LCF82 at different oxygen partial pressures.

the thermodynamic factor of oxygen, which is given by the following equation [90–92].

$$\gamma_O = \frac{1}{2}\left(\frac{\partial \ln pO_2}{\partial \ln c_O}\right)_T = \frac{1}{2}\left(\frac{\partial \ln pO_2}{\partial \ln(3-\delta)}\right)_T \tag{3}$$

The concentration of the oxygen ions, c_O was calculated from experimental data of the oxygen nonstoichiometry δ. Values for D_V can be calculated analogously from the relation $D_{chem} = \gamma_V D_V$, where γ_V is given by

$$\gamma_V = -\frac{1}{2}\left(\frac{\partial \ln pO_2}{\partial \ln c_V}\right)_T = -\frac{1}{2}\left(\frac{\partial \ln pO_2}{\partial \ln(3-\delta)}\right)_T. \tag{4}$$

The thermodynamic factors of oxygen are in the range of 260–1750 for LCF82 (900–700 °C), and 700 for PCF82 (900 °C) (see also Fig. S-7 in the Supplementary material). The further analysis could only be performed for LCF82, due to lack of experimental data of the oxygen nonstoichiometry of PCF82 (compare Sections 3.2 and 3.3). Estimated values of the self-diffusion coefficients of LCF82 are plotted in Fig. 7, and activation energies for D_O and D_V are listed in Table 3. The oxygen vacancy diffusion coefficients of LCF82 are in good agreement with literature data of $La_{0.9}Ca_{0.1}FeO_{3-\delta}$ [34], $La_{1-x}Sr_xFeO_{3-\delta}$ (x=0.1–0.5) [4,47,90,93], and $La_{1-x}Sr_xCoO_{3-\delta}$ (x=0.1–0.4) [47,88]. In Fig. 8, oxygen surface exchange coefficients, k_O (estimated from $k_{chem} \approx k_O\gamma_O$), are given. The activation energies of k_O are listed in Table 3.

The ionic conductivities σ_{ion} of LCF82 were estimated via the Nernst-Einstein equation (neglecting contributions from the correlation factor and the Haven ratio) [88,94,95] at 700–800 °C for LCF82 (Fig. 9).

$$\sigma_{ion} = \frac{4\,F^2\,c_O\,D_O}{R\,T} \tag{5}$$

Ionic conductivities of LCF82 as measured by Bidrawn et al. [96] agree quite well with the estimated values from the present study. Zink et al. [31] also published data on the ionic conductivity of LCF82 which

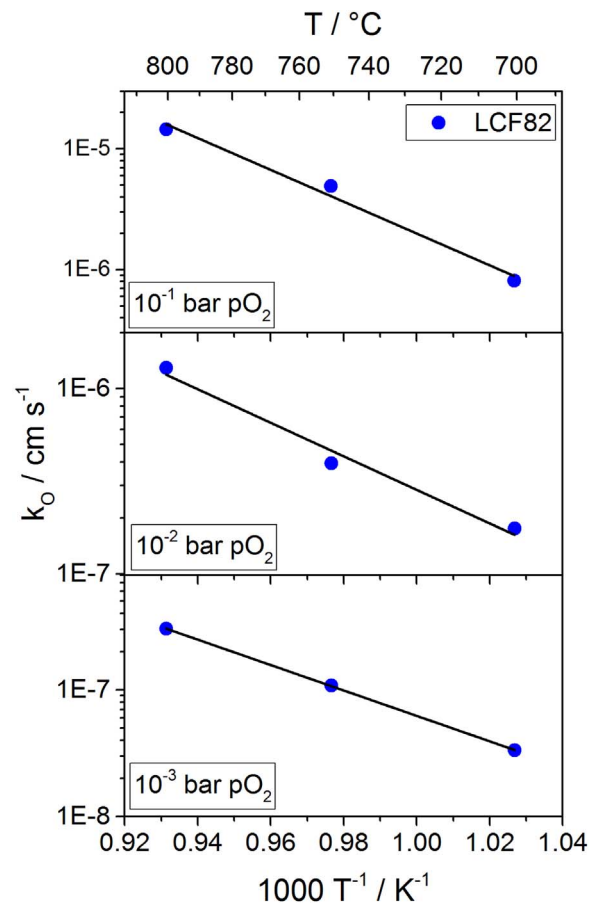

Fig. 8. Arrhenius plots of the surface exchange coefficient of oxygen of LCF82 at different oxygen partial pressures.

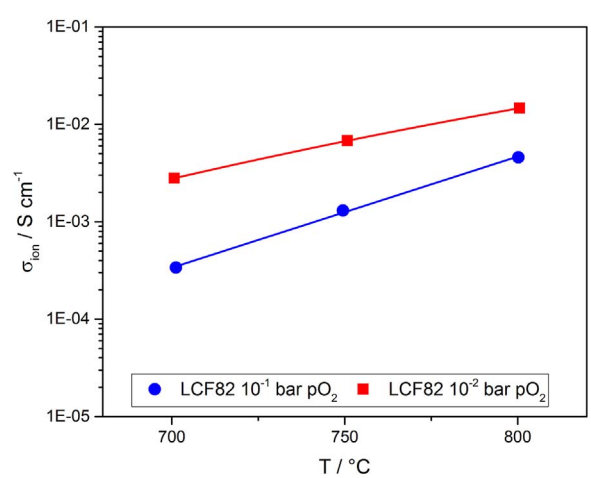

Fig. 9. Ionic conductivities of LCF82 as a function of temperature at different oxygen partial pressures; Lines are guides for the eye.

are approximately one order of magnitude higher than those we report here.

To study the possible oxygen migration pathways computationally, first the different O sites of the structures had to be determined. The oxygen vacancy formation energies, E_{vac}, can be expressed by

$$E_{vac} = E_{ACF_{3-x}} + \frac{1}{2}E_{O_2} - E_{ACF} \tag{6}$$

where $E_{ACF_{3-x}}$ is the total energy of the oxygen vacant supercell, while E_{ACF} is that of the stoichiometric supercell and E_{O_2} is the energy of an isolated oxygen molecule in the gas phase calculated in a 8×8×8 Å

Table 4
Oxygen vacancy formation energies of the 80 atoms supercell of LCF and PCF at 1000 K and at 0 K (in parentheses).

O site	LCF E_{vac} / eV	PCF E_{vac} / eV
V1	2.43 (3.49)	2.33 (3.50)
V2	2.49 (3.63)	2.45 (3.65)
V3	2.44 (3.44)	2.29 (3.44)
V4	2.42 (3.50)	2.35 (3.53)

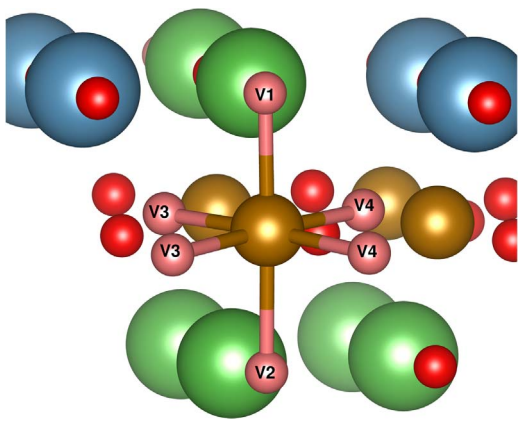

Fig. 10. Different oxygen positions in the FeO_6 octahedron of the supercells of LCF and PCF used for DFT calculations, Fe=orange, oxygen=red, calcium=blue, La/Pr=green. (For interpretation of the references to color in this figure legend, the reader is referred to the web version of this article.)

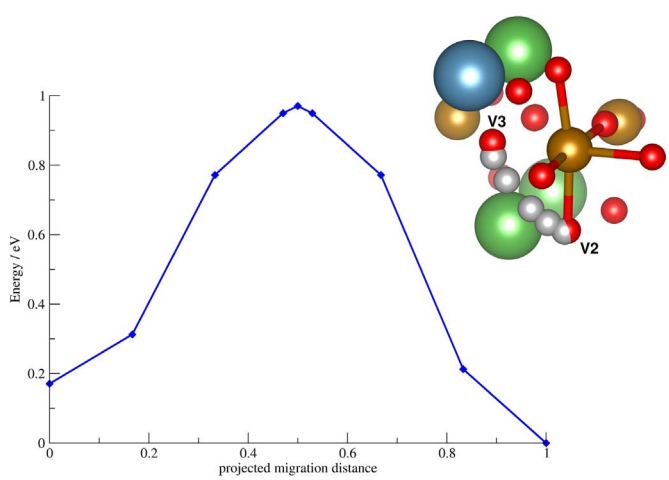

Fig. 11. A possible hopping route of oxygen (V2-V3) in LCF and its corresponding energy profile. The energy of the last image of the path was set 0.

simulation cell. According to the symmetry of the supercells, four different oxygen sites were expected and also confirmed by the calculation. The energies can be found in Table 4 ranging from 3.44 to 3.65 eV at 0 K and from 2.42 to 2.49 at 1000 K. In the literature, experimental values for similar perovskites ($La_{1-x}Sr_xFeO_{3-\delta}$) vary between 1 and 3.5 eV [39,40,97]. The positions of the O sites in the perovskite structures are shown in Fig. 10. The position closest to the rare earth layer, V2, shows significantly higher vacancy formation energy. It follows that the formation energy is dependent on the influence of the calcium atom on the oxygen position with respect to the arrangement within the structure.

The oxygen migration along the octahedron edges was investigated for LCF. Due to the four different octahedron positions, there are seven possible migration pathways, which are listed in Table S-5 (Supplementary material) with their corresponding activation energy. The Cl-NEB method predicted curved pathways with the energy maximum midway between the two oxygen sites. A possible hopping route as well as its corresponding energy profile is shown in Fig. 11. Difference in vacancy formation between the O sites causes asymmetric migration energies, whereas for Path 3 and Path 7 the energies are symmetrical around the hopping routes. The larger migration energy defines the rate-determining step of each path. In accordance with the experimental data of LCF82 (Table 3, activation energies of D_O, which are between 82 and 92 kJ mol^{-1} depending on oxygen partial pressure), migration energies between 66.5 and 132.8 kJ mol^{-1} were calculated.

4. Conclusions

Two calcium acceptor-doped perovskites, $La_{0.8}Ca_{0.2}FeO_{3-\delta}$ (LCF82) and $Pr_{0.8}Ca_{0.2}FeO_{3-\delta}$ (PCF82), were synthesized and characterized with respect to their material properties like crystal structure, thermal expansion coefficients, and phase stability, as well as their oxygen exchange kinetics and mass and charge transport properties (surface exchange coefficient, chemical diffusion coefficient of oxygen, electronic and ionic conductivities). The thermal expansion coefficients of both LCF82 and PCF82 are in good agreement with those of state-of-the-art solid electrolytes. LCF82 exhibits electronic conductivities of > 100 S cm^{-1}, whereas those of PCF82 are lower (> 50 S cm^{-1}). Chemical surface exchange coefficients and chemical diffusion coefficients of oxygen were determined for both materials at 600–800 °C and pO_2=0.1 – 1×10^{-3} bar, respectively. LCF82 exhibits very high values of k_{chem} at pO_2=0.1 bar, whereas PCF82 provides faster exchange kinetics at lower oxygen partial pressures (0.01 – 1×10^{-3} bar). The chemical diffusion coefficients of LCF82 are approximately one order of magnitude higher than those of PCF82. The kinetic parameters of both LCF82 and PCF82 are higher than those of state-of-the-art SOFC cathode materials like $La_{0.6}Sr_{0.4}CoO_{3-\delta}$. Further, LCF82 shows good ionic conductivities at 700–800 °C. Due to these results, LCF82 and PCF82 are considered promising materials for air electrodes in SOFCs and SOECs. However, further investigations on the long-term stability of these materials should be performed under application relevant conditions (humid atmospheres, presence of Cr and Si impurities). The computational and experimental results agree well, independently confirming each other. Thus, calculations may be helpful in supporting experimental studies of further perovskites, especially of those which are more difficult to prepare and investigate experimentally.

Acknowledgements

Financial support by the Austrian 'Klima- und Energiefonds' and AVL List GmbH (Austria) within the program 'Mobilität der Zukunft' (project no. 845334, project title ASYSII) is gratefully acknowledged. Furthermore, the authors would like to thank V. Terziyska from Montanuniversitaet Leoben for XRD measurements and Grygoriy Dolgonos from Karl-Franzens-Universität Graz for useful discussions.

Appendix A. Supplementary material

Supplementary data associated with this article can be found in the online version at doi:10.1016/j.jssc.2017.12.019.

References

[1] F. Ramadhani, M.A. Hussain, H. Mokhlis, S. Hajimolana, Renew. Sustain. Energy Rev. 76 (2017) 460–484.
[2] A. Choudhury, H. Chandra, A. Arora, Renew. Sustain. Energy Rev. 20 (2013) 430–442.
[3] N. Mahato, A. Banerjee, A. Gupta, S. Omar, K. Balani, Progress Mater. Sci. 72 (2015) 141–337.
[4] J. Yoo, A. Verma, S. Wang, A.J. Jacobson, J. Electrochem. Soc. 152 (2005)

A497–A505.
[5] K.-D. Kreuer, Fuel Cells - Selected Entries from the Encyclopedia of Sustainability Science and Technology, 1st ed., Springer-Verlag, New York, 2013.
[6] K. Kendall, M. Kendall, High-temperature Solid Oxide Fuel Cells for the 21st Century, Academic Press, Oxford, UK, 2016.
[7] S.P. Simner, J.F. Bonnett, N.L. Canfield, K.D. Meinhardt, J.P. Shelton, V.L. Sprenkle, J.W. Stevenson, J. Power Sources 113 (2003) 1–10.
[8] A. Mai, V.A.C. Haanappel, S. Uhlenbruck, F. Tietz, D. Stöver, Solid State Ion. 176 (2005) 1341–1350.
[9] J.M. Ralph, C. Rossignol, R. Kumar, J. Electrochem. Soc. 150 (2003) A1518–A1522.
[10] W. Wang, Y. Huang, S. Jung, J.M. Vohs, R.J. Gorte, J. Electrochem. Soc. 153 (2006) A2066–A2070.
[11] W. Preis, E. Bucher, W. Sitte, Solid State Ion. 175 (2004) 393–397.
[12] O. Bartels, K.D. Becker, E. Bucher, W. Sitte, Solid State Ion. 177 (2006) 1677–1680.
[13] E. Bucher, W. Sitte, J. Electroceram. 13 (2004) 779–784.
[14] J. Mizusaki, T. Sasamoto, W.R. Cannon, H.K. Bowen, J. Am. Ceram. Soc. 66 (1983) 247–252.
[15] J. Mizusaki, M. Yoshihiro, S. Yamauchi, K. Fueki, J. Solid State Chem. 58 (1985) 257–266.
[16] E. Bucher, Department of General, Analytical, and Physical Chemistry (Ph.D. Thesis), Montanuniversitaet Leoben, Austria, Leoben, 2003.
[17] T. Horita, H. Kishimoto, K. Yamaji, M.E. Brito, T. Shimonosono, D. Cho, M. Izuki, F. Wang, H. Yokokawa, in: S.C. Singhal, K. Eguchi (Eds.) 12th Intern. Symp. Solid Oxide Fuel Cells (SOFC-XII), The Electrochemical Society, Pennington, USA, Montréal, Canada, 2011, pp. 511–517.
[18] H. Yokokawa, H. Tu, B. Iwanschitz, A. Mai, J. Power Sources 182 (2008) 400–412.
[19] N.H. Menzler, A. Mai, D. Stöver, Durability of cathodes including Cr poisoning, in: W. Vielstich, H. Yokokawa, H.A. Gasteiger (Eds.), Handbook of Fuel Cells - Fundamentals, Technology and Applications, John Wiley & Sons, Ltd., 2009, pp. 566–578.
[20] W. Araki, M. Miyashita, Y. Arai, Solid State Ion. 290 (2016) 18–23.
[21] R.D. Shannon, Acta Cryst. A 32 (1976) 751–767.
[22] N. Schrödl, E. Bucher, A. Egger, P. Kreiml, C. Teichert, T. Höschen, W. Sitte, Solid State Ion. 276 (2015) 62–71.
[23] N. Schrödl, E. Bucher, C. Gspan, A. Egger, C. Ganser, C. Teichert, F. Hofer, W. Sitte, Solid State Ion. 288 (2016) 14–21.
[24] M. Perz, E. Bucher, C. Gspan, J. Waldhäusl, F. Hofer, W. Sitte, Solid State Ion. 288 (2016) 22–27.
[25] T.C. Geary, S.B. Adler, Solid State Ion. 253 (2013) 88–93.
[26] R. Andoulsi, K. Horchani-Naifer, M. Férid, Powder Technol. 230 (2012) 183–187.
[27] R. Andoulsi, K. Horchani-Naifer, M. Férid, Ceram. Int. 39 (2013) 6527–6531.
[28] G. Pecchi, M.G. Jiliberto, A. Buljan, E.J. Delgado, Solid State Ion. 187 (2011) 27–32.
[29] R. Pushpa, D. Daniel, D.P. Butt, Solid State Ion. 249–250 (2013) 184–190.
[30] P. Ciambelli, S. Cimino, L. Lisi, M. Faticanti, G. Minelli, I. Pettiti, P. Porta, Appl. Catal. B: Environ. 33 (2001) 193–203.
[31] P.A. Zink, K.J. Yoon, U.B. Pal, S. Gopalan, Electrochem. Solid-State Lett. 12 (2009) B141–B143.
[32] Y. Nagata, S. Yashiro, T. Mitsuhashi, A. Koriyama, Y. Kawashima, H. Samata, J. Magn. Magn. Mater. 237 (2001) 250–260.
[33] S.K. Pandey, R. Bindu, P. Bhatt, S.M. Chaudhari, A.V. Pimpale, Physica B: Condens. Matter 365 (2005) 47–54.
[34] C. Berger, E. Bucher, W. Sitte, Solid State Ion. 299 (2017) 46–54.
[35] C. Berger, E. Bucher, C. Gspan, A. Menzel, W. Sitte, J. Electrochem. Soc. 164 (2017) F3008–F3018.
[36] K.T. Lee, A. Manthiram, J. Electrochem. Soc. 153 (2006) A794–A798.
[37] J.M. Serra, V.B. Vert, M. Betz, V.A.C. Haanappel, W.A. Meulenberg, F. Tietz, J. Electrochem. Soc. 155 (2008) B207–B214.
[38] K. Kammer, Solid State Ion. 177 (2006) 1047–1051.
[39] A.M. Ritzmann, A.B. Muñoz-García, M. Pavone, J.A. Keith, E.A. Carter, Chem. Mater. 25 (2013) 3011–3019.
[40] H.-Y. Su, K. Sun, J. Mater. Sci. 50 (2015) 1701–1709.
[41] D. Maiti, Y.A. Daza, M.M. Yung, J.N. Kuhn, V.R. Bhethanabotla, J. Mater. Chem. A 4 (2016) 5137–5148.
[42] L. Lutterotti, Nucl. Inst. Methods Phys. Res., B (2010) 334–340.
[43] M.V. Patrakeev, J.A. Bahteeva, E.B. Mitberg, I.A. Leonidov, V.L. Kozhevnikov, K.R. Poeppelmeier, J. Solid State Chem. 172 (2003) 219–231.
[44] W. Preis, M. Holzinger, W. Sitte, Monatshefte Chem. 132 (2001) 499–508.
[45] M.W. den Otter, H.J.M. Bouwmeester, B.A. Boukamp, H. Verweij, J. Electrochem. Soc. 148 (2001) J1–J6.
[46] W. Preis, E. Bucher, W. Sitte, J. Power Sources 106 (2002) 116–121.
[47] T. Ishigaki, S. Yamauchi, K. Kishio, J. Mizusaki, K. Fueki, J. Solid State Chem. 73 (1988) 179–187.
[48] VASP TST Tools, ⟨http://theory.cm.utexas.edu/vtsttools/12.01⟩.
[49] G. Kresse, J. Hafner, Phys. Rev. B 48 (1993) 13115–13118.
[50] G. Kresse, J. Furthmüller, Phys. Rev. B 54 (1996) 11169–11186.
[51] G. Kresse, J. Furthmüller, Comput. Mater. Sci. 6 (1996) 15–50.
[52] G. Kresse, D. Joubert, Phys. Rev. B 59 (1999) 1758–1775.
[53] J.P. Perdew, K. Burke, M. Ernzerhof, Phys. Rev. Lett. 77 (1996) 3865–3868.
[54] S. Grimme, J. Antony, S. Ehrlich, H. Krieg, J. Chem. Phys. 132 (2010) 154104.
[55] S. Grimme, S. Ehrlich, L. Goerigk, J. Comput. Chem. 32 (2011) 1456–1465.
[56] H. Jònsson, G. Mills, K.W. Jacobsen, Nudged elastic band method for finding minimum energy paths of transitions, classical and quantum dynamics in condensed phase simulations, World Sci. (2011) 385–404.
[57] G. Henkelman, B.P. Uberuaga, H. Jónsson, J. Chem. Phys. 113 (2000) 9901–9904.
[58] G. Henkelman, H. Jónsson, J. Chem. Phys. 113 (2000) 9978–9985.
[59] J.M. Hudspeth, G.A. Stewart, A.J. Studer, D.J. Goossens, J. Phys. Chem. Solids 72 (2011) 1543–1547.
[60] T. Sato, S. Takagi, S. Deledda, B.C. Hauback, S.-i. Orimo, Sci. Rep. 6 (2016) 23592.
[61] Y. Ren, R. Küngas, R.J. Gorte, C. Deng, Solid State Ion. 212 (2012) 47–54.
[62] H.M. Taguchi, Y. Hirota, K. Yamaguchi, O, Mat. Res. Bull. 40 (2005) 773–780.
[63] P.M. Price, E. Rabenberg, D. Thomsen, S.T. Misture, D.P. Butt, J. Am. Ceram. Soc. 97 (2014) 2241–2248.
[64] S.J. Hong, A.V. Virkar, J. Am. Ceram. Soc. 78 (1995) 433–439.
[65] N.Q. Minh, T. Takahashi, Chapter 4 - Electrolyte, in: N.Q.M. Takahashi (Ed.) Science and Technology of Ceramic Fuel Cells, Elsevier Science Ltd, Oxford, 1995, pp. 69–116.
[66] T. Ishihara, N.P. Bansal (Ed.)Fuel Cells and Hydrogen Energy, Springer, New York, 2009.
[67] V.V. Kharton, A.A. Yaremchenko, E.N. Naumovich, J. Solid State Electrochem. 3 (1999) 303–326.
[68] M.-H. Hung, M.V.M. Rao, D.-S. Tsai, Mater. Chem. Phys. 101 (2007) 297–302.
[69] W. Sitte, E. Bucher, W. Preis, Solid State Ion. 154–155 (2002) 517–522.
[70] A.N. Petrov, V.A. Cherepanov, O.F. Kononchuk, L.Y. Gavrilova, J. Solid State Chem. 87 (1990) 69–76.
[71] E. Bucher, Habilitation Thesis, Chair of Physical Chemistry, Montanuniversität Leoben, Leoben, 2013.
[72] J. Mizusaki, Y. Mima, S. Yamauchi, K. Fueki, H. Tagawa, J. Solid State Chem. 80 (1989) 102–111.
[73] V.V. Kharton, A.V. Kovalevsky, M.V. Patrakeev, E.V. Tsipis, A.P. Viskup, V.A. Kolotygin, A.A. Yaremchenko, A.L. Shaula, E.A. Kiselev, J.C. Waerenborgh, Chem. Mater. 20 (2008) 6457–6467.
[74] L.-W. Tai, M.M. Nasrallah, H.U. Anderson, D.M. Sparlin, S.R. Sehlin, Solid State Ion. 76 (1995) 259–271.
[75] L.-W. Tai, M.M. Nasrallah, H.U. Anderson, D.M. Sparlin, S.R. Sehlin, Solid State Ion. 76 (1995) 273–283.
[76] T. Montini, M. Bevilacqua, E. Fonda, M.F. Casula, S. Lee, C. Tavagnacco, R.J. Gorte, P. Fornasiero, Chem. Mater. 21 (2009) 1768–1774.
[77] S. Uhlenbruck, F. Tietz, Mater. Sci. Eng.: B 107 (2004) 277–282.
[78] S. Yamaguchi, Y. Okimoto, Y. Tokura, Phys. Rev. B 54 (1996) R11022–R11025.
[79] J.S. Zhou, J.B. Goodenough, Phys. Rev. B 69 (2004) 153105.
[80] J.S. Zhou, J.B. Goodenough, Phys. Rev. Lett. 94 (2005) 065501.
[81] J.B. Goodenough, J.S. Zhou, J. Mater. Chem. 17 (2007) 2394–2405.
[82] J.S. Zhou, J.B. Goodenough, Phys. Rev. B 77 (2008) 132104.
[83] M. Søgaard, P. Vang Hendriksen, M. Mogensen, J. Solid State Chem. 180 (2007) 1489–1503.
[84] M.V. Patrakeev, I.A. Leonidov, V.L. Kozhevnikov, K.R. Poeppelmeier, J. Solid State Chem. 178 (2005) 921–927.
[85] H.W. Brinks, H. Fjellvåg, A. Kjekshus, B.C. Hauback, J. Solid State Chem. 150 (2000) 233–249.
[86] J.E. ten Elshof, H.J.M. Bouwmeester, H. Verweij, Solid State Ion. 81 (1995) 97–109.
[87] M.A. Tamimi, A.C. Tomkiewicz, A. Huq, S. McIntosh, J. Mater. Chem. A 2 (2014) 18838–18847.
[88] A. Egger, E. Bucher, M. Yang, W. Sitte, Solid State Ion. 225 (2012) 55–60.
[89] M. Cherry, M.S. Islam, C.R.A. Catlow, J. Solid State Chem. 118 (1995) 125–132.
[90] J.E. ten Elshof, M.H.R. Lankhorst, H.J.M. Bouwmeester, J. Electrochem. Soc. 144 (1997) 1060–1067.
[91] J.A. Lane, S.J. Benson, D. Waller, J.A. Kilner, Solid State Ion. 121 (1999) 201–208.
[92] R. Merkle, J. Maier, J. Fleig, Mechanistic understanding and electrochemical modeling of mixed conducting (SOFC) electrodes, in: W. Vielstich, H. Yokokawa, H.A. Gasteiger (Eds.), Handbook of Fuel Cells - Fundamentals, Technology and Applications, John Wiley & Sons, Ltd., 2009, pp. 425–440.
[93] M. Søgaard, P.V. Hendriksen, M. Mogensen, J. Solid State Chem. 180 (2007) 1489–1503.
[94] E. Bucher, A. Egger, P. Ried, W. Sitte, P. Holtappels, Solid State Ion. 179 (2008) 1032–1035.
[95] V.V. Vashook, M. Al Daroukh, H. Ullmann, Ionics 7 (2001) 59–66.
[96] F. Bidrawn, S. Lee, J.M. Vohs, R.J. Gorte, J. Electrochem. Soc. 155 (2008) B660–B665.
[97] Y.A. Mastrikov, R. Merkle, E.A. Kotomin, M.M. Kuklja, J. Maier, Phys. Chem. Chem. Phys. 15 (2013) 911–918.

Supplementary Material

Strontium-free rare earth perovskite ferrites with fast oxygen exchange kinetics: Experiment and theory

Christian Berger[1], Edith Bucher[1*], Andreas Windischbacher[2],

A. Daniel Boese[2], Werner Sitte[1]

1 Chair of Physical Chemistry, Montanuniversitaet Leoben, Franz-Josef-Straße 18, A-8700 Leoben, Austria

2 Institute of Chemistry, Karl-Franzens-Universität Graz, Heinrichstraße 28, 8010 Graz, Austria

Contents

1. Particle size distribution 3

2. Density and chemical composition of sintered ceramic samples 4

3. Crystal structure 5

4. Differential scanning calorimetry and thermal/chemical expansion 6

5. Defect chemistry 8

5.1. Defect model 8

5.2. Brouwer Diagrams 10

5.3. Thermodynamic factors 12

6. Computational work 13

6.1. Validation of method 14

6.2. HSE-calculation 16

6.3. Soft potentials 16

7. References 17

1. Particle size distribution

The particle size distributions (PSD) of the calcined LCF82 and PCF82 powders showed broad bimodal characteristics with an average particle size of 15 µm for both materials. Subsequently, 6 g of the calcined powders and 60 g of ethanol were milled with 100 g of zirconia grinding balls in a polyethylene bottle on a benchtop roller system for 24 h. After this procedure, the PSD was monomodal with an average particle size of 0.90 µm for LCF82 and 0.77 µm for PCF82. Figure S-1 shows the particle size distributions of the two powder samples.

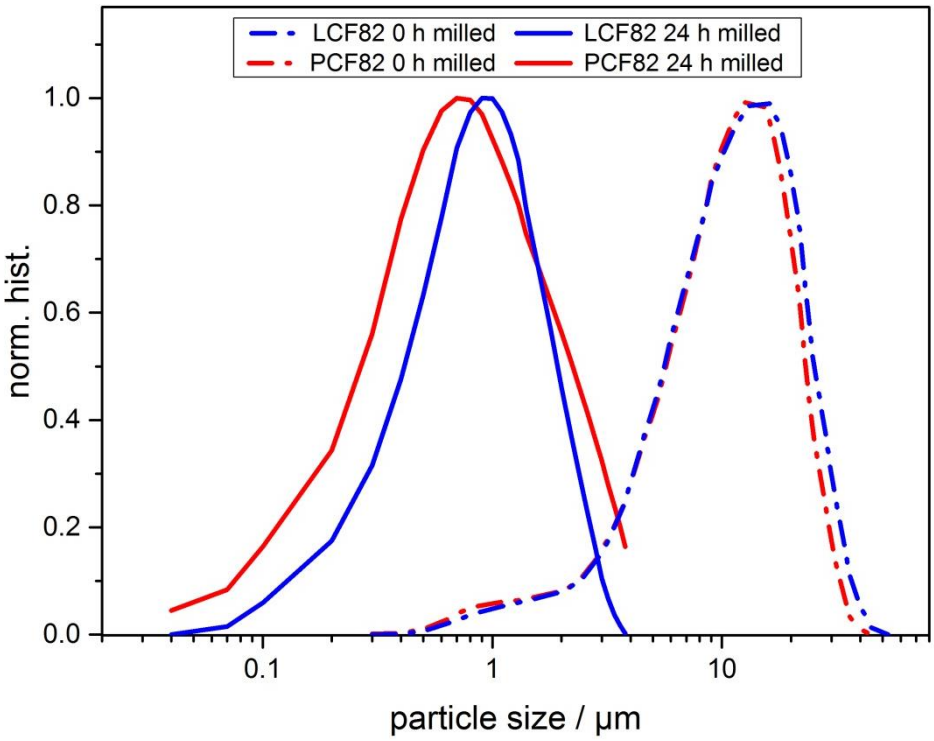

Figure S-1 Particle size distributions of LCF82 and PCF82; calcined powders before milling (dotted lines) and after 24 h of milling (solid lines).

2. Density and chemical composition of sintered ceramic samples

Table S-1 Bulk density and relative density of sintered LCF82 and PCF82 pellets. Theoretical densities were obtained from XRD measurements.

Sample	Bulk density / g cm^{-3}	Theoretical density / g cm^{-3} (based on XRD results)	Relative density / %
LCF82	6.145	6.3195	97.24
PCF82	6.023	6.3181	95.32

Table S-2 Cation stoichiometry of sintered LCF82 and PCF82 pellets. Measured atomic percent as obtained from EDX analyses are compared to theoretical values calculated from nominal compositions. The measurement uncertainty is estimated to ±(2-3) at-%.

Element	LCF82 measured / at-%	PCF82 measured / at-%	LCF82/PCF82 theoretical / at-%
Ca K	9.71	9.87	10.00
Fe K	50.87	48.59	50.00
La L	39.42	--	40.00
Pr L	--	41.54	40.00

3. Crystal structure

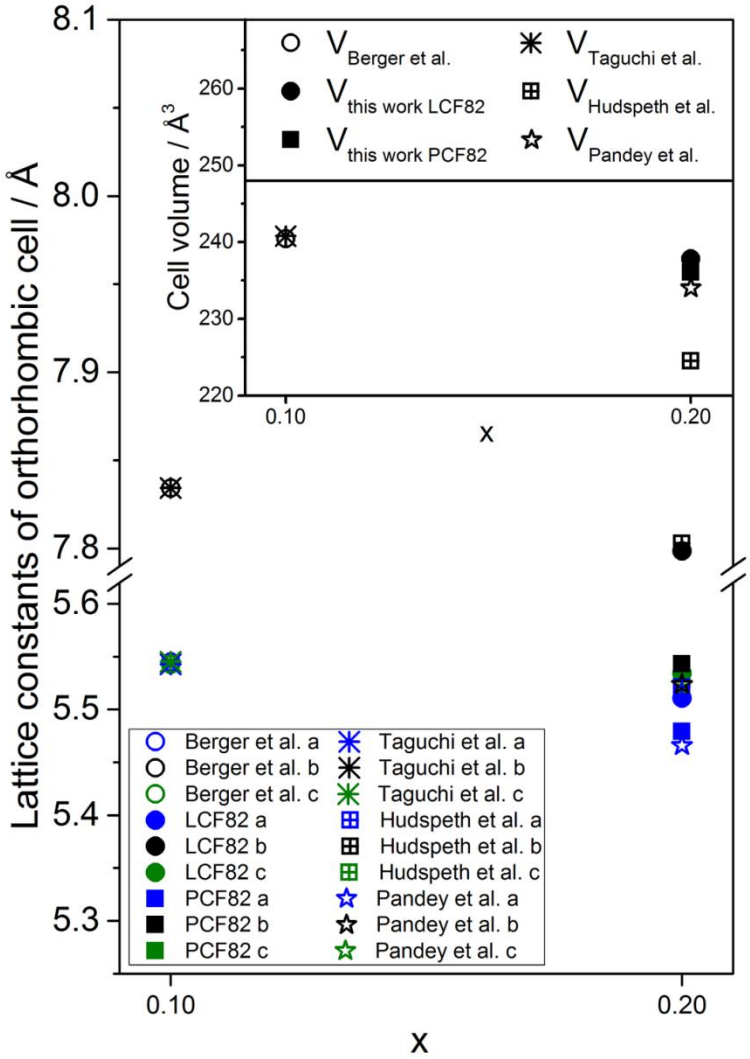

Figure S-2 Lattice parameters (a, b, c) and cell volumes (V) of various Ca^{2+} substituted rare earth ferrites $(Ln_{1-x}Ca_x)FeO_3$ with Ln=La, Pr. Berger et al. and Taguchi et al. reported lattice constants for LCF91 [1, 2]. Hudspeth et al. published lattice constants for LCF82 [3], and Pandey et al. for PCF82 [4].

4. Differential scanning calorimetry and thermal/chemical expansion

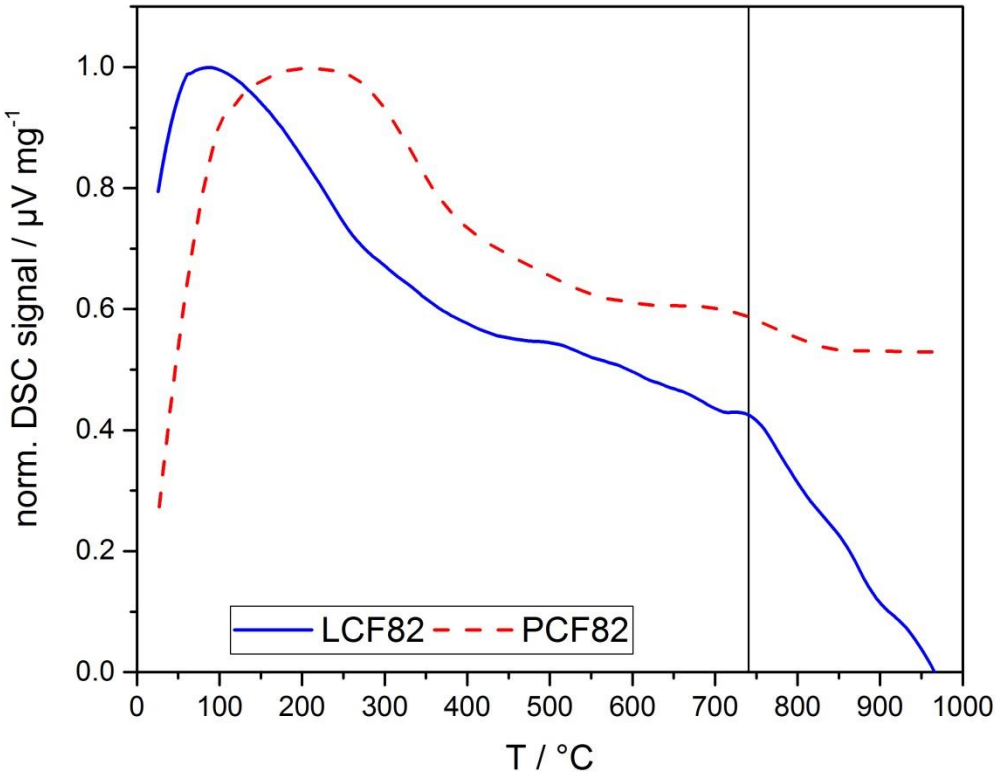

Figure S-3 Differential scanning calorimetry (DSC) of LCF82 in 100 % Ar (solid line) and PCF82 in 100 % Ar (dashed line); the peak at approximately 740°C (for LCF82) is due to the reversible phase transformation from the orthorhombic to the rhombohedral modification, which was also reported by Price *et al.* [5]. Under similar conditions, no phase transformation was observed for PCF82.

Table S-3 Expansion coefficients α of LCF82 (temperature ranges 30-750 °C (region I), and 750-1000°C (region II)) and PCF82 (temperature range 30-1000°C) at different oxygen partial pressures. The specified errors represent twofold standard deviations. The expansion behaviour includes contributions from thermal and chemical expansion.

	LCF82		PCF82
pO_2 / bar	α(I) E-06 / K^{-1}	α(II) E-06 / K^{-1}	α E-06 / K^{-1}
1	12.78 ± 0.07	15.81 ± 0.13	13.14 ± 0.06
0.1	12.79 ± 0.04	16.03 ± 0.12	13.03 ± 0.08
0.01	13.31 ± 0.13	19.38 ± 0.16	14.02 ± 0.09
0.001	13.53 ± 0.04	19.18 ± 0.12	13.99 ± 0.12

5. Defect chemistry

5.1. Defect model

The oxygen nonstoichiometry of LCF82 (700-900°C) and PCF82 (900°C) can be described by an ideal point defect model, which was developed by Mizusaki et al. [6]. The redox reaction may be formulated as:

$$\mathrm{O_O^x} + 2\,\mathrm{Fe_{Fe}^{\bullet}} \rightleftharpoons \frac{1}{2}\,\mathrm{O_2} + \mathrm{V_O^{\bullet\bullet}} + 2\,\mathrm{Fe_{Fe}^x} \tag{1}$$

The electroneutrality condition is given by

$$2\,[\mathrm{V_O^{\bullet\bullet}}] + [\mathrm{Fe_{Fe}^{\bullet}}] = [\mathrm{Ca'_{La}}] \tag{2}$$

for LCF82 and

$$2\,[\mathrm{V_O^{\bullet\bullet}}] + [\mathrm{Fe_{Fe}^{\bullet}}] = [\mathrm{Ca'_{Pr}}] \tag{3}$$

for PCF82, where $[\mathrm{V_O^{\bullet\bullet}}] = \delta$ and $[\mathrm{Ca'_{La}}] = [\mathrm{Ca'_{Pr}}] = x$ with x =0.2 given by the chemical composition. Under consideration of the site conservation conditions for Fe and O

$$[\mathrm{Fe_{Fe}^x}] + [\mathrm{Fe_{Fe}^{\bullet}}] = 1 \tag{4}$$

$$[\mathrm{V_O^{\bullet\bullet}}] + [\mathrm{O_O^x}] = 3 \tag{5}$$

the equilibrium constant K_{red} of equilibrium 1 is given by:

$$K_{red} = \frac{p\mathrm{O_2}^{1/2}\,[\mathrm{V_O^{\bullet\bullet}}]\,[\mathrm{Fe_{Fe}^x}]^2}{[\mathrm{O_O^x}]\,[\mathrm{Fe_{Fe}^{\bullet}}]^2} = \frac{p\mathrm{O_2}^{1/2}\,\delta\,(1-x+2\delta)^2}{(3-\delta)(x-2\delta)^2} \tag{6}$$

All defect concentrations are given in formula unit concentrations (mole/mole formula unit), and δ represents the formula unit concentration of oxygen vacancies. It should be remarked that the charge disproportionation reaction (2 $Fe^{3+} \rightleftharpoons Fe^{2+} + Fe^{4+}$), and thus the occurrence of Fe^{2+} ($\mathrm{Fe'_{Fe}}$) is neglected in the defect model. This assumption is commonly used for LSF and similar perovskite-type ferrites in oxidizing atmospheres and at moderate temperatures [6-8]. Further, when $2\,[\mathrm{V_O^{\bullet\bullet}}] \ll [\mathrm{Fe_{Fe}^{\bullet}}]$ (which is the case for LCF82 and PCF82 at $1\times10^{-3} \leq p\mathrm{O_2}/\mathrm{bar} \leq 0.1$), the electroneutrality condition may be simplified to

$$[\mathrm{Fe_{Fe}^{\bullet}}] \cong [\mathrm{Ca'_{La}}] = x \tag{7}$$

for LCF82 and

$$[\mathrm{Fe}_{\mathrm{Fe}}^{\bullet}] \cong [\mathrm{Ca}_{\mathrm{Pr}}'] = x \tag{8}$$

for PCF82.

The expression for the thermodynamic equilibrium constant may then be formulated as

$$K_{red} \cong \frac{p\mathrm{O}_2^{1/2}\,\delta\,(1-x)^2}{3\,x^2} \tag{9}$$

The thermodynamic equilibrium constants K_{red} for LCF82 and PCF82 were obtained from the defect model (equation 9) and are shown as a function of temperature in Figure S-4. Due to deviations between data and fit in the case of PCF82 at 900°C (Figure 4f) in the manuscript), the value for K_{red} of PCF82 and the Brouwer diagram may be associated with higher uncertainty.

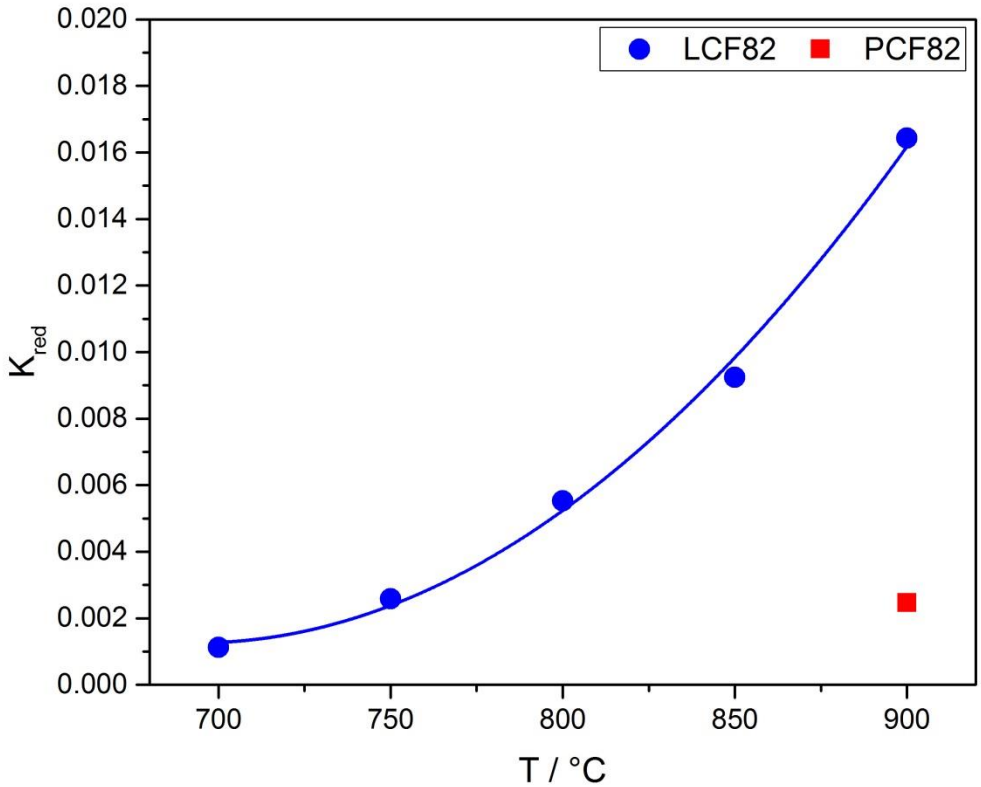

Figure S-4 Equilibrium constants for LCF82 and PCF82 as a function of temperature.

5.2. Brouwer Diagrams

The pO_2 dependences of the formula-unit concentrations of the defect species $[Fe_{Fe}^{x}], [Fe_{Fe}^{\bullet}], [V_O^{\bullet\bullet}]$ were calculated using K_{red} (see Figure S-4) and are plotted in the following Brouwer diagrams.

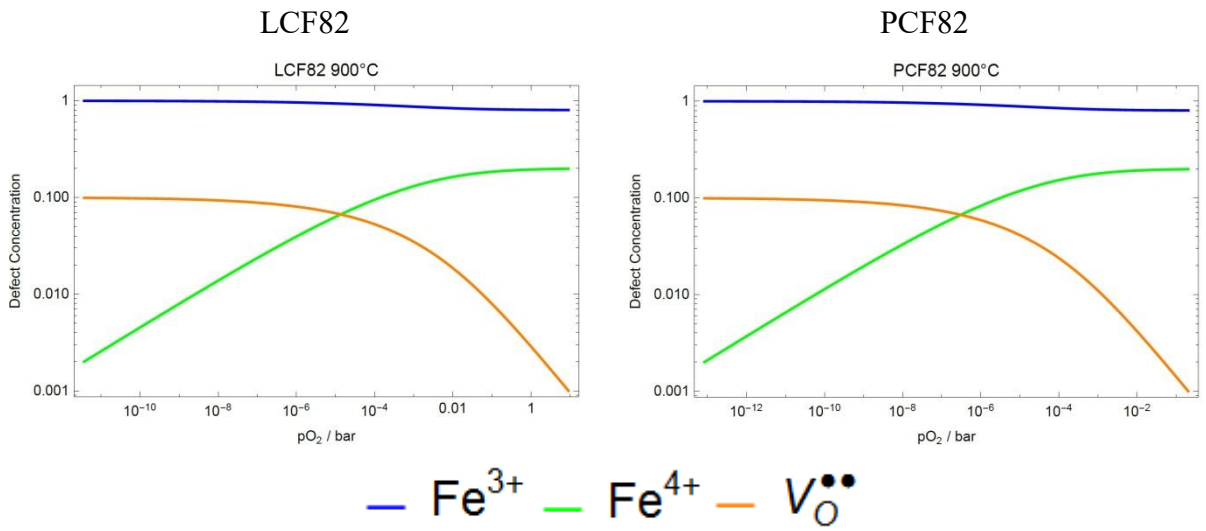

Figure S-5 Brouwer diagrams of LCF82 and PCF82 at 900°C. Calculations are based on experimental data from precision thermogravimetry. All defect concentrations are given in formula-unit concentrations.

LCF82

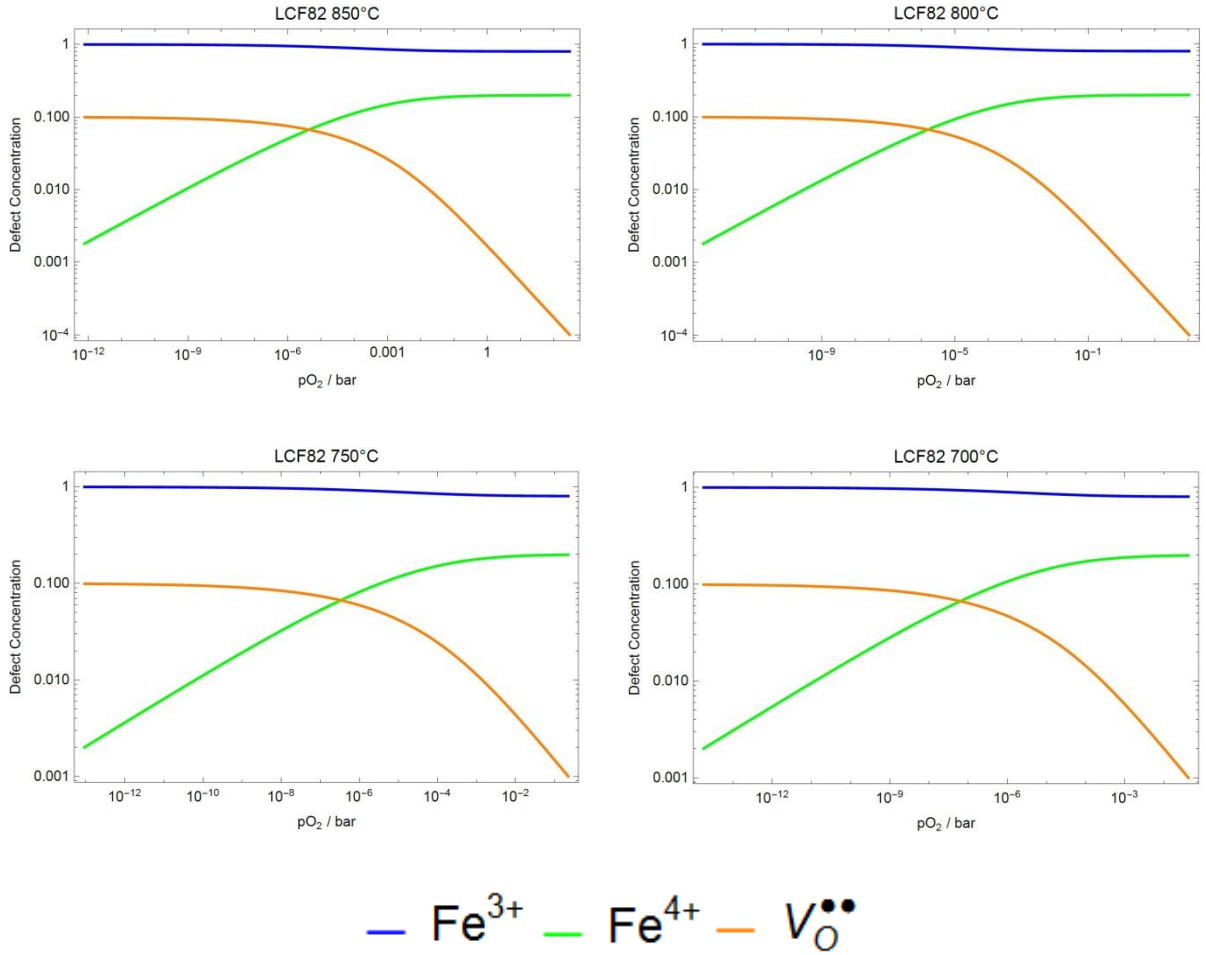

Figure S-6 Brouwer diagrams of LCF82 in the temperature range of 850 to 700°C. Calculations are based on experimental data from precision thermogravimetry. All defect concentrations are given in formula-unit concentrations.

5.3. Thermodynamic factors

The thermodynamic factors of oxygen and oxygen vacancies, γ_O and γ_V, were calculated according to equations 11 and 12 in the manuscript from linear fits of experimental data of ln(3-δ) vs. ln(pO_2) and ln(δ) vs. ln(pO_2) at constant temperatures.

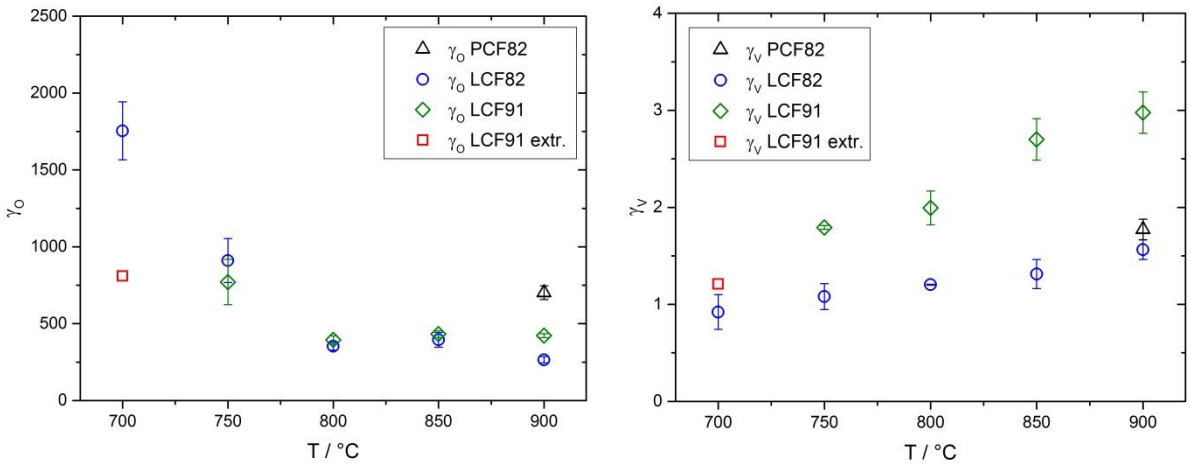

Figure S-7 Thermodynamic factors of oxygen and oxygen vacancies of LCF82 and PCF82; calculations are based on experimental data from precision thermogravimetry. Data of $La_{0.9}Ca_{0.1}FeO_{3-\delta}$ (LCF91) [2] are given for comparison.

6. Computational work

Supercells, which were 4-times (11x8x11 Å) and 8-times (11x16x11 Å) bigger than the unit cells (5.5x7x5.5 Å), were created and their oxygen vacancy formation energies (Table S-4) compared. There was no change in energy found.

Table S-4 The vacancy formation energies of LCF and PCF of (super)cells of different size at 0 K.

O-site	11x8x11 Å LCF	11x16x11 Å LCF	11x11x8 Å PCF	11x11x16 Å PCF
V1	3.49	3.47	3.50	3.49
V2	3.63	3.64	3.65	3.67
V3	3.44	3.45	3.44	3.43
V4	3.50	3.52	3.53	3.54

Table S-5 Oxygen migration activation energies of different pathways for LCF at 1000 K and at 0 K (in parentheses).

Pathway	Jump route	Oxygen migration energy / kJ mol^{-1}
Path 1	V3-V1 V1-V3	94.4 (74.3) 81.1 (69.5)
Path 2	V3-V2 V2-V3	104.9 (91.7) 89.3 (73.3)
Path 3	V3-V3	132.8 (98.4)
Path 4	V4-V1 V1-V4	79.5 (62.7) 66.5 (61.8)
Path 5	V4-V2 V2-V4	97.5 (87.8) 81.9 (73.3)
Path 6	V4-V3 V3-V4	105.4 (81.1) 104.4 (84.9)
Path 7	V4-V4	122.8 (108.1)

6.1. Validation of method

To validate the choice of the DFT-GGA approach for simulation of the doped perovskite materials, the host material $LaFeO_3$ (=LFO) was investigated and the results compared to previous theoretical studies. LFO was computed with the same settings as described in the paper using VASP and the PBE-D3BJ method with PAW-potentials. The unit cell was optimized in a 4x3x4 Monkhorst-Pack k-point mesh and energy convergence was within 10^{-5} eV. Comparison of the calculated cell parameters to experimental data [9] can be found in Table S-6. The average relative error is 1.7%. The experiment in reference [9] was performed at room temperature, whereas the calculations were performed at 0 K. Thus, a lattice elongation of about 1% due to thermal expansion always has to be expected.

Table S-6 Calculated and experimental cell parameters of LFO.

property	a / Å	b / Å	c / Å
exp.	5.553	7.862	5.563
PBE	5.462	7.681	5.492

For the calculation of the oxygen vacancy formation energy, an oxygen atom was removed (□=0.25) and the ionic position optimized while fixing the lattice constants. In Table S-7, the calculated energy is compared to literature data from various theoretical calculations using different approaches: GGA [10, 11] and GGA+U [12, 13]. Recent studies [9, 12] suggest that the oxygen vacancy formation energies of ABO_3-structures are largely unaffected by the supercell size. We found similar results for $La_{0.75}Ca_{0.25}FeO_3$ (LCF). Nevertheless, we want to point out that for reasonable simulation of experimental materials the simulated oxygen nonstoichiometry should match the experimental one, as done in this work and as often neglected.

Table S-7 Comparison of calculated oxygen defect formation energy with literature.

	calculated	**Ref 4**	**Ref 5**	**Ref 3**	**Ref 6**
E_{vac} / eV	3.90	3.75	4.26	4.04	4.05

The good agreement with the reference material indicates that the LFO is well described by PBE, even though the lattice constants are 1% off the experimental results.

6.2. HSE-calculation

For further comparison, single point calculations at the optimized PBE-structures of LFO and LCF (□=0.25) were performed using the Heyd-Scuseria-Ernzerhof [14] functional (HSE06) with 25% Hartree-Fock exchange. Here, the calculated oxygen defect formation energy of LFO is 5.02 eV and thus in between the evaluated values of GGA+U, 4.04 eV [13], and diffusion quantum Monte Carlo, 6.24 eV [15] calculations, whereas our PBE values yielded 3.90 eV. When augmenting the HSE electronic energy with the results of the PBE frequency analysis to obtain the oxygen vacancy enthalpy at 1000 K, we obtain 5.06 eV. The temperature-independent experimental oxygen vacancy enthalpy determined from a fit using the van`t Hoff equation is about 5.2±1.1 eV [16]. Thus, the HSE-results of the computed enthalpy are in the error range of the experimental data. As expected, the more sophisticated hybrid functional HSE gives a better description of the system. HSE-calculations of LCF hence lead to oxygen vacancy formation energy of 3.92 – 4.03 eV at 0 K, which is in contrast to LFO close to the PBE values of 3.49-3.63 eV (see above, Table S-4).

6.3. Soft potentials

Due to known convergence problems of the available VASP Pr-potentials, "softer" potentials were used. To justify this decision the oxygen defect formation energies of LCF (□=0.25) were calculated with soft potentials and compared to regular calculations (Table S-8) of the unit cell. The difference is about 0.1 eV.

Table S-8 Comparison of the soft potentials to the regular calculations.

O-site	soft	regular
V1	3.44	3.59
V2	3.61	3.72
V3	3.62	3.74
V4	3.59	3.77

7. References

[1] H.M. Taguchi, Y. Hirota, K. Yamaguchi, O., *Materials Research Bulletin* **40** (2005) 773.

[2] C. Berger, E. Bucher, W. Sitte, *Solid State Ionics* **299** (2017) 46.

[3] J.M. Hudspeth, G.A. Stewart, A.J. Studer, D.J. Goossens, *Journal of Physics and Chemistry of Solids* **72** (2011) (12) 1543.

[4] S.K. Pandey, R. Bindu, P. Bhatt, S.M. Chaudhari, A.V. Pimpale, *Physica B: Condensed Matter* **365** (2005) (1–4) 47.

[5] P.M. Price, E. Rabenberg, D. Thomsen, S.T. Misture, D.P. Butt, *Journal of the American Ceramic Society* **97** (2014) (7) 2241.

[6] J. Mizusaki, Y. Mima, S. Yamauchi, K. Fueki, H. Tagawa, *Journal of Solid State Chemistry* **80** (1989) 102.

[7] L.Y. Gavrilova, V.A. Cherepanov, Oxygen nonstoichiometry and defect structure of $La_{1-x}Me_xCoO_{3-\delta}$, *6th Intern. Symp. Solid Oxide Fuel Cells*, The Electrochemical Society, Pennington, NJ (1999), p.404-414.

[8] A. Ringuedé, J. Fouletier, *Solid State Ionics* **139** (2001) 167.

[9] M.T. Curnan, J.R. Kitchin, *The Journal of Physical Chemistry C* **118** (2014) (49) 28776.

[10] H.-Y. Su, K. Sun, *Journal of Materials Science* **50** (2015) (4) 1701.

[11] Y.A. Mastrikov, R. Merkle, E.A. Kotomin, M.M. Kuklja, J. Maier, *Physical Chemistry Chemical Physics* **15** (2013) (3) 911.

[12] A.A. Emery, C. Wolverton, *Scientific Data* **4** (2017) 170153.

[13] A.M. Ritzmann, A.B. Muñoz-García, M. Pavone, J.A. Keith, E.A. Carter, *Chemistry of Materials* **25** (2013) (15) 3011.

[14] A.V. Krukau, O.A. Vydrov, A.F. Izmaylov, G.E. Scuseria, *The Journal of Chemical Physics* **125** (2006) (22) 224106.

[15] J.A. Santana, J.T. Krogel, P.R.C. Kent, F.A. Reboredo, *The Journal of Chemical Physics* **147** (2017) (3) 034701.

[16] J. Mizusaki, M. Yoshihiro, S. Yamauchi, K. Fueki, *Journal of Solid State Chemistry* **58** (1985) 257.

Solid State Ionics 316 (2018) 93–101

Contents lists available at ScienceDirect

Solid State Ionics

journal homepage: www.elsevier.com/locate/ssi

Synthesis and characterization of the novel K_2NiF_4-type oxide $Pr_2Ni_{0.9}Co_{0.1}O_{4+\delta}$

Christian Berger[a], Edith Bucher[a,*], Andreas Egger[a], Anna Theresa Strasser[a], Nina Schrödl[a], Christian Gspan[b], Johannes Hofer[a], Werner Sitte[a]

[a] Chair of Physical Chemistry, Montanuniversitaet Leoben, Franz-Josef-Straße 18, A-8700 Leoben, Austria
[b] Institute of Electron Microscopy and Nanoanalysis (FELMI), Graz University of Technology, Graz Centre for Electron Microscopy (ZFE), Austrian Cooperative Research (ACR), Steyrergasse 17, A-8010 Graz, Austria

ARTICLE INFO

Keywords:
$Pr_2Ni_{0.9}Co_{0.1}O_{4+\delta}$
K_2NiF_4-type oxide
Crystal structure
Oxygen exchange kinetics
Electronic conductivity
Phase stability

ABSTRACT

$Pr_2Ni_{0.9}Co_{0.1}O_{4+\delta}$ (PNCO) powder was synthesized via a freeze drying process by mixing and shock freezing of aqueous metal acetate solutions, vacuum freeze drying of the resulting precursor and thermal treatment to obtain the complex oxide. X-ray powder diffraction and Rietveld refinement confirmed that the material was mainly single phase (< 1 wt% Pr_6O_{11} as secondary phase) with an orthorhombic K_2NiF_4-type unit cell at room temperature. Precision thermogravimetry between 30 °C and 900 °C showed an irreversible mass increase at $T \geq 750$ °C and $pO_2 = 0.2$ bar which indicated the transition to a higher order Ruddlesden-Popper phase $Pr_4(Ni,Co)_3O_{10-x}$ and PrO_y. Differential scanning calorimetry in pure Ar and 20% O_2/Ar showed a structural phase transition from the orthorhombic to a tetragonal modification at approximately 440 °C. Thermal expansion measurements between 30 °C and 1000 °C at different oxygen partial pressures ($1 \times 10^{-3} \leq pO_2/\text{bar} \leq 1$) indicated two different regions, corresponding to the orthorhombic low-temperature phase up to 400 °C and the tetragonal high-temperature phase from 400 °C to 1000 °C. The electronic conductivity of PNCO was in the range of $65 \leq \sigma_e/\text{S cm}^{-1} \leq 90$ (600–800 °C). The chemical surface exchange coefficient for oxygen (k_{chem}) was obtained from in-situ dc-conductivity relaxation experiments between 600 °C and 800 °C and 10^{-3} bar oxygen partial pressure. At temperatures close to 600 °C PNCO exhibited significantly faster oxygen exchange kinetics than the Co-free material $Pr_2NiO_{4+\delta}$ (PNO). For example, the surface exchange coefficient of PNCO at 600 °C was around 2×10^{-5} cm s^{-1}, while k_{chem} of PNO was approximately one order of magnitude smaller. However, at 800 °C both compounds showed similar oxygen exchange rates due to a lower activation energy of k_{chem} for PNCO (~80 kJ mol^{-1}) as compared to PNO (~160 kJ mol^{-1}). Post-test analyses of the specimens used for conductivity relaxation measurements showed the formation of small Pr_6O_{11} particles on the surface.

1. Introduction

In the last 20 years, K_2NiF_4-type materials attracted a lot of attention after the discovery of high temperature superconductivity in the La-cuprate system [1–3]. The K_2NiF_4-structure is the first member of the Ruddlesden-Popper (RP) series, which was originally described by Ruddlesden and Popper for the strontium titanates Sr_2TiO_4 [4], $Sr_3Ti_2O_7$ and $Sr_4Ti_3O_{10}$ [5]. From a crystallographic point of view, RP-phases $A_{n+1}B_nO_{3n+1}$ consist of alternatingly stacked $(ABO_3)_n$ perovskite slabs and AO rock salt layers, differing in the number n of single perovskite layers that make up the perovskite slabs of the structure. Formally, the perovskite structure can be considered an end member of the RP-series for $n = \infty$ [6,7]. RP-type rare earth nickelates $Ln_{n+1}B_nO_{3n+1}$, where Ln = La, Nd, Pr and B = Ni, have been extensively studied due to their exceptionally high oxygen diffusivities, high catalytic activity for the oxygen reduction reaction, good electronic and ionic conductivities and relatively low thermal expansion coefficients [8–11]. Possible applications include oxygen-permeable membranes and air electrodes for solid oxide fuel cells (SOFCs) or solid oxide electrolyzer cells (SOECs) [12–15].

In the field of SOFC research, large efforts are currently devoted towards lowering the operating temperature to 600 °C in order to reduce degradation rates of ceramic components and increase the long-term stability of the system [16–18]. Furthermore, it may be advantageous to use ceramic components without alkaline earth substituents (Sr, Ba, Ca), which often segregate to the surface and react with impurities, thereby decreasing the life-time of oxygen-permeable membranes and SOFC/SOEC systems [19–21]. In this respect, rare earth

* Corresponding author at: Montanuniversitaet Leoben, Franz-Josef-Straße 18, 8700 Leoben, Austria.
E-mail address: edith.bucher@unileoben.ac.at (E. Bucher).

https://doi.org/10.1016/j.ssi.2017.12.024
Received 29 September 2017; Received in revised form 18 December 2017; Accepted 18 December 2017
Available online 04 January 2018
0167-2738/ © 2017 Elsevier B.V. All rights reserved.

nickelates show great promise due to the absence of alkaline earth elements and high oxygen diffusivities even at reduced temperatures.

Ni-containing RP-phases are mixed ionic-electronic conductors with electronic conductivities in the order of 100 S cm^{-1} and ionic conductivities between 10^{-2} and 10^{-1} S cm^{-1} [22,23]. This is a consequence of the high oxygen over-stoichiometry of up to $\delta = 0.25$ observed for $La_2NiO_{4+\delta}$ [24], which leads to *p*-type electronic conductivity and a fast transport of oxygen interstitials within the AO rock-salt layers [25].

However, it is well known that oxygen transport through membranes of rare earth nickelates is limited by the surface exchange process [22,26]. This limitation may also be an issue for potential application of these materials as SOFC and SOEC electrodes. Previous studies on the oxygen exchange kinetics of first order (n = 1) RP-type rare earth nickelates show that the highest surface exchange rates are obtained in the $Pr_2NiO_{4+\delta}$ system [27,28]. To further improve the surface exchange kinetics of Ni-based RP-phases, partial substitution of Ni by Co was proposed in recent studies [29–31]. So far, this B-site doping effect has been investigated for the lanthanum and neodymium containing Ruddlesden-Popper phases [32–34] but no information on the oxygen exchange kinetics of Co-containing praseodymium nickelates is available.

In the present study, the effect of low-level substitution of Ni by Co was investigated for the first time in $Pr_2NiO_{4+\delta}$ with respect to crystal structure, phase stability, electronic conductivity, oxygen surface exchange kinetics and thermal expansion coefficients.

2. Experimental

2.1. Sample preparation

For the synthesis of PNCO, stock solutions of 0.1 M Pr$(OOCCH_3)_3 \cdot xH_2O$ (Alfa Aesar, 99.9%), 0.5 M $Ni(OOCCH_3)_2 \cdot 4H_2O$ (Aldrich, ≥ 99.0%) and $Co(OOCCH_3)_2$ (Alfa Aesar, ≥ 98%) were prepared. The exact concentration was determined by complexometric titration with EDTA (Titriplex® III, Merck) [35]. The solutions were thoroughly mixed in stoichiometric ratios to achieve the nominal composition of $Pr_2Ni_{0.9}Co_{0.1}O_{4+\delta}$. The resulting homogeneous solution was transferred by a peristaltic pump (ISMATEC Ecoline) and injected through a fine needle into a Dewar containing liquid nitrogen. During injection, the liquid nitrogen was continuously agitated by a metallic stirrer in order to prevent agglomeration of the frozen droplets. The liquid nitrogen-precursor mixture was then stored in a freezer until the liquid nitrogen was completely vaporized. This step is necessary because liquid nitrogen would evaporate violently under freeze drying conditions, leading to an uncontrolled spray of the precursor in the freeze drying device. The freeze drying process was performed in an Alpha 2–4 LDplus freeze drying unit (Christ, Germany) using two pressure steps. In the first and main drying step, the pressure was set at 2.6 mbar. This corresponds to an equilibrium temperature of − 10 °C, which is the recommended operation point for drying aqueous solutions. The precursor was dried for nine days, followed by a second drying step at 0.001 mbar for three days. The dried powder was homogenized in an agate mortar, transferred into a Pt-crucible and fired at 600 °C for 6 h in air. After grinding in an agate mortar, a final calcination step was performed at 1200 °C for 8 h with heating and cooling rates of 5 K min^{-1}. The resulting powder was of high phase purity with 1 wt% of Pr_6O_{11} secondary phase as determined by X-ray powder diffraction (XRD). Laser scattering measurements with a CILAS 1064 L showed a broad monomodal particle size distribution of the calcined powder. To achieve smaller particle sizes, the powder was ball milled in ethanol for 20 h yielding a median particle diameter of 0.6 μm (see Fig. S-1, Supplementary Material).

For thermal expansion measurements, a cylindrical pellet of 5 mm diameter and 9.5 mm length was prepared by uniaxial pressing at 500 MPa and sintering at 1350 °C for 10 h. For electrical conductivity (EC) and conductivity relaxation (CR) measurements, the powder was isostatically pressed at 250 MPa and sintered at 1200 °C for 2 h with heating and cooling rates of 5 K min^{-1}. Sample densities were calculated from the mass and geometrical dimensions of the pellets. The relative density of the sintered PNCO samples was ~97% of the theoretical density as obtained by X-ray diffraction (ρ_{XRD} = 7.342 g cm^{-3}). The cation stoichiometry was evaluated by energy dispersive X-ray (EDX) spectroscopy with an Oxford Instruments Mod. 6272 detector. The measured cation ratio fits well to the nominal composition (see Table 3). Further, inductively coupled plasma with optical emission spectrometry (ICP-OES, SPECTRO CIROS from SPECTRO Analytical Instruments GmbH) was used to check the cation ratios (Pr:Ni:Co equals 2.0 ± 0.02:0.9 ± 0.01:0.09 ± 0.001).

Co-free commercial PNO powder (Marion Technologies, France) was used as reference material to assess the effect of Co-substitution on the physical properties of PNCO. The K_2NiF_4-type main phase of PNO was verified by XRD with small amounts of secondary phases of Pr_6O_{11} (1.6 wt%) and NiO (1.2 wt%) present. A Pr:Ni ratio of 1.97 ± 0.03:1.03 ± 0.03 was stated by the supplier, the median particle size of the powder was 0.43 μm as determined by laser scattering. Samples for electrochemical measurements were prepared by isostatic pressing at 250 MPa and sintering at 1300 °C for 2 h with heating and cooling rates of 2 K min^{-1}. The resulting relative density was above 95% of the theoretical density as obtained by X-ray diffraction (ρ_{XRD} = 7.340 g cm^{-3}).

2.2. Crystallographic and microstructural analysis

XRD-analyses were performed at room temperature with a Bruker AXS D8 Advance ECO using a Cu K*α* radiation source operated at 40 kV and 25 mA. XRD patterns were recorded at a scanning rate of 0.02°s^{-1} with 1–2 s measuring time per step. Lattice parameters were obtained by fitting peak positions to an orthorhombic unit cell using the computer software MAUD [36].

X-ray diffraction measurements of reduced samples of PNO and PNCO were performed with a PANalytical Empyrean X-ray diffractometer (Cu K*α* radiation source operated at 40 kV and 40 mA) to confirm the reduction of PNO and PNCO to Pr_2O_3 and elemental transition metals (compare Section 2.3).

Scanning electron microscopy with energy dispersive X-ray spectroscopy (SEM-EDXS) was performed using a Zeiss EVO50 microscope with an EDX Oxford Instruments Inca detector. High resolution SEM images were recorded in secondary electron (SE) and backscattered electron (BSE) mode at an acceleration voltage of 15 kV.

TEM and STEM images ((Scanning) Transmission Electron Microscopy) were acquired using a Tecnai F20 (operated at 200 kV) and a FEI Titan^3 G2 60–300 (operated at 300 kV). Both microscopes are equipped with a post-column electron energy filter from Gatan Inc. (GIF) and an EDX spectrometer. The Tecnai F20 operates with one Si (Li) detector (EDAX) and the Titan^3 G2 is equipped with 4 high-sensitivity silicon drift detectors in a windowless design (Bruker). The Titan microscope also features a C_s probe corrector for STEM mode, which gives atomic high-resolution STEM images with a spatial resolution below 1 Å.

2.3. Thermal analysis

The thermal expansion properties of PNCO were measured between 30 °C and 1000 °C with heating rates of 1 K min^{-1} in the oxygen partial pressure range of $1 \times 10^{-3} \leq pO_2/\text{bar} \leq 1$ using a single-rod dilatometer DIL 402/PC4 (NETZSCH, Germany). Different atmospheres were realized by O_2-Ar gas mixtures using mass flow controllers (Teledyne HFC-302) at flow rates of 10 l h^{-1}.

Differential scanning calorimetry (DSC) was performed on sintered and finely ground powders of PNCO and PNO using a High Temperature DSC 404C Pegasus (NETZSCH). The samples were

contained in 85 µl Pt-Rh crucibles with typical powder amounts of 33–34 mg. In order to remove irreversible effects (adsorbed water, CO_2 etc.) and to assure thermal and chemical equilibrium, the samples were conditioned in a temperature cycle between room temperature and 600 °C in 20% O_2/Ar before each measurement. DSC analyses were performed between 20 °C and 1000 °C (10 min dwell) in both 20% O_2/Ar and pure Ar (5.0). Fresh powder subjected to the conditioning cycle described above was used for each experiment. Temperature ramps were 20 K min^{-1} and the gas flow rate was 50 ml min^{-1}.

The thermal decomposition of the freeze dried acetate precursor of PNCO was studied by precision thermogravimetry (TG) in a symmetric thermobalance TAG 16 (Setaram, France) coupled with a quadrupole mass spectrometer (Pfeiffer Thermostar). Approximately 7 mg of the precursor powder was placed in a 130 µl platinum crucible and heated from 20 °C to 900 °C at rates of 1 or 5 K min^{-1} in 20% O_2/Ar and pure Ar (5.0). Additional TG and TG-MS measurements were performed with sintered and finely ground PNCO and PNO powders. For these experiments the typical sample mass was ~90 mg. In order to test the thermal stability of PNCO and PNO, the powders were thermally cycled between 20 °C and 900 °C in 20% O_2/Ar with heating and cooling rates of 5 K min^{-1} and isotherms of 2 h at 20 °C and 900 °C. In order to monitor the oxygen release from the sintered and ground PNCO powder, TG-MS analysis was performed during heating from 20 °C to 900 °C at a rate of 5 K min^{-1} in pure Ar (5.0). An oxygen sensor with Ir/IrO_2-reference (Setnag, France) was used to determine the oxygen partial pressure close to the sample.

To determine the absolute values for the oxygen non-stoichiometry for PNO and PNCO, thermogravimetry (STA449C Jupiter, Netzsch, Germany) was carried out with approximately 350 mg of sample in an alumina crucible at gas flow rates of 60 ml min^{-1}. Oxygen partial pressures of 100 ppm for PNO and 1000 ppm for PNCO were adjusted using pre-mixed O_2/Ar test gases. Both samples were heated to 600 °C and equilibrated until no significant mass change was observed. The reduction of the samples was achieved at 900 °C in 8% H_2/N_2.

2.4. Electronic conductivity and oxygen exchange measurements

The chemical surface exchange coefficient of oxygen (k_{chem}) of PNCO and PNO was determined by in-situ dc-conductivity relaxation experiments on thin rectangular slabs contacted in van der Pauw electrode configuration [37]. Samples with dimensions of $7.1 \times 7.5\ mm^2$ with a thickness of 562 µm and $8.0 \times 8.5\ mm^2$ with a thickness of 493 µm were prepared for PNCO and PNO, respectively. Small pO_2-steps between 1.0×10^{-3} and 1.5×10^{-3} bar were used in the relaxation measurements in order to obtain near-equilibrium values for k_{chem}. The measurements were performed in both pO_2-directions (i.e. oxidizing and reducing exchange processes) at a constant total gas flow of 2 l h^{-1}. Further details about the test setup and experimental procedures are described elsewhere [38,39]. Surface exchange coefficients of oxygen were obtained from nonlinear least squares fits of the solution of the diffusion equation to the conductivity relaxation data [40–42]. The model assumes that the oxygen surface exchange reaction obeys first-order kinetics and that k_{chem} is constant during the relaxation process.

3. Results and discussions

3.1. Crystal structure and microstructure

The X-ray diffraction pattern and the crystal structure of PNCO are shown in Fig. 1. All reflections of the K_2NiF_4 type structure could be indexed within the orthorhombic space group *Fmmm*. PNCO is isostructural to the well investigated PNO (see e.g. Chung et al. [43]). Both sets of lattice parameters of the orthorhombic unit cells of PNCO and PNO are given in Table 1. The smaller unit cell volume of PNCO as compared to PNO stems primarily from a large difference in the lattice parameter *c* (direction perpendicular to the perovskite and rock salt layers) (Table 1). Atomic positions and bond lengths of PNCO and PNO obtained from Rietveld refinement are shown in Table 2.

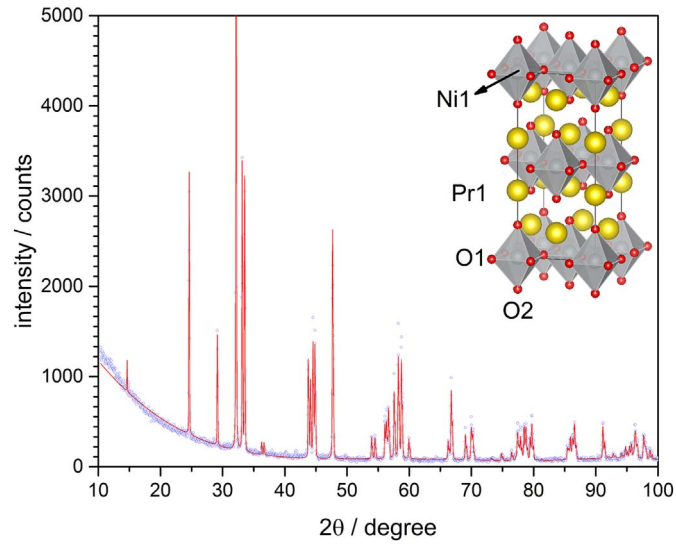

Fig. 1. Room temperature powder diffraction pattern (circles) of PNCO. The inset shows the K_2NiF_4-type crystal structure as obtained by Rietveld refinement (solid line).

Table 1
Lattice parameters and unit cell volume of PNCO and PNO (latter taken from [43]).

Sample	a/Å	b/Å	c/Å	V/Å^3	Literature
PNCO	5.45130(1)	5.38820(1)	12.3815(3)	363.68	This work
PNO	5.45670(9)	5.39292(9)	12.4464(2)	366.27	Chung et al. [43]

Table 2
Atomic positions and bond lengths of the oxygen octahedra in PNCO and PNO [43]. Atomic positions of Co cannot be distinguished from Ni by X-ray diffraction and are therefore neglected in the Rietveld refinement. Isotropic displacement parameters of PNCO were fixed to the values of PNO according to results of Chung et al. [43].

	x	y	z	Ni-O1/Å	Ni-O2/Å	Literature
PNCO						
Pr	0	0	0.3591	1.919	2.138	This work
Ni	0	0	0			
O1	0.2500	0.2500	0			
O2	0	0	0.1726			
PNO						
Pr	0	0	0.3591	1.917	2.103	Chung et al. [43]
Ni	0	0	0			
O1	0.2500	0.2500	0			
O2	0	0	0.169			

SEM images of freshly polished (Fig. 2, Fig. S-2) and thermally etched samples (Fig. S-3) of PNO and PNCO were recorded using secondary electron (SE) and backscattered electron (BSE) microscopy. The freshly polished samples show some scratches and grain pull-outs from the polishing procedure. EDX-analysis for PNO and PNCO confirms the nominal composition of the bulk (Table 3). From the thermally etched samples an average grain size of 1.58 µm for PNO and 1.64 µm for PNCO was determined using the image analysis software ImageJ [44].

3.2. Thermal expansion coefficients, phase stability and oxygen non-stoichiometry

Fig. 3 shows the thermal expansion behaviour of PNCO as a function of temperature and oxygen partial pressure. Results of the thermal expansion coefficient (TEC) are reported in Table 4. The thermal

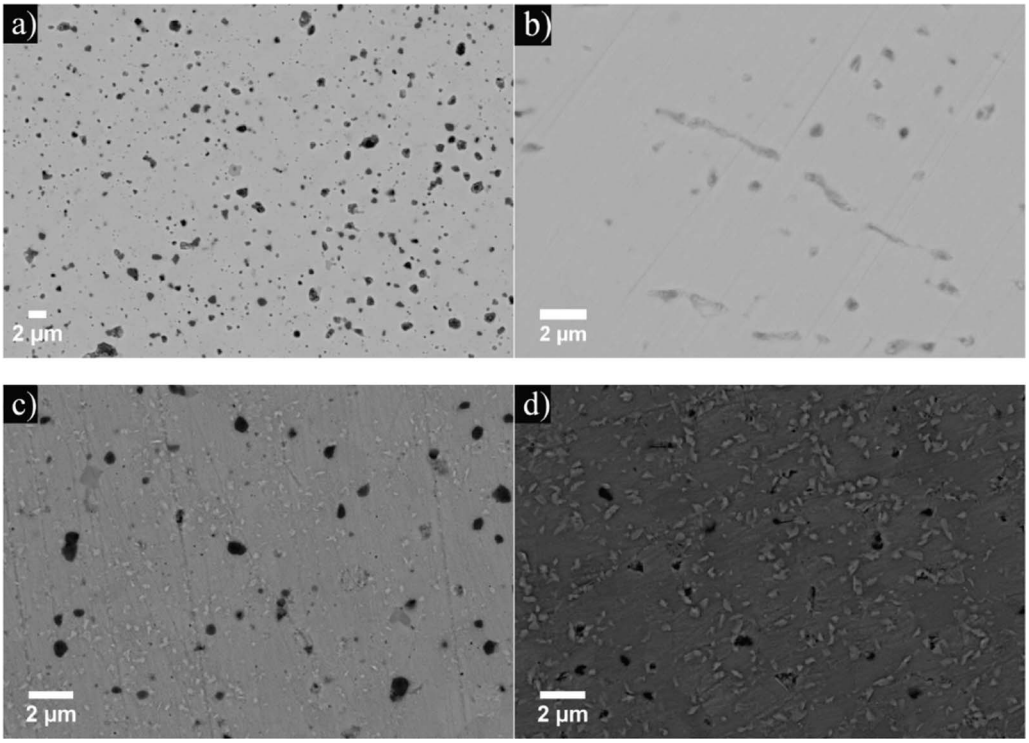

Fig. 2. a) BSE-SEM image of freshly polished PNO, b) BSE-SEM image of freshly polished PNCO, c) BSE-SEM image of PNO after EC/CR measurements and d) BSE-SEM image of PNCO after EC/CR measurements.

expansion curves consist of two regions (region I from 30 °C to 400 °C and region II from 400 °C to 1000 °C) with different slopes. Similarly to PNO, the change in slope is associated with the previously described phase transition from the orthorhombic to the tetragonal structure [45]. At 0.1 bar pO_2, the TEC of PNCO in region II is $16.2 \times 10^{-6}\,K^{-1}$, which is somewhat larger than what has been reported for the Co-free compound PNO ($13.4 \times 10^{-6}\,K^{-1}$) or its homologues $La_2NiO_{4+\delta}$ ($13.0 \times 10^{-6}\,K^{-1}$) and $Nd_2NiO_{4+\delta}$ ($12.4 \times 10^{-6}\,K^{-1}$) [46] in air. However, the TEC of PNCO is still smaller than that of $La_{0.6}Sr_{0.4}CoO_{3-\delta}$ ($18.9 \times 10^{-6}\,K^{-1}$ [47]) and similar to the well-known SOFC cathode material $La_{0.6}Sr_{0.4}Co_{0.8}Fe_{0.2}O_{3-\delta}$ ($16.0 \times 10^{-6}\,K^{-1}$) [48].

PNCO and PNO were investigated by differential scanning calorimetry (DSC) up to 1000 °C in a test gas of 20% O_2/Ar and in pure Ar (Fig. 4). In 20% O_2 the transition from the orthorhombic to the tetragonal structure modification occurs as an endothermal process at 448 °C for PNO and at 485 °C for PNCO during heating (Fig. 4a). This transition was previously described for PNO in the literature [45]. The transition is fully reversible and thus an exothermal transition from the tetragonal to the orthorhombic structure modification occurs upon cooling at 439 °C for PNO and at 474 °C for PNCO. Thus, partial replacement of Ni with Co in PNCO has shifted the structural transition to higher temperatures by approximately 35–40 °C. The transition is also visible in the TG-curves of both compounds as a mass loss upon heating and a mass gain upon cooling (Fig. 5) with the transition of PNCO occurring at higher temperatures than for PNO. The transition is further

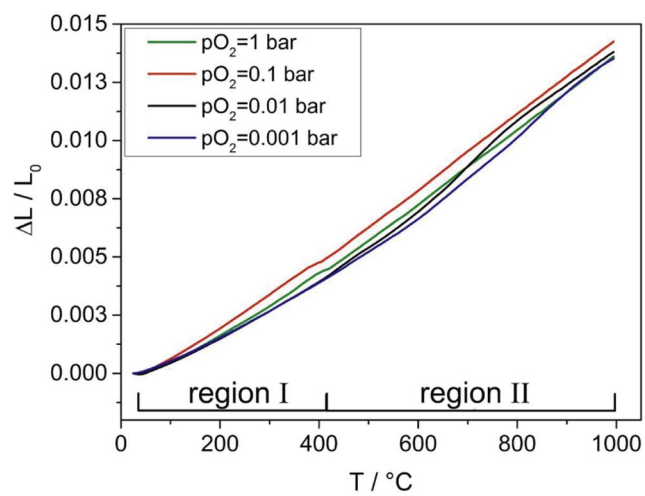

Fig. 3. Thermal expansion curves of PNCO in different atmospheres. Regions 1 and 2 correspond to the orthorhombic and tetragonal structure modification, respectively.

observed as a change in slope in the thermal expansion measurements (see Fig. 3).

In pure Ar the transition from the orthorhombic to the tetragonal structure modification occurs as an endothermal process at 399 °C for PNO and at 442 °C for PNCO upon heating (Fig. 4b). Again, the effect is shifted to higher temperatures for the Co-containing compound. The

Table 3
Nominal and experimental values on cation ratios measured by EDX for PNO and PNCO in the as-received or as-prepared state, in comparison to analyses of both samples after EC/CR experiments.

Element	PNO nominal	PNCO nominal	PNO (as received)	PNCO (as prepared)	PNO after measurements	PNCO after measurements
	at.%	at.%	at.%	at.%	at.%	at.%
Pr L	66.67	66.67	64.13	65.90	64.42	66.34
Ni K	33.33	30.00	35.87	30.57	35.58	30.42
Co K	–	3.33	–	3.53	–	3.24

Table 4
Thermal expansion coefficients of PNCO for the temperature ranges 30–400 °C (I) and 400–1000 °C (II) at different oxygen partial pressures.

pO_2/bar	PNCO	
	α(I)/10^{-6} K^{-1}	α(II)/10^{-6} K^{-1}
1	12.23	15.89
0.1	13.75	16.19
0.01	11.19	16.06
0.001	10.82	16.87

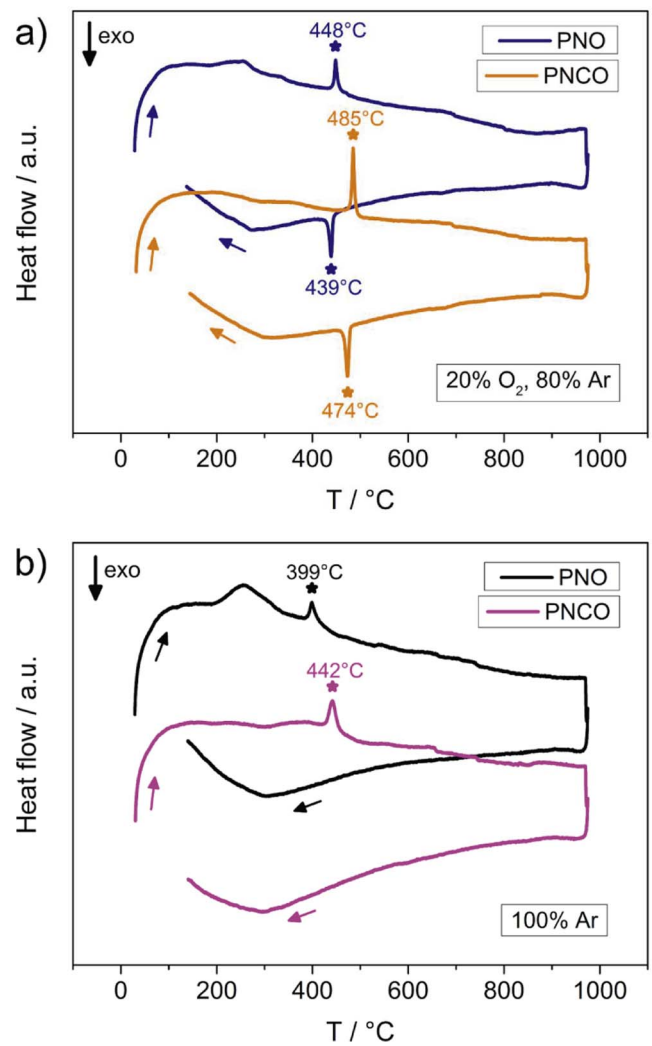

Fig. 4. Differential scanning calorimetry of PNCO and PNO in different atmospheres in (a) 20% O_2 and (b) in pure Ar (heating and cooling rates 20 K min^{-1}, 10 min isotherm at 975 °C).

transition is irreversible in pure Ar since it is coupled to oxygen loss (heating) and oxygen uptake (cooling), with the latter process being suppressed in pure Ar.

In order to develop an efficient calcination procedure for the acetate precursor of PNCO as obtained by freeze drying, precision thermogravimetry coupled with mass spectroscopy (TG-MS) was performed. The temperature dependence of the mass loss of the acetate precursor and its first derivative are shown in Fig. S-4a and Fig. S-4b, respectively, for 20% oxygen and pure Ar. Mass spectroscopy in pure Ar was performed to gain information on the decomposition products during the continuous mass loss of the precursor (Fig. S-5 and Fig. S-6). The first mass loss between 100 °C and 150 °C is due to the loss of H_2O from the

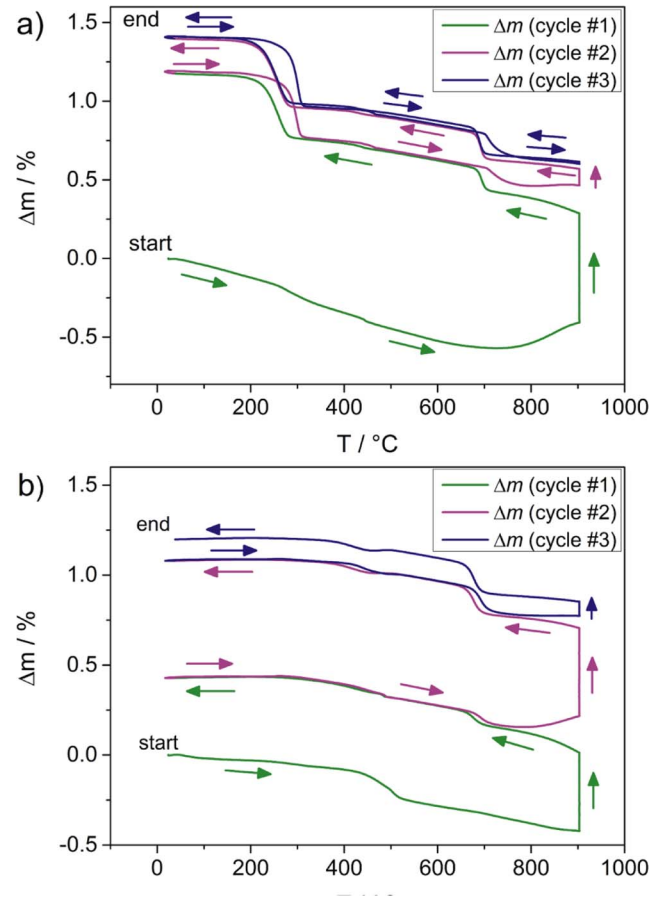

Fig. 5. Mass changes obtained by precision thermogravimetry during thermal cycles between 20 °C and 900 °C in 20% O_2 for (a) PNO and (b) PNCO. Heating and cooling rates were 5 K min^{-1}, the dwell time at 900 °C was 2 h in each case.

acetate precursor, followed by the consumption of O_2 at 300 °C to 350 °C. In this temperature region, the main decomposition products of the acetates consist mainly of formic acid (250–350 °C), ketene (200–400 °C), ethanol (250–350 °C) and acetone (200–450 °C). At temperatures above 450 °C the main desorbed species are CO (350–450 °C and 500–600 °C) and CO_2 (350–450 °C and 500–700 °C). Similar results were observed for the thermal decomposition of the pure acetates $Pr(CH_3COO)_3{\cdot}H_2O$, $Ni(CH_3COO)_2{\cdot}4H_2O$ and $Co(CH_3COO)_2{\cdot}4H_2O$ [49–54]. Based on results from TG in 20% O_2, a calcination temperature of 600 °C in air was chosen in order to attain a complete decomposition of the acetate precursors (Fig. S-4).

Fig. 5 shows the mass change as a function of temperature for PNO (Fig. 5a) and PNCO (Fig. 5b). A minor mass loss occurred in the heating cycle at approximately 400 °C for PNO and 450 °C for PNCO in 20% O_2. This is caused by the previously described orthorhombic-to-tetragonal phase transition [45]. These results are in good agreement with the thermal expansion curves (Fig. 3). The main process, however, starts around 750 °C for both compounds and manifests itself as significant mass gain caused by an irreversible uptake of oxygen, as previously reported for PNO [55]. This is due to the decomposition of the nickelate compound to a higher order RP-phase (n = 3) and Pr-oxides [55–57] as observed for PNO according to Eq. (1).

$$3\ Pr_2(NiCo)O_{4+\delta_1} + x\ O_2 \rightarrow Pr_4(NiCo)_3O_{10-\delta_2} + \frac{1}{3}\ Pr\ O_{\delta_3} \quad (1)$$

Mass change combined with the corresponding *m/z* signals from mass spectroscopy was recorded for PNCO in pure Ar (Fig. S-7). Due to the low amount of oxygen in the gas phase, the mass increase caused by the decomposition reaction (Eq. (1)) is not observed. A detailed

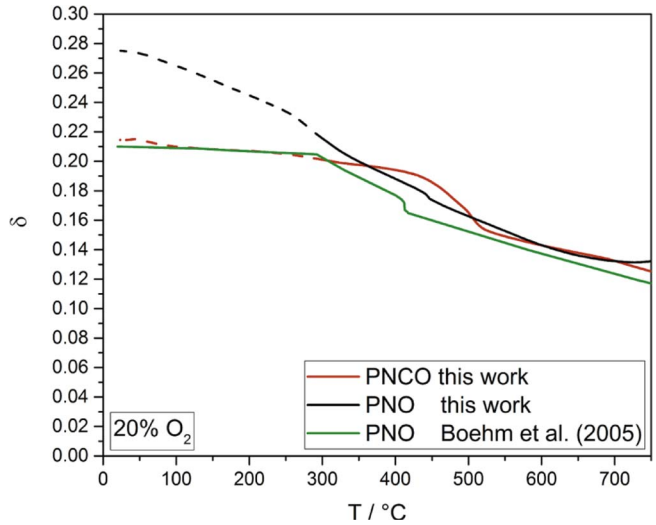

Fig. 6. Oxygen excess δ of PNO and PNCO in 20% O_2 as a function of temperature. Literature data for PNO were taken from Boehm et al. [14]. δ-values below ~300 °C (dashed lines) do not necessarily correspond to equilibrium states due to slow oxygen exchange kinetics.

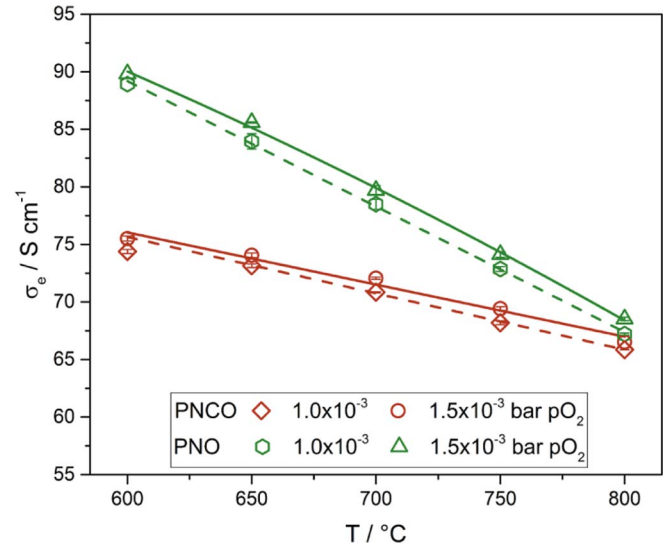

Fig. 7. Electronic conductivity of PNCO and PNO as a function of temperature at different oxygen partial pressures. Error bars show 2σ standard deviations between multiple measurements. Lines are guides for the eye; solid lines correspond to 1.5×10^{-3} bar pO_2 and dashed lines to 1.0×10^{-3} bar pO_2.

breakdown of the mass loss and selected mass spectroscopy (m/z) is plotted in Fig. S-8 as a function of temperature. The main contribution to the overlapping mass loss signals is due to the loss of CO_2 at 250–300 °C and the loss of O_2 in three steps between 300 °C and 600 °C and above 800 °C. Fig. S-9 indicates the mass loss and dTG (1st derivative of mass curve) of sintered and crushed PNCO as a function of temperature in Ar. No mass gain occurs upon cooling due to the absence of O_2 in the carrier gas.

Fig. 6 shows data on the oxygen non-stoichiometry δ as a function of temperature. Absolute values for δ were obtained by equilibrating approximately 350 mg of each sample at 600 °C (heating rate 1 K min^{-1}) in 0.1% O_2 for PNCO and 0.01% O_2 for PNO in a thermogravimetric setup. After the samples were fully equilibrated (no further significant mass loss occurred) the gas atmosphere was changed to reducing conditions (8% H_2, rest N_2) by simultaneous heating to 900 °C (heating rate 5 K min^{-1}). The absolute value for δ was calculated from the mass change of the reduction reaction (Eq. (2)).

$$Pr_2Ni_{0.9}Co_{0.1}O_{4+\delta} \rightarrow Pr_2O_3 + 0.9\,Ni + 0.1\,Co + \frac{1+\delta}{2}O_2 \quad (2)$$

Completion of the reduction reaction was confirmed by XRD. Relative changes of the oxygen non-stoichiometry calculated from the mass change of the first heating cycle of PNO and PNCO (Fig. 5) are shifted on the y-axis according to the absolute reference value determined by total reduction at 600 °C to obtain δ as a function of temperature (Fig. 6). Both materials show similar values for δ above 500–550 °C. The structural phase transition from the orthorhombic to a tetragonal modification [45] shifts by approximately 50 °C to higher temperatures for PNCO. At 20% O_2 PNO starts to decompose above 700 °C, while PNCO remains stable until approximately 750 °C (Fig. 5 and Fig. 6). Values for δ of PNO at higher temperatures (500–750 °C) are close to previously reported data of Boehm et al. [14], whereas values below 300 °C show significant deviations most likely caused by non-equilibrium oxygen stoichiometry of PNO before the start of the measurement (dashed line in Fig. 6).

Due to the structural instability of PNO and PNCO above 700 °C in air, investigations of the electronic conductivity and the surface exchange kinetics were performed at reduced pO_2 where the decomposition reaction (Eq. (1)) is suppressed [58] since it is accompanied by an uptake of oxygen.

3.3. Electronic conductivity and chemical surface exchange coefficient

In Fig. 7 the electronic conductivities of PNO and PNCO are shown as a function of temperature at 1.0×10^{-3} bar and 1.5×10^{-3} bar oxygen partial pressure. At each temperature, electronic conductivities at 1.5×10^{-3} bar pO_2 are consistently higher than those at 1.0×10^{-3} bar pO_2, which indicates p-type electronic conduction in both compounds [33]. At 600 °C and 1.0×10^{-3} bar pO_2 the electronic conductivity of PNCO is 76 S cm^{-1}, which is somewhat higher than a previously reported value for PNCO of approximately 60 S cm^{-1} [34] and lower than that of PNO obtained in this work (90 S cm^{-1}). Raising the temperature to 800 °C leads to a decrease in conductivity of both compounds, albeit to a varying extent, so that at 800 °C the conductivity of PNCO and PNO is almost the same. Thus, partial substitution of Co on the B-site does not improve the electronic conductivity, contrary to what is usually observed for perovskite materials like $La_{1-x}Sr_xCo_{1-y}Fe_yO_{3-\delta}$ [59]. This trend has also been reported previously for various RP-type nickelates [12,30,34].

The chemical surface exchange coefficients k_{chem} of oxygen for PNCO and PNO between 600 °C and 800 °C at 1.0×10^{-3} bar oxygen partial pressure are presented in Fig. 8. Within the investigated ranges of temperature and pO_2, the oxygen exchange of both materials was limited by the surface exchange reaction which made it impossible to determine values for the chemical diffusion coefficient D_{chem} of oxygen. The effect of Co-doping on the surface exchange rate of oxygen is clearly evident at 600 °C, where k_{chem} of PNCO is roughly one order of magnitude larger than that of PNO under the same conditions. Small hysteresis effects between heating and cooling run are observed for both compounds, which might be caused to a minor extent by the decomposition of the base materials during the measurement (see following section). Activation energies (E_a) of k_{chem} differ significantly between PNCO and PNO, with E_a of PNCO (94 kJ mol^{-1}) being almost half the value found for PNO (178 kJ mol^{-1}) during the heating run. Consequently, the difference in oxygen surface exchange rates of both nickelates becomes increasingly smaller at higher temperatures and at 800 °C both compounds show a similar value of k_{chem} around 1×10^{-4} cm s^{-1}.

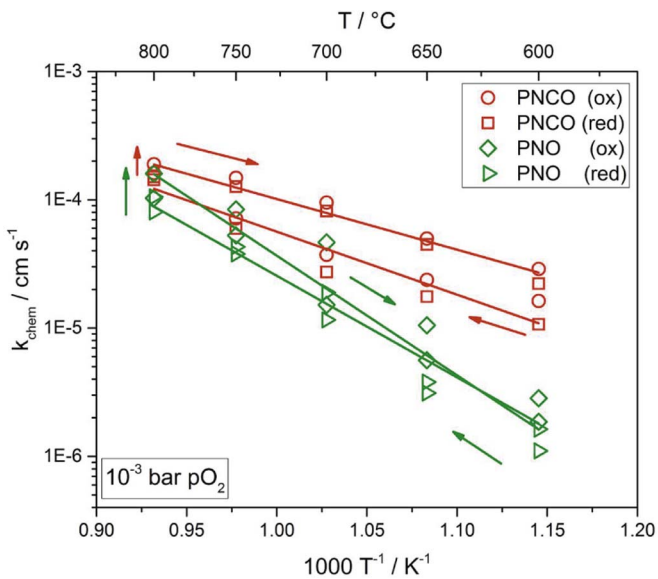

Fig. 8. Arrhenius plot of the chemical surface exchange coefficients (k_{chem}) of PNCO and PNO at $pO_2 = 10^{-3}$ bar. Reversibility was checked by performing measurements in a heating run from 600 °C to 800 °C ($E_a = 94 \pm 8$ kJ mol^{-1} for PNCO and $E_a = 178 \pm 15$ kJ mol^{-1} for PNO), followed by a cooling run back to 600 °C ($E_a = 76 \pm 5$ kJ mol^{-1} for PNCO and $E_a = 152 \pm 8$ kJ mol^{-1} for PNO), as indicated by arrows.

3.4. Post-test analyses by X-ray diffraction, scanning electron microscopy and scanning transmission electron microscopy

After the EC and CR-measurements, XRD patterns of the samples were recorded and compared with the as-prepared state (see Fig. S-10). The fresh sample of PNCO showed a small amount of secondary phase (below 1 wt% Pr_6O_{11}), whereas no secondary phases were found in the sample after the CR measurements. Gold peaks (Au) stem from traces of gold paste used for electrical contacts. Fig. S-11 compares XRD patterns of PNO before and after the measurements. The fresh sample shows small amounts of secondary phases (Pr_6O_{11} and NiO), however, no secondary phases are visible after the electrochemical measurements. Again, gold peaks (Au) are from electrical contacts.

Fig. 2 shows BSE images of freshly polished PNO (Fig. 2a) and PNCO (Fig. 2b), as well as post-test images of PNO (Fig. 2c) and PNCO (Fig. 2d) recorded after EC/CR measurements. The BSE image of PNO (Fig. 2a) shows black and dark grey patches as well as many finely dispersed light-grey spots. According to EDX analysis the dark grey patches correspond to Si-impurities, while the black spots were identified as NiO (Fig. S-2). The BSE image of PNCO (Fig. 2b) shows the freshly polished surface with grain pull-outs caused by the polishing process. In contrast to the PNO sample, no impurities where observed. The surface of the degraded PNO (Fig. 2c) and PNCO (Fig. 2d) samples show small crystallites in addition to the previously described features. Since the light-grey crystallites proved to be too small for a reliable EDX-analysis in the SEM, TEM lamellae of the crystallite covered surfaces were prepared by the focused ion beam (FIB) technique and analysed with STEM.

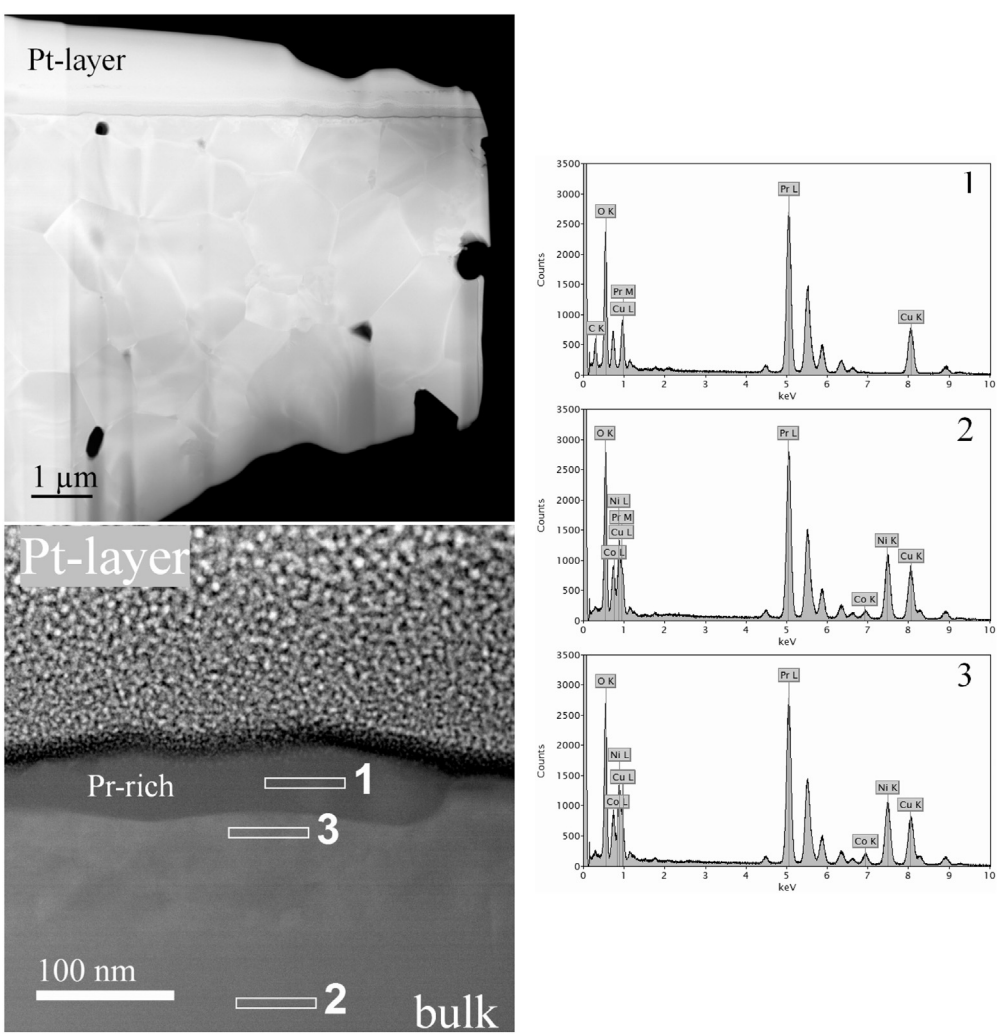

Fig. 9. Cross sectional STEM-HAADF image of PNCO with EDX spectra recorded at different positions. Spectrum 1 was recorded on the darker spot on the surface of the lamella, indicating the formation of Pr_6O_{11} (EDX gives a Pr:O ratio of 35.7:64.3 at.%), spectrum 2 shows the bulk of the specimen (Pr:Ni:Co:O ratio equals 27:14:2:57 at.%) and spectrum 3 indicates a slightly Co-enriched area next to the Pr-rich spot. Cu-peaks in the EDX spectra originate from the sample holder, the Pt-layer was deposited as a protective coating for FIB sample preparation.

Scanning transmission electron microscopy with high angle annular dark field (STEM-HAADF) images and spectra from EDX and Electron Energy Loss Spectroscopy (EELS) were recorded for PNCO (Fig. 9 and Fig. S-12) and PNO (Fig. S-13). EDX confirms the nominal composition of PNCO in the sub-surface region of the measured sample with a slightly higher Co-content close to the surface crystallites. The crystallites themselves are Ni-free and contain Pr and O in a ratio of 6:10.8, suggesting the exsolution of Pr-oxides from the nickelate matrix at high temperatures and transformation to the low temperature equilibrium phase Pr_6O_{11} upon cooling to room temperature in air [60]. Interestingly, the exsolution of Pr_6O_{11} appears to be limited to the topmost surface layer as no secondary phases of Pr_6O_{11} can be found in the subsurface region of the lamella. Similar results are obtained for PNO (Fig. S-13), showing the presence of Pr_6O_{11} crystallites on the surface of the tested sample. In addition, the bulk region contains NiO inclusions (Fig. S-14) which were already present in the freshly sintered sample, as determined by SEM-EDX analysis.

The results from SEM and TEM analyses suggest that the differences in k_{chem} between the heating and cooling run most likely originate from the formation of Pr_6O_{11} on the surface, which is known to increase oxygen reduction rates [22,26,61,62]. It is assumed that the exsolution of Pr-oxide particles is occurring gradually in the course of the EC/CR measurements. This can also be appreciated directly from a comparison of the normalised relaxation curves of PNO and PNCO at each temperature recorded during the heating and cooling runs (Fig. S-15).

4. Conclusions

The novel K_2NiF_4-type oxide $Pr_2Ni_{0.9}Co_{0.1}O_{4+\delta}$ (PNCO) was synthesized from metal acetate solutions by applying a shock freezing and freeze drying technique as an efficient synthesis route for ceramic materials. The thermal decomposition of the acetate precursor was investigated by precision thermogravimetry in both 20% O_2 and pure Ar combined with mass spectroscopy. X-ray diffraction with Rietveld analysis of a sintered sample of PNCO gave information on phase purity, lattice constants and atomic positions. Several characterization methods such as dilatometry, differential scanning calorimetry, precision thermogravimetry, electrical conductivity and conductivity relaxation measurements were performed at various temperatures and oxygen partial pressures for both compounds.

PNCO features a somewhat lower electronic conductivity compared to PNO, but shows faster oxygen exchange kinetics in the temperature range of 600 °C to 800 °C at 10^{-3} bar pO_2. At 800 °C PNCO and PNO show similar values for the surface exchange coefficient of oxygen (k_{chem}), but due to significant differences in activation energies, k_{chem} of PNCO is approximately one order of magnitude higher than for the Co-free compound at 600 °C. Based on the results presented in this work, PNCO seems to be a promising SOFC cathode material at lower operating temperatures around 600 °C. For higher temperatures, the applicability of the materials is compromised by a transformation to the 3rd-order Ruddlesden-Popper phase $Pr_4(Ni,Co)_3O_{10-\delta}$ and Pr-oxide. It is interesting to note, however, that at least in the early stages of decomposition the exsolution of catalytically active Pr-oxide particles appears to be confined to the immediate surface, which leads to an improvement of the oxygen surface exchange kinetics.

Acknowledgements

This research was supported by the Austrian Research Promotion Agency FFG (project no. 853538). Financial support by the "Klima- und Energiefonds" (KR15EF0F12735) within the program "Energieforschung (e!MISSION)" is gratefully acknowledged. Furthermore, the authors would like to thank Gerhard Hawranek for SEM analysis and Karin Stanglauer for EDX analysis (both Montanuniversitaet Leoben), Sebastian Rauch for FIB preparation (Graz Centre for Electron Microscopy), Rotraut Merkle for determination of the absolute non-stoichiometry of PNO and PNCO, Helga Hoier for XRD analysis of reduced PNO and PNCO (both Max Planck Institute for Solid State Research) and Samir Hammoud (Max Planck Institute for Intelligent Systems) for ICP-OES measurement of PNCO.

Appendix A. Supplementary data

Supplementary data to this article can be found online at https://doi.org/10.1016/j.ssi.2017.12.024.

References

[1] J.G. Bednorz, K.A. Müller, Rev. Mod. Phys. 60 (3) (1988) 585.
[2] D. Pavuna, G. Dubuis, A.T. Bollinger, J. Wu, X. He, I. Bozovic, J. Supercond. Nov. Magn. 30 (3) (2017) 731.
[3] P. Orgiani, A. Galdi, C. Sacco, R. Arpaia, S. Charpentier, F. Lombardi, C. Barone, S. Pagano, D.G. Schlom, L. Maritato, J. Supercond. Nov. Magn. 28 (12) (2015) 3481.
[4] S.N. Ruddlesden, P. Popper, Acta Crystallogr. 10 (8) (1957) 538.
[5] S.N. Ruddlesden, P. Popper, Acta Crystallogr. 11 (1958) 54.
[6] P.V. Balachandran, D. Puggioni, J.M. Rondinelli, Inorg. Chem. 53 (1) (2014) 336.
[7] R.E. Schaak, T.E. Mallouk, Chem. Mater. 14 (4) (2002) 1455.
[8] A. Murata, C. Hai, M. Matsuda, Mater. Lett. 136 (2014) 292.
[9] T. Nakamura, K. Yashiro, K. Sato, J. Mizusaki, Mater. Chem. Phys. 122 (1) (2010) 250.
[10] T. Nakamura, K. Yashiro, K. Sato, J. Mizusaki, Solid State Ionics 181 (8) (2010) 402.
[11] M. Greenblatt, Curr. Opin. Solid State Mater. Sci. 2 (2) (1997) 174.
[12] V.V. Kharton, A.A. Yaremchenko, A.L. Shaula, M.V. Patrakeev, E.N. Naumovich, D.I. Logvinovich, J.R. Frade, F.M.B. Marques, J. Solid State Chem. 177 (1) (2004) 26.
[13] M.S.D. Read, M.S. Islam, G.W. Watson, F.E. Hancock, J. Mater. Chem. 11 (2001) 2597.
[14] E. Boehm, J.M. Bassat, P. Dordor, F. Mauvy, J.C. Grenier, P. Stevens, Solid State Ionics 176 (37–38) (2005) 2717.
[15] A. Egger, E. Bucher, W. Sitte, C. Lalanne, J.M. Bassat, Oxygen exchange kinetics and chemical stability of the IT-SOFC cathode material $Nd_2NiO_{4+\delta}$, in: S.C. Singhal (Ed.), 11th Intern. Symp. Solid Oxide Fuel Cells (SOFC-XI), The Electrochemical Society, Vienna, Austria, 2009, pp. 2547–2556.
[16] B. Singh, S. Ghosh, S. Aich, B. Roy, J. Power Sources 339 (2017) 103.
[17] K. Kendall, A. Meadowcroft, Int. J. Hydrog. Energy 38 (3) (2013) 1725.
[18] W. Bujalski, C.A. Dikwal, K. Kendall, J. Power Sources 171 (1) (2007) 96.
[19] W. Lee, J.W. Han, Y. Chen, Z. Cai, B. Yildiz, J. Am. Chem. Soc. 135 (21) (2013) 7909.
[20] E. Bucher, A. Egger, G.B. Caraman, W. Sitte, J. Electrochem. Soc. 155 (11) (2008) B1218.
[21] X. Tong, F. Zhou, S.B. Yang, S.H. Zhong, M.R. Wei, Y.H. Liu, Ceram. Int. 43 (14) (2017) 10927.
[22] A.L. Shaula, E.N. Naumovich, A.P. Viskup, V.V. Pankov, A.V. Kovalevsky, V.V. Kharton, Solid State Ionics 180 (11 − 13) (2009) 812.
[23] S.Y. Jeon, M.B. Choi, H.N. Im, J.H. Hwang, S.J. Song, J. Phys. Chem. Solids 73 (5) (2012) 656.
[24] A. Demourgues, A. Wattiaux, J.C. Grenier, M. Pouchard, J.L. Soubeyroux, J.M. Dance, P. Hagenmuller, J. Solid State Chem. 105 (2) (1993) 458.
[25] J.D. Jorgensen, B. Dabrowski, S. Pei, D.R. Richards, D.G. Hinks, Phys. Rev. B 40 (4) (1989) 2187.
[26] V.V. Kharton, E.V. Tsipis, A.A. Yaremchenko, J.R. Frade, Solid State Ionics 166 (3–4) (2004) 327.
[27] F. Mauvy, J.M. Bassat, E. Boehm, P. Dordor, J.C. Grenier, J.P. Loup, J. Eur. Ceram. Soc. 24 (6) (2004) 1265.
[28] T. Ishihara, K. Tominaga, J. Hyodo, M. Matsuka, Int. J. Hydrog. Energy 37 (9) (2012) 8066.
[29] C.N. Munnings, S.J. Skinner, G. Amow, P.S. Whitfield, I.J. Davidson, Solid State Ionics 176 (23–24) (2005) 1895.
[30] G. Amow, J. Au, I. Davidson, Solid State Ionics 177 (19) (2006) 1837.
[31] J.A. Kilner, C.K.M. Shaw, Solid State Ionics 154 (2002) 523.
[32] S. Li, H. Tu, F. Li, M.T. Anwar, L. Yu, J. Alloys Compd. 694 (2017) 17.
[33] A.A. Yaremchenko, V.V. Kharton, M.V. Patrakeev, J.R. Frade, J. Mater. Chem. 13 (5) (2003) 1136.
[34] T. Nomura, S. Nishimoto, Y. Kameshima, M. Miyake, J. Ceram. Soc. Jpn. 120 (1407) (2012) 534.
[35] Merck, Komplexometrische Bestimmungsmethoden mit Titriplex®.
[36] L. Lutterotti, Nucl. Inst. Methods Phys. Res. B 334 (268) (2010).
[37] W. Preis, M. Holzinger, W. Sitte, Monatsh. Chem. 132 (2001) 499.
[38] C. Berger, E. Bucher, C. Gspan, A. Menzel, W. Sitte, J. Electrochem. Soc. 164 (10) (2017) F3008.
[39] C. Berger, E. Bucher, W. Sitte, Solid State Ionics 299 (2017) 46.
[40] M.W. den Otter, H.J.M. Bouwmeester, B.A. Boukamp, H. Verweij, J. Electrochem. Soc. 148 (2) (2001) J1.
[41] W. Preis, E. Bucher, W. Sitte, J. Power Sources 106 (2002) 116.
[42] W. Preis, E. Bucher, W. Sitte, Solid State Ionics 175 (2004) 393.
[43] Y.K. Chung, Y.-U. Kwon, S.H. Byeon, Bull. Kor. Chem. Soc. 16 (2) (1995) 120.
[44] C.A. Schneider, W.S. Rasband, K.W. Eliceiri, Nat. Methods 9 (7) (2012) 671.
[45] E. Niwa, K. Wakai, T. Hori, K. Yashiro, J. Mizusaki, T. Hashimoto, Thermochim.

Acta 575 (2014) 129.
[46] A. Flura, S. Dru, C. Nicollet, V. Vibhu, S. Fourcade, E. Lebraud, A. Rougier, J.-M. Bassat, J.-C. Grenier, J. Solid State Chem. 228 (0) (2015) 189.
[47] V.V. Kharton, A.A. Yaremchenko, E.N. Naumovich, J. Solid State Electrochem. 3 (1999) 303.
[48] M. Kuhn, S. Hashimoto, K. Sato, K. Yashiro, J. Mizusaki, Solid State Ionics 241 (2013) 12.
[49] B.M. Abu-Zied, S.A. Soliman, Thermochim. Acta 470 (1–2) (2008) 91.
[50] B.A.A. Balboul, J. Anal. Appl. Pyrolysis 88 (2) (2010) 192.
[51] J.C. De Jesus, I. González, A. Quevedo, T. Puerta, J. Mol. Catal. A Chem. 228 (1–2) (2005) 283.
[52] M.A. Mohamed, S.A. Halawy, M.M. Ebrahim, J. Anal. Appl. Pyrolysis 27 (2) (1993) 109.
[53] J. Hong, G. Guo, K. Zhang, J. Anal. Appl. Pyrolysis 77 (2) (2006) 111.
[54] T. Wanjun, C. Donghua, Chem. Pap. 61 (4) (2007) 329.
[55] A.V. Kovalevsky, V.V. Kharton, A.A. Yaremchenko, Y.V. Pivak, E.V. Tsipis, S.O. Yakovlev, A.A. Markov, E.N. Naumovich, J.R. Frade, J. Electroceram. 18 (3) (2007) 205.
[56] T. Broux, C. Prestipino, M. Bahout, S. Paofai, E. Elkaim, V. Vibhu, J.-C. Grenier, A. Rougier, J.-M. Bassat, O. Hernandez, Dalton Trans. 45 (7) (2016) 3024.
[57] L. Fan, M. Chen, H. Zhang, C. Wang, C. He, Int. J. Hydrog. Energy 42 (27) (2017) 17544.
[58] J.D. Sullivan, D.J. Buttrey, D.E. Cox, J. Hriljac, J. Solid State Chem. 94 (2) (1991) 337.
[59] E.V. Tsipis, V.V. Kharton, J. Solid State Electrochem. 12 (2008) 1367.
[60] B.G. Hyde, D.J.M. Bevan, L. Eyring, Philos. Trans. R. Soc. London, Ser. A 259 (1106) (1966) 583.
[61] C. Nicollet, A. Flura, V. Vibhu, A. Rougier, J.-M. Bassat, J.-C. Grenier, Int. J. Hydrog. Energy 41 (34) (2016) 15538.
[62] R. Chiba, H. Aono, K. Kato, ECS Trans. 57 (1) (2013) 1831.

Supplementary Material

Synthesis and characterization of the novel K_2NiF_4-type oxide $Pr_2Ni_{0.9}Co_{0.1}O_{4+\delta}$

Christian Berger[a], Edith Bucher[a*], Andreas Egger[a], Anna Theresa Strasser[a],

Nina Schrödl[a], Christian Gspan[b], Johannes Hofer[a], Werner Sitte[a]

[a] *Chair of Physical Chemistry, Montanuniversitaet Leoben, Franz-Josef-Straße 18,*

8700 Leoben, Austria

[b] *Institute of Electron Microscopy and Nanoanalysis (FELMI), Graz University of Technology &*

Graz Centre for Electron Microscopy (ZFE),

Austrian Cooperative Research (ACR) Steyrergasse 17, A-8010 Graz, Austria

Contents

1. Particle size distribution 3

2. Scanning electron microscopy 4

3. Precision thermogravimetry 6

4. Post-test analysis by X-ray diffraction and transmission electron microscopy 12

5. Conductivity relaxation curves 17

6. References 18

1. Particle size distribution

The particle size distribution (PSD) of the calcined $Pr_2Ni_{0.9}Co_{0.1}O_{4+\delta}$ (PNCO) powder showed a broad monomodal distribution with an average particle size of 56 µm (d_{50}). 35 g of the calcined powder and 210 g absolute ethanol were milled with 280 g of zirconia grinding balls in a polyethylene bottle on a benchtop roller system for 75 h as previously described [1]. After this procedure, the average particle size was 0.60 µm. Figure S-1 shows the PSD before and after milling.

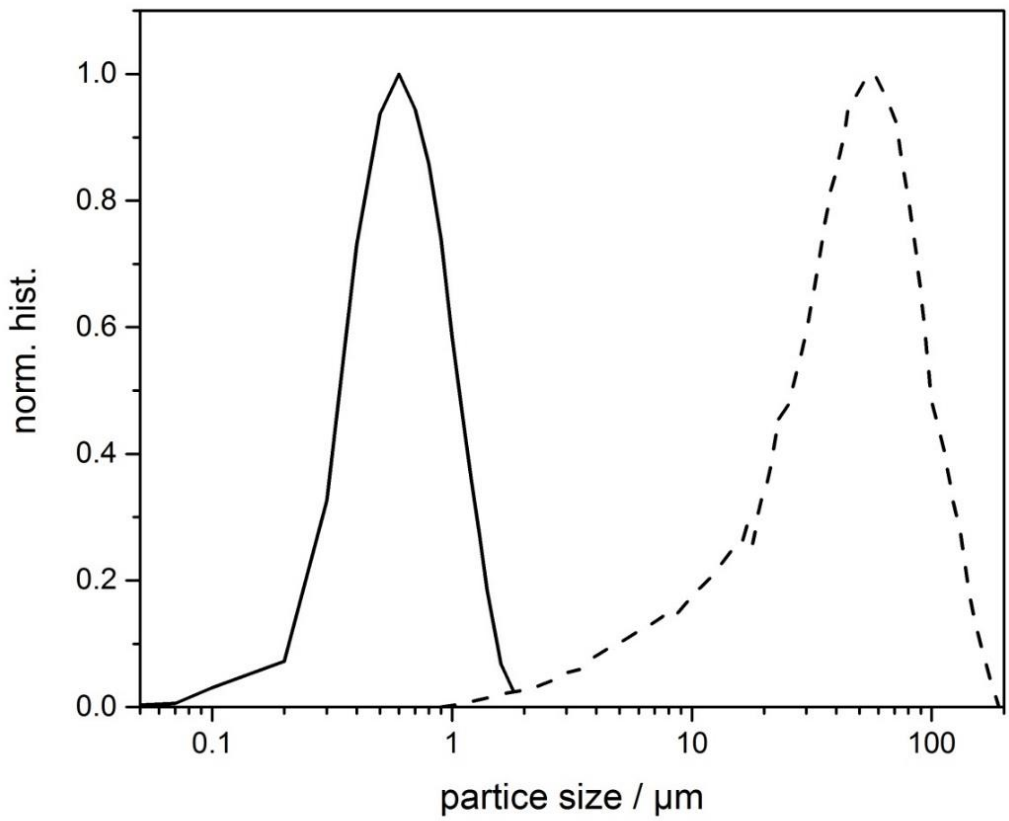

Fig. S-1. Particle size distribution of the calcined PNCO powder (dashed line) and after 75 h of milling (solid line).

2. Scanning electron microscopy

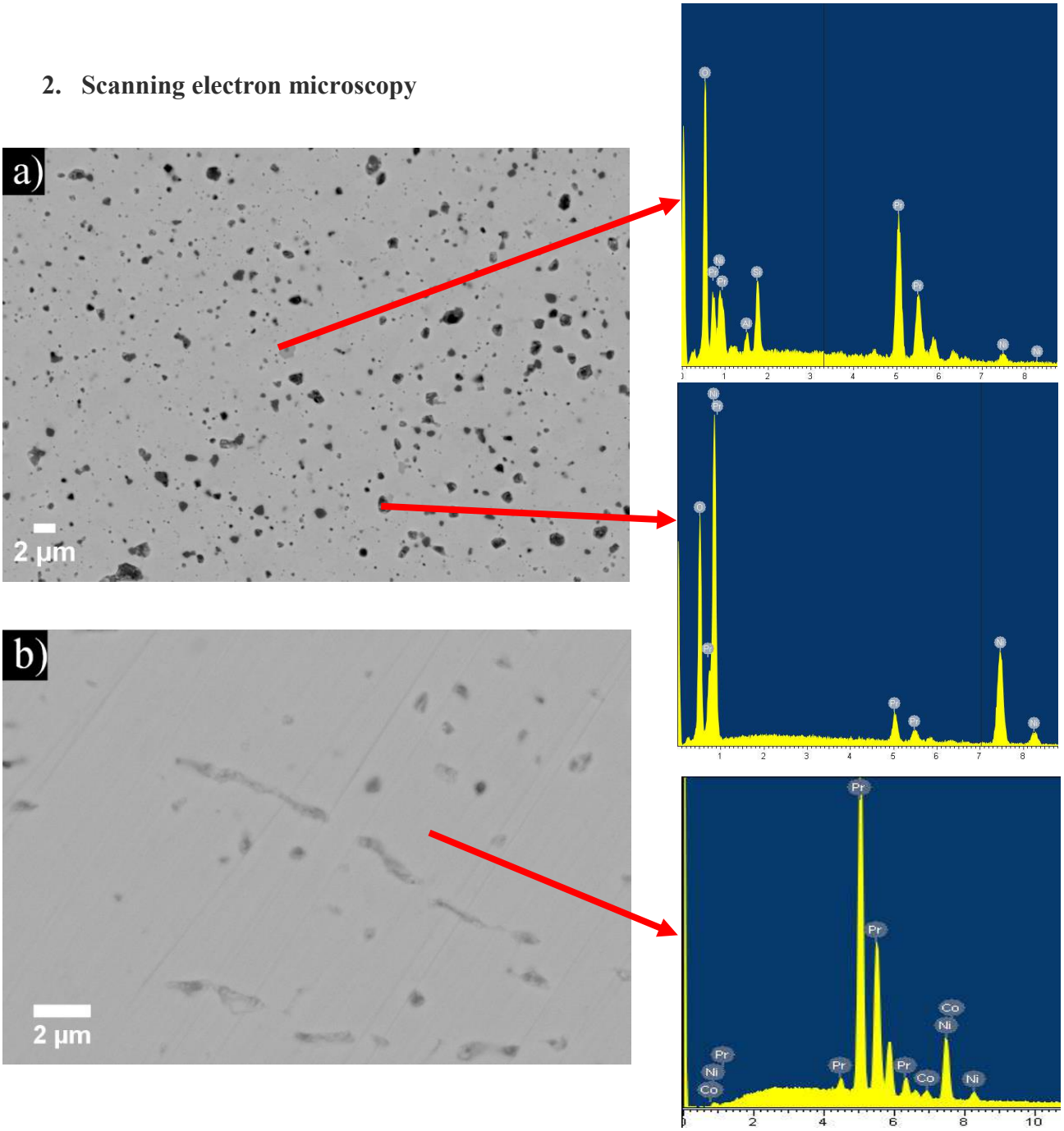

Fig. S-2. SEM-EDX images in backscattered electron mode of (a) the surface of freshly polished PNO and (b) the surface of freshly polished PNCO. Pores result mainly from grain pull-out during the polishing process. Grey spots in (a) mark a Si-containing impurity, dark patches are caused by a NiO secondary phase. Energies in the EDX spectra are given in keV.

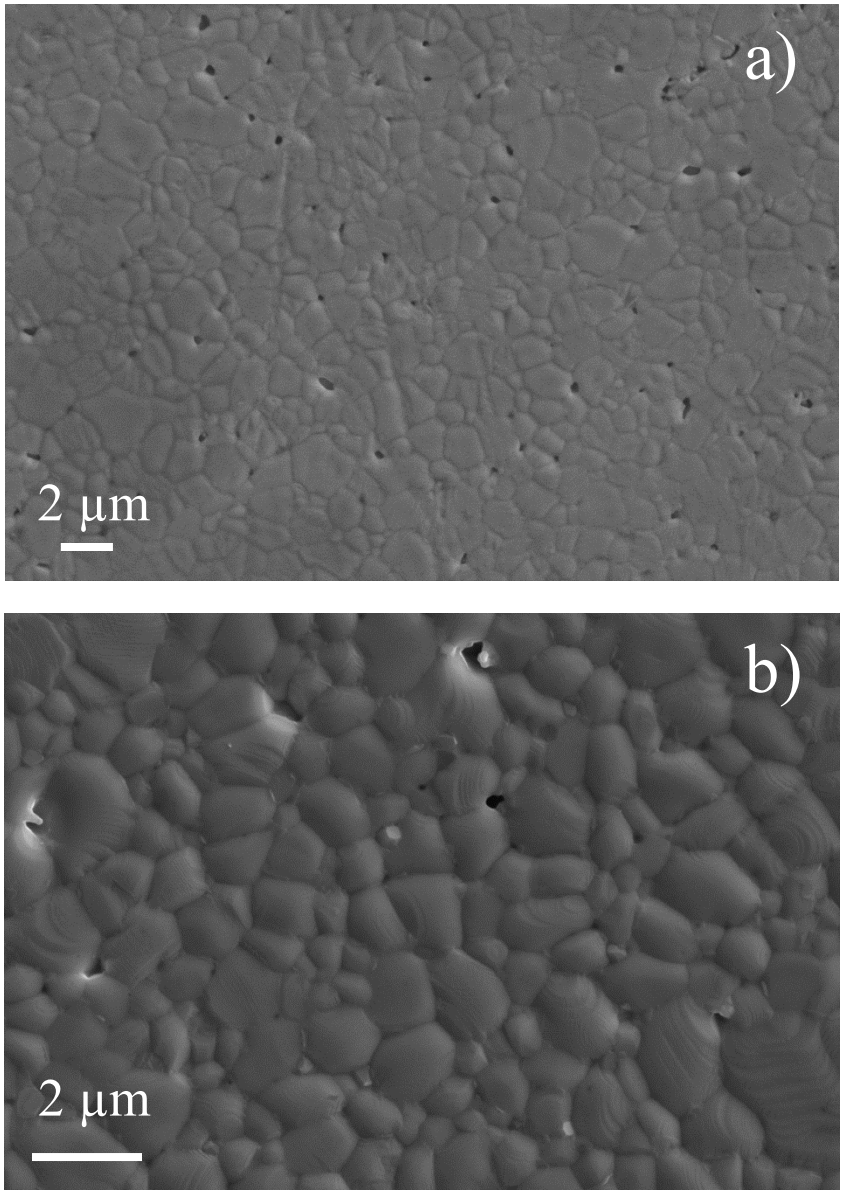

Fig. S-3. Secondary electron SEM images of thermally etched samples of (a) PNCO and (b) PNO. Thermal etching was performed at 1200°C (no isothermal segment) with heating and cooling rates of 10 K min^{-1} for PNCO and 1250°C for 20 minutes with heating and cooling rates of 5 K min^{-1} for PNO.

3. Precision thermogravimetry

3.1 Acetate precursor of PNCO in 20% O_2 and Ar (5.0)

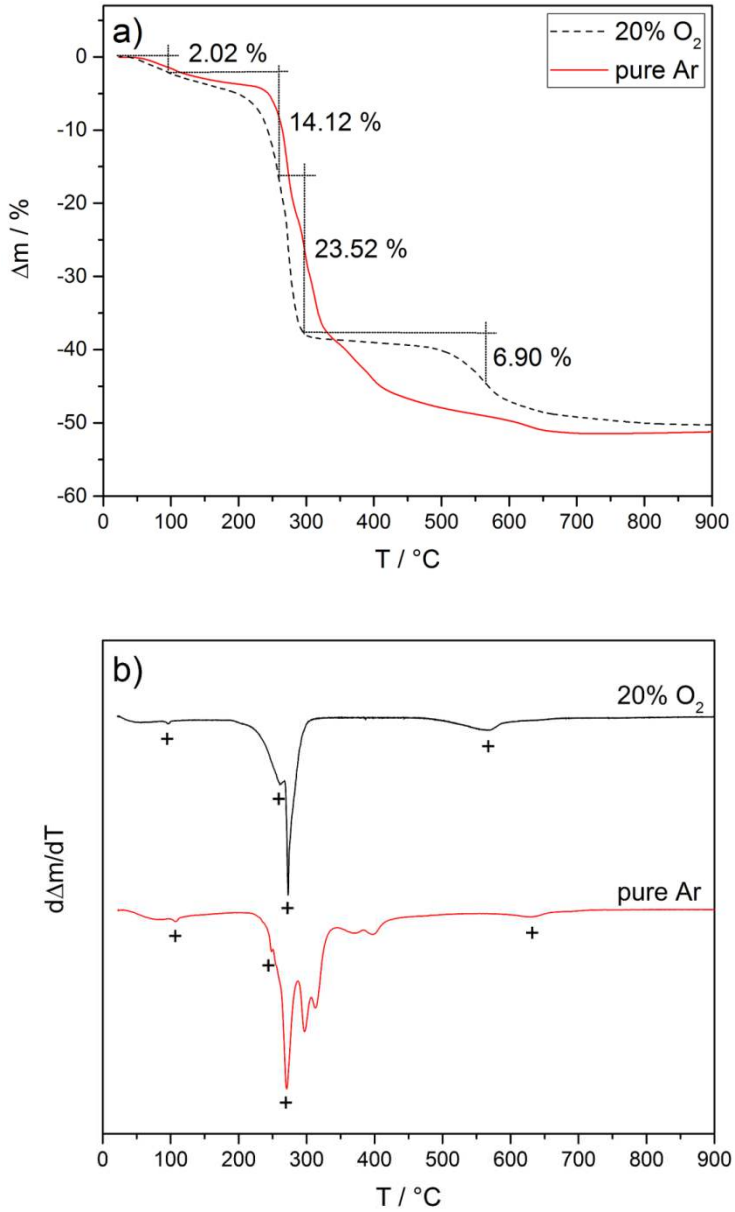

Fig. S-4. a) Thermogravimetric heating curves of the acetate precursor in Ar (5.0) (solid line) and in 20% oxygen (rest Ar) (dashed line) (heating rate 5 K min^{-1}); b) First derivative of the mass change over time for the acetate precursor in 20% oxygen (rest Ar) and in Ar (5.0). The "+" symbol indicates peak temperatures.

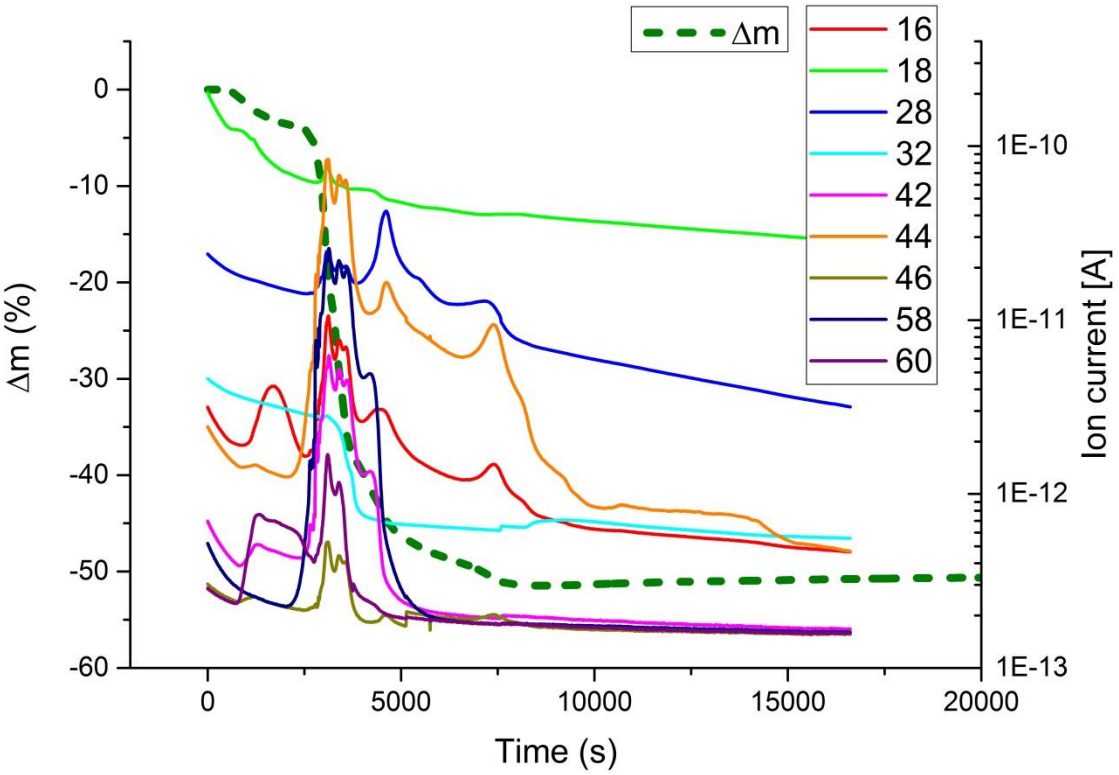

Fig. S-5. Mass loss (Δm) and mass spectrometry signals (m/z) during thermal decomposition of the PNCO acetate precursor as a function of time measured in pure argon.

For reasons of clarity, a detailed breakdown of the mass loss and selected mass spectrometry signals (m/z) as a function of temperature are given in the following figure.

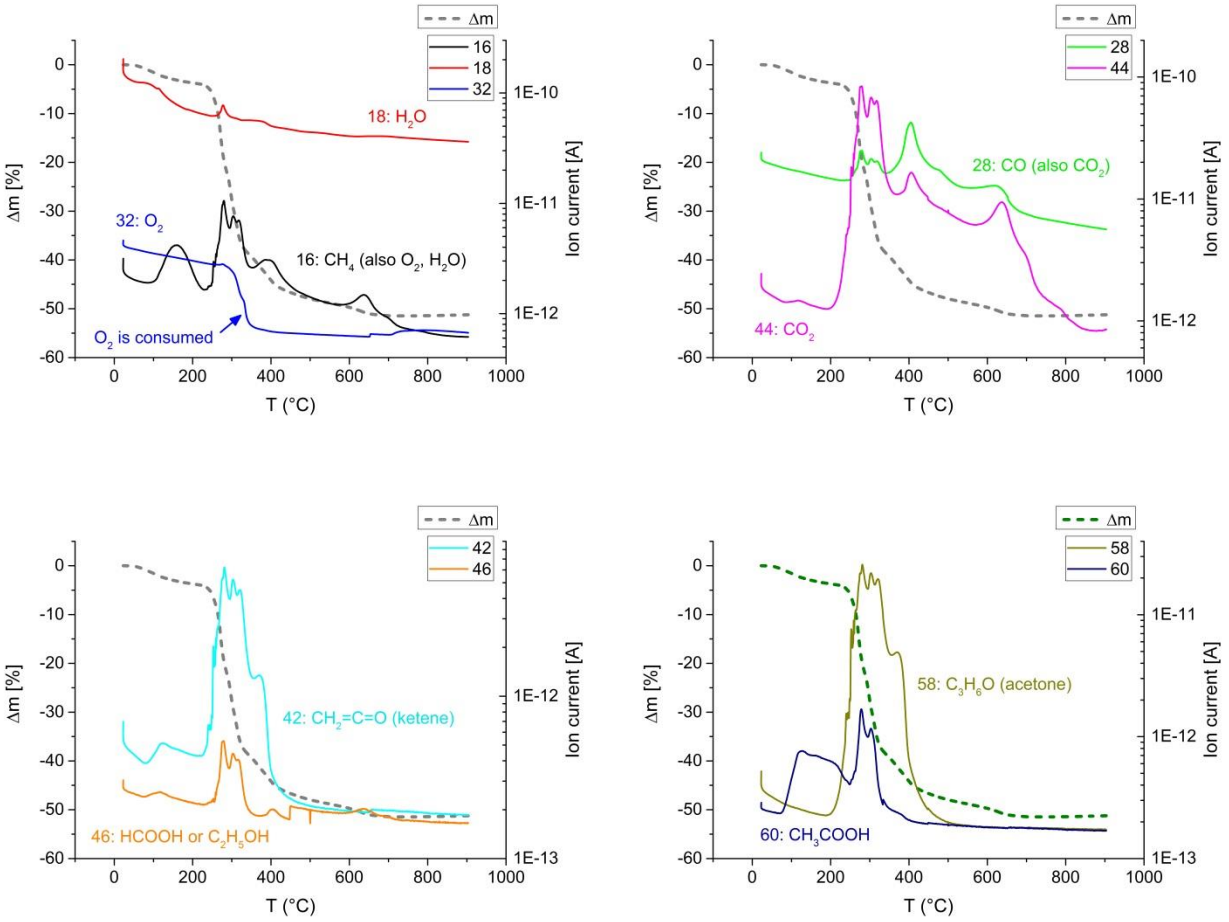

Fig. S-6. Thermal decomposition of the acetate precursor of PNCO monitored with precision thermogravimetry and mass spectrometry (heating rate 5 K min^{-1}). The mass loss occurs in several overlapping steps and is due to the release of O_2, H_2O, CO, CO_2, ketene, formic acid, ethanol, acetone and acetic acid.

3.2 PNCO in Ar (5.0)

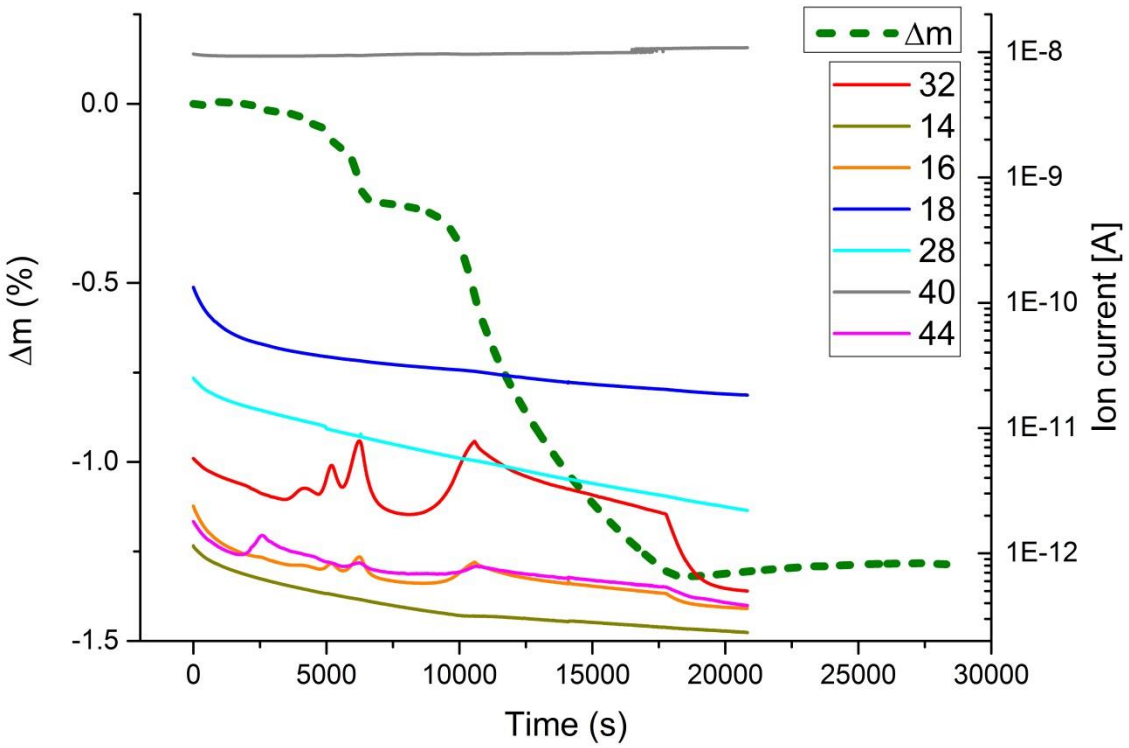

Fig. S-7. Mass loss and mass spectrometry signals (m/z) of sintered PNCO powder as a function of time measured in pure argon.

For reasons of clarity, a detailed breakdown of the mass loss and selected mass spectrometry signals (m/z) as a function of temperature is given in the following figure.

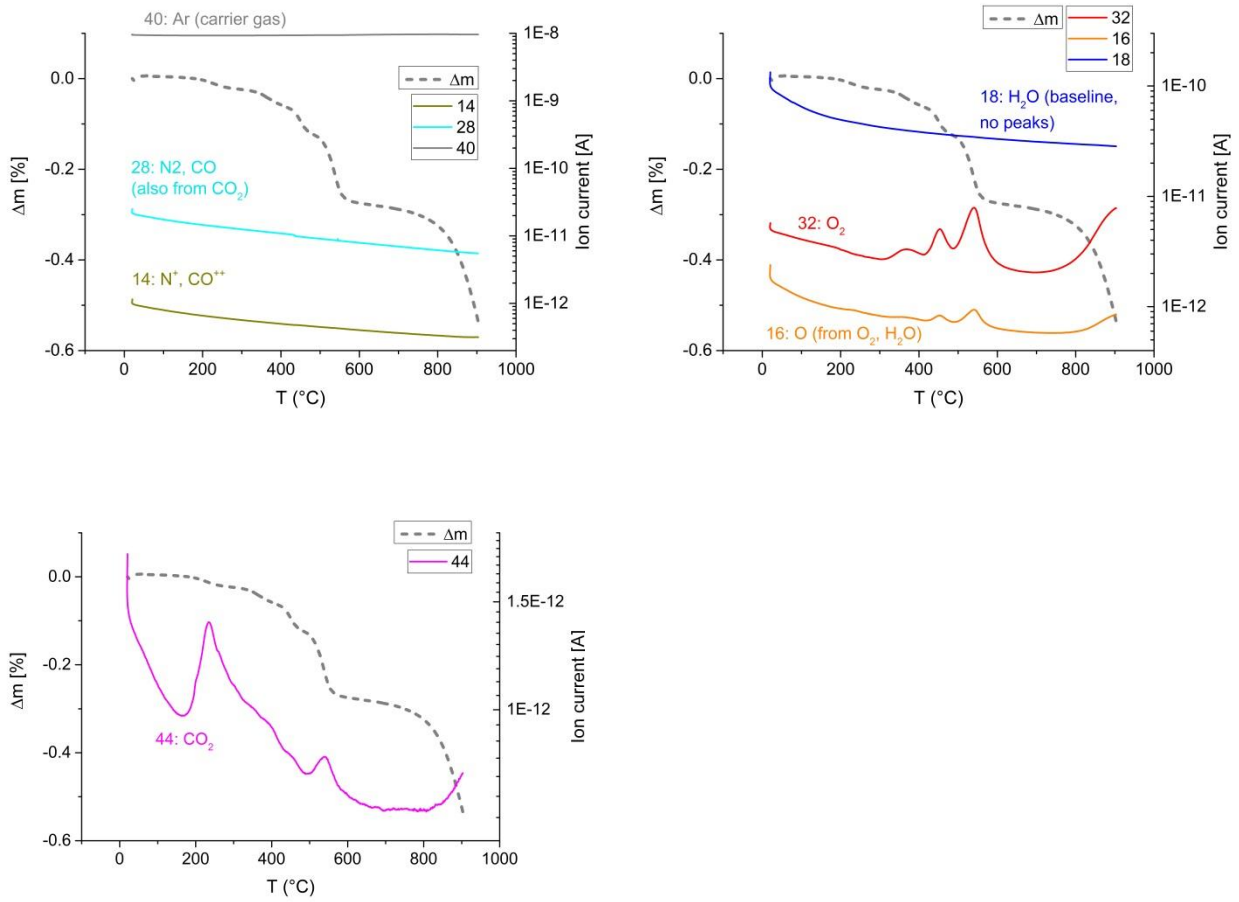

Fig. S-8. Mass loss of sintered and ground PNCO powder in Ar (5.0) monitored with precision thermogravimetry and mass spectrometry (heating rate 5 K min^{-1}). The mass loss occurs in several overlapping steps and is mainly due to the loss of O_2 in three steps between 300°C and 600°C and in a final step at T > 800°C. Desorption of minor amounts of CO_2 occurs at 250-300°C.

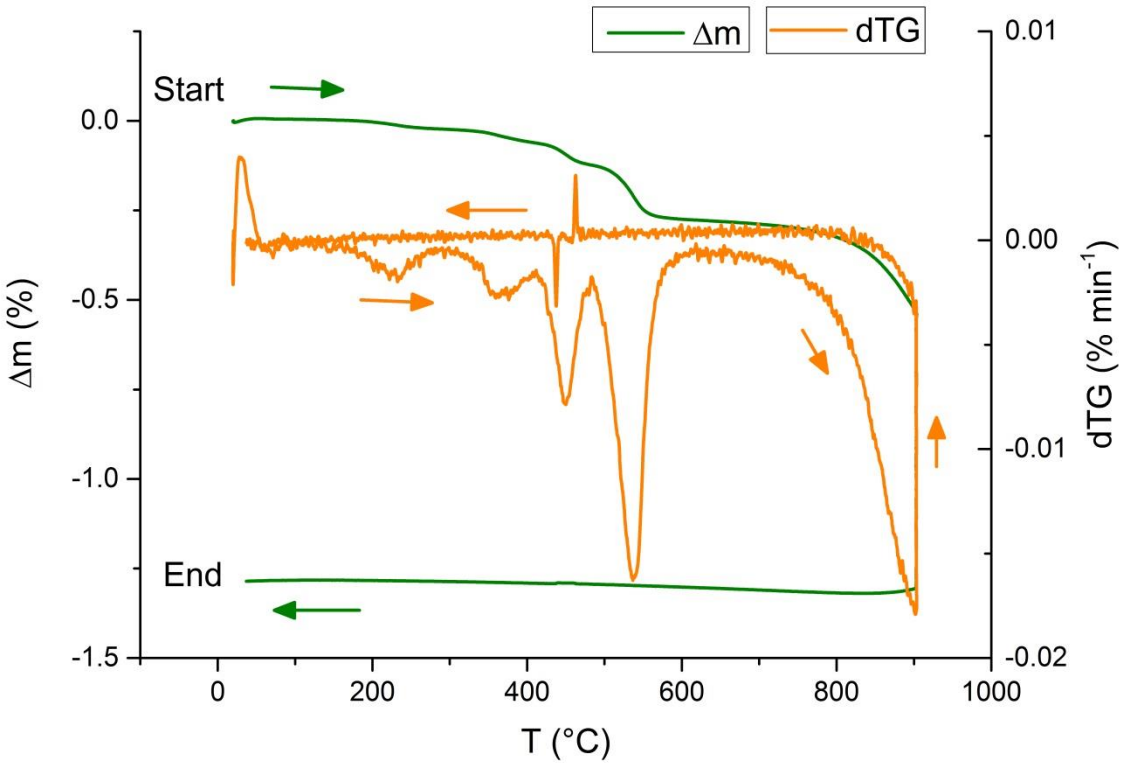

Fig. S-9. Mass loss and dTG (1st derivative of mass curve) of the sintered PNCO powder as a function of temperature in Ar (5.0). Due to the absence of O_2 in the carrier gas no mass gain occurs upon cooling.

4. Post-test analysis by X-ray diffraction and transmission electron microscopy

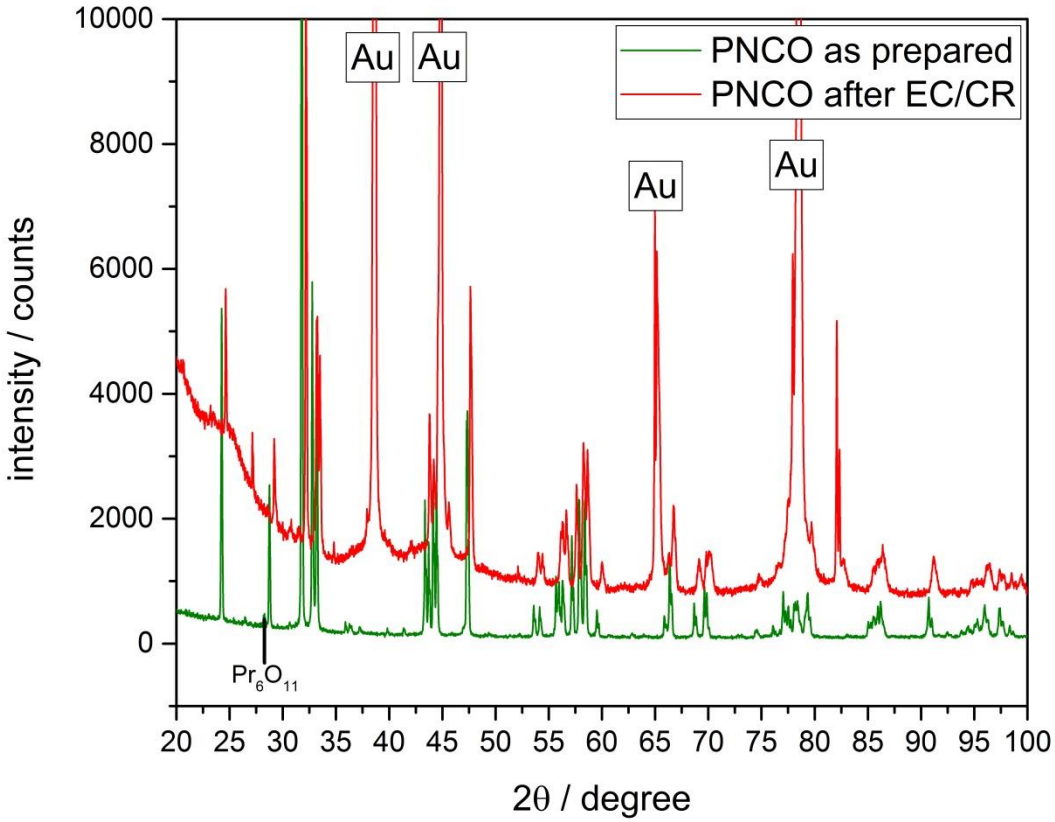

Fig. S-10. X-ray diffraction patterns of fresh PNCO (as prepared by freeze drying) and after electronic conductivity and dc-conductivity relaxation measurements (EC/CR). The fresh sample showed a small amount of secondary phase (below 1 wt% Pr_6O_{11}), whereas no secondary phases were found in the sample after the CR measurements. Gold peaks (Au) are due to electrical contacts used for electrochemical measurements.

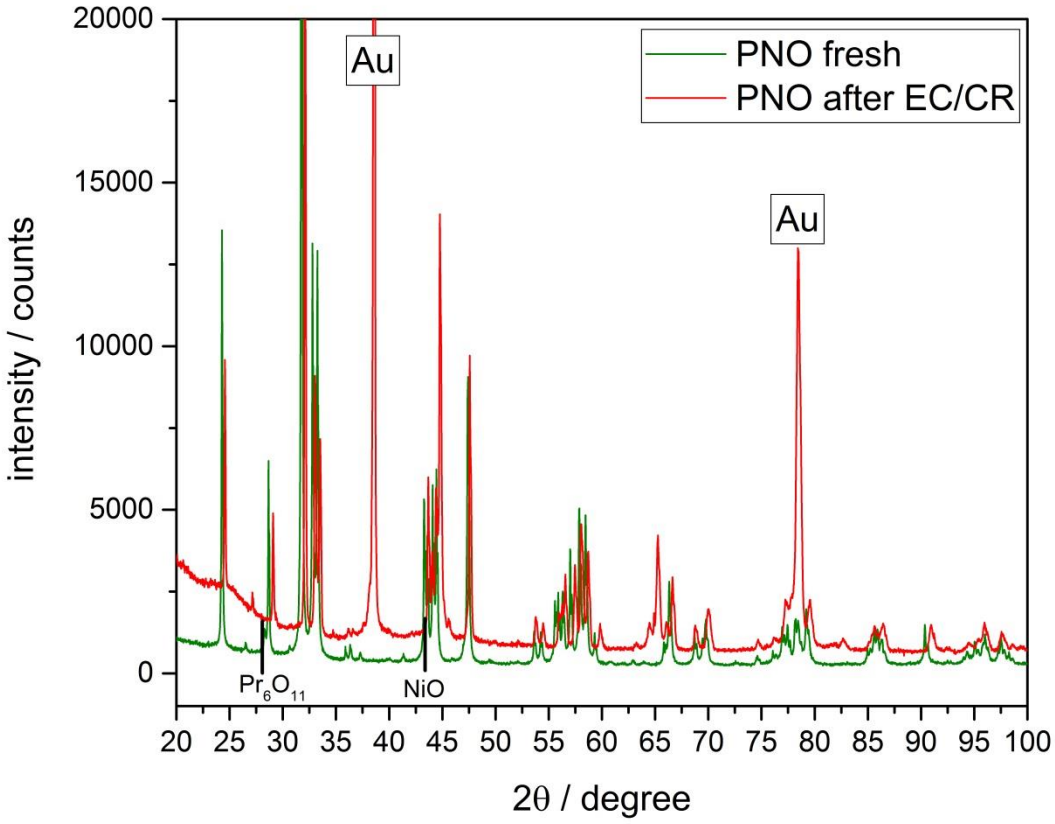

Fig. S-11. X-ray diffraction measurements of fresh PNO and after electronic conductivity and dc-conductivity relaxation measurements (EC/CR). The fresh sample showed small amounts of secondary phases (Pr_6O_{11} and NiO), whereas no secondary phases were found in the sample after the CR measurements. Gold peaks (Au) originate from electrical contacts.

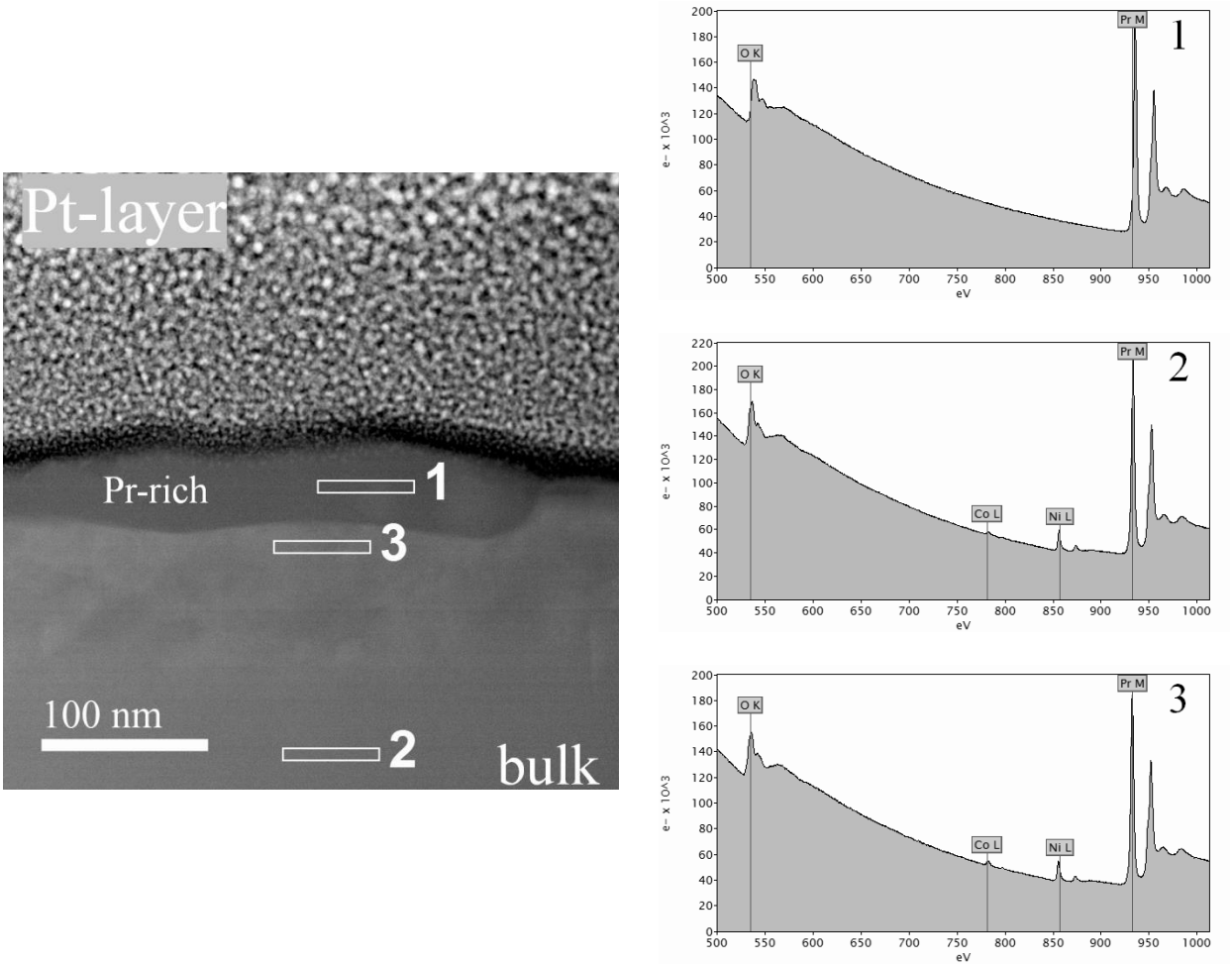

Fig. S-12. STEM-HAADF image of PNCO with selected EELS spectra. Spectrum 1 was recorded on the darker region on the surface of the lamella, indicating the formation of Pr-oxide (quantitative EDX analysis suggests Pr_6O_{11}) by the complete absence of Ni. Spectrum 2 corresponds to the bulk composition of the specimen, while spectrum 3 indicates a slight Co enrichment close to the Pr_6O_{11} phase. Energies in the EELS spectra are denoted in eV. The Pt-layer on top was deposited as a protection layer for FIB preparation.

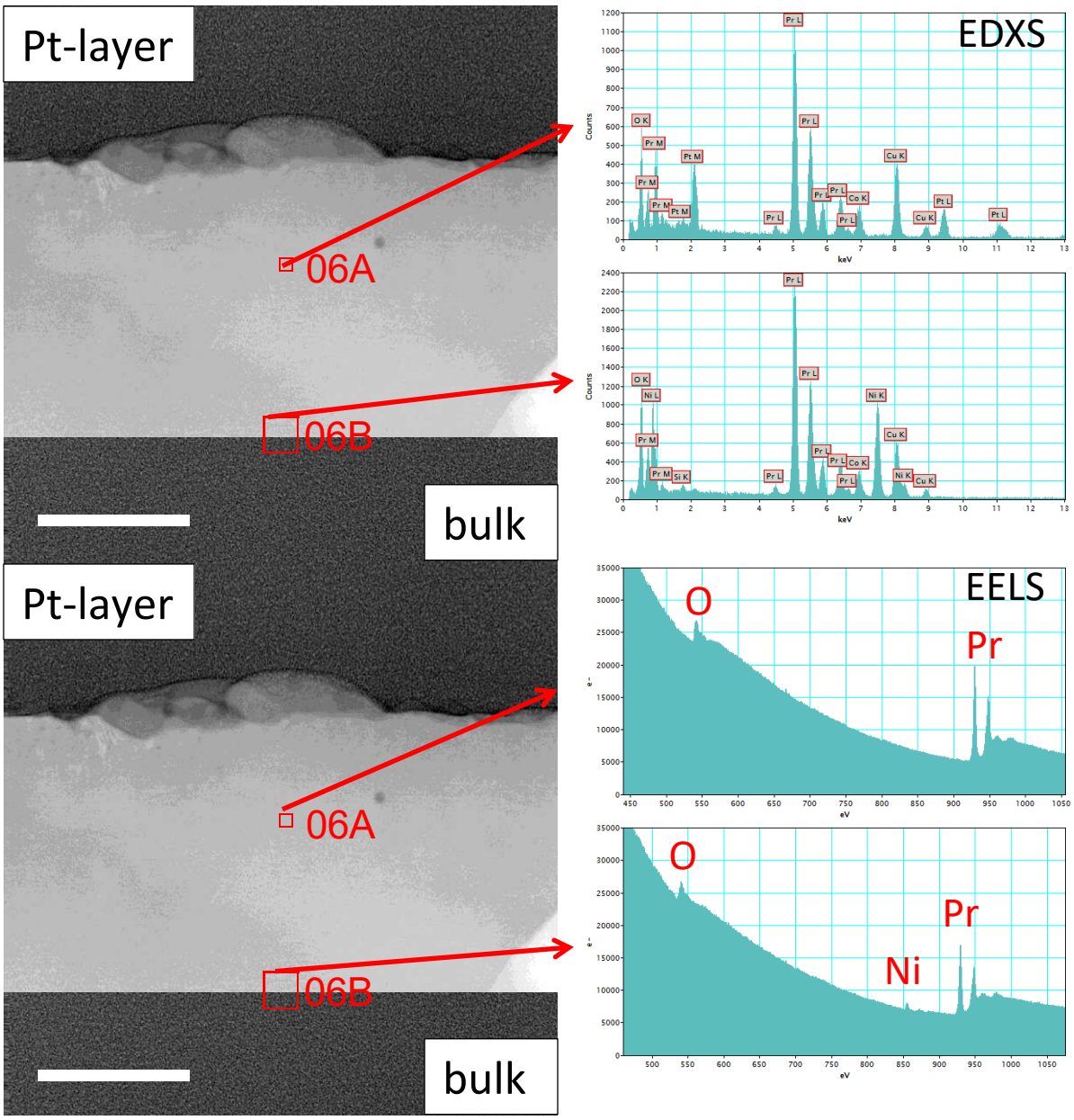

Fig. S-13. STEM-HAADF images with results from EDX and EELS analysis for PNO. EDX spectra of the topmost area (position 06A) show the absence of Ni and the formation of Pr_6O_{11}, whereas position 06B indicates nominal bulk composition. This finding is confirmed by EELS analysis on the same positions. The Pt-layer on top of the lamella was deposited during sample preparation. Energies are in keV and eV for EDX and EELS spectra, respectively.

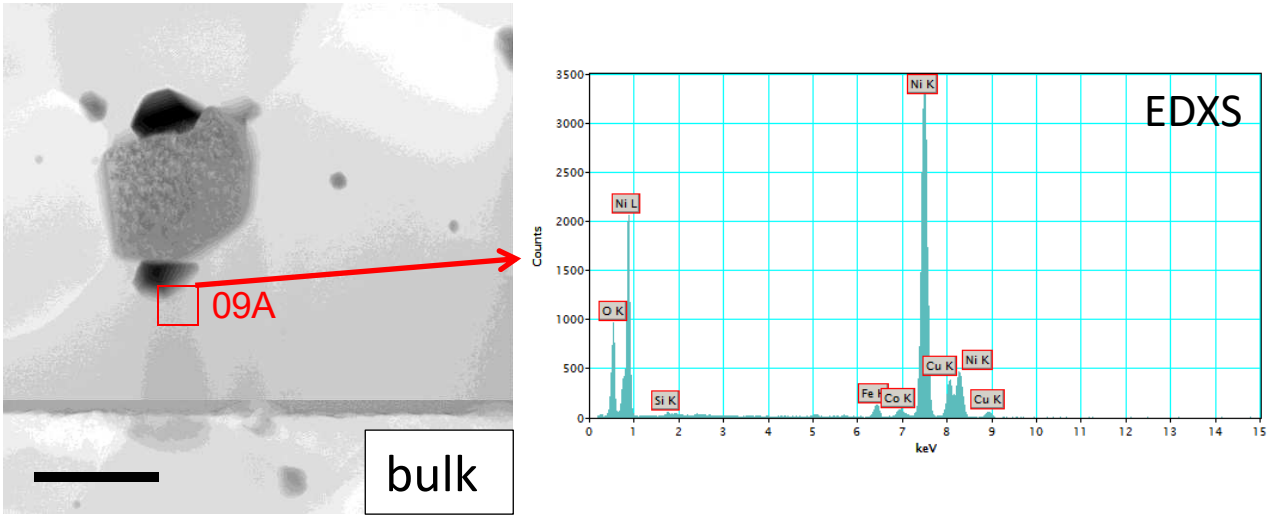

Fig. S-14. STEM-HAADF image and EDX spectrum of a NiO secondary phase in PNO. Energies in the EDX spectrum are denoted in keV.

5. Conductivity relaxation curves

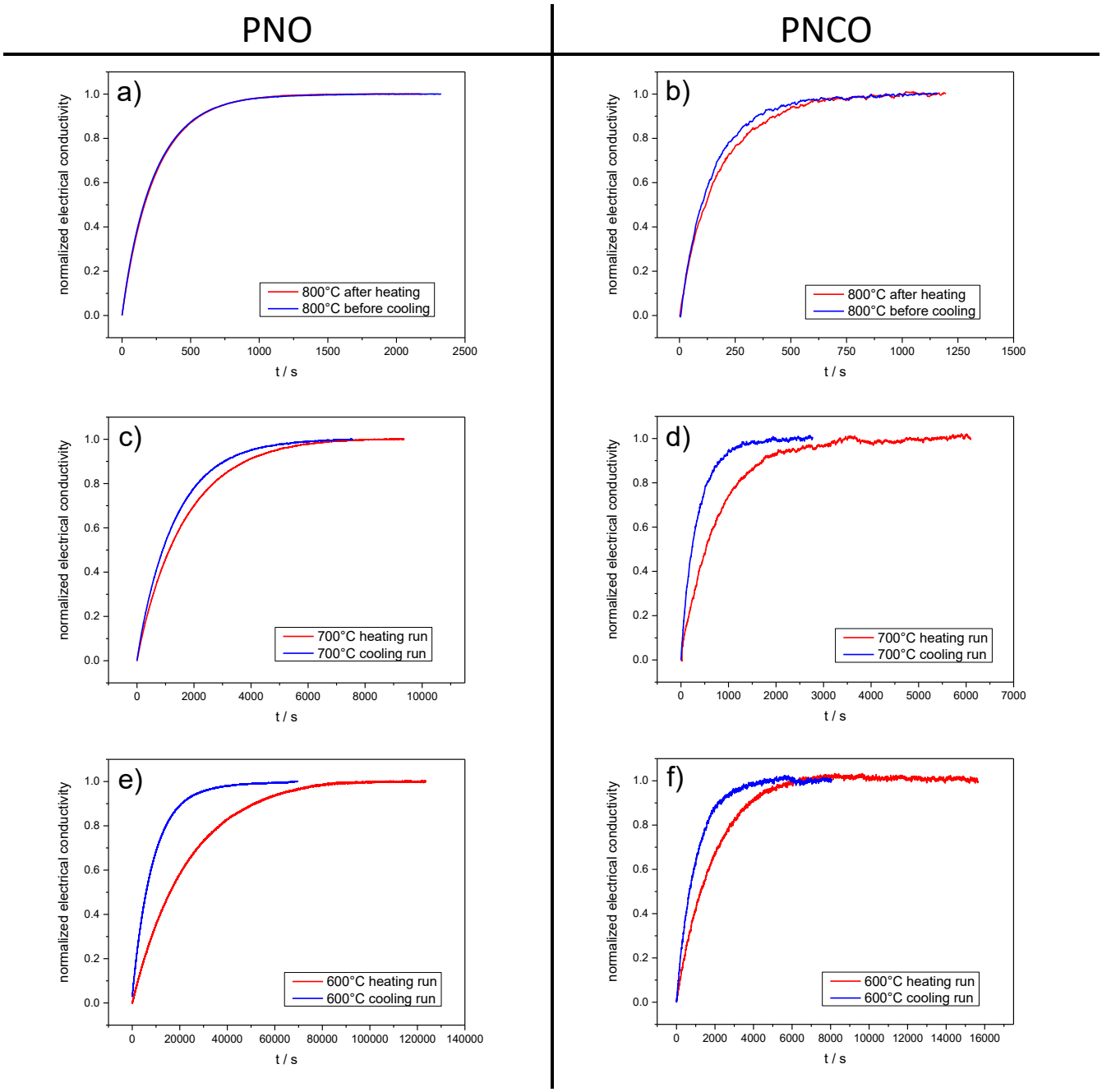

Fig. S-15. Comparison of normalised conductivity relaxation curves of PNO and PNCO obtained during the heating run (600°C → 800°C) and the subsequent cooling run (800°C → 600°C), see Fig. 8. In almost all cases an increase in the oxygen surface exchange rate can be observed, which is ascribed to the formation of catalytically active Pr-oxide particles on the sample surfaces in the course of the experimental study.

6. References

[1] C. Berger, E. Bucher, W. Sitte, *Solid State Ionics* **299** (2017) 46.

Journal of Solid State Chemistry 273 (2019) 92–100

Contents lists available at ScienceDirect

Journal of Solid State Chemistry

journal homepage: www.elsevier.com/locate/jssc

Crystal structure, oxygen nonstoichiometry, and mass and charge transport properties of the Sr-free SOFC/SOEC air electrode material $La_{0.75}Ca_{0.25}FeO_{3-\delta}$

Christian Berger [a], Edith Bucher [a,*], Christian Gspan [b], Werner Sitte [a]

[a] Chair of Physical Chemistry, Montanuniversitaet Leoben, Franz-Josef-Straße 18, A-8700 Leoben, Austria
[b] Institute of Electron Microscopy and Nanoanalysis (FELMI), Graz University of Technology & Graz Centre for Electron Microscopy (ZFE), Austrian Cooperative Research (ACR), Steyrergasse 17, A-8010 Graz, Austria

ARTICLE INFO

Keywords:
Lanthanum calcium ferrite
Solid oxide fuel cell cathode
Solid oxide electrolyser cell anode
Oxygen exchange kinetics

ABSTRACT

The mixed ionic-electronic conducting perovskite $La_{0.75}Ca_{0.25}FeO_{3-\delta}$ (LCF7525) was synthesized via a citric acid – ethylenediaminetetraacetate sol-gel route. Crystal structure, phase purity, and lattice constants were determined by powder X-ray diffraction and Rietveld refinement. The oxygen exchange kinetics (chemical surface exchange coefficients and chemical diffusion coefficients of oxygen) and the electronic conductivity were studied by in-situ dc-conductivity (relaxation) measurements at 600–800 °C and $1 \times 10^{-3} \leq pO_2/bar \leq 0.1$. The thermal expansion coefficient was determined by dilatometry at 30–1000 °C and $1 \times 10^{-3} \leq pO_2/bar \leq 1$. The oxygen nonstoichiometry was measured as a function of temperature and oxygen partial pressure by thermogravimetry and could be described by a point defect model. Experimental data of the chemical diffusion coefficient of oxygen and results from defect chemical modelling were used to estimate self-diffusion coefficients of oxygen and oxygen vacancies, as well as the ionic conductivity. Based on the results obtained for the mass and charge transport properties and the thermal expansion behaviour, it can be concluded that LCF7525 may be an attractive Sr- and Co-free material for air electrodes in intermediate temperature solid oxide fuel cells and solid oxide electrolyser cells.

1. Introduction

Solid oxide fuel cells (SOFC) and solid oxide electrolyser cells (SOEC) provide a basis for highly efficient and environmentally benign technologies for the conversion of chemical energy of various fuels into electrical energy and storage of electrical energy in the form of a chemical energy carrier [1–6]. However, the limited lifetime of the cells is a major obstacle for the broad market introduction of SOFC- and SOEC-based systems. On the cell level, degradation is frequently caused by impurity poisoning of the air electrode (SOFC cathode/SOEC anode). In state-of-the-art air electrode materials like $(La,Sr)(Co,Fe)O_{3-\delta}$ or $(La,Sr)CoO_{3-\delta}$, which are optimized for operation in the intermediate temperature-range (600–850 °C), the acceptor substituent ion Sr^{2+} has a strong tendency to segregate towards the surface [7–12]. The Sr-rich surface regions react with critical impurities like volatile Cr- and Si-species, or SO_2, and form secondary phases (chromates, silicates, or sulphates) [13–18]. Because of these processes, the oxygen exchange activity of the air electrodes decreases significantly [19–23].

In recent years, considerable research efforts have been made to gain deeper insights into the mechanisms of degradation and to develop SOFC and SOEC air electrode materials with higher stability against impurity poisoning. At the same time, these alternative compounds should exhibit sufficient electronic and ionic conductivities, fast oxygen exchange kinetics, and thermal expansion coefficients similar to those of common solid electrolytes. Several recent studies showed that Sr- and Co-free mixed ionic-electronic conductors (MIECs) from the $(La,Ca)FeO_{3-\delta}$ or $(Pr,Ca)FeO_{3-\delta}$ series may be suitable candidates which can fulfil these complex demands [24–27]. However, in comparison to the extensively investigated series of solid solutions $(La,Sr)(Co,Fe)O_{3-\delta}$ and $(La,Sr)CoO_{3-\delta}$, relatively few systematic studies on the mass and charge transport properties, oxygen exchange kinetics, oxygen nonstoichiometry, and defect chemistry of $(La,Ca)FeO_{3-\delta}$ or $(Pr,Ca)FeO_{3-\delta}$ as functions of temperature and oxygen partial pressure are available. With the $(La,Ca)FeO_{3-\delta}$ series it was previously shown that increasing Ca-concentrations

* Corresponding author.
E-mail address: edith.bucher@unileoben.ac.at (E. Bucher).

https://doi.org/10.1016/j.jssc.2019.02.032
Received 11 December 2018; Received in revised form 14 February 2019; Accepted 21 February 2019
Available online 23 February 2019
0022-4596/© 2019 Elsevier Inc. All rights reserved.

lead to an increase in the electronic and ionic conductivities and the oxygen exchange kinetics [24,28–30]. However, the phase stability of $(La,Ca)FeO_{3-\delta}$ solid solutions is limited to approximately 38 mol-% Ca on the La-site, with formation of secondary phases like $Ca_2LaFe_3O_8$ or $Ca_2Fe_2O_5$ occurring for higher Ca-concentrations [31–33]. In the present work, the compound $La_{0.75}Ca_{0.25}FeO_{3-\delta}$ was investigated with the aim of optimizing the material properties due to a relatively high Ca-concentration, while remaining well within the phase stability limit. Comprehensive data on the crystal structure, thermal expansion behaviour, oxygen exchange kinetics, as well as electronic and ionic conductivity of $La_{0.75}Ca_{0.25}FeO_{3-\delta}$ were acquired in order to assess the material properties for potential application in intermediate temperature SOFC and SOEC air electrodes.

2. Experimental

2.1. Sample preparation

$La_{0.75}Ca_{0.25}FeO_{3-\delta}$ powder was synthesized via a citric acid – ethylenediaminetetraacetate (EDTA) sol-gel process starting with stoichiometric amounts of the corresponding metal-nitrates ($La(NO_3)_3{\cdot}6H_2O$, $Ca(NO_3)_2{\cdot}4H_2O$, and $Fe(NO_3)_3{\cdot}9H_2O$; all chemicals obtained from Sigma Aldrich, analytical grade quality). These were mixed with approximately 200 ml distilled H_2O in a stainless steel vessel. Anhydrous citric acid and EDTA (1 mol each per cation) were added after all metal-nitrates were completely dissolved. Then, a 25% aqueous NH_3 solution was added until pH = 8 was reached and a clear, dark blue solution was obtained. The temperature was slowly raised to remove water and form a gel. Self-ignition and combustion of the dried gel occurred at approximately 500 °C.

The raw ash was crushed in an agate mortar and calcined at 1000 °C for 4 h (5 K/min ramps for heating and cooling) in air. The calcined powder was single phase according to XRD and showed a broad particle size distribution (measured with laser scattering using a CILAS 1064L particle size analyser) (Figure S-1, supplementary material). A bench top roll-mill was used to grind the calcined powder until a final average particle size of $d_{50} = 0.55$ µm was obtained (Figure S-1, supplementary material).

For thermal expansion measurements, a cylindrical pellet was uniaxially pressed. After sintering at 1100 °C for 2 h with heating and cooling rates of 5 K/min, the sample was 5 mm in diameter and 8 mm long. The relative density of the sintered pellet was 96% of the theoretical density as obtained by X-ray diffraction ($\rho_{XRD} = 6.123$ g cm^{-3}). Samples for electrical measurements were isostatically pressed at 3 kbar, sintered at 1100 °C for 2 h (heating and cooling rates of 5 K/min) and showed a relative density of ≥98% of the theoretical value.

2.2. Crystallographic and microstructural characterisation

XRD of the calcined LCF7525 powder was performed with a diffractometer (BRUKER-AXS D8 Advance ECO) using a Cu Kα radiation source operated at 40 kV and 25 mA. The diffractogram was recorded at a scanning rate of 0.01° s^{-1}. Lattice parameters were obtained from fitting the peak positions to an orthorhombic unit cell (space group *Pnma*). Rietveld refinement was performed by using the commercially available software TOPAS (Bruker) [34]. Reflection broadening was described by convolution of a Voigt function with a modified pseudo Voigt function according to Thompson–Cox–Hastings [35].

Scanning electron microscopy with energy dispersive X-ray spectroscopy (SEM-EDXS) was performed by using a Zeiss EVO50 microscope with an EDX Oxford Instruments Inca detector. High-resolution SEM images were recorded in secondary electron (SE) and backscattered electron (BSE) mode at an acceleration voltage of 15 kV. The cation stoichiometry was determined by EDXS with an Oxford Instruments Mod. 6272 detector.

Sample preparation for the TEM investigation was carried out on a focused ion beam (FIB) microscope FEI NOVA 200 Nanolab. TEM investigations were performed with a TITAN^3 G2 60–300 from FEI at 300 keV accelerating voltage. The microscope is equipped with a C_S–probe corrector for the scanning transmission electron microscopy mode (STEM) and with the Super-X detector system (Bruker). STEM images were recorded simultaneously with a high angle annular dark field (HAADF) and a bright field (BF) detector.

2.3. Thermal analysis

The thermal expansion of LCF7525 was measured between 30 and 1000 °C with heating rates of 1 K/min using a single-rod dilatometer DIL 402/PC4 (NETZSCH). Atmospheres with different oxygen partial pressures in range of $1 \times 10^{-3} \leq pO_2/\text{bar} \leq 1$ were obtained by O_2-Ar gas mixtures using mass flow controllers (Teledyne HFC-302) at flow rates of 10 l h^{-1}.

Differential scanning calorimetry (DSC) was performed on sintered (1100 °C, 2 h, air) and finely ground LCF7525 powder using a High Temperature DSC 404 C Pegasus (NETZSCH). The sample (approximately 70 mg) was placed in an 85 µl Pt-Rh crucible. To minimize the influence of adsorbed humidity or CO_2, the powder was heated in the dilatometer to 800 °C, kept in 20% O_2 (rest Ar) for 6 h, and cooled to 20 °C before the actual experiment was started. The DSC measurement was performed between 20 and 1000 °C in 20% O_2 (rest Ar) with heating and cooling rates of 20 K/min and a gas flow rate of 50 ml min^{-1}.

The oxygen nonstoichiometry δ of LCF7525 was determined by precision thermogravimetry (TG) using a symmetric thermobalance (Setaram, model TAG 16). Small amounts (approximately 80–100 mg) of the sintered and finely ground powder were placed in a 130 µl platinum crucible. Oxygen partial pressures were adjusted with mass flow controllers (red-y, Vögtlin Instruments AG) using O_2-Ar gas mixtures. To determine the oxygen partial pressure close to the sample, an in-situ oxygen sensor with Ir/IrO_2-reference (Setnag, France) was used. TG experiments were performed in isothermal and isobaric modes. The agreement between δ-values obtained from isotherms and isobars was checked, in order to ensure that all data were acquired under equilibrium conditions. According to literature data for the similar compounds $La_{0.80}Ca_{0.20}FeO_{3-\delta}$ (LCF82) [25,36], $La_{0.90}Sr_{0.10}FeO_{3-\delta}$ and $La_{0.75}Sr_{0.25}FeO_{3-\delta}$ [37], and $La_{0.80}Sr_{0.20}FeO_{3-\delta}$ [38] it was assumed that δ of LCF7525 is close to zero at room temperature and $pO_2 = 0.2$ bar.

2.4. Electrical conductivity and conductivity relaxation measurements

Chemical surface exchange coefficients (k_{chem}) and chemical diffusion coefficients of oxygen (D_{chem}) of LCF7525 were determined by in-situ dc-conductivity relaxation experiments on thin rectangular slabs contacted in van der Pauw electrode configuration [39]. Samples with dimensions of 7.0×6.9 mm^2 with a thickness of 560 µm (for the determination of k_{chem}) and 7.0×7.0 mm^2 with a thickness of 1380 µm (for the determination of D_{chem}) were prepared from sintered LCF7525 bulk samples (relative density ≥ 98%). Small pO_2-steps between 1.0×10^{-3} and 1.5×10^{-3} bar, 1.0×10^{-2} and 1.5×10^{-2} bar, and 1.0×10^{-1} and 1.5×10^{-1} bar, respectively, were used in the relaxation measurements in order to obtain values for k_{chem} and D_{chem} under conditions close to equilibrium. Oxidation and reduction experiments were performed at a constant total gas flow of 2 l h^{-1}. The electrical dc-conductivity was obtained from four-point measurements on the 560 µm thick sample (see above). Further details about the test setup and experimental procedures were described elsewhere [24,26]. The kinetic parameters (k_{chem}, D_{chem}) were obtained from nonlinear least squares fits of the solution of the diffusion equation to the conductivity relaxation data [40–42]. The oxygen surface exchange process consists of several reaction steps (such as adsorption, dissociation, reduction, and incorporation into the lattice) which are usually not known in detail. Thus, the overall oxygen surface exchange process is commonly assumed to obey first-order kinetics to allow for an analytical solution of the diffusion equation. The model

further assumes that the kinetic parameters remain constant during the relaxation process. Both assumptions will hold as long as the pO_2-steps in the conductivity relaxation experiments are sufficiently small (for instance, changes in pO_2 by factors of 1.5 were used in the present study).

3. Results and discussion

3.1. Crystal structure

The X-ray diffraction pattern of LCF7525 and the results of Rietveld refinement are shown in Fig. 1. All reflections could be indexed within the orthorhombic space group *Pnma* of the perovskite structure. The determined lattice parameters of the orthorhombic unit cell of LCF7525 are shown in comparison with those of other compounds $La_{1-x}Ca_xFeO_{3-\delta}$ ($0 \leq x \leq 0.20$) in Table 1. The unit cell volume, as well as the lattice parameters a, b, and c decrease with increasing Ca-concentration. The tolerance factor *t* (Table 1), which describes the deviation from the ideal cubic perovskite structure, was calculated according to Goldschmidt's rule (Equation (1)) [43,44].

$$t = \frac{x_A r_A + x_{A'} r_{A'} + r_O}{\sqrt{2}(r_B + r_O)} \quad (1)$$

The pre-factors x_A and $x_{A'}$ represent the site occupancy on the A-site of the ABO_3 (perovskite) lattice with A = La and A′ = Ca (for example: $x_A = 0.75$ and $x_{A'} = 0.25$ in LCF7525). The symbols r_i denote the ionic radii of the species *i* (A- and B-site cations, oxygen). The following ionic radii from Ref. [45] were used: $r(La^{3+})(XII) = 1.36$ Å; $r(Ca^{2+})(XII) = 1.34$ Å, $r(Fe^{3+}(\text{high spin}))(VI) = 0.645$ Å, $r(O^{2-})(VI) = 1.40$ Å. For ideal cubic perovskites, the tolerance factor is unity. In the $La_{1-x}Ca_xFeO_{3-\delta}$ series, *t* decreases with increasing Ca concentration from $LaFeO_3$ ($t = 0.9543$) [46] to LCF7525 ($t = 0.9526$) [25]. The crystal structure of LCF7525 is shown in Fig. 2. Bond lengths and bond angles of LCF7525 are given in Table 2 in comparison with values obtained for $La_{1-x}Ca_xFeO_{3-\delta}$ ($0 \leq x \leq 0.20$) [24,25]. The atomic positions of LCF7525, which are given in Table 3, are similar to those reported for other compounds from the series $La_{1-x}Ca_xFeO_{3-\delta}$ ($0 \leq x \leq 0.20$) [24,25,46]. Only minor deviations in the equatorial oxygen positions (O1) were observed.

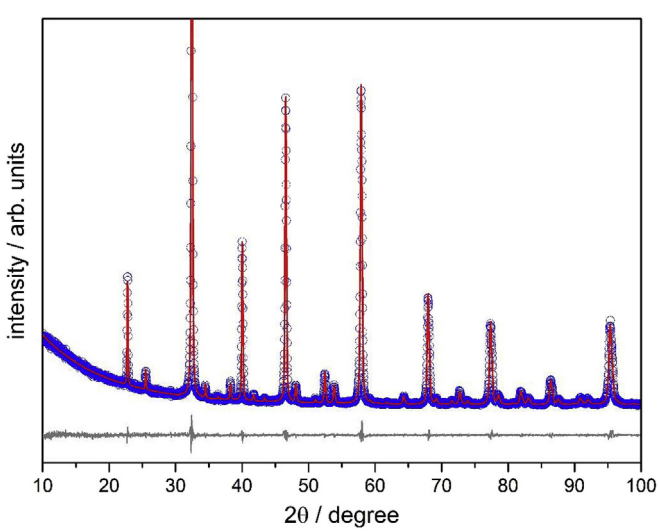

Fig. 1. Room temperature powder diffraction pattern of LCF7525 (circles) and fit obtained from Rietveld refinement (solid line); the grey line represents the difference plot between measured and calculated data. The high fit quality is indicated by the reliability parameters $R_{exp} = 5.28$, $R_{wp} = 6.96$, and $\chi^2 = 1.32$.

3.2. Microstructure and chemical composition

Surface analysis of a sintered and polished LCF7525 specimen was performed with SEM-EDX. Images were recorded in the SE and BSE mode, respectively (Figure S-2, supplementary material). The fresh sample shows a homogeneous surface without secondary phases (Figure S-2a and b, supplementary material). Minor grain pull-out effects and some scratches are evident, which stem from the polishing procedure. According to EDX-analysis, the cation stoichiometry is in agreement with the nominal composition within the estimated measurement uncertainty of the method (±2–3 at-%) (Table S-1, supplementary material).

Fig. 3 shows a cross-sectional scanning transmission electron microscopy image of the fresh sample acquired with an annular dark field detector (STEM-ADF). No secondary phases were found on the surface or in the bulk area of the lamella. The average grain size, determined by linear intercept method [47] from the STEM image, is 300 ± 100 nm. An EDX line scan across a grain boundary indicates that the grain boundary is slightly enriched with Ca and Fe, while La is slightly depleted (Figure S-3, supplementary material). This is in agreement with results from previous studies [9,26,48–51], which showed that alkaline earth elements tend to segregate along grain boundaries of rare earth transition metal perovskites towards the surface.

3.3. Thermal expansion properties and oxygen nonstoichiometry

The relative thermal expansion ($\Delta L/L_0$) of LCF7525 is shown in Fig. 4 as a function of temperature and oxygen partial pressure. Since two regions with different thermal expansion behaviour are evident, the thermal expansion coefficients (TECs) were determined separately by linear regression in these two temperature segments. Region I extends from 30 to approximately 750 °C; region II from 750 to 1000 °C. The corresponding thermal expansion coefficients are shown in Table 4. The TECs in region I are in good agreement with those of common solid electrolytes like 8YSZ ($10.8 \times 10^{-6}\,K^{-1}$ [52]), or $Ce_{0.90}Gd_{0.10}O_{2-\delta}$ ($12.5 \times 10^{-6}\,K^{-1}$ [53]), as well as with those of other lanthanum calcium ferrites like $La_{0.90}Ca_{0.10}FeO_{3-\delta}$ (LCF91) ($12.4 \times 10^{-6}\,K^{-1}$ [24]) and LCF82 ($12.8 \times 10^{-6}\,K^{-1}$ [25]). At the same time, the TECs of LCF7525 are much smaller than those of the state-of-the-art SOFC cathode material $La_{0.60}Sr_{0.40}CoO_{3-\delta}$ ($18.9 \times 10^{-6}\,K^{-1}$ [54]). In region II (T > 750 °C) the TECs of LCF7525 are higher than in region I (Table 4). Differential scanning calorimetry (DSC) (Figure S-4, supplementary material) in 20% O_2 (rest Ar) showed a reversible phase transition from the orthorhombic to the rhombohedral structure which was also reported by Price et al. [32] for $La_{1-x}Ca_xFeO_{3-\delta}$ (x = 0.20, 0.30). With LCF7525, the transition occurs at approximately 700–750 °C, which coincides with the change in the thermal expansion behaviour (Fig. 4, Table 4). An additional factor, which contributes to the increase of the TEC at elevated temperatures, is the chemical expansion, which is coupled to the reduction of Fe (and the corresponding increase in the ionic radius of the Fe ions) as oxygen vacancies are formed [55–57] (compare also Fig. 5 and Figure S-5 (supplementary material)).

Table 1
Lattice parameters, unit cell volume and tolerance factor of selected compounds from the $La_{1-x}Ca_xFeO_3$ series.

Compound	a/Å	b/Å	c/Å	V/Å^3	t	Ref.
$La_{0.75}Ca_{0.25}FeO_{3-\delta}$	5.5091(3)	7.7879(5)	5.5123(4)	236.50	0.9526	This work
$La_{0.80}Ca_{0.20}FeO_{3-\delta}$	5.521(2)	7.803(2)	5.523(2)	237.93	0.9530	[71]
$La_{0.90}Ca_{0.10}FeO_{3-\delta}$	5.5425(5)	7.8330(11)	5.5387(7)	240.46	0.9536	[72]
$LaFeO_3$	5.5647(1)	7.8551(1)	5.5560(1)	242.86	0.9543	[46]

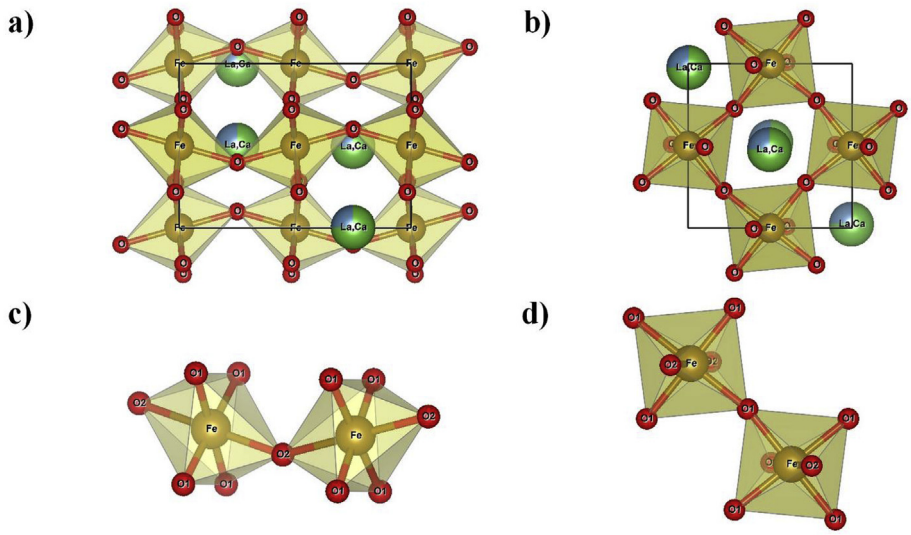

Fig. 2. Crystal structure and octahedral distortion of LCF7525 displayed a) along the x-axis, b) along the y-axis, c) detail of the oxygen octahedra tilted between x- and y-axis and d) detail in the oxygen octahedra along the y-axis; the structure was visualised with VESTA [70].

Table 2
Bond lengths and bond angles of selected compounds from the $La_{1-x}Ca_xFeO_3$ series.

Compound	Fe-O1/Å	Fe-O1/Å	Fe-O2/Å	Fe-O1-Fe/°	Fe-O2-Fe/°	Ref.
$La_{0.75}Ca_{0.25}FeO_{3-\delta}$	1.93305(9)	1.99671(10)	2.02515(13)	148.1	165.1	This work
$La_{0.80}Ca_{0.20}FeO_{3-\delta}$	1.972(18)	2.00(3)	1.988(10)	158.4	157.9	[71]
$La_{0.90}Ca_{0.10}FeO_{3-\delta}$	1.995(14)	1.988(15)	2.002(6)	159.2	155.9	[72]
$LaFeO_3$	2.00(5)	2.01(4)	2.002(3)	157.6	157.6	[46]

Table 3
Atomic positions, site occupancy and isotropic displacement parameters of LCF7525. Atomic positions of Ca were fixed to those of La.

Site	x	y	z	Occupancy	B_{iso}/Å^2
La	0.0233	0.2500	0.9957	0.75	0.69
Ca	0.0233	0.2500	0.9957	0.25	0.69
Fe	0	0	0.5000	1	0.55
O1	0.2741	0.4835	0.7177	1	0.73
O2	0.4920	0.2500	0.1008	1	0.73

The oxygen nonstoichiometry δ of LCF7525 increases with increasing temperature and decreasing oxygen partial pressure at $20 \leq T/°C \leq 800$ and $2 \times 10^{-4} \leq pO_2/bar \leq 0.2$ (Fig. 5 and Figure S-5 (supplementary material)). LCF7525 shows smaller oxygen deficiencies than other SOFC cathode materials with high Co- and/or Sr-content, such as $La_{0.40}Sr_{0.60}CoO_{3-\delta}$ [58,59] and $La_{0.40}Sr_{0.60}FeO_{3-\delta}$ [37,60]. By comparing the data obtained for LCF7525 in the present work with previous studies on $La_{1-x}Ca_xFeO_{3-\delta}$, $(0.10 \leq x \leq 0.20)$ [24,25], it is evident that δ increases with increasing Ca-concentration. The oxygen nonstoichiometry of

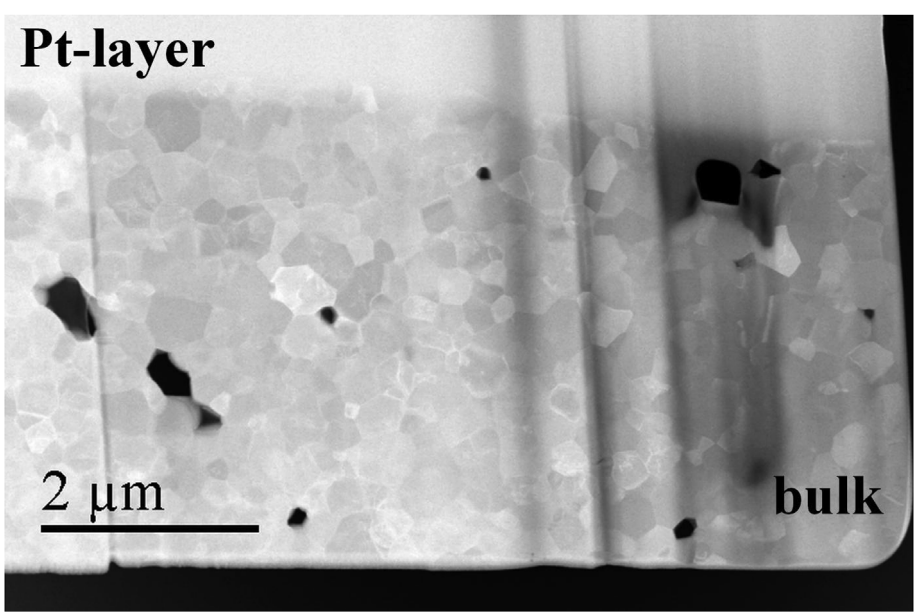

Fig. 3. Cross-sectional STEM-ADF image of the fresh LCF7525 specimen; the Pt-layer on top was deposited during the preparation of the TEM-lamella.

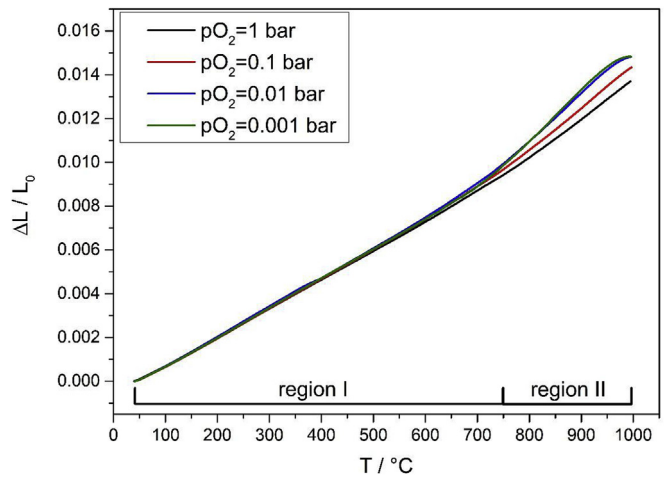

Fig. 4. Thermal expansion curves of LCF7525 as a function of temperature at different oxygen partial pressures; thermal expansion coefficients for temperature region I (30–750 °C) and II (750–1000 °C) are given in Table 4.

Table 4
Thermal expansion coefficients of LCF7525 for the temperature ranges 30–750 °C (I) and 750–1000 °C (II) at different oxygen partial pressures; The specified errors represent twofold standard deviations.

pO_2/bar	TEC(I)/10^{-6} K^{-1}	TEC(II)/10^{-6} K^{-1}
1	13.3 ± 0.03	17.5 ± 0.1
0.1	13.6 ± 0.05	18.9 ± 0.1
0.01	14.0 ± 0.07	19.7 ± 0.3
0.001	13.9 ± 0.06	19.9 ± 0.4

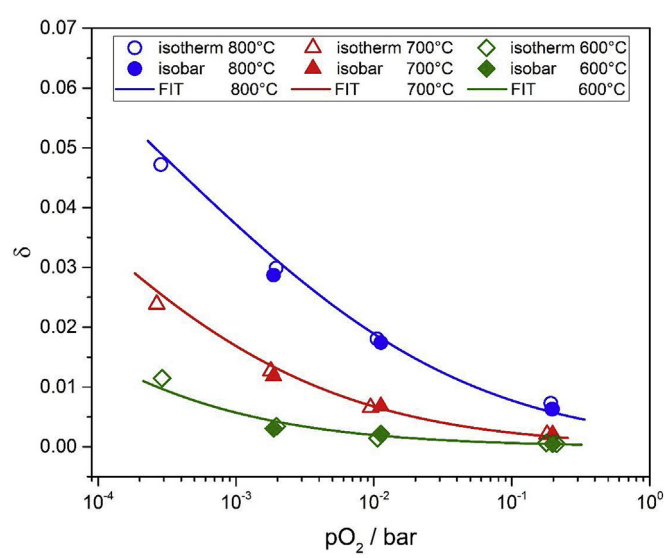

Fig. 5. Oxygen non-stoichiometry of LCF7525 as a function of the oxygen partial pressure at different temperatures; data points were obtained from isothermal and isobaric measurements; lines are nonlinear least squares fits to the point defect model.

LCF7525 can be described as a function of pO_2 by an ideal point defect model, which was developed by Mizusaki et al. [61]. Defect chemical modelling was performed as reported in Ref. [25]. The resulting fits of the defect model to the experimental data are shown in Fig. 5. The thermodynamic equilibrium constants K_{red}, obtained as fit parameters from the point defect model at different temperatures, are shown in Table S-2 (supplementary material).

3.4. Mass and charge transport properties

The chemical surface exchange coefficients k_{chem} and the chemical diffusion coefficients D_{chem} of oxygen of LCF7525 are given in Fig. 6 and Fig. 7 as functions of temperature (600–800 °C) at different oxygen partial pressures ($1 \times 10^{-3} \leq pO_2/bar \leq 0.1$). The kinetic parameters obtained from oxidation and reduction experiments at a certain temperature and pO_2 are in good agreement with each other. The highest

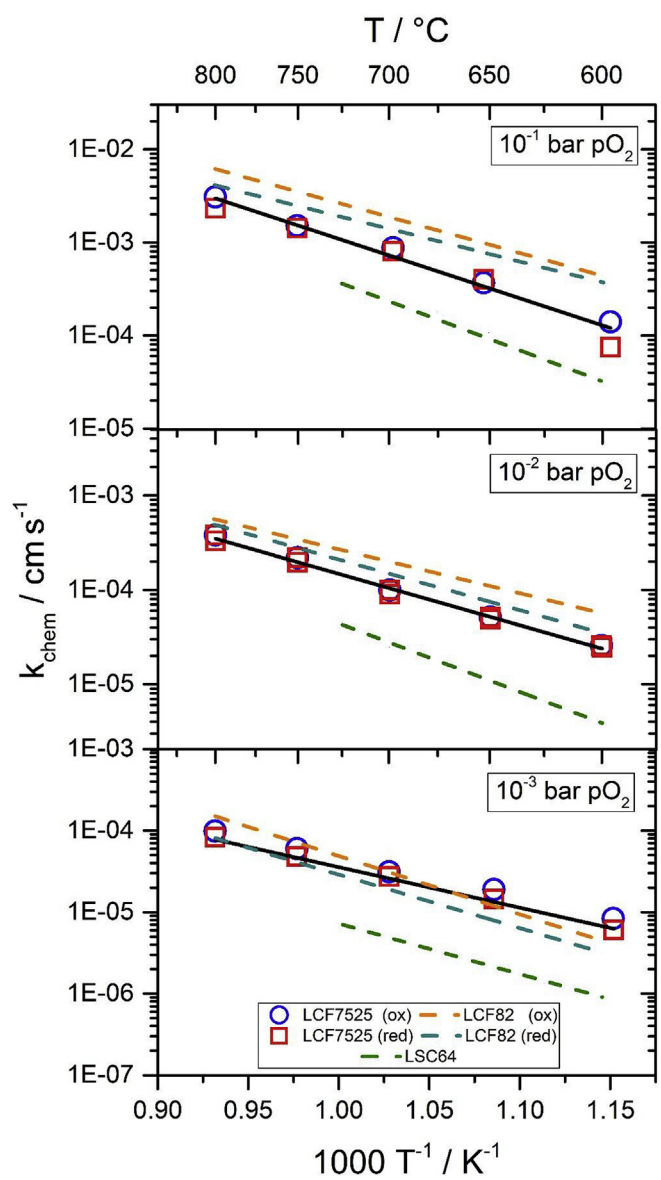

Fig. 6. Arrhenius plots of the chemical surface exchange coefficients of oxygen of LCF7525 at different oxygen partial pressures; data of LCF82 [25] and LSC64 [62] are shown in comparison; activation energies for LCF7525 are given in Table 5.

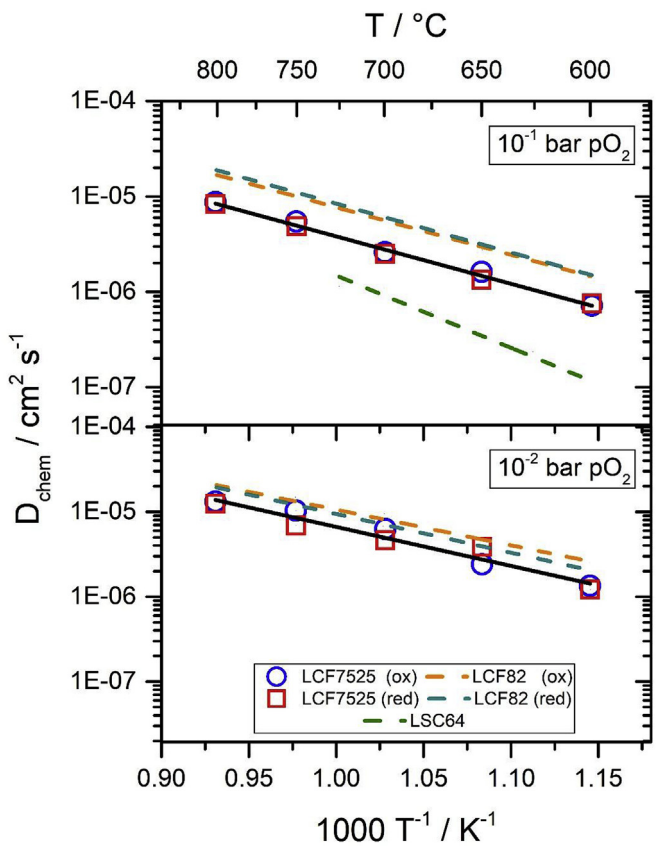

Fig. 7. Arrhenius plots of the chemical diffusion coefficients of oxygen of LCF7525 at different oxygen partial pressures; data of LCF82 [25] and LSC64 [62] are shown in comparison; activation energies for LCF7525 are given in Table 5.

value for $k_{chem} = 3 \times 10^{-3}$ cm s^{-1} was obtained at $pO_2 = 0.1$ bar and T = 800 °C. Values for k_{chem} decrease with decreasing oxygen partial pressure from 0.1 to 1×10^{-3} bar, whereas D_{chem} is almost independent of pO_2 at 0.1 to 1×10^{-2} bar. In Figs. 6 and 7, the kinetic parameters of LCF7525 are compared with those of the state-of-the-art SOFC cathode material $La_{0.60}Sr_{0.40}CoO_{3-\delta}$ (LSC64) [62] and those of LCF82 [25] (all data shown in Figs. 6 and 7 were obtained in-house with the same experimental setup). The values of k_{chem} and D_{chem} of LCF7525 are slightly lower than those of LCF82, but higher than those of LSC64 [62]. However, especially with k_{chem}, it should be considered that comparison of different datasets from the literature may be difficult. Even with the same compound, experimental data obtained by different groups under identical measurement conditions (same temperature and pO_2) may show large deviations. This is usually due to the strong influence of sample pretreatment, as k_{chem} is very sensitive to trace impurities introduced during preparation procedures or measurements. Another influencing factor are changes in k_{chem} over time, which arise during the measurements, when T- or pO_2-runs are performed for days or weeks. For this reason, we intentionally compare only the datasets for LCF7525, LCF82, and LSC64 obtained in our lab, in order to minimize potential issues arising from differences in the sample pretreatment and impurities introduced through contacting pastes, test gases, sample holder, etc.

Self-diffusion coefficients of oxygen D_O were estimated from the measured chemical diffusion coefficients of oxygen according to the relation $D_{chem} = \gamma_O D_O$, where γ_O is the thermodynamic factor of oxygen, which is given by Equation (2) [63–65].

$$\gamma_O = \frac{1}{2}\left(\frac{\partial \ln pO_2}{\partial \ln c_O}\right)_T = \frac{1}{2}\left(\frac{\partial \ln pO_2}{\partial \ln(3-\delta)}\right)_T \tag{2}$$

The concentration of the oxygen ions c_O was obtained from experimental data of the oxygen nonstoichiometry δ. Values for the self-diffusion coefficients for oxygen vacancies D_V were obtained from the relation $D_{chem} = \gamma_V D_V$, with the thermodynamic factor γ_V given by Equation (3)

$$\gamma_V = -\frac{1}{2}\left(\frac{\partial \ln pO_2}{\partial \ln c_V}\right)_T = -\frac{1}{2}\left(\frac{\partial \ln pO_2}{\partial \ln \delta}\right)_T. \tag{3}$$

The thermodynamic factors of oxygen and oxygen vacancies are summarized in Table S-3 (supplementary material). A comparison of the thermodynamic factors of selected compounds from the $La_{1-x}Ca_xFeO_{3-\delta}$ series ($0.10 \le x \le 0.25$) is given in Figure S-6 (supplementary material).

Calculated values of the self-diffusion coefficients of LCF7525 are given in Fig. 8a. The activation energies for D_O and D_V are shown in Table 5. The oxygen vacancy diffusion coefficients of LCF7525 are similar to data reported earlier for LCF91 [24] and LCF82 [25]. The oxygen surface exchange coefficients k_O (estimated from $k_{chem} \approx k_O \gamma_O$) are shown in Fig. 8b. The activation energies of k_O are given in Table 5.

The electronic conductivity σ_e of LCF7525 is given as a function of temperature at different oxygen partial pressures in Fig. 9a. The maximum electronic conductivity of $\sigma_e = 115$ S cm^{-1} is reached at 700 °C and $pO_2 = 0.1$ bar. The activation energies for electronic conduction were obtained from the slopes of $\ln(\sigma_e T)$ vs. T^{-1} plots, and are summarized in Table 5. In comparison with LCF91 and LCF82, LCF7525 shows the highest electronic conductivities (Fig. 9a).

The ionic conductivities σ_{ion} of LCF7525 were estimated via the Nernst-Einstein relation (neglecting contributions from the correlation factor and the Haven ratio) [62,66,67].

$$\sigma_{ion} = \frac{4F^2 c_O D_O}{RT} \tag{4}$$

The values of σ_{ion} obtained for LCF7525 at 600–800 °C and 10^{-1} to 10^{-2} bar pO_2 are given in Fig. 9b. Data from the literature for selected oxygen ion conductors (solid electrolytes) and mixed ionic-electronic conductors (MIECs) [24,25,68,69] are shown in comparison (Fig. 9b). At 800 °C and $pO_2 = 0.1$ bar, the ionic conductivity of LCF7525 is higher than that of LCF91 and LCF82, and lower than that of LSC64 (at $pO_2 = 0.2$ bar).

4. Summary and conclusions

The Sr- and Co-free perovskite $La_{0.75}Ca_{0.25}FeO_{3-\delta}$ (LCF7525) was synthesized and characterised with respect to crystal structure, chemical composition, microstructure, thermal expansion behaviour, oxygen exchange kinetics, oxygen nonstoichiometry, and electronic as well as ionic conductivities. LCF7525 crystallizes in the perovskite structure within the orthorhombic space group *Pnma*. The material shows fast oxygen exchange kinetics with maximum values of $k_{chem} = 3 \times 10^{-3}$ cm s^{-1} and $D_{chem} = 9 \times 10^{-6}$ cm^2 s^{-1} at 800 °C and $pO_2 = 0.1$ bar. The electronic conductivity is in the range of $107 \le \sigma_e$/S cm^{-1} ≤ 110 at $800 \le T/°C \le 600$ and $pO_2 = 0.1$ bar. The thermal expansion coefficient is 13–14 $\times 10^{-6}$ K^{-1} at 20–750 °C and $1 \times 10^{-3} \le pO_2$/bar ≤ 1 and thus close to the TECs of solid electrolytes like 8YSZ and GDC. The oxygen nonstoichiometry of LCF7525 is $0 \le \delta < 0.05$ at 20–800 °C and $2 \times 10^{-4} \le pO_2$/bar $\le 2 \times 10^{-1}$ and can be described by an ideal point defect model. Ionic conductivities were estimated from the chemical diffusion coefficients with a maximum value of $\sigma_{ion} = 1 \times 10^{-2}$ S cm^{-1} at 800 °C and $pO_2 = 0.01$ bar. Due to these results, LCF7525 may be considered a promising Sr- and Co-free material for SOFC and SOEC air electrodes. However, it should be emphasized that further experiments, especially cell tests, are required to assess the electrochemical performance of porous LCF7525 electrodes. In addition, the reactivity of LCF7525 with common solid electrolyte materials such as YSZ, GDC, or LSGM needs to be tested with respect to formation of

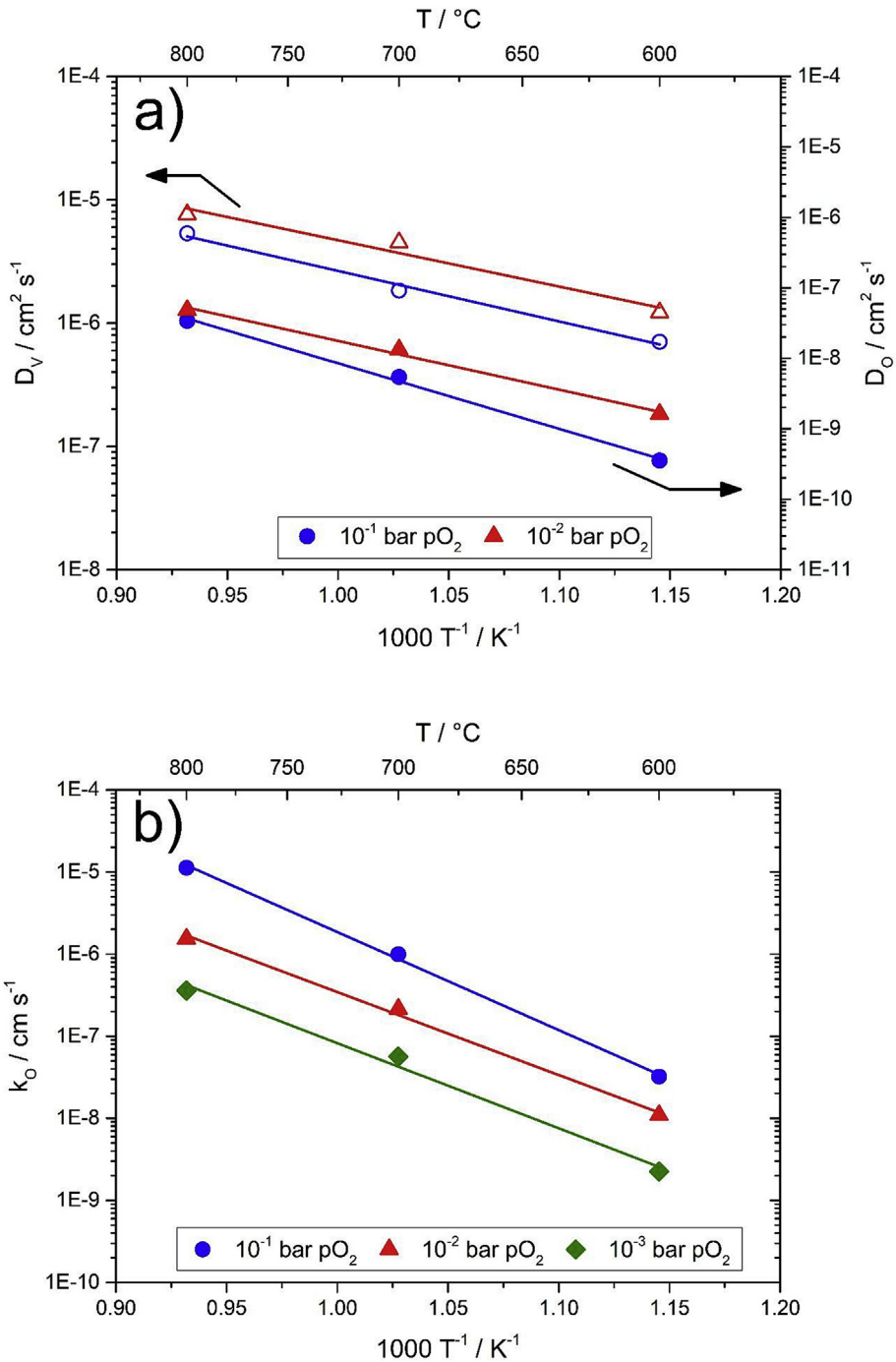

Fig. 8. a) Arrhenius plot of the self-diffusion coefficients of oxygen and oxygen vacancies of LCF7525 at different oxygen partial pressures; b) Arrhenius plot of the surface exchange coefficients of oxygen; activation energies are given in Table 5.

Table 5
Activation energies of various material parameters of LCF7525 at different oxygen partial pressures.

Parameter	E_a/kJ mol^{-1}		
	$pO_2 = 0.1$ bar	$pO_2 = 0.01$ bar	$pO_2 = 0.001$ bar
σ_e	17 ± 1	14 ± 1	9 ± 2
k_{chem}	128 ± 9	102 ± 3	102 ± 2
k_O	229 ± 8	194 ± 10	199 ± 17
D_{chem}	100 ± 4	85 ± 3	–
D_O	178 ± 8	133 ± 9	–
D_V	79 ± 6	72 ± 12	–
σ_{ion}	178 ± 30	161 ± 13	–

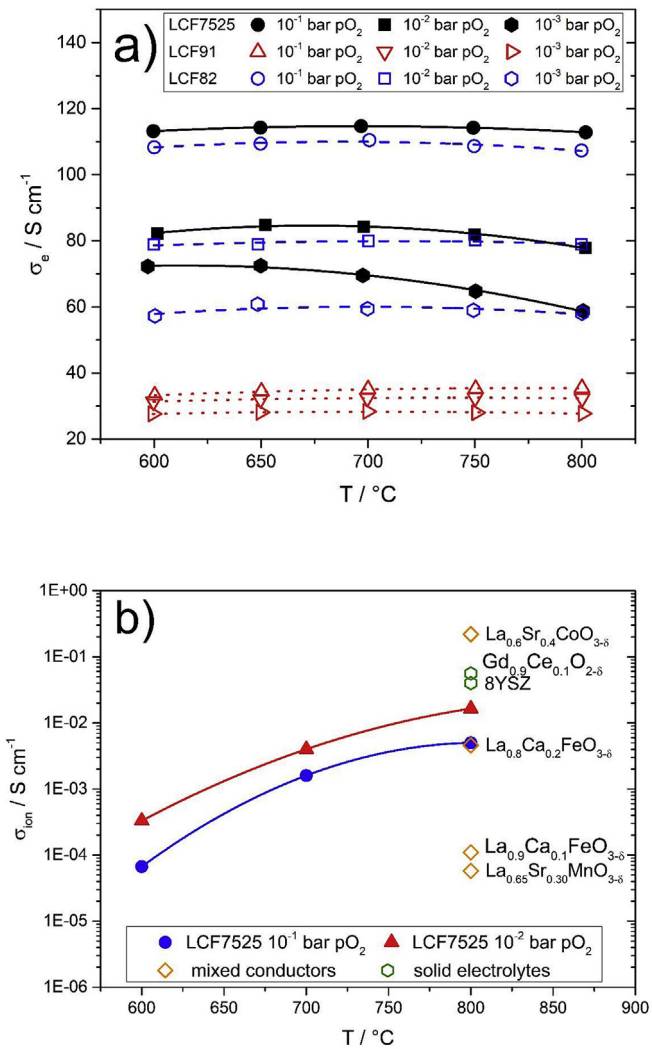

Fig. 9. a) Electronic conductivities of LCF7525 as a function of temperature at different oxygen partial pressures; data of LCF82 [25] and LCF91 [24] are given in comparison; b) ionic conductivities of LCF7525 as a function of temperature at different oxygen partial pressures; data of solid electrolytes ($Gd_{0.90}Ce_{0.10}O_{2-\delta}$ [69] at $pO_2 = 0.2$ bar, 8YSZ at $pO_2 = 0.2$ bar [69]) and mixed conductors ($La_{0.65}Sr_{0.30}MnO_{3-\delta}$ at $pO_2 = 0.2$ bar [68], LCF91 at $pO_2 = 0.1$ bar [24], LSC64 at $pO_2 = 0.2$ bar [68], LCF82 at $pO_2 = 0.1$ bar [25]) are given in comparison; activation energies for LCF7525 are given in Table 5.

secondary phases at the air electrode-electrolyte interface during sintering or longer operation times.

Acknowledgements

Financial support by the Austrian Ministry for Transport, Innovation and Technology (bmvit) and AVL List GmbH (Austria) within the program 'Mobilität der Zukunft' (project no. 845334) and 'Energieforschung (e!MISSION)' (project no. 853626) is gratefully acknowledged. Furthermore, the authors would like to thank Ms. Christina Nader for laboratory work assistance, Mrs. Karin Stanglauer for EDX analysis, Mr. Gerhard Hawranek for SEM analysis (all Montanuniversitaet Leoben), and Mrs. Martina Dienstleder (Graz Centre for Electron Microscopy) for the FIB preparation.

Appendix A. Supplementary data

Supplementary data to this article can be found online at https://doi.org/10.1016/j.jssc.2019.02.032.

References

[1] K. Kendall, M. Kendall (Eds.), High-temperature Solid Oxide Fuel Cells for the 21st Century, Academic Press, Oxford, UK, 2016.
[2] K.-D. Kreuer (Ed.), Fuel Cells - Selected Entries from the Encyclopedia of Sustainability Science and Technology, Springer-Verlag, New York, 2013.
[3] S.C. Singhal, K. Kendall, High Temperature Solid Oxide Fuel Cells: Fundamentals, Design and Applications, Elsevier Advanced Technology, The Boulevard, Langford lane, Kidlington, Oxford OX5, UK, 2004.
[4] S.D. Ebbesen, S.H. Jensen, A. Hauch, M.B. Mogensen, Chem. Rev. 114 (21) (2014) 10697.
[5] M.A. Laguna-Bercero, J. Power Sources 203 (2012) 4.
[6] J.B. Hansen, Faraday Discuss 182 (2015) 9.
[7] P.A.W. van der Heide, Surf. Interface Anal. 33 (5) (2002) 414.
[8] G.M. Rupp, H. Téllez, J. Druce, A. Limbeck, T. Ishihara, J. Kilner, J. Fleig, J. Mater. Chem. A 3 (45) (2015) 22759.
[9] W. Araki, M. Miyashita, Y. Arai, Solid State Ionics 290 (2016) 18.
[10] H. Ding, A.V. Virkar, M. Liu, F. Liu, Phys. Chem. Chem. Phys. 15 (2013) 489.
[11] Z. Cai, M. Kubicek, J. Fleig, B. Yildiz, Chem. Mater. 24 (6) (2012) 1116.
[12] M. Niania, R. Podor, T. Ben Britton, C. Li, S.J. Cooper, N. Svetkov, S. Skinner, J. Kilner, J. Mater. Chem. A 6 (2018) 14120–14135.
[13] N. Schrödl, E. Bucher, C. Gspan, A. Egger, C. Ganser, C. Teichert, F. Hofer, W. Sitte, Solid State Ionics 288 (2016) 14.
[14] C.C. Wang, K. O'Donnell, L. Jian, S.P. Jiang, J. Electrochem. Soc. 162 (6) (2015) F507.
[15] L. Zhao, J. Drennan, C. Kong, S. Amarasinghe, S.P. Jiang, J. Mater. Chem. A 2 (29) (2014) 11114.
[16] E. Bucher, C. Gspan, W. Sitte, Solid State Ionics 272 (2015) 112.
[17] C.C. Wang, K. Chen, S.P. Jiang, J. Electrochem. Soc. 161 (12) (2014) F1133.
[18] F. Wang, K. Yamaji, D.H. Cho, T. Shimonosono, M. Nishi, H. Kishimoto, M.E. Brito, T. Horita, H. Yokokawa, Fuel Cells 13 (4) (2013) 520.
[19] E. Bucher, C. Gspan, T. Höschen, F. Hofer, W. Sitte, Solid State Ionics 299 (2017) 26.
[20] N. Schrödl, E. Bucher, A. Egger, P. Kreiml, C. Teichert, T. Höschen, W. Sitte, Solid State Ionics 276 (2015) 62.
[21] E. Bucher, C. Gspan, F. Hofer, W. Sitte, Solid State Ionics 238 (2013) 15.
[22] E. Bucher, W. Sitte, F. Klauser, E. Bertel, Solid State Ionics 208 (2012) 43.
[23] E. Bucher, W. Sitte, F. Klauser, E. Bertel, Solid State Ionics 191 (2011) 61.
[24] C. Berger, E. Bucher, W. Sitte, Solid State Ionics 299 (2017) 46.
[25] C. Berger, E. Bucher, A. Windischbacher, A.D. Boese, W. Sitte, J. Solid State Chem. 259 (2018) 57.
[26] C. Berger, E. Bucher, C. Gspan, A. Menzel, W. Sitte, J. Electrochem. Soc. 164 (10) (2017) F3008.
[27] C. Berger, E. Bucher, C. Gspan, A. Menzel, W. Sitte, Solid State Ionics 326 (2018) 82.
[28] M.-H. Hung, M.V.M. Rao, D.-S. Tsai, Mater. Chem. Phys. 101 (2–3) (2007) 297.
[29] R. Andoulsi, K. Horchani-Naifer, M. Férid, Ceram. Int. 39 (6) (2013) 6527.
[30] M. James, D. Cassidy, D.J. Goossens, R.L. Withers, J. Solid State Chem. 177 (6) (2004) 1886.
[31] P.M. Price, D.P. Butt, J. Am. Ceram. Soc. 98 (9) (2015) 2881–2886.
[32] P.M. Price, E. Rabenberg, D. Thomsen, S.T. Misture, D.P. Butt, J. Am. Ceram. Soc. 97 (7) (2014) 2241.
[33] R.J.D. Tilley, Perovskites: Structure–Property Relationships, John Wiley & Sons, Ltd., 2016.
[34] Bruker AXS Topas V5, General Profile and Structure Analysis Software for Powder Diffraction Data, User's Manual, Karlsruhe, Germany, 2014.
[35] P. Paufler, Cryst. Res. Technol. 30 (4) (1995) 494.
[36] T.C. Geary, S.B. Adler, Solid State Ionics 253 (2013) 88.
[37] J. Mizusaki, M. Yoshihiro, S. Yamauchi, K. Fueki, J. Solid State Chem. 58 (1985) 257.
[38] M.V. Patrakeev, J.A. Bahteeva, E.B. Mitberg, I.A. Leonidov, V.L. Kozhevnikov, K.R. Poeppelmeier, J. Solid State Chem. 172 (2003) 219.
[39] W. Preis, M. Holzinger, W. Sitte, Monatsh. Chem. 132 (2001) 499.
[40] M.W. den Otter, H.J.M. Bouwmeester, B.A. Boukamp, H. Verweij, J. Electrochem. Soc. 148 (2) (2001) J1.
[41] W. Preis, E. Bucher, W. Sitte, J. Power Sources 106 (2002) 116.
[42] W. Preis, E. Bucher, W. Sitte, Solid State Ionics 175 (2004) 393.
[43] J.M. Serra, V.B. Vert, M. Betz, V.A.C. Haanappel, W.A. Meulenberg, F. Tietz, J. Electrochem. Soc. 155 (2) (2008) B207.
[44] T. Sato, S. Takagi, S. Deledda, B.C. Hauback, S.-I. Orimo, Sci. Rep. 6 (2016) 23592.
[45] R.D. Shannon, Acta Crystallogr. A 32 (1976) 751.
[46] H. Falcón, A.E. Goeta, G. Punte, R.E. Carbonio, J. Solid State Chem. 133 (2) (1997) 379.
[47] S. Jerban, S. Elkoun, Mater. Char. 119 (2016) 216.
[48] W. Lee, J.W. Han, Y. Chen, Z. Cai, B. Yildiz, J. Am. Chem. Soc. 135 (21) (2013) 7909.
[49] T. Horita, M. Ishikawa, K. Yamaji, N. Sakai, H. Yokokawa, M. Dokiya, Solid State Ionics 124 (3) (1999) 301.
[50] T. Horita, N. Sakai, T. Kawada, H. Yokokawa, M. Dokiya, J. Am. Ceram. Soc. 81 (2) (1998) 315.
[51] M. Kubicek, G.M. Rupp, S. Huber, A. Penn, A. Opitz, J. Bernardi, M. Stöger-Pollach, H. Hutter, J. Fleig, Phys. Chem. Chem. Phys. 16 (6) (2014) 2715.
[52] N.Q. Minh, T. Takahashi, in: N.Q.M. Takahashi (Ed.), Science and Technology of Ceramic Fuel Cells, Elsevier Science Ltd, Oxford, 1995, pp. 69–116.
[53] S.J. Hong, A.V. Virkar, J. Am. Ceram. Soc. 78 (2) (1995) 433.

[54] V.V. Kharton, A.A. Yaremchenko, E.N. Naumovich, J. Solid State Electrochem. 3 (1999) 303.
[55] S.R. Bishop, K.L. Duncan, E.D. Wachsman, J. Am. Ceram. Soc. 93 (12) (2010) 4115.
[56] H.L. Lein, K. Wiik, T. Grande, Solid State Ionics 177 (19–25) (2006) 1795.
[57] C. Chatzichristodoulou, P. Norby, P.V. Hendriksen, M.B. Mogensen, J. Electroceram. 34 (1) (2015) 100.
[58] W. Sitte, E. Bucher, W. Preis, Solid State Ionics 154–155 (2002) 517.
[59] A.N. Petrov, V.A. Cherepanov, O.F. Kononchuk, L.Y. Gavrilova, J. Solid State Chem. 87 (1990) 69.
[60] O. Bartels, K.D. Becker, E. Bucher, W. Sitte, Solid State Ionics 177 (19–25) (2006) 1677.
[61] J. Mizusaki, Y. Mima, S. Yamauchi, K. Fueki, H. Tagawa, J. Solid State Chem. 80 (1989) 102.
[62] A. Egger, E. Bucher, M. Yang, W. Sitte, Solid State Ionics 225 (2012) 55.
[63] J.E. ten Elshof, M.H.R. Lankhorst, H.J.M. Bouwmeester, J. Electrochem. Soc. 144 (3) (1997) 1060.
[64] J.A. Lane, S.J. Benson, D. Waller, J.A. Kilner, Solid State Ionics 121 (1999) 201.
[65] R. Merkle, J. Maier, J. Fleig, in: W. Vielstich, H. Yokokawa, H.A. Gasteiger (Eds.), Handbook of Fuel Cells - Fundamentals, Technology and Applications, John Wiley & Sons, Ltd., 2009, pp. 425–440.
[66] E. Bucher, A. Egger, P. Ried, W. Sitte, P. Holtappels, Solid State Ionics 179 (2008) 1032.
[67] V.V. Vashook, M. Al Daroukh, H. Ullmann, Ionics 7 (2001) 59.
[68] E.V. Tsipis, V.V. Kharton, J. Solid State Electrochem. 12 (2008) 1039.
[69] V.V. Kharton, F.M.B. Marques, A. Atkinson, Solid State Ionics 174 (1–4) (2004) 135.
[70] K. Momma, F. Izumi, J. Appl. Crystallogr. 44 (2011) 1272.
[71] J.M. Hudspeth, G.A. Stewart, A.J. Studer, D.J. Goossens, J. Phys. Chem. Solid. 72 (12) (2011) 1543.
[72] H.M. Taguchi, Y. Hirota, K. Yamaguchi, Mater. Res. Bull. 40 (2005) 773.

Supplementary Material

Crystal structure, oxygen nonstoichiometry, and mass and charge transport properties of the Sr-free SOFC/SOEC air electrode material $La_{0.75}Ca_{0.25}FeO_{3-\delta}$

Christian Berger [a], Edith Bucher [a,*], Christian Gspan [b], Werner Sitte [a]

[a] *Chair of Physical Chemistry, Montanuniversitaet Leoben, Franz-Josef-Straße 18, A-8700 Leoben, Austria*

[b] *Institute of Electron Microscopy and Nanoanalysis (FELMI), Graz University of Technology & Graz Centre for Electron Microscopy (ZFE), Austrian Cooperative Research (ACR) Steyrergasse 17, A-8010 Graz, Austria*

Contents

1. Sample preparation and microstructural analysis 3

1.1 Powder processing 3

1.2 Surface and bulk analysis of LCF7525 4

2. Thermal analysis 7

2.1 Differential scanning calorimetry 7

2.2 Thermogravimetry 8

3. Defect chemistry 9

4. Thermodynamic factors 9

References 11

1. Sample preparation and microstructural analysis

1.1 Powder processing

The particle size distribution (PSD) of the calcined $La_{0.75}Ca_{0.25}FeO_{3-\delta}$ (LCF7525) powder shows a broad bimodal distribution with d_{50} = 24.8 µm. For the milling procedure, 10 g of the calcined powder, 100 g of ethanol, and 190 g of zirconia grinding balls (3 mm in diameter) were put in a 500 ml polyethylene bottle on a benchtop roller system for 48 h with a rotation speed of 300 rpm (rotations per minute). After this procedure, the PSD was monomodal with d_{50} = 0.55 µm as shown in Figure S-1.

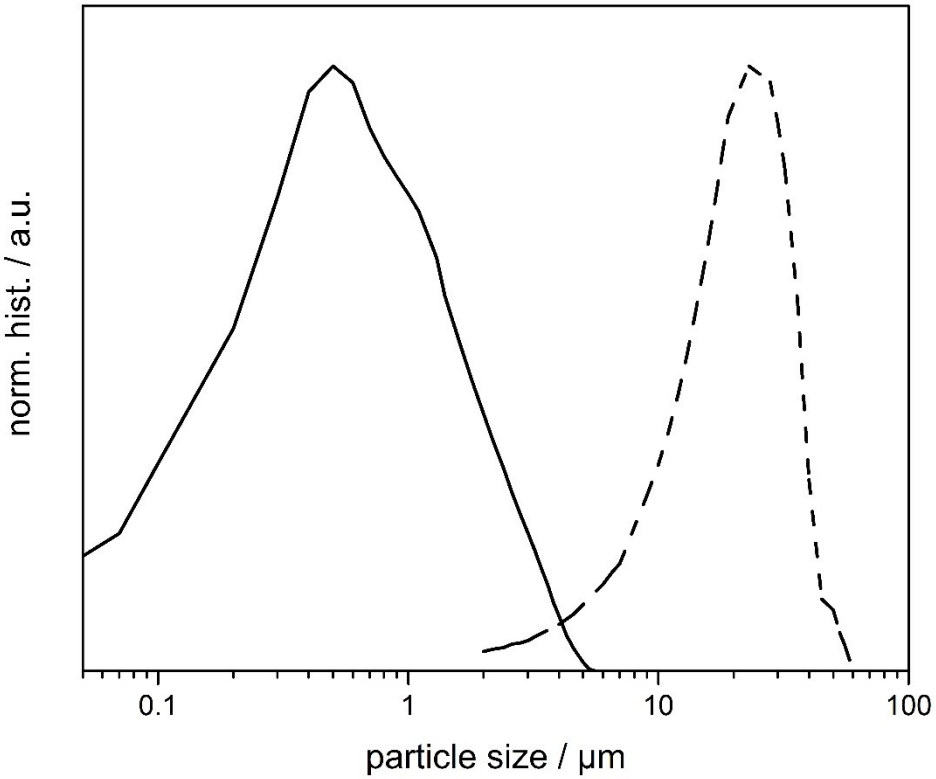

Figure S-1. Particle size distribution of the calcined LCF7525 powder (dashed line) and after 48 h of milling (solid line).

1.2 Surface and bulk analysis of LCF7525

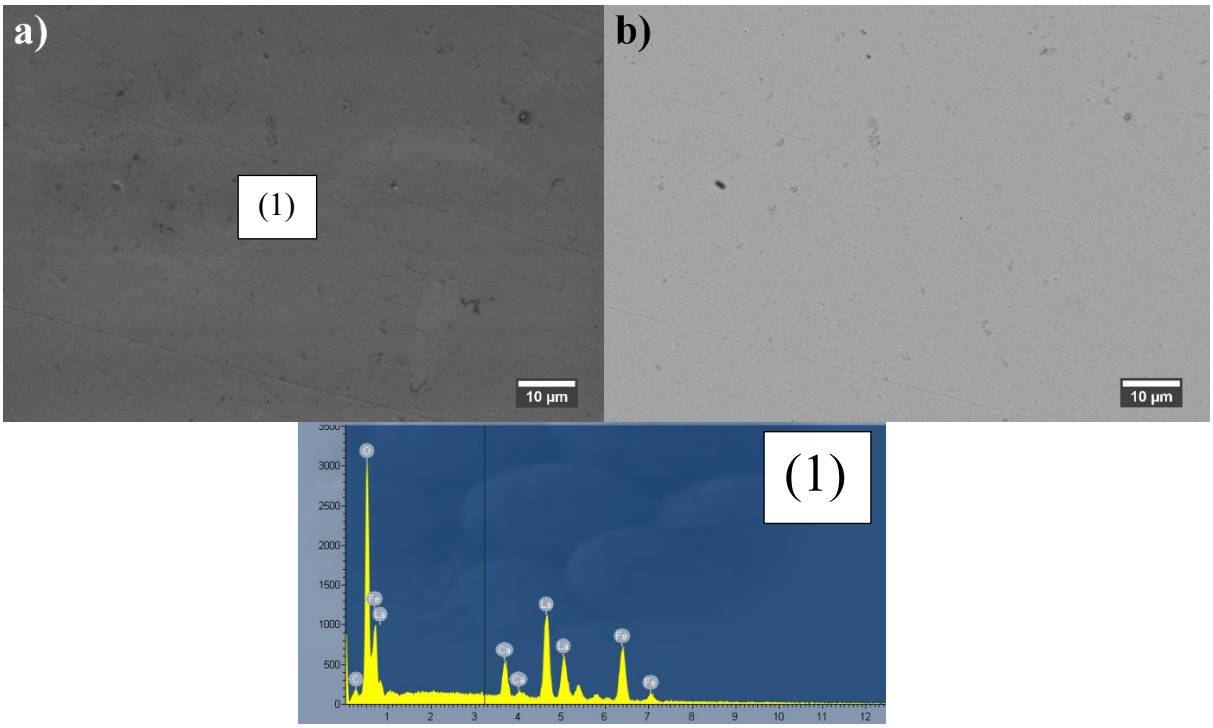

Figure S-2. Secondary electron microscopy (SEM) images from the surface of the fresh polished LCF7525 specimen a) in secondary electron imaging mode, and b) in backscattered electron imaging mode; the energy dispersive X-ray spectrum (EDXS) of the fresh sample surface shows only the expected elements La-Ca-Fe-O (1). The energy in the EDXS is given in keV.

Table S-1. Cation stoichiometry of sintered LCF7525 pellet; measured atomic percent as obtained from EDX analyses are compared to theoretical values calculated from the nominal composition. The measurement uncertainty is estimated to ± (2-3) at-%.

Element	Measured / at-%	Theoretical / at-%
La L	37.6	37.5
Ca K	11.6	12.5
Fe K	50.8	50.0

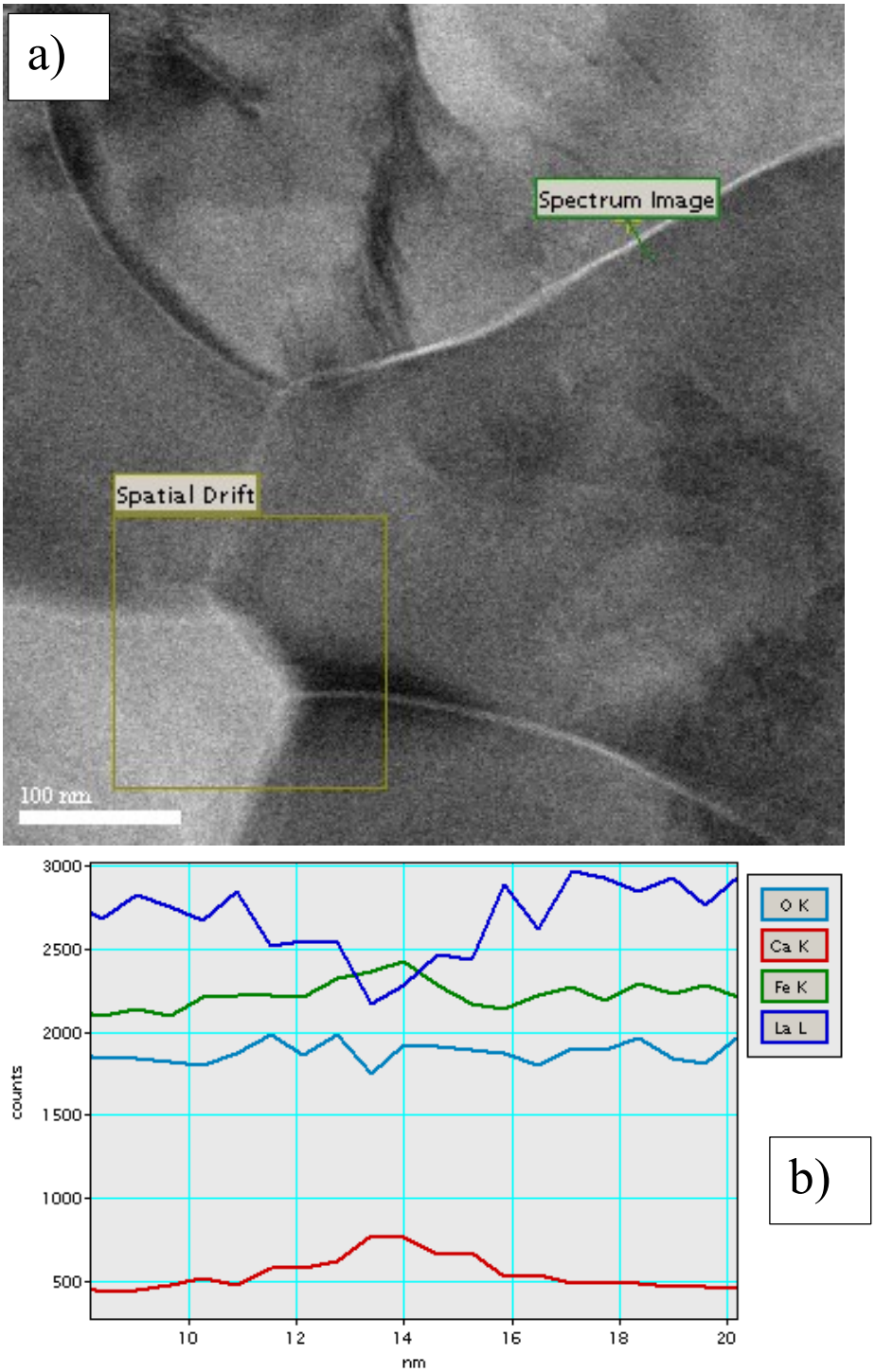

Figure S-3. a) Cross-sectional scanning transmission electron microscopy image acquired with bright field detector (STEM-BF); b) The EDX line scan across the green line marked in image a) shows a slight enrichment of Ca and Fe along the grain boundary.

2. Thermal analysis

2.1 Differential scanning calorimetry

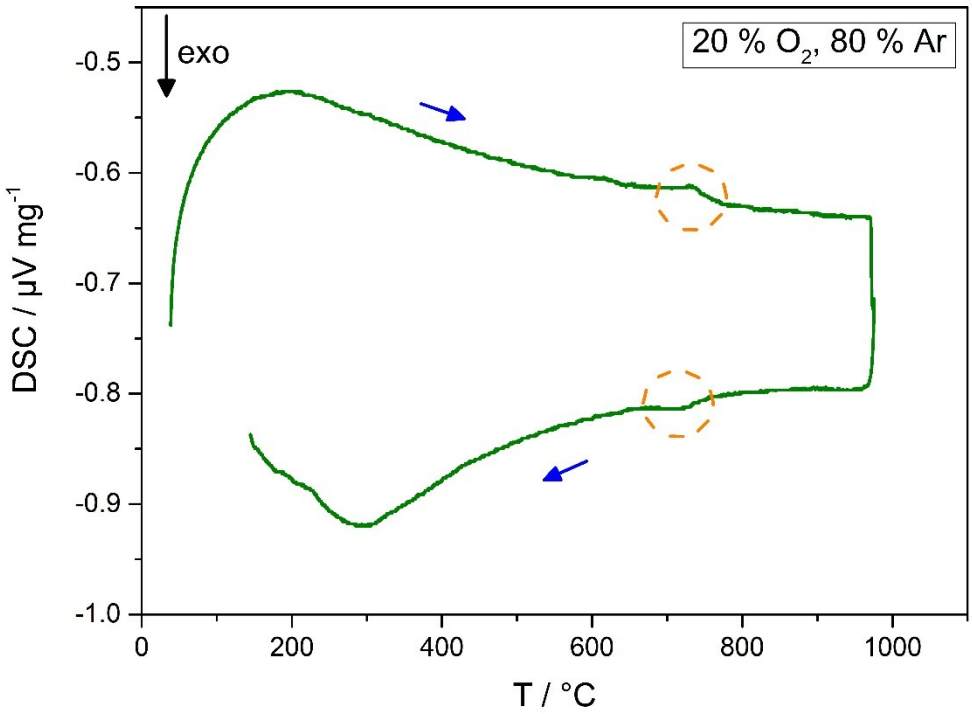

Figure S-4. Differential scanning calorimetry of LCF7525 in 20 % O_2 (rest Ar); the peaks at approximately 750°C (highlighted with dashed circles) are due to the reversible phase transformation from the orthorhombic to the rhombohedral modification, which was also reported by Price et al. for similar lanthanum calcium ferrite compounds [1]. The blue arrows indicate the heating and cooling sequence.

2.2 Thermogravimetry

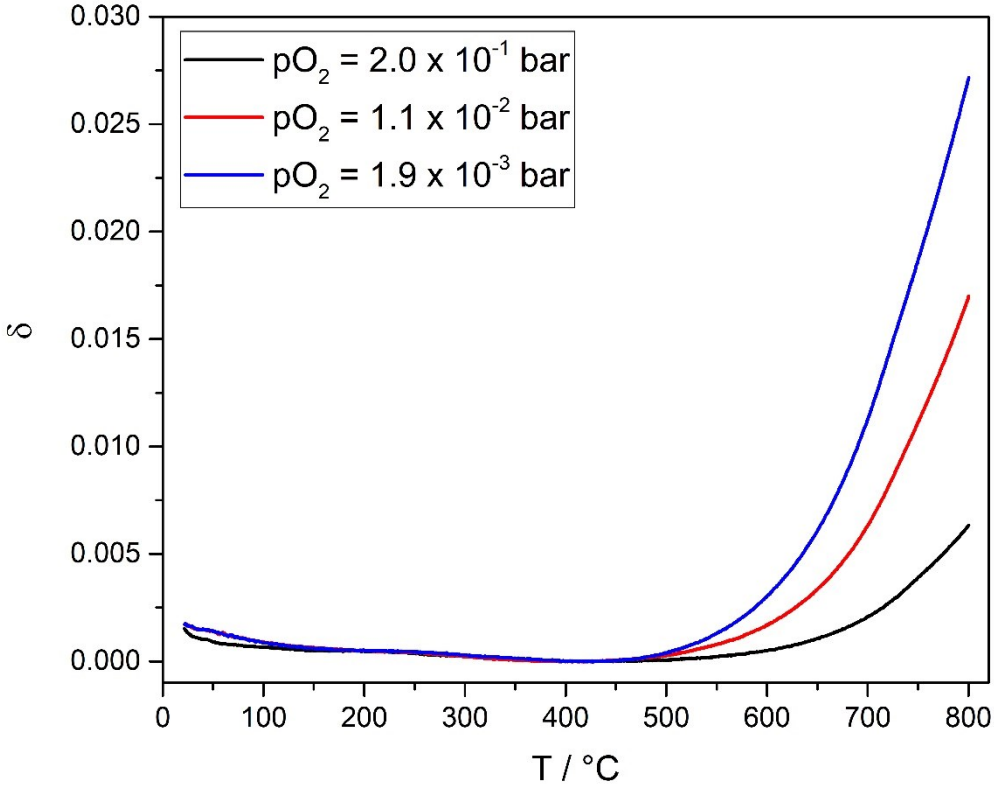

Figure S-5. Oxygen nonstoichiometry of LCF7525 as a function of temperature at different oxygen partial pressures.

3. Defect chemistry

Table S-2. Fit parameters obtained from the point defect model of LCF7525 at different temperatures.

T / °C	K_{red}	Standard error*
600	6.16×10^{-4}	5.47×10^{-4}
700	2.35×10^{-3}	1.12×10^{-3}
800	8.75×10^{-3}	1.48×10^{-3}

$$*Standard\ error = \sqrt{\frac{\sum_{i=1}^{n}(\delta_{calc}-\delta_{meas})^2}{n}};$$

4. Thermodynamic factors

Table S-3. Thermodynamic factors of oxygen (γ_O) and oxygen vacancies (γ_V) of LCF7525 at different temperatures.

T / °C	γ_O	γ_V
600	2490 ± 300	1.25 ± 0.10
700	452 ± 73	1.33 ± 0.03
800	252 ± 23	1.60 ± 0.06

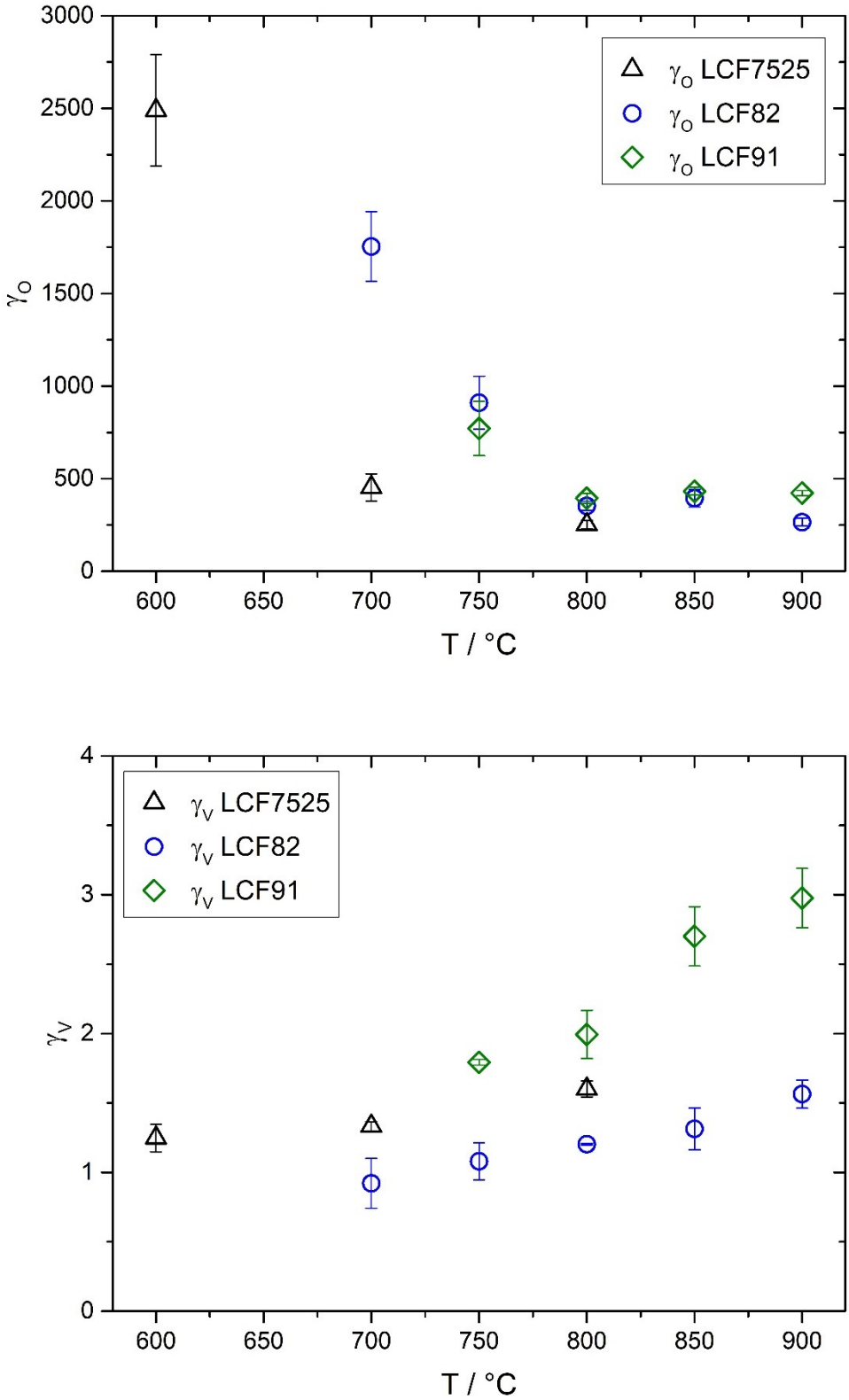

Figure S-6. Thermodynamic factors of oxygen (γ_O) and oxygen vacancies (γ_V) of LCF7525 (this work), $La_{0.8}Ca_{0.2}FeO_{3-\delta}$ (LCF82) [2], and $La_{0.9}Ca_{0.1}FeO_{3-\delta}$ (LCF91) [3].

References

[1] P.M. Price, E. Rabenberg, D. Thomsen, S.T. Misture, D.P. Butt, *Journal of the American Ceramic Society* **97** (2014) (7) 2241.

[2] C. Berger, E. Bucher, A. Windischbacher, A.D. Boese, W. Sitte, *Journal of Solid State Chemistry* **259** (2018) 57.

[3] C. Berger, E. Bucher, W. Sitte, *Solid State Ionics* **299** (2017) 46.